

$Zn_{1-x}Cd_xS$ SEMICONDUCTOR NANOSTRUCTURES FOR OPTOELECTRONIC APPLICATIONS

A THESIS

*Submitted in partial fulfilment of the
requirements for the award of the degree*

of

DOCTOR OF PHILOSOPHY

in

ELECTRICAL ENGINEERING

by

SONAL SINGHAL



DEPARTMENT OF ELECTRICAL ENGINEERING
INDIAN INSTITUTE OF TECHNOLOGY ROORKEE
ROORKEE-247 667 (INDIA)

JUNE, 2011

**©INDIAN INSTITUTE OF TECHNOLOGY ROORKEE, ROORKEE, 2011
ALL RIGHTS RESERVED**



INDIAN INSTITUTE OF TECHNOLOGY ROORKEE ROORKEE


CANDIDATE'S DECLARATION


I hereby certify that the work which is being presented in the thesis entitled "**Zn_{1-x}Cd_xS Semiconductor Nanostructures for Optoelectronic Applications**" in partial fulfilment of the requirements for the award of degree of Doctor of Philosophy, submitted in the Department of Electrical Engineering, Indian Institute of Technology Roorkee, Roorkee is an authentic record of my own work carried out during a period from July 2007 to June 2011 under the supervision of Dr. H. O. Gupta, Professor, Department of Electrical Engineering and Dr. Ramesh Chandra, Associate Professor, Institute Instrumentation Centre, Indian Institute of Technology Roorkee, Roorkee.

The matter embodied in this thesis has not been submitted by me for the award of any other degree of this or any other Institute.


(SONAL SINGHAL)

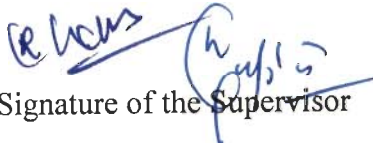
This is to certify that the above statement made by the candidate is correct to the best of our knowledge.



(Ramesh Chandra)
Supervisor



(H. O. Gupta)
Supervisor

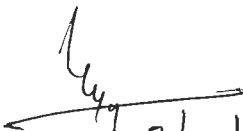
Date: ..30..6..2011

The Ph. D. Viva-Voce Examination of Ms. Sonal Singhal, Research Scholar, has been held on ..31..10..2011.


Signature of the Supervisor


Signature of the External Examiner


Chairman DRC


3/10/2011

ABSTRACT

In recent past, the understanding and applications of quantum-confined structures in the development of LEDs and PV devices has spurt interest in the studies of such structures. However, the difficulties faced in the fabrication of appropriate quantum-confined structures have hampered their applications in photonics and energy generations technologies. The difficulties such as, the size distribution; in the prepared samples and the dominance of the surface non-radiative recombination have been identified as the major limitations in their use in LEDs. Dominance of the non-radiative contribution from the surface states in undoped nanostructures forbids their applications in photonics. By the introduction of an impurity in a nanostructure, the dominant recombination can be transferred from the surface states to the impurity states. The best light emitters for display and lighting industry are the II–VI group semiconductors doped with the transition or rare earth impurities which incur localized states in the band gap. The physics and technology of doped nanostructures is in infancy and little effort has been made in this direction.

For the energy generation purposes, the nanostructured thin films provide more cost-effective solution and use a cheap support onto which the active component is applied as a thin coating. Solar cells, or photovoltaics (PV), convert the energy of the sun into electricity. In theory all parts of the visible spectrum from near-infrared to ultraviolet can be harnessed. The mainstay at present is use of CdS thin films as *n* partner of *p-n* junction of thin film solar cell structure. Nanotechnology (“nano”) incorporation into the films shows special promise to both; the enhanced efficiency and lower total cost. The energy band gap of various layers can be tailored to the desired value by varying the size of nano-particles. This allows for more design flexibility in the absorber and window layers in the solar cells.

Recent advances have demonstrated that it is an effective route to tune the energy band-gap and thus, emission wavelength by changing their constituent stoichiometries. II-VI group $Zn_{1-x}Cd_xS$ nanostructures are of considerable interest for a variety of optoelectronic applications. With increasing zinc content, a composition tunable emission across the whole visible spectrum can be obtained by a systematic blue-shift in the emission wavelength of $Zn_{1-x}Cd_xS$ ternary nanostructures.

$Zn_{1-x}Cd_xS$ semiconductor nanostructures are ubiquitous in photonic applications such as LED's because their properties may change when the luminescence transitions are modified by doping with external impurities. The energy of activator-related emission remains nearly unchanged while the excitation can be tuned by quantum confinement effects. On the other hand, an improvement in the photo-conversion efficiency of PV devices such as CdS/CdTe solar cell is expected if $Zn_{1-x}Cd_xS$ solid solution films are used in place of the CdS alone because of their higher forbidden gap. In hetero-junction solar cells, the part of the cell which serves as a window should have the highest forbidden gap possible.

This work includes preparation of uniform and luminescent $Zn_{1-x}Cd_xS$ nanoparticles via low temperature (280 K) co-precipitation technique. A detailed particle size investigation and studies on the optical and emission properties with variation in mole fraction (x) is carried out, to obtain a well characterized system apt to be used in light emitting applications. The lattice constant, a of $Zn_{1-x}Cd_xS$ nanoparticles, is found to obey the Vegard's law and possesses a nearly linear relationship with x , indicates the successful formation of $Zn_{1-x}Cd_xS$ ternary semiconductor. Combination of XRD, UV-Vis and TEM methods allows a realistic statement on the particle size and is found in the range of 3.0 - 4.0 nm with relative standard deviation of 12-15%. It is shown that the as-prepared $Zn_{1-x}Cd_xS$ nanoparticles possess both: the quantum confinement effect (QCE) and the composition effect. Energy band gap is found to increase with increased QCE, while it decreases with increase in ' x '. Light emissions from $Zn_{1-x}Cd_xS$ nanoparticles are obtained in UV region via near band edge (NBE) transitions. Emissions in blue and green spectral regions are obtained via defect assisted transitions. QCE shifts the NBE emissions to higher energies compared to the absorption band of bulk counterpart, while it red-shifts with increase in x . Blue and green emission wavelengths do not change with QCE and composition. This study provides two-fold benefits: (i) as-prepared $Zn_{1-x}Cd_xS$ nanoparticles can be used as the target material for the preparation of their nanocrystalline thin films and, (ii) provides a framework by the preparation of host nanoparticles for their use in light emitting applications.

In next step, as-prepared nanoparticles are utilized as the target material for the synthesis of $Zn_{1-x}Cd_xS$ nanocrystalline thin films. The major focus is on the growth and characterizations of the micro structural features and optical properties of $Zn_{1-x}Cd_xS$ thin films fabricated by pulsed laser deposition technique. In particular, effect of pulsed laser deposition parameters such as laser flux density, working pressure, deposition

temperature and mole fraction on the structural, morphological and optical properties have been investigated. The variation in laser flux density provides regulation on surface roughness of deposited $Zn_{1-x}Cd_xS$ nanocrystalline thin films. The laser flux density at 3.33 J/cm^2 results in minimum rms surface roughness of $\sim 8.0 \text{ nm}$, and is attributed to moderate kinetic energies of the laser ablated plume species. The variation in working pressure provides a control on the particle size of $Zn_{1-x}Cd_xS$ nanocrystalline thin films. The wide-ranging particle sizes from ~ 15 to 80 nm are obtained with working pressure variation from 0.015 to 200 mtorr . Structural phase transformation from zincblende to wurtzite structure is obtained in the as-deposited $Zn_{1-x}Cd_xS$ nanocrystalline thin films. The structure transformation is found to depend on both: the deposition temperature and the mole fraction. It is established that the structure transformation temperature decreases with increase in mole fraction in $Zn_{1-x}Cd_xS$ nanocrystalline thin films. Values in parentheses ($0.1; > 400 \text{ }^\circ\text{C}$), ($0.3; > 300 \text{ }^\circ\text{C}$), ($0.5; > 200 \text{ }^\circ\text{C}$) shows the mole fractions and deposition temperatures at which zincblende to wurtzite structure transformation takes place. For mole fractions > 0.5 , the structure transformation is independent of deposition temperature and remains in wurtzite structure. The above findings provide well regulated/controlled properties of the as-deposited nanocrystalline thin films and provide a process window for fabrication of the full device structure.

$Zn_{1-x}Cd_xS$ nanostructures for light emitting applications have been achieved by successful incorporation of manganese as dopant in the $Zn_{1-x}Cd_xS$ host. An approach has been devised and tested to enhance the emission intensity by reducing the lattice mismatch between the host ($Zn_{1-x}Cd_xS$) and dopant (Mn^{2+}), thereby increasing the dopant concentration. Maximum of characteristic i.e. orange emission is obtained at mole fraction, $x = 0.45$, with 0.10% lattice mismatch between MnS and $Zn_{0.55}Cd_{0.45}S$. The maximum orange emission intensity of the order $\sim 10^5$ (counts) is obtained at $5 \text{ mol}\%$ manganese concentration from $Zn_{0.55}Cd_{0.45}S$ nanoparticles. The defect assisted i.e. blue and green emissions are significantly reduced in $Zn_{0.55}Cd_{0.45}S$ nanoparticles, suggesting the efficient transfer of carriers from host states to dopant incurred excited states. It is shown that manganese is homogeneously distributed in the lattice which rules out the possibility of concentration quenching at higher manganese concentration ($10 \text{ mol}\%$). It is therefore suggested that decline in the emission intensity at higher manganese concentration is due to the formation of separate MnS phase.

In further experiments an attempt has been made to increase the orange emission intensity via fabrication of core-shell nanostructures. An inorganic shell coating leads to an increase in emission intensity by effectively reducing the surface states. XRD of core-shell nanoparticles showed profound dependence of shell thickness characterized via systematic change in the peak shift from $Zn_{0.55}Cd_{0.45}S$ to ZnS phase with increase in shell to core (s/c) ratio from 0.05 to 1.0. Particle size differences between the core and the core-shell nanoparticles have been utilized to estimate the ZnS shell thickness. The shell thickness is estimated as ~ 0.55 nm at s/c ratio of 0.5. The enhancement in orange emission intensity (s/c ratio at 0.5) is ~ 15 times with respect to core nanoparticles. The Mn^{2+} doped $Zn_{0.55}Cd_{0.45}S$ nanocrystalline thin films are deposited at previously optimized pulsed laser deposition parameters. Deposition parameters such as laser flux density, deposition temperature, and working pressure are kept constant at 3.33 J/cm², 200 °C and 0.015 mtorr respectively. The orange emission intensity of the order $\sim 10^4$ (counts) is obtained from nanocrystalline thin films. It is found that orange emission from thin film structures decreases by a factor of ~ 5 when compared to the nanoparticles. In order to enhance the orange emission from $Zn_{0.55}Cd_{0.45}S:Mn$ nanocrystalline thin films, nanocomposites of $Zn_{0.55}Cd_{0.45}S:Mn$ and ZnS have been fabricated. Thickness of ZnS top layer has been varied and its effect on orange emission is investigated. The orange emission intensity enhancement from nanocomposite $Zn_{0.55}Cd_{0.45}S:Mn/ZnS$ increases by a factor of ~ 2 only. It is suggested that the enhanced orange emission in nanostructures is due to passivation of surface states and is justified by the electron affinity model.

The work on PV device includes the utilization of $Zn_{0.9}Cd_{0.1}S$ nanocrystalline thin films as the window layer of thin film solar cell structure. The $Zn_{0.9}Cd_{0.1}S$ nanocrystalline thin films were deposited at 3.33 J/cm² laser flux density and 200 mtorr working pressure, so as to obtain minimal surface roughness and particle size of ~ 80 nm. The work on PV devices is divided into two parts. The first part established a test by which the uniform coverage by $Zn_{0.9}Cd_{0.1}S$ on the indium tin oxide (ITO) (front contact) is examined. This test is undertaken in order to probe the area for back contact deposition. Gold (Au) is used for this purpose because it makes a Schottky contact with $Zn_{0.9}Cd_{0.1}S$. The test on the uniform coverage by $Zn_{0.9}Cd_{0.1}S$ on ITO is performed by gauging the $I-V$ characteristics of Au/ $Zn_{0.9}Cd_{0.1}S$ /ITO structure. The direct contact between Au and ITO results in Ohmic $I-V$ characteristic and detects the presence of pin holes in $Zn_{0.9}Cd_{0.1}S$ films. The appearance of Schottky characteristic shows the uniform coverage of ITO by $Zn_{0.9}Cd_{0.1}S$ film. Use of this test allowed the optimization of cell preparation method, which led to the

fabrication of devices having a low density of pinholes. The interface between $Zn_{0.9}Cd_{0.1}S/ITO$ forms Ohmic junction. The junction properties may change at higher processing temperatures steps involved in device fabrication. It is with this aim, the pre-heat treatment of $Zn_{0.9}Cd_{0.1}S/ITO$ stack is carried out in both the oxidizing and the reducing atmosphere, for various durations. Indium (In) is chosen as contact to this stack as it makes an Ohmic junction with $Zn_{0.9}Cd_{0.1}S$. All conditions tested in this study results in Ohmic $I-V$ characteristics. It has been ensured by the Au test method that the obtained Ohmic characteristics are not due to pin holes. It is therefore attributed to the $Zn_{0.9}Cd_{0.1}S/ITO$ interface junction properties. This study shows that $Zn_{0.9}Cd_{0.1}S/ITO$ interface preserves its characteristic during heat treatment steps involved in this study.

The second part is a study of the photovoltaic conversion mechanism. It is a study of the photovoltaic response of the cells when the physical properties of the layer constituting thin films solar cell structure changes. This includes changes caused by varying the pulsed laser deposition parameters of $Zn_{1-x}Cd_xS$ films (window layer of the cell structure). It also includes the changes caused by cell activation step i.e. $CdCl_2$ treatment. Total of 22 cells are fabricated and tested with variation in above mentioned device fabrication parameters. Two types of $CdCl_2$ treatment: wet (chemical dipping in $CdCl_2$) and dry (vapor deposition of $CdCl_2$) have been given to the cells. $CdCl_2$ application along with the heat treatment results in the grain growth and recrystallization in $CdTe$ (absorber layer of the cell structure) which leads to the better cell performance. In this study, the dry $CdCl_2$ treatment was found to be more effective than the wet $CdCl_2$ treatment because the higher grain growth and recrystallization. The grain size of $\sim 3.0 \mu m$ is obtained at heat treatment temperature of $425 \text{ }^\circ C$ while the grain size of $\sim 0.8 \mu m$ is obtained at $450 \text{ }^\circ C$. The recrystallization was gauged by the texture coefficient of the XRD peak intensities of $CdTe$ films. Texture coefficient analysis also shows higher recrystallization for dry treated cells. The photo conversion efficiencies (η) of 5.2 and 3.1% are obtained for dry and wet $CdCl_2$ treatment respectively. The variation in $Zn_{0.1}Cd_{0.9}S$ film deposition parameters includes the change in the thickness and deposition temperature. With a reduction of $Zn_{0.1}Cd_{0.9}S$ film thickness from 200 to 150 nm, photo conversion efficiency, η increases from 4.85 to 5.2%. This increase in photo conversion efficiency is attributed to the increased short circuit current density (J_{sc}). Further reduction in thickness results in lower efficiencies, and is attributed to the higher surface roughness of $Zn_{0.1}Cd_{0.9}S$ films. Higher films thickness ($>150 \text{ nm}$) results in higher series resistance which degrades the overall cell performance. Deposition temperature of

the $Zn_{0.1}Cd_{0.9}S$ film significantly affects the cell parameters. Deposition of $Zn_{0.1}Cd_{0.9}S$ films at 400 °C results in 5.2% efficiency. At lower temperature (350 °C) the efficiency is almost similar \sim 5.0%. It is attributed to the similar crystalline quality and surface roughness (\sim 4.2 nm) of the $Zn_{0.1}Cd_{0.9}S$ films. Higher deposition temperature (500 °C) results in poor surface quality (i.e. increased pin holes accompanying non-uniformed grains), higher interdiffusion between $Zn_{0.1}Cd_{0.9}S$ and CdTe, and impurity diffusion from glass substrate to above lying layers. It eventually decreases the efficiencies close to \sim 2.2%. Best cell (η is 5.2%) in this work is obtained at $Zn_{0.1}Cd_{0.9}S$ film deposition temperature and films thickness at 400 °C and 150 nm respectively along with dry $CdCl_2$ treatment at 425 °C. Comparatively lower efficiency (than previously achieved for CdS/CdTe solar cell) obtained in this work suggests that there are efficiency limiting factors such as (a) increased resistivity of $Zn_{0.1}Cd_{0.9}S$ films with respect to CdS, (b) series resistance of the cell is contributing significantly, (c) there was not any special large area contact designing for increased light absorption and, (d) increased lattice mismatch between $Zn_{0.1}Cd_{0.9}S$ and CdTe films, (e) thermal and electrical stability issues of back contact, (f) solar concentrators were not used. These issues should be analyzed and presents the future scope of this work.

Indeed, the above results showed that there is a great potential in the $Zn_{1-x}Cd_xS$ nanostructures for both the light emitting, and PV applications. This work is a step forward towards applicability of this technology.

ACKNOWLEDGEMENTS

Looking back, I am surprised and at the same time very grateful for all I have received throughout these years. It has certainly shaped me as a person and has led me where I am now.

I owe my deep and sincere gratitude to my supervisor Dr. H. O. Gupta for all the hope he has put on me, before I thought I could do any research at all. He has always encouraged me to live intensively. During more than half a decade of knowing him, he has helped me to see life and science in their full depth. I especially thank him for the interest he has shown in my academic as well as personal well-being.

I am deeply indebted for the enthusiastic supervision of Dr. Ramesh Chandra. He taught me how to appreciate the good scientific work that helps other researchers to build on it. He has enlightened me through his wide knowledge of nanoscience and his deep intuitions about where it should go and what is necessary to get there. I also thank him for his friendship, patience and sincere supervision. My supervisors definitely have been a source of inspiration for me.

I wish to express my warm and sincere thanks to Prof. Vinod Kumar, Head of the Department of Electrical Engineering and all other faculty members of the Department for their keen interest in this work. I am also thankful to the members of my SRC committee, Prof. S. P. Shrivastava (Chairman), Dr. Indra Gupta (Internal member), Department of Electrical Engineering and Dr. Ravi Kumar (External Member), Department of Mechanical and Industrial Engineering, IIT Roorkee for their invaluable suggestions and encouragement to carry out this work and unwearingly listening to my presentations.

I am thankful to Prof. A. K. Choudhary, Head of the Institute Instrumentation Centre for extending the characterization facilities for my work.

The Financial support from Ministry of human resources and development, MHRD, New Delhi, INDIA for this investigation is thankfully acknowledged. Additional thanks are extended to the Commonwealth Scholarship for financially supporting my final year at University of Nottingham, United Kingdom.

I express my sincere thanks to Mr. Subash Pai for giving encouragement and advice in various ways.

I owe my sincere gratitude to Prof. A. C. Pandey, Nanophosphor Application Centre, Allahabad University, who rendered me an opportunity for performing the

photoluminescence measurements in their lab. I am thankful to Dr. Raghvendra Yadav for their help during the experimental work in Nanophosphor Application Centre.

I thank the Institute Instrumentation Centre office and workshop staff for the amount of help they have provided. Xeroxing, instrumentation, fabricating furniture, etc. are only a few among the long list that I have in mind.

Without the pleasant atmosphere in our group writing this thesis would not have been even half as much fun. Therefore I would like to thank the my lab buddies Yogendra Kumar Gautam, Rajan Walia, Mukesh Kumar, Sushant Rawal, Paritosh Dubey, and Ravish Jain at the Nano Science Laboratory, Institute Instrumentation Centre. Thank you all, not only for numerous scientific discussions but also for the fun we had during our time at Nano Science Laboratory. I express my sincere thanks to Ravish for giving a proof read to this thesis. It has also been pleasure to met Chandan Bhardwaj, Ashish K. Pandey, Ajay Kaushal, Deepak, Nitin, R. Kathiravan, Hetal Shah, Ritu Vishnoi, Atikur Rahman, Dr. Subhash Kamal, Navjot Kaur, Gurpreet Kaur, Kirandeep Singh and Rutu during my course. Special thanks go to my former lab mates- Dr. Vipin Chawla and Dr. Ashvani Kumar for frequently supplying good ideas.

This thesis would not have been possible without the strong support of Dr. Amit Kumar Chawla. Though I fall short of words to express my sincere gratitude, I want to thank him, for always listening me and for always being there through everything.

The informal support and encouragement of many friends has been indispensable, and I would like particularly to acknowledge the contribution of Kriti Mangal, Saurabh Gupta, Narendra Singh Beniwal, Ruby Beniwal and all the members of my Nottingham Office. I wish to thank all those whose names have not figured alone but helped me directly or indirectly throughout my career.

I am highly obliged and express sincere thanks to Mrs. Kusam Gupta, who always made me, feel at home in Roorkee.

I wish to thank my entire extended family for providing a loving environment for me. My sisters Ms Sheetal Garg, Ms Neha Agarwal and Ms Rajlaxmi Singhal and my brother Shivam Singhal are particularly supportive. I especially thank my sisters for always giving me an emotional and unconditional support during my thin times. My co-brothers Neeraj Garg and Vinay Agarwal also deserve special thanks for their encouragement and love.

I wish to express my warm thanks to my in-laws family for their love and unconditional support. I especially thank my father and mother in-law for giving me their love none lesser than my parents.

I am forever grateful to my grandparents, whose foresight and values paved the way for a privileged education. My grandfather is my role model. He always had offered counsel and unconditional support at each turn of the road.

My deepest gratitude goes to my family for their unflagging love and support throughout my life; this thesis is simply impossible without them. My parents have been a constant source of support – emotional, moral and of course financial, and this thesis would certainly not have existed without them. It is thanks to my father that I first became interested in science fiction. My mother has always stood with me when I needed her most, and never once complaining about how infrequently I visit, she deserves far more credit than I can ever give her. Thank you mummy and papa for always being there through everything. Your love and care are what have made possible the many opportunities I have had.

My final, and most heartfelt, acknowledgment must go to my husband Dr. Gopal Das Singhal. Gopal has worked diligently, and successfully, for more than five years to show me life outside the Roorkee. His support, encouragement, and companionship has turned my journey through graduate school into a pleasure.

Above all, I express my gratitude from the core of my heart to the almighty God for giving courage, strength and patience to carryout my research work.

(SONAL SINGHAL)

Dedication

I dedicate this work to my parents and to my husband. My parents influenced my life and determination tremendously by the example they provided me in my early years. They inspires me to think, dream, and stand tall on a daily basis. My husband Gopal, has been, always, my pillar, my joy and my guiding light.

CONTENTS

| DESCRIPTION | PAGE NO. |
|---|----------|
| ABSTRACT | i |
| ACKNOWLEDGEMENT | vi |
| CONTENTS | x |
| LIST OF FIGURES | xvii |
| LIST OF PLATES | xxv |
| LIST OF TABLES | xxvi |
| LIST OF NOTATIONS | xxviii |
| LIST OF ABBREVIATIONS | xxx |
| | |
| CHAPTER 1 INTRODUCTION | 1 |
| 1.1 NANOSTRUCTURES | |
| 1.1.1 Semiconductor Nanoparticles | 1 |
| 1.1.2 Semiconductor Nanostructured Thin Films | 2 |
| 1.2 II-VI $Zn_{1-x}Cd_xS$ TERNARY SEMICONDUCTOR NANOSTRUCTURES | 3 |
| 1.3 $Zn_{1-x}Cd_xS$ NANOSTRUCTURES FOR LIGHT EMITTING APPLICATIONS | 3 |
| 1.3.1 Transition Metal (TM) Doped $Zn_{1-x}Cd_xS$ Nanostructures | 6 |
| 1.3.1.1 Manganese (Mn) doped nanostructures | 6 |
| 1.3.2 $Zn_{1-x}Cd_xS$ Core-Shell Nanostructures | 7 |
| 1.4 $Zn_{1-x}Cd_xS$ NANOSTRUCTURES FOR PHOTOVOLTAIC APPLICATIONS | 8 |
| 1.4.1 Photovoltaic Background and Development | 9 |
| 1.4.2 Thin Film Solar Cell Structure | 10 |
| 1.4.3 $Zn_{1-x}Cd_xS$ as Window Layer | 11 |
| 1.5 OBJECTIVES OF THE STUDY | 12 |
| 1.6 THE AUTHOR'S CONTRIBUTION | 13 |
| 1.7 ORGANISATION OF THE THESIS | 15 |
| | |
| CHAPTER 2 LITERATURE REVIEW | 17 |
| 2.1 $Zn_{1-x}Cd_xS$ TERNARY SYSTEM | 17 |

| | | |
|--|---|-----------|
| 2.2 | BINARY CONSTITUENTS | 17 |
| 2.2.1 | Zinc Sulphide (ZnS) | 18 |
| 2.2.1.1 | Crystal structure and physical properties of ZnS | 18 |
| 2.2.2 | Cadmium Sulphide (CdS) | 19 |
| 2.2.2.1 | Crystal structure and physical properties of CdS | 19 |
| 2.3 | RECENT DEVELOPMENTS IN $Zn_{1-x}Cd_xS$ | 21 |
| | NANOSTRUCTURES | |
| 2.3.1 | Doped $Zn_{1-x}Cd_xS$ Nanostructures | 22 |
| 2.3.2 | Mn Doped $Zn_{1-x}Cd_xS$ Nanostructures | 23 |
| 2.3.3 | Core-Shell Nanostructures | 25 |
| 2.4 | $Zn_{1-x}Cd_xS$ NANOCRYSTALLINE FILMS AS WINDOW LAYER IN CdTe SOLAR CELL | 26 |
| CHAPTER 3 EXPERIMENTAL TECHNIQUES | | 28 |
| 3.1 | GENERAL | 28 |
| 3.2 | SYNTHESIS TECHNIQUES | 28 |
| 3.2.1 | Nanoparticles Synthesis Techniques | 28 |
| 3.2.1.1 | Co-precipitation technique | 29 |
| 3.2.1.2 | Controlled co-precipitation technique | 30 |
| 3.2.2 | Thin Film Deposition Technique | 30 |
| 3.2.2.1 | Pulsed laser deposition technique | 30 |
| 3.2.2.2 | Thermal evaporation technique | 32 |
| 3.3 | CHARACTERIZATION TECHNIQUES | 33 |
| 3.3.1 | X-ray Diffraction (XRD) | 33 |
| 3.3.1.1 | Basic principle | 33 |
| 3.3.1.2 | Working principle | 34 |
| 3.3.1.3 | XRD in practice | 35 |
| 3.3.1.4 | Particle/grain size | 35 |
| 3.3.1.5 | Lattice constant | 36 |
| 3.3.1.6 | Texture coefficient | 36 |
| 3.3.2 | Field Emission Scanning Electron Microscope (FE-SEM) | 36 |
| 3.3.2.1 | Working principle | 36 |
| 3.3.2.2 | FE-SEM in practice | 37 |
| 3.3.2.3 | Composition analysis | 38 |

| | | |
|------------------|--|-----------|
| 3.3.3 | Atomic Force Microscopy (AFM) | 38 |
| 3.3.3.1 | Working principle | 38 |
| 3.3.3.2 | AFM in practice | 39 |
| 3.3.4 | Transmission Electron Microscope (TEM) | 39 |
| 3.3.4.1 | Working principle | 39 |
| 3.3.4.2 | Modes of operation | 40 |
| 3.3.4.3 | Lattice spacing determination | 40 |
| 3.3.4.4 | TEM in practice | 40 |
| 3.3.5 | UV-Vis Absorption Spectrophotometer | 41 |
| 3.3.5.1 | Basic principle | 41 |
| 3.3.5.2 | Energy band gap determination | 42 |
| 3.3.5.3 | Refractive index determination | 42 |
| 3.3.5.4 | Film thickness determination | 43 |
| 3.3.5.5 | UV-Vis in practice | 43 |
| 3.3.6 | <i>J-V</i> Characterization | 44 |
| 3.3.6.1 | Solar simulator in practice | 44 |
| 3.3.7 | Photoluminescence (PL) Spectrophotometer | 44 |
| 3.3.7.1 | Basic principle | 45 |
| 3.3.7.2 | PL in practice | 45 |
| 3.3.8 | Superconducting Quantum Interference Device (SQUID) Magnetometer | 46 |
| 3.3.8.1 | SQUID in practice | 46 |
| 3.3.9 | Electron Probe Micro Analyzer (EPMA) | 47 |
| 3.3.9.1 | EPMA in practice | 47 |
| CHAPTER 4 | Zn_{1-x}Cd_xS NANOPARTICLES: COMPOSITION | 48 |
| | TUNABILITY, PARTICLE SIZING & LIGHT EMISSION | |
| 4.1 | GENERAL | 48 |
| 4.2 | CHAPTER PREFACE | 48 |
| 4.3 | SYNTHESIS DETAILS | 49 |
| 4.3.1 | Chemicals | 49 |
| 4.3.2 | Procedure | 49 |
| 4.4 | RESULTS & DISCUSSION | 51 |
| 4.4.1 | Structural Properties of Zn _{1-x} Cd _x S Nanoparticles | 51 |

| | | |
|---|---|-----------|
| 4.4.2 | Particle Sizing | 54 |
| 4.4.2.1 | Transmission electron microscopy | 54 |
| 4.4.2.2 | X-ray diffraction technique | 57 |
| 4.5 | SURFACE MORPHOLOGY & COMPOSITIONAL ANALYSIS | 57 |
| 4.6 | COMPOSITION DEPENDENT ENERGY BAND GAP DETERMINATION OF $Zn_{1-x}Cd_xS$ NANOPARTICLES | 60 |
| 4.7 | COMPOSITION DEPENDENT PL IN $Zn_{1-x}Cd_xS$ NANOPARTICLES | 64 |
| 4.8 | SUMMARY | 67 |
| CHAPTER 5 $Zn_{1-x}Cd_xS$ NANOCRYSTALLINE THIN FILMS: PROCESSING & CHARACTERIZATION | | 68 |
| 5.1 | GENERAL | 68 |
| 5.2 | CHAPTER PREFACE | 69 |
| 5.3 | SYNTHESIS DETAILS | 69 |
| 5.3.1 | Target Fabrication | 69 |
| 5.3.2 | Synthesis Conditions | 70 |
| 5.4 | LASER FLUX DENSITY VARIATION | 72 |
| 5.4.1 | Results & Discussions | 72 |
| 5.4.1.1 | Effect of laser flux density on structural properties | 75 |
| 5.4.1.2 | Effect of laser flex density on surface morphology | 77 |
| 5.5 | PARTICLE SIZE VARIATION | 80 |
| 5.6 | DEPOSITION TEMPERATURE VARIATION | 82 |
| 5.6.1 | Results & Discussions | 83 |
| 5.6.1.1 | Effect of deposition temperature on crystal structure | 83 |
| 5.6.1.2 | Phase transition investigation via TEM | 86 |
| 5.6.1.3 | Effect of deposition temperature on energy band gap | 87 |
| 5.6.1.4 | Effect of deposition temperature on PL emission intensity | 89 |
| 5.7 | MOLE FRACTION VARIATION | 91 |
| 5.7.1 | Results & Discussions | 91 |

| | | |
|--|--|-----------|
| 5.7.1.1 | Effect of mole fraction on structural properties | 91 |
| 5.7.1.2 | Effect of mole fraction on energy band gap | 93 |
| 5.7.1.3 | Effect of mole fraction on PL emission intensity | 95 |
| 5.8 | SUMMARY | 98 |
| CHAPTER 6 Zn_{1-x}Cd_xS:Mn NANOSTRUCTURES FOR LIGHT | | 99 |
| | EMISSION | |
| 6.1 | GENERAL | 99 |
| 6.2 | CHAPTER PREFACE | 100 |
| 6.3 | SYNTHESIS DETAILS | 101 |
| 6.3.1 | Chemicals | 101 |
| 6.3.2 | Synthesis Procedure | 101 |
| 6.3.3 | Synthesis Conditions | 101 |
| 6.4 | TUNING OF HOST LATTICE FOR DOPANT INCORPORATION | 104 |
| 6.5 | Mn ²⁺ HOMOGENOUS SUBSTITUTION VERIFICATION | 114 |
| 6.6 | CORE-SHELL NANOPARTICLES | 116 |
| 6.6.1 | Synthesis of Core-Shell Nanoparticles | 117 |
| 6.6.2 | Effect of s/c Ratio on the Structural Properties of Zn _{0.55} Cd _{0.45} S:Mn/ZnS Core-Shell Nanoparticles | 118 |
| 6.6.3 | Effect of s/c Ratio on Absorption Band Edge of Zn _{0.55} Cd _{0.45} S:Mn/ZnS Core-Shell Nanoparticles | 119 |
| 6.6.4 | Shell Thickness Determination of Zn _{0.55} Cd _{0.45} S:Mn/ZnS Core-Shell Particles | 121 |
| 6.6.5 | PL Enhancement in Zn _{0.55} Cd _{0.45} S:Mn/ZnS Core-Shell Nanoparticles | 122 |
| 6.7 | Mn ²⁺ DOPED Zn _{0.55} Cd _{0.45} S NANOCRYSTALLINE THIN FILMS | 123 |
| 6.7.1 | Preface | 124 |
| 6.7.2 | Synthesis Details | 124 |
| 6.7.3 | Results & Discussion | 127 |
| 6.8 | Zn _{0.55} Cd _{0.45} S:Mn/ZnS NANOCOMPOSITE FILMS | 130 |
| 6.9 | RESULTS & DISCUSSION | 131 |
| 6.9.1 | Structural Characterization | 131 |

| | | |
|---|--|------------|
| 6.9.2 | PL Enhancement in $Zn_{0.55}Cd_{0.45}S:Mn/ZnS$ Nanocomposite | 132 |
| 6.10 | SUMMARY | 134 |
| CHAPTER 7 PHOTOVOLTAICS DEVICE APPLICATION OF | | 136 |
| $Zn_{1-x}Cd_xS$ NANOSTRUCTURED THIN FILMS | | |
| 7.1 | INTRODUCTION | 136 |
| | 7.1.1 Framework of the Work | 137 |
| 7.2 | CHAPTER PREFACE | 139 |
| 7.3 | $Zn_{0.1}Cd_{0.9}S/TCO$ INTERFACE PROPERTIES | 139 |
| | 7.3.1 TCO Pre Heat Treatment Conditions and $Zn_{0.1}Cd_{0.9}S/TCO$ Stack Formation | 140 |
| | 7.3.2 Accessing Uniform Coverage of $Zn_{0.1}Cd_{0.9}S$ Films Grown on TCO | 142 |
| | 7.3.3 Effect of Pre Heat Treatment of ITO Substrates | 144 |
| 7.4 | DEVICE FABRICATION STEPS | 147 |
| 7.5 | EFFECT OF $CdCl_2$ HEAT TREATMENT ON CELL PROPERTIES | 152 |
| | 7.5.1 Structural Properties – Recrystallization | 152 |
| | 7.5.2 Surface Morphology-Grain Enhancement | 155 |
| | 7.5.3 Solar Cell Performance with $CdCl_2$ Treatment | 158 |
| | 7.5.3.1 Wet $CdCl_2$ treatment | 159 |
| | 7.5.3.2 Dry $CdCl_2$ treatment | 161 |
| | 7.5.4 Series Resistance (R_s) of Wet and Dry Treated Cell | 163 |
| | 7.5.5 Effect of $Zn_{0.1}Cd_{0.9}S$ Film Thickness on Cell Parameters | 165 |
| | 7.5.6 Series Resistance (R_s) of Cells with Variation in $Zn_{0.1}Cd_{0.9}S$ Film Thickness | 168 |
| | 7.5.7 Effect of $Zn_{0.1}Cd_{0.9}S$ Film Deposition Temperature on Cell Parameters | 169 |
| | 7.5.8 Series Resistance (R_s) of Cells with $Zn_{0.1}Cd_{0.9}S$ Film Deposition Temperature | 172 |
| 7.6 | IDENTIFICATION OF EFFICIENCY LIMITING FACTORS | 173 |
| 7.7 | SUMMARY | 175 |

| | |
|---|------------|
| CHAPTER 8 CONCLUSIONS AND FUTURE SCOPE | 176 |
| 8.1 CONCLUSIONS | 176 |
| 8.2 FUTURE SCOPE | 181 |
| REFERENCES | 182 |
| APPENDIX-A1 | 208 |
| APPENDIX-A2 | 215 |
| APPENDIX-A3 | 217 |
| APPENDIX-A4 | 219 |
| APPENDIX-A5 | 224 |
| APPENDIX-A6 | 226 |
| LIST OF PUBLICATIONS | 229 |

LIST OF FIGURES

| Figure No. | Description | Page No. |
|------------|--|----------|
| 1.1 | Schematic of two simple processes of an activated radiative emission | 5 |
| 1.2 | (a) The relative d-orbital crystal field splitting for tetrahedral symmetry and (b) Schematic representation of the emission levels of the ZnS:Mn | 7 |
| 1.3 | Variety of core shell particles: (a) Surface-modified core particles anchored with shell particles, (b) More shell particles reduced onto core to form a complete shell, and (c) Smooth coating of core with shell | 8 |
| 1.4 | The average manufacturing cost of Si solar modules in the time range from 1992 to 2004 | 10 |
| 1.5 | Schematic of thin film solar cell (a) Superstrate approach and (b) Substrate approach | 11 |
| 2.1 | ZnS crystal structures: (a) Zinc Blende crystal structure (Zn^{2+} : Gray spheres and S^{2-} : Yellow spheres) and (b) $E-k$ diagram of ZnS in zincblende structure | 19 |
| 2.2 | CdS crystal structures: (a) Wurtzite crystal structure (Cd^{2+} : Gray spheres and S^{2-} : Yellow spheres) and (b) $E-k$ diagram of CdS in wurtzite structure | 21 |
| 3.1 | Schematic of the PLD process | 32 |
| 3.2 | Schematic of thermal evaporation deposition | 33 |
| 3.3 | Diffraction of X-ray by a single crystal material | 34 |
| 3.4 | Working principles of a XRD | 34 |
| 3.5 | Effect of grain size on X-ray diffraction peak | 35 |
| 3.6 | (a) The emission of various particles including secondary electrons, X-ray, and backscattered electrons and (b) Schematic diagram of the FE-SEM | 37 |
| 3.7 | The working principles of the AFM | 38 |
| 3.8 | Schematic diagram of a TEM | 39 |
| 3.9 | Schematic of a UV-Vis spectrophotometer | 41 |

| | | |
|------|--|----|
| 3.10 | (a) Reflection and transmission of light by a thin film and (b) Transmission spectrum for a thin ZnO film | 42 |
| 3.11 | Schematic of a photoluminescence spectrophotometer | 45 |
| 4.1 | Reaction set up for the synthesis of nanoparticles | 50 |
| 4.2 | XRD patterns of $Zn_{1-x}Cd_xS$ nanoparticles with mole fractions, x as 0.1, 0.2, 0.3, 0.4, 0.5, 0.75, and 0.9 | 52 |
| 4.3 | Lattice constants of $Zn_{1-x}Cd_xS$ nanoparticles with mole fractions, x as 0.1, 0.2, 0.3, 0.4, 0.5, 0.75, and 0.9 in zincblende structure for (111) orientation | 53 |
| 4.4 | Error plot between observed and computed lattice constants of $Zn_{1-x}Cd_xS$ nanoparticles | 53 |
| 4.5 | (a) TEM image of $Zn_{0.5}Cd_{0.5}S$ nanoparticles (sample NP-5); Inset: lattice fringes, (b) corresponding SAED pattern, (c) TEM image of sample $Zn_{0.7}Cd_{0.3}S$ (sample NP-3); Inset: corresponding SAED pattern, and (d) TEM image of sample $Zn_{0.9}Cd_{0.1}S$ (sample NP-1); Inset: corresponding SAED pattern | 55 |
| 4.6 | Histograms of (a) $Zn_{0.5}Cd_{0.5}S$ (sample NP-5), (b) $Zn_{0.7}Cd_{0.3}S$ (sample NP-3), and (c) $Zn_{0.9}Cd_{0.1}S$ (sample NP-1) nanoparticles; corresponding to TEM images (a), (c), and (d) respectively in figure. 4.5 | 56 |
| 4.7 | FE-SEM images of $Zn_{0.25}Cd_{0.75}S$ nanoparticles (sample NP-6) at magnification of (a) x 50k, (b) x 100k, (c) x 200k, and (d) x 600k | 58 |
| 4.8 | EDS spectrum of samples (a) $Zn_{0.9}Cd_{0.1}S$ (sample NP-1), (b) $Zn_{0.5}Cd_{0.5}S$ (sample NP-5), and (c) $Zn_{0.1}Cd_{0.9}S$ (sample NP-7); Inset shows at % of the constituent elements | 59 |
| 4.9 | $(ah\nu)^2$ with $h\nu$ of $Zn_{1-x}Cd_xS$ nanoparticles with mole fractions, x as 0.1, 0.2, 0.3, 0.4, 0.5, 0.75, and 0.9 | 60 |
| 4.10 | A polynomial fit to the energy band gap values of $Zn_{1-x}Cd_xS$ nanoparticles | 61 |
| 4.11 | Composition dependence of calculated absorption energies of bulk crystals (dashed lines) and nanoparticles with a size of 3.6 nm (solid line) | 63 |
| 4.12 | Error plot between observed and computed energy band gap value of $Zn_{1-x}Cd_xS$ nanoparticles | 63 |

| | | |
|------|--|----|
| 4.13 | Normalized self activated PL spectra of the $Zn_{1-x}Cd_xS$ nanoparticles with mole fraction, x as 0.1, 0.2, 0.3, 0.4, 0.5, 0.75, and 0.9 | 65 |
| 4.14 | Normalized blue and green emissions in PL spectra of the $Zn_{1-x}Cd_xS$ nanoparticles with mole fraction, x as 0.1, 0.3, 0.5, 0.75, and 0.9 | 65 |
| 4.15 | Variation of peak intensity ratio ($I_{G/B}$) with mole fraction, x as 0.1, 0.3, 0.5, 0.75, and 0.9 | 66 |
| 4.16 | Schematic energy level diagram for transition between different levels of $Zn_{1-x}Cd_xS$ nanoparticles | 66 |
| 5.1 | (a) Dye for pellet preparation; <i>as-fabricated</i> pellets in laboratory with mole fraction as: (b) 0.3, (c) 0.5, and (d) 0.7 | 71 |
| 5.2 | Pulsed wave for 10 Hz repetition rate with $t_{ON} = 2.5 \times 10^{-8}$ sec and $t_{OFF} = \sim 0.1$ sec | 72 |
| 5.3 | XRD patterns of $Zn_{0.1}Cd_{0.9}S$ films corresponding to laser flux densities of 2.5, 3.0, 3.33, 3.75, and 4.16 J/cm^{2s} | 75 |
| 5.4 | Texture coefficient of (002) orientation of $Zn_{0.1}Cd_{0.9}S$ films corresponding to laser flux densities of 2.5, 3.0, 3.33, 3.75, and 4.16 J/cm^2 | 76 |
| 5.5 | $Zn_{0.1}Cd_{0.9}S$ film (sample NTF-10) at 3.33 J/cm^2 (a) TEM image, (b) Lattice spacing, and (c) SAED pattern | 77 |
| 5.6 | Surface morphology of $Zn_{0.1}Cd_{0.9}S$ films corresponding to laser flux densities of (a) 2.5, (b) 3.33, and (c) 4.16 J/cm^2 respectively | 78 |
| 5.7 | Average surface roughness of $Zn_{0.1}Cd_{0.9}S$ films corresponding to laser flux densities of 2.5, 3.0, 3.33, 3.75, and 4.16 J/cm^2 | 78 |
| 5.8 | Transmittance $T(\lambda)$ of $Zn_{0.1}Cd_{0.9}S$ films of 2.5, 3.0, 3.33, 3.75, and 4.16 J/cm^2 | 79 |
| 5.9 | AFM images of $Zn_{0.1}Cd_{0.9}S$ films corresponding to working pressures of (a) 10, (b) 50, and (c) 200 mtorr respectively | 81 |
| 5.10 | Variation of particle size of $Zn_{0.1}Cd_{0.9}S$ films with working pressures of 0.015, 10, 20, 50, 100, and 200 mtorr | 82 |
| 5.11 | X-ray diffraction spectra of $Zn_{0.9}Cd_{0.1}S$ films corresponding to deposition temperatures of 200, 300, 400, 500, and 600 $^{\circ}C$ | 83 |
| 5.12 | X-ray diffraction spectra of $Zn_{0.7}Cd_{0.3}S$ films corresponding to | 84 |

| | | |
|------|---|----|
| | deposition temperatures of 200, 300, 400, 500, and 600 °C | |
| 5.13 | X-ray diffraction spectra of Zn _{0.5} Cd _{0.5} S films corresponding to deposition temperatures of 200, 300, 400, 500, and 600 °C | 85 |
| 5.14 | XRD patterns of three samples of Zn _{1-x} Cd _x S with mole fractions and deposition temperatures of (0.1, 500°C), (0.3, 400°C), and (0.5, 300°C) | 86 |
| 5.15 | (a) TEM image of Zn _{0.9} Cd _{0.1} S sample deposited at 300 °C, (b) corresponding SAED pattern, (c) TEM image of Zn _{0.9} Cd _{0.1} S sample deposited at 500°C, and (d) corresponding SAED pattern | 86 |
| 5.16 | (a) Transmittance T(λ) and (b) $(ahv)^2$ with $h\nu$ profiles of Zn _{0.5} Cd _{0.5} S films at 200, 300, 400, 500, and 600 °C | 87 |
| 5.17 | Energy band gap of the Zn _{1-x} Cd _x S (x as 0.1, 0.3, and 0.5) nanocrystalline thin films at 200, 300, 400, 500, and 600 °C | 88 |
| 5.18 | PL emission spectra of Zn _{0.9} Cd _{0.1} S films at 200, 300, 400, 500, and 600 °C | 89 |
| 5.19 | Variation of $I_{NBE/DEF}$ ratio of Zn _{0.9} Cd _{0.1} S films corresponding to deposition temperatures of 200, 300, 400, 500, and 600 °C | 90 |
| 5.20 | X-ray diffraction spectra of Zn _{1-x} Cd _x S films with mole fractions 0, 0.1, 0.2, 0.3, 0.4, 0.5, 0.75, and 0.9 | 91 |
| 5.21 | Lattice constants of Zn _{1-x} Cd _x S films with varying mole fraction deposited at 400 °C both in zincblende and wurtzite structure | 92 |
| 5.22 | Error plot between observed and computed lattice constants of Zn _{1-x} Cd _x S films with varying mole fraction. | 93 |
| 5.23 | Transmittance T(λ) of Zn _{1-x} Cd _x S films with mole fractions 0.1, 0.2, 0.3, 0.4, 0.5, 0.75, and 0.9 | 94 |
| 5.24 | Energy band gap of Zn _{1-x} Cd _x S films with mole fractions 0.1, 0.2, 0.3, 0.4, 0.5, 0.75, and 0.9 | 94 |
| 5.25 | PL spectra at 300 K: (a) Zn _{0.6} Cd _{0.4} S and (b) Zn _{0.5} Cd _{0.5} S films at 400°C | 95 |
| 5.26 | PL NBE peak energy positions of Zn _{1-x} Cd _x S films | 96 |
| 5.27 | Plot of energy band gaps of Zn _{1-x} Cd _x S films obtained via PL measurements | 97 |
| 5.28 | Error plot between band gap energies of Zn _{1-x} Cd _x S films obtained via absorption and PL measurement | 97 |

| | | |
|------|---|-----|
| 6.1 | XRD patterns of Mn^{2+} (1 mol%) doped $\text{Zn}_{1-x}\text{Cd}_x\text{S}$ nanoparticles at mole fractions, x as 0, 0.1, 0.25, 0.45, and 0.75 | 104 |
| 6.2 | PL emission spectra of Mn^{2+} (1 mol%) doped $\text{Zn}_{1-x}\text{Cd}_x\text{S}$ nanoparticles at mole fractions, x as 0, 0.1, 0.25, 0.45, and 0.75 | 106 |
| 6.3 | Plot of maximum PL intensity at ~ 585 nm of Mn^{2+} (1 mol%) doped $\text{Zn}_x\text{Cd}_{1-x}\text{S}$ nanoparticles with mole fraction | 106 |
| 6.4 | $\pm 5\%$ error plot between computed and observed lattice constants | 107 |
| 6.5 | The plot of % difference of lattice mismatch of MnS and $\text{Zn}_{1-x}\text{Cd}_x\text{S}$ with mole fraction | 108 |
| 6.6 | XRD patterns of Mn^{2+} doped $\text{Zn}_{0.55}\text{Cd}_{0.45}\text{S}$ nanoparticles with Varying manganese concentrations of 0, 1, 2, 3, 5, and 10 mol% | 109 |
| 6.7 | Manganese mol% in synthesized MNPs with manganese precursor | 110 |
| 6.8 | PLE spectrum of Mn^{2+} (5 mol%) doped $\text{Zn}_{0.55}\text{Cd}_{0.45}\text{S}$ nanoparticles | 111 |
| 6.9 | PL emission spectra of Mn^{2+} doped $\text{Zn}_{0.55}\text{Cd}_{0.45}\text{S}$ nanoparticles at Mn^{2+} concentrations of 1, 2, 3, 5, and 10 mol% | 111 |
| 6.10 | (a) Plot of orange emission intensity with manganese concentrations of 1, 2, 3, 5, and 10 mol% | 112 |
| | (b) Plot of $I_{O/B}$ with manganese concentrations as 1, 2, 3, 5, and 10 mol% | 113 |
| 6.11 | Schematic energy level diagram of transitions between host and Mn^{2+} related energy levels | 114 |
| 6.12 | Magnetic moment with applied magnetic field of Mn^{2+} doped $\text{Zn}_{0.55}\text{Cd}_{0.45}\text{S}$ nanoparticles (a) At 5 K with Mn^{2+} concentrations as 0, 1, 2, 3, 5 and 10 mol% (b) At 5, 50, 100, 200, and 300 K of Mn^{2+} (5 mol%, sample MNP-21) | 115 |
| 6.13 | XRD patterns of $\text{Zn}_{0.55}\text{Cd}_{0.45}\text{S}:\text{Mn}$ (5 mol%)/ ZnS nanoparticles at s/c ratio of 0, 0.05, 0.1, 0.2, 0.5, and 1 | 118 |
| 6.14 | Peak intensity variation of $\text{Zn}_{0.55}\text{Cd}_{0.45}\text{S}:\text{Mn}$ (5 mol%)/ ZnS nanoparticles at s/c ratio of 0, 0.05, 0.1, 0.2, 0.5, and 1 | 119 |
| 6.15 | Absorption spectra of $\text{Zn}_{0.55}\text{Cd}_{0.45}\text{S}:\text{Mn}$ (5 mol%)/ ZnS nanoparticles corresponding to s/c ratio of 0, 0.05, 0.1, 0.2, 0.5, and 1 | 120 |

| | | |
|------|---|-----|
| 6.16 | Variation in particle size of $Zn_{0.55}Cd_{0.45}S:Mn$ (5 mol%)/ZnS nanoparticles with s/c ratio | 120 |
| 6.17 | Variation in shell thickness of $Zn_{0.55}Cd_{0.45}S:Mn$ (5 mol%)/ZnS nanoparticles with s/c ratio | 121 |
| 6.18 | PL emission spectra of $Zn_{0.55}Cd_{0.45}S:Mn$ (5 mol%)/ZnS nanoparticles with varying s/c ratio | 122 |
| 6.19 | Plot of I_{scr} of $Zn_{0.55}Cd_{0.45}S:Mn$ (5 mol%)/ZnS nanoparticles with s/c ratio | 123 |
| 6.20 | XRD patterns of Mn^{2+} doped $Zn_{0.55}Cd_{0.45}S$ films at Mn^{2+} concentrations of 1, 2, 3, 5, and 10 mol% | 127 |
| 6.21 | Transmittance $T(\lambda)$ of Mn^{2+} doped $Zn_{0.55}Cd_{0.45}S$ films at Mn^{2+} concentrations of 1, 2, 3, 5, and 10 mol% | 128 |
| 6.22 | PL emission spectra of Mn^{2+} doped $Zn_{0.55}Cd_{0.45}S$ films at Mn^{2+} concentrations of 0, 1, 2, 3, 5, and 10 mol% | 129 |
| 6.23 | Peak intensity variation of blue and orange emission of Mn^{2+} doped $Zn_{0.55}Cd_{0.45}S$ films at Mn^{2+} concentrations of 0, 1, 2, 3, 5, and 10 mol% | 129 |
| 6.24 | The plot of maximum PL intensity at ~ 585 nm of Mn^{2+} doped $Zn_{0.55}Cd_{0.45}S$ films at Mn^{2+} concentrations of 0, 1, 2, 3, 5, and 10 mol% | 130 |
| 6.25 | XRD patterns of $Zn_{0.55}Cd_{0.45}S:Mn/ZnS$ films at 0, 3000, 4000, 5000, and 6000 laser shots | 131 |
| 6.26 | Transmittance $T(\lambda)$ of $Zn_{0.55}Cd_{0.45}S:Mn/ZnS$ films corresponding to laser shots of 0, 3000, 4000, 5000, and 6000 | 132 |
| 6.27 | PL emission spectra of $Zn_{0.55}Cd_{0.45}S:Mn/ZnS$ films with ZnS top layer laser shots of 0, 3000, 4000, 5000, and 6000 | 133 |
| 6.28 | Plot of $I_{top/c}$ with ZnS top layer variation of $Zn_{0.55}Cd_{0.45}S:Mn/ZnS$ films corresponding to laser shots of 0, 3000, 4000, 5000, and 6000 | 133 |
| 6.29 | (a) Schematic of type-I (straddling) structure, (b) Electron affinity model of system under consideration, and (c) Schematic of as formed type-I (straddling) structure of $Zn_{0.55}Cd_{0.45}S:Mn/ZnS$ nanocomposite | 134 |
| 7.1 | Au mask patterns: circle represents the Au dots with diameter of 2 μ m (a) Sixteen dot geometry and (b) Nine dot geometry | 142 |

| | | |
|------|---|------------|
| 7.2 | <i>I-V</i> curves for (a) An Au/Zn _{0.1} Cd _{0.9} S/ITO stack depicting rectifying behavior and (b) An Au/Zn _{0.1} Cd _{0.9} S/ITO stack depicting Ohmic behavior | 143 |
| 7.3 | The electronic details of each layer of the stack. VL, CB, VB, E_F , E_g , χ , and Φ represents the vacuum level, conduction band, valance band, fermi energy level, energy band gap, electron affinity and work function respectively | 146 |
| 7.4 | Band alignments of the In/Zn _{0.1} Cd _{0.9} S/ITO stack representing Ohmic junction | 146 |
| 7.5 | XRD patterns of CdTe films treated with (a) Wet CdCl ₂ and (b) Dry CdCl ₂ | 153 |
| 7.6 | (a) Texture coefficient of CdTe films with wet CdCl ₂ treatment with variation in heat treatment temperature (b) Texture coefficient of CdTe films at dry CdCl ₂ treatment with variation in heat treatment temperature | 154 155 |
| 7.7 | AFM images of CdTe films: (a) As deposited, (b) wet CdCl ₂ Treated at 450 °C, and (c)-(f) dry CdCl ₂ treated at 400-500 °C | 157 |
| 7.8 | (a) Transmittance of CdTe films with temperature dry CdCl ₂ treatment heat and (b) Average transmittance of CdTe films for both wet and dry CdCl ₂ treatment | 158 |
| 7.9 | Cell parameters of the CdTe/Zn _{0.1} Cd _{0.9} S/ITO/Glass device with wet CdCl ₂ treatment (a) photo conversion efficiency, η (%) (b) fill factor, FF (%) (c) short circuit density, J_{sc} (mA/cm ²) and (d) open circuit voltage, V_{oc} (mV) | 160 |
| 7.10 | Cell parameters of the CdTe/Zn _{0.1} Cd _{0.9} S/ITO/Glass device with dry CdCl ₂ treatment (a) photo conversion efficiency, η (%) (b) fill factor, FF (%) (c) short circuit density, J_{sc} (mA/cm ²) and (d) open circuit voltage, V_{oc} (mV) | 162 |
| 7.11 | Series resistance of the CdTe/Zn _{0.1} Cd _{0.9} S/ITO/Glass device structure with wet and dry CdCl ₂ treatment | 164 |
| 7.12 | AFM image of the Zn _{0.1} Cd _{0.9} S layer structure with varying film thickness: (a) 150, (b) 100, and (c) 60 nm | 166 |
| 7.13 | Cell parameters of the CdTe/Zn _{0.1} Cd _{0.9} S/ITO/Glass device with variation in Zn _{0.1} Cd _{0.9} S film thickness: (a) photo conversion | 167 |

| | | |
|------|---|-----|
| | efficiency, η (%) (b) fill factor, FF (%) (c) short circuit density, J_{sc} (mA/cm ²) and (d) open circuit voltage, V_{oc} (mV) | |
| 7.14 | Series resistance of the CdTe/Zn _{0.1} Cd _{0.9} S/ITO/Glass device structure with Zn _{0.1} Cd _{0.9} S film thickness | 169 |
| 7.15 | AFM image of the Zn _{0.1} Cd _{0.9} S layer with deposition temperature (a) 400 and (b) 500 °C | 170 |
| 7.16 | Cell parameters of the CdTe/Zn _{0.1} Cd _{0.9} S/ITO/Glass device with variation in Zn _{0.1} Cd _{0.9} S film deposition temperature: (a) photo conversion efficiency, η (%) (b) fill factor, FF (%) (c) short circuit density, J_{sc} (mA/cm ²) (d) open circuit voltage, V_{oc} (mV) | 172 |
| 7.17 | Series resistance of the CdTe/Zn _{0.1} Cd _{0.9} S/ITO/Glass device structure with Zn _{0.1} Cd _{0.9} S film deposition temperature | 173 |
| A1.1 | Solar Cell AM1.5 Spectrum | 210 |
| A1.2 | Absorption coefficient of few direct and indirect band gap semiconductors | 211 |
| A1.3 | Schematic of thin film solar cell in superstrate configuration | 212 |
| A3.1 | Absorption spectra of Zn _{0.55} Cd _{0.45} S:Mn nanoparticles with variation in manganese concentration | 218 |
| A4.1 | equivalent circuit for solar cell under illumination | 220 |
| A4.2 | The current-voltage curve of a p - n junction solar cell (a) in the dark and (b) under illumination | 221 |
| A4.3 | Typical J - V curves for solar cells under illumination. Figure shows the division of the curve from which R_s is measured | 223 |
| A5.1 | The energy band diagrams of a p -type semiconductor and metal before contact (a) $\phi_m < \phi_s$ and (b) $\phi_m > \phi_s$ | 224 |
| A5.2 | The energy band diagrams of a p -type semiconductor and metal after contact (a) $\phi_m < \phi_s$ resulting in Schottky contact and (b) $\phi_m > \phi_s$ resulting in Ohmic contact | 225 |

LIST OF PLATES

| Plate No. | Description | Page No. |
|------------------|--|-----------------|
| 3.1 | PLD unit set up in Nano Science Laboratory | 32 |
| 3.2 | Photograph of XRD | 34 |
| 3.3 | Photograph of FE-SEM | 37 |
| 3.4 | Photograph of atomic force microscope | 38 |
| 3.5 | Photograph of TEM | 43 |
| 3.6 | Photograph of UV-Vis spectrophotometer | 43 |
| 3.7 | Photograph of solar simulator | 44 |
| 3.8 | Photograph of PL measurement | 46 |
| 3.9 | Photograph of SQUID quantum design | 47 |
| 3.10 | Photograph of EPMA | 47 |

LIST OF TABLES

| Table No. | Description | Page No. |
|-----------|---|----------|
| 2.1 | Properties of ZnS and CdS at room temperature | 20 |
| 2.2 | Synthesis of $Zn_{1-x}Cd_xS$ nanostructures by solution route | 24 |
| 3.1 | Various thin film deposition techniques | 31 |
| 4.1 | Standard conditions used in this study for synthesis of $Zn_{1-x}Cd_xS$ nanoparticles | 50 |
| 4.2 | Sample composition (x), crystal structure, particle size, excitation wavelength, and emission wavelength of $Zn_{1-x}Cd_xS$ nanoparticles characterized in this study | 57 |
| 5.1 | Synthesis conditions of $Zn_{1-x}Cd_xS$ nanocrystalline thin films prepared in this study. It also contains the obtained phase | 73 |
| 5.2 | Sample roughness, average particle size, refractive index and film thickness with laser flux density | 80 |
| 5.3 | Working pressure, mean free path, and corresponding particle sizes as observed from AFM | 82 |
| 5.4 | Sample composition, crystal structure, emission wavelengths, and binding energy of $Zn_{1-x}Cd_xS$ thin films deposited at substrate temperature of 400 °C | 95 |
| 6.1 | Standard synthesis conditions of Mn^{2+} doped $Zn_{1-x}Cd_xS$ nanoparticles. It also contains the synthesis parameters for core-shell nanoparticles | 102 |
| 6.2 | Mole fraction (x), crystal structure, and interplanar spacing of Mn^{2+} (1 mol%) doped $Zn_{1-x}Cd_xS$ nanoparticles | 105 |
| 6.3 | Lattice constant from references and those obtained from XRD patterns for (111) orientation in zincblende structure | 107 |
| 6.4 | XRD peak positions, particle size via UV-Vis, and shell thickness of $Zn_{0.55}Cd_{0.45}S:Mn/ZnS$ core-shell nanoparticles | 121 |
| 6.5 | Synthesis conditions of Mn^{2+} doped $Zn_{0.55}Cd_{0.45}S$ nanocrystalline thin films and their nanocomposites | 124 |
| 7.1 | Synthesis parameters for $Zn_{0.1}Cd_{0.9}S/TCO$ stack and treatment conditions of TCO tested in this study. The table also contains the | 141 |

| | | |
|------|---|-----|
| | contact types and the results of the I - V characteristics | |
| 7.2 | The references/method for the electron affinity, work function, energy band gap values adopted in this work for indium, $Zn_{0.1}Cd_{0.9}S$ and ITO | 145 |
| 7.3 | Summary of the growth and treatment conditions of cells | 150 |
| 7.4 | Series resistances of the cells with wet and dry $CdCl_2$ treatment | 163 |
| 7.5 | Deposition parameters of the $Zn_{0.1}Cd_{0.9}S$ film with variation in film thickness | 165 |
| 7.6 | Series resistance of the cells with $Zn_{0.1}Cd_{0.9}S$ film thickness | 168 |
| 7.7 | Processing parameters of $Zn_{0.1}Cd_{0.9}S$ film with variation in deposition temperature | 170 |
| 7.8 | Series resistance of the cells with variation in $Zn_{0.1}Cd_{0.9}S$ film deposition temperature | 172 |
| A1.1 | Energy band gap of bulk $Zn_{1-x}Cd_xS$ with mole fraction in zincblende structure and corresponding wavelength | 208 |
| A1.2 | Energy band gap of bulk $Zn_{1-x}Cd_xS$ with mole fraction in wurtzite structure and corresponding wavelength | 208 |
| A1.3 | $Zn_{1-x}Cd_xS$ lattice constant, a , with mole fraction in zincblende structure | 209 |
| A1.4 | $Zn_{1-x}Cd_xS$ Lattice Constant, a , with mole fraction in wrutzite structure | 209 |
| A1.5 | $Zn_{1-x}Cd_xS$ lattice constant, c , with mole fraction in wrutzite structure | 210 |
| A4.1 | Properties of CdTe at room temperature | 219 |
| A5.1 | Four possible metal-semiconductor junction configurations and the resulting contact type | 225 |

LIST OF NOTATIONS

The following symbols are used in this thesis

| Symbol | Description | Units |
|-----------------|---|-------------------|
| ϵ | Dielectric constant | F/m |
| e | Electronic charge | eV |
| E_g | Energy band gap | eV |
| δ_m | Molecular diameter | Cm |
| h | Planck's constant | J-sec |
| α | Absorption coefficient | cm ⁻¹ |
| λ_{mfp} | Mean free path | Cm |
| ν | Photon frequency | sec ⁻¹ |
| a_B | Bulk-exciton bohr radius | Å |
| d | Inter atomic spacing | Å |
| E_F | Fermi energy | eV |
| FF | Fill factor | --- |
| $I_{G/B}$ | Green to blue emission peak intensitiy ratio | --- |
| $I_{NBE/DEF}$ | Near band edge emission to defect center emission intensity ratio | --- |
| $I_{O/B}$ | Orange to blue emission intensity ratio | --- |
| $I_{s/c}$ | Shell to core emission intensity ratio | --- |
| $I_{top/c}$ | Top to core layer emission intensity ratio | --- |
| J_{sc} | Short circuit current density | A/cm ² |
| m_e | Electron effective mass | Kg |
| m_h | Hole effective mass | Kg |
| n | Refractive index | --- |
| P | Pressure | Torr |
| R | Nanoparticle radius | Nm |
| R^2 | Regression coefficient | --- |
| R_s | Series resistance | Ω-cm ² |
| t | Film thickness | Nm |
| T_s | Deposition temperature | °C |
| V_{Cd} | Cadmium vacancy | --- |

| | | |
|----------|-----------------------------|--------|
| V_{oc} | Open circuit voltage | Volt |
| V_s | Sulfur vacancy | --- |
| V_{Zn} | Zinc vacancy | --- |
| x | Mole fraction | --- |
| η | Photo conversion efficiency | --- |
| μ | Exciton reduced mass | --- |
| Φ | Work function | eV |
| χ | Electron affinity | eV |
| α | Lattice constant | Å |
| d_p | Particle/grain size | Nm |
| B | Full width at half maximum | radian |

LIST OF ABBREVIATIONS

The following abbreviations are used in this thesis

| Symbol | Description |
|---------------|---|
| a. u. | Arbitrary unit |
| AFM | Atomic force microscope |
| CB | Conduction band |
| CBD | Chemical bath deposition |
| DI | De-ionized |
| EDS | Energy dispersive spectroscopy |
| EPMA | Electron probe micro analyzer |
| FE-SEM | Field emission scanning electron microscope |
| FWHM | Full width at half maximum |
| ITO | Indium tin oxide |
| KrF | Krypton fluoride |
| kV | Kilo volts |
| NBE | Near band edge |
| NIR | Near infra red |
| NPs | Nanoparticles |
| PL | Photoluminescence |
| PLD | Pulsed laser deposition |
| PV | Photovoltaic |
| PVD | Physical vapor deposition |
| QCE | Quantum confinement effect |
| SAED | Selected area electron diffraction |
| SQUID | Superconducting quantum interference device |
| <i>TC</i> | Texture coefficient |
| TCO | Transparent conducting oxide |
| TEM | Transmission electron microscope |
| UV | Ultra violet |
| VB | Valance band |
| Vis | Visible |
| VL | Vacuum level |

| | |
|-----|-------------------|
| W | Wurtzite |
| XRD | X-ray diffraction |
| ZB | Zincblende |

CHAPTER 1

INTRODUCTION

1.1 NANOSTRUCTURES

Nanoscience and technology is a broad and interdisciplinary area of research and development activity that has been growing explosively worldwide from late 1990s [130]. The investigation of low-dimensional semiconductor structures, such as nanoparticles, nanowires and nanocrystalline thin films has attracted much attention in recent years, because they not only demonstrate interesting electronic and optical properties, but also show promise for their application to electronic and optoelectronic devices [50].

1.1.1 Semiconductor Nanoparticles

Semiconductor nanoparticles are made up of semiconducting material and can be characterized as systems where the carriers are confined in all the three spatial directions. The consequence of such confinement is that the lowest part of the electronic structure of nanoparticles represents a series of discrete levels, contrary to the continuous density of states of bulk semiconductors, or to their higher dimensional relatives, such as quantum wells and quantum wires [7, 127].

Semiconductor nanoparticles synthesized in colloidal solutions are the smallest quantum dots with the strongest three-dimensional confinement. Their sizes can vary from 1 to 10 nm. They have symmetrical shapes and can be fabricated as multi-shell structures, i.e., built of concentric layers (shells) of different semiconductors with the shell thickness down to a single monolayer [86, 154]. Size of the nanoparticles and the composition of layers can be manipulated with ease in the process of fabrication, which makes it possible to tailor their discrete energy spectra to a large extent. This makes them attractive for applications in novel optoelectronic devices [197].

Nanoparticles offer the unique ability to tune the band gap and hence the emission wavelength (appendix A1.1). Two fundamental factors, both related to the size of the individual nanoparticle, distinguish their behaviour from the corresponding macrocrystalline material [147]. The first is the large surface - to- volume ratio associated with the particles, with both the physical and chemical properties of the semiconductor being particularly sensitive to the surface structure. The second factor is the actual size of the particle, also known as volume size effect, which determines the electronic and

physical properties of the material. Such size dependent optical properties are examples of size quantization effect that occurs when the size of the nanoparticle is smaller than the bulk-exciton Bohr radius, a_B , of the semiconductor [13]. Brus showed that the size dependence on the energy of the first electronic transition of the exciton (or the band gap shift with respect to the typical bulk value) can be approximately calculated using the equation (1.1),

$$\Delta E = \frac{\hbar^2 \pi^2}{2 R^2} \left(\frac{1}{m_e} + \frac{1}{m_h} \right) - \frac{1.8 e^2}{\epsilon R} \quad (1.1)$$

where ΔE is the shift in the energy band gap, R is the radius of the nanoparticle, $1/\mu = 1/m_e + 1/m_h$ (μ being the reduced mass; and m_e and m_h being the electron and hole effective masses respectively), ϵ is the dielectric constant and e is the electronic charge [23]. In equation (1.1) the Coulomb term shifts the first excited electronic state to lower energy R^{-1} , while the quantum localization terms shift the state to higher energy, R^{-2} . Consequently, the first excitonic transition (or band gap) increases in energy with decreasing particle diameter.

1.1.2 Semiconductor Nanostructured Thin Films

Thin films as a two dimensional system are of great importance to many real-world problems. A thin film is a material created *ab initio* by the random nucleation and growth processes of individually condensing / reacting atomic / ionic / molecular species on a substrate. The structural, chemical, optical and physical properties of such a material are strongly dependent on large number of deposition parameters and may also be thickness dependent [4]. Thin-films may encompass a considerable thickness range, varying from a few nanometers to tens of micrometers.

The nanostructured coatings behave in a different manner compared to that of the conventional material due to (i) very small (10 nm) grains of which they are composed and (ii) a significant role of boundary regions surrounding individual grains, and therefore exhibit superior properties such as high temperature stability, high erosion resistance and superior optoelectronic properties [32, 71]. At the same time material costs are very small as compared to the corresponding bulk material and they perform the same function when it comes to the surface processes. Thin film technology is based on three foundations: fabrication, characterization and applications. Semiconductor nanostructures thin films are fabricated by semiconducting material with exciting applications in microelectronics,

communication, optoelectronics, catalysis, energy generation and conservation strategies [114].

1.2 II-VI $Zn_{1-x}Cd_xS$ TERNARY SEMICONDUCTOR NANOSTRUCTURES

Direct wide-band gap II–VI compound semiconductors are expected to be one of the most vital materials for high-performance optoelectronic devices such as light-emitting diodes (LEDs) operating in the blue or ultraviolet spectral range and photovoltaic (PV) devices for energy generation purposes [203]. Zinc sulphide (ZnS) is an important II–VI semiconducting material with a wide direct energy band gap of 3.65 eV in bulk [175]. Cadmium sulfide (CdS) is structurally very similar to ZnS and belongs to the same II–VI group of semiconductors with a direct bulk energy band gap of 2.42 eV [209].

In the last decade, the main efforts have been focused on the preparation of different color-emitting nanostructures with different particle sizes [156]. Recent advances have demonstrated that it is an effective route to tune the energy band-gap of semiconductor nanostructures by changing their constituent stoichiometries in ternary nanostructures [195, 220].

With increasing zinc content, a composition-tunable emission across the whole visible spectrum can be obtained by a systematic blue-shift in the emission wavelength of $Zn_{1-x}Cd_xS$ ternary nanostructures, where x is defined as mole fraction and is the mole ratio of cadmium to zinc. So obtained $Zn_{1-x}Cd_xS$ nanostructures are of considerable interest for a variety of applications such as light emitting diodes and solar cells. In the former case when doped with suitable active centres this layer works as an active layer of the LED's. In the latter case it forms the window layer for the variety of solar cell systems in which partial substitution of zinc to cadmium increases the width of optical window of the hetero-junction and also the diffusion potential [96, 217]. A brief overview of $Zn_{1-x}Cd_xS$ nanostructure applications focused in this thesis is presented in the following sections.

1.3 $Zn_{1-x}Cd_xS$ NANOSTRUCTURES FOR LIGHT EMITTING APPLICATIONS

Erwin *et al* described a mechanism to control the inclusion of transition metal impurities in semiconductor nanostructures - *impurity inclusion* is the process known as doping [55]. $Zn_{1-x}Cd_xS$ semiconductor is ubiquitous in device applications because their properties may change when the luminescence transitions are modified by doping with

external impurities. With one more added feature of quantum confinement, doped nanostructured semiconductors possess markedly different optical properties.

Doped nanostructures contains luminescent center as “*activators*” (dopant). The activator-related quantum states are formed in the “*semiconductor host*” and their localized (atomic transition) emission results. Thus the energy of activator-related emission remains nearly unchanged while the excitation can be tuned by both the composition and the quantum confinement [120].

Controlled amounts of impurities identified as activators are introduced into semiconductor (host) to create localized energy levels in the forbidden energy gap of the host [177]. These localized levels may be of two types:

- Levels of activator atoms,
- Perturbed energy levels of the host lattice

Figure 1.1 shows two possibilities of emission. In the first process, an electron in conduction band (excited from the valence band) can drops to an activator excited state and produces radiation by descending to the activator ground state. This process is frequent only when the free carrier density is high. The other process involves a trap (located in the forbidden gap), which include energy levels associated with lattice imperfections/defects such as vacancies in the semiconductor host. An electron falls from the conduction band to be trapped at a level from which no radiative transition is allowed (metastable state). If the transition is taking place from conduction band to these traps, they are referred as non-radiative transitions. Such transition results in the evolution of heat.

For efficient light emission, the host and the dopant must fulfill the following requirements:

- **Requirement of host semiconductor**
 - Bandgap of the host must be greater than the photon energy to ensure that absorption of visible light does not occur,
 - Host material must have good high field transport properties,
 - Host must interact with luminescent center which affects the energy and probability of the radiative relaxation process.

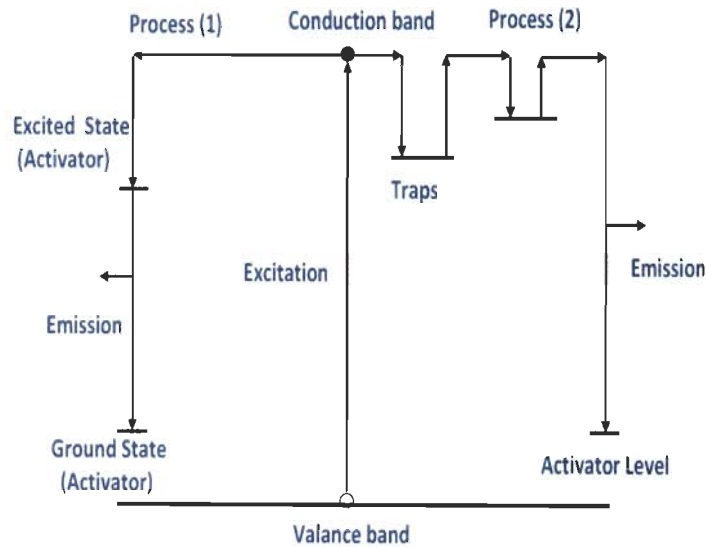


Figure 1.1: Schematic of two simple processes of an activated radiative emission
[177]

- **Requirement of activator**

Activator dominates the optical emission properties and ensures the radiative recombination of the carriers from activator induced states. The radiative mechanism is an atomic transition. The atomic transition energy is not dominated by the properties of the solid but rather elemental or free ion quantum properties of the luminescent center. Atomic transitions can be categorized as either

- Inter shell transitions: change in the angular momentum quantum number (l),
- Intra shell transitions: occur between states in the same quantum shell (s).

- **Laporte selection rule**

The probability of an optical transition (absorption or emission) is a function of the initial and final state wave functions and is represented by a term called the oscillator strength. Laporte selection rule suggests that the wave function of the initial state or the final state must be even and the other wave function must be odd. Applying the Laporte selection rule [132] to the two types of atomic transitions demonstrates that intra shell transitions ($d-d$, $l-l$, ...) are forbidden and certain inter shell transitions ($s-p$, $p-d$, $d-l$, ...) are allowed, such that (equation 1.2)

$$\Delta l = \pm 1 \ \& \ \Delta s = 0 \quad (1.2)$$

1.3.1 Transition Metal (TM) Doped $\text{Zn}_{1-x}\text{Cd}_x\text{S}$ Nanostructures

When a TM ion exists in space, the electrons arrange themselves in a way that minimizes the total energy of the ion. This free ion arrangement is perturbed, however in the presence of an electric or magnetic field. In a pseudo-ionic solid, cations and anions behave like positive and negative charges respectively. Atomic energy levels are modified because columbic force exists between the oppositely charged ions. The columbic forces induce a crystal field in the solid. This induced crystal field largely depend upon the ion arrangement (symmetry) and ion spacing and to a lesser extent to valence or charge of the ion in the solid [132]. Consequently this lattice symmetry and the ion spacing of the cations and anions will decide the final energy position of the activator. Various transition metals such as manganese (Mn), cobalt (Co), and copper (Cu) have been identified as suitable activators for visible light emission from II-VI group host semiconductor [177].

1.3.1.1 Manganese (Mn) doped nanostructures

When manganese is introduced into a pseudo-ionic solid (such as ZnS), it substitutes a cation site. Therefore the nearest neighbour anions are arranged with respect to the cation site. The electronic configuration of Mn atom is straightforward ($1s^2 2s^2 2p^6 3s^2 3p^6 3d^5 4s^2$), where the d -orbitals are unshielded by any other electron orbitals. The shape and symmetry of the d -orbitals have essentially five orientations namely d_{xy} , d_{xz} , d_{yz} , d_z^2 , and $d_{x^2-y^2}$. With zincblende/wurtzite structure ZnS possesses a tetrahedral symmetry. Each of these orientations in tetrahedral symmetry has an energy associated with it which is dependent on the orbital-ligand interaction [132]. Figure 1.2(a) shows the d -orbital crystal field splitting (D) in tetrahedral symmetry.

For Mn^{2+} doped ZnS system, Mn^{2+} ions substitute directly on Zn^{2+} lattice sites. Figure 1.2(b) shows the emission spectra of ZnS:Mn which results from the $\text{Mn } ^4T_1(3d) - ^6A_1(3d)$ intrashell transition. Since the Mn^{2+} transition is an intrashell transition ($3d-3d$), there is no angular momentum difference between the ground and the excited state ($\Delta l = 0$). Consequently this transition should be forbidden by the Laporte selection rule (section 1:3). This selection rule is relaxed, however, as Mn^{2+} ions substitute directly on Zn^{2+} sites which have tetrahedral symmetry. Laporte forbidden transitions are efficient if their lattice sites does not have center of symmetry (tetrahedral symmetry does not possess the center of symmetry) [132].

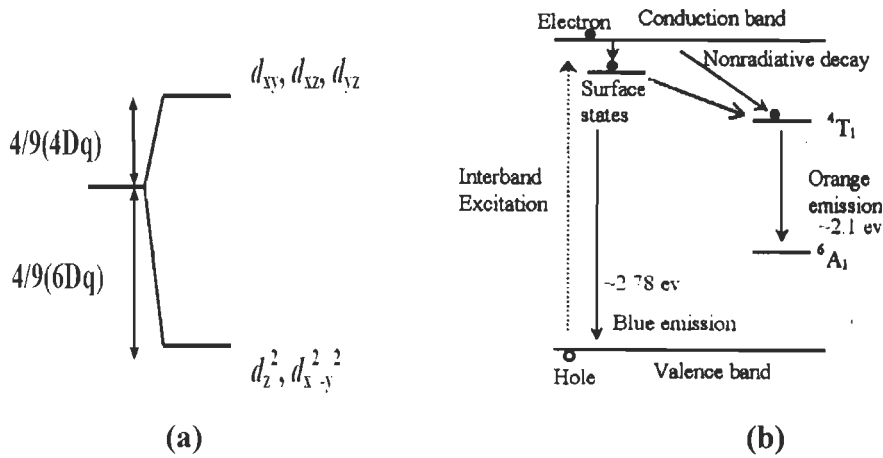


Figure 1.2: (a) The relative d -orbital crystal field splitting for tetrahedral symmetry and (b) Schematic representation of the emission levels of the ZnS:Mn [132]

1.3.2 $\text{Zn}_{1-x}\text{Cd}_x\text{S}$ Core-Shell Nanostructures

In semiconductor nanostructures, high emission efficiency from band-edge states is required, if they are to be used as efficient light emitters in any application. Unfortunately, the band-edge emission from nanostructures has to compete with both radiative and non-radiative decay channels. These non-radiative decay channels originate due to surface electronic states [85] and can be passivated by forming a layer (shell) on top of nanostructures (core).

Core-shell nanostructures consist of concentric/capping layer, in which particles of one material are coated with a thin layer of another material using specialized procedures. Core-shell nanostructures show modified and/or improved properties than their single-component counterparts [86, 101, 151]. Their properties can be modified by changing either the constituting materials or shell-to-core (s/c) ratio. Figure 1.3 shows a schematic of a variety of core shell particles. Surface of the core particle can be modified using bifunctional molecules and then small particles can be anchored on it (figure 1.3 (a)). Nanoparticles grow around the core particle and form a complete shell (figure 1.3 (b)). A smooth layer of shell material can be deposited directly on the core by co-precipitation method (figure 1.3(c)).

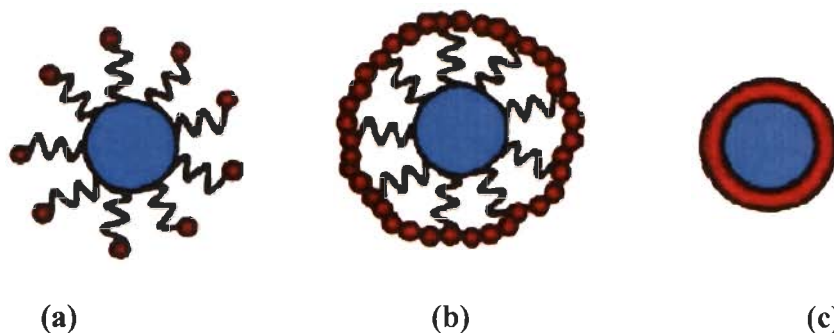


Figure 1.3: Variety of core-shell particles: (a) Surface-modified core particles anchored with shell particles, (b) More shell particles reduced onto core to form a complete shell, and (c) Smooth coating of core with shell [86]

1.4 $Zn_{1-x}Cd_xS$ NANOSTRUCTURES FOR PHOTOVOLTAIC APPLICATIONS

Major advances have occurred in thin film photovoltaic (PV) technologies (solar cells) based on cadmium telluride (CdTe) in past few years. CdTe/CdS is widely pursued thin film PV technology for their number of applications including roof-top and utility-scale applications.

Several technology issues, in CdTe/CdS thin film solar cell are identified as the limiting factors for multi-megawatt production [194]. For thin-film CdTe/CdS technology, short wavelength spectral response limit is imposed by the use of CdS. The back-contact stability is other major challenge for the further advancement and applicability of CdTe based PV technology. The short wavelength spectral region can also be harnessed for energy generation from CdTe based thin film structures. Higher energy band gap semiconductor in place of CdS (transparent down only to ~ 510 nm; E_g is 2.42 eV) can rectify this issue. Being a higher energy band gap semiconductor, ZnS (transparent to ~ 340 nm, E_g is 3.6 eV) can replace CdS. However, it had still been very difficult to get the photo conversion efficiencies greater than $\sim 3\%$ with CdTe/ZnS solar cells [35]. The limit on photo conversion efficiency by the use of ZnS is due to its highly resistive nature in comparison to CdS, and increased lattice mismatch with CdTe ($\sim 30\%$), which makes it poorer hetero junction partner with CdTe [140].

$Zn_{1-x}Cd_xS$ nanocrystalline thin films can be identified as a practical solution for CdTe thin film PV technology. Efficiency limiting mechanism caused by poor short wavelength spectral can be overcome by the increased band gap via composition

tunability offered by $\text{Zn}_{1-x}\text{Cd}_x\text{S}$ ternary semiconductor. In addition, the lattice mismatch between $\text{Zn}_{1-x}\text{Cd}_x\text{S}$ and CdTe can be minimized compared to ZnS .

1.4.1 Photovoltaic Background and Development

Photovoltaic conversion of solar energy is one of the most promising ways of meeting the increasing energy demands of the future when conventional sources of energy are being exhausted. Most of the energy currently consumed is supplied from fossil fuels. The main issue of those sources is sustainability, especially with the continuous increase of the demand for energy. Moreover, fossil fuel produces pollutants such as carbon dioxide, carbon monoxide, and others. These pollutants are responsible for the green house effect and global warming. Nuclear power and renewable energy seem to be promising candidates to replace fossil fuels [2]. However, each alternative has its own problems such as the treatment of the nuclear waste and the cost of photovoltaics.

Photovoltaics came in picture with the discovery of photovoltaic effect by Becquerel while experimenting with a solid electrode in an electrolyte solution, in 1839; he observed that voltage developed when light fell upon an electrode [2]. In 1876 Adams and Day reported photovoltaic behavior in selenium [3]. About 20 years later, Charles Fritts constructed the first true solar cell by coating the selenium with an ultra-thin layer of gold. Fritts' devices convert less than 1% of the absorbed light into electrical energy [158]. By 1927, another metal semiconductor-junction solar cell, which was made of copper and the semiconductor copper oxide, had been demonstrated. These early solar cells, still had energy-conversion efficiencies of $< 1\%$ [157, 158]. By the late 1980s Si cells, as well as those made of gallium arsenide (GaAs), with efficiencies of more than 20% had been fabricated [201]. Today, the best single crystal Si solar cells have reached an efficiency of 24.7%, compared with the maximum theoretical value of 30% [35].

Despite tremendous progress in all aspects of production of Si-based solar cells and the rapid decrease of production cost from \$5.9/Wp in 1992 to \$2.5/Wp in 2004. Figure 1.4 shows the average cost of Si based solar module in the timeframe from 1992 to 2004. Due to such high cost large-scale household applications are not yet commercially viable [118]. With respect to single crystal Si technology, single most important factor in determining the cost of production is the cost of the 250–300 mm-thick Si wafer used for the fabrication of solar cells. Unless a much thinner wafer, and thus less amount of Si, is used and the production process is made cheaper and simpler, any further decrease in Si cells cost will only be in small increments.

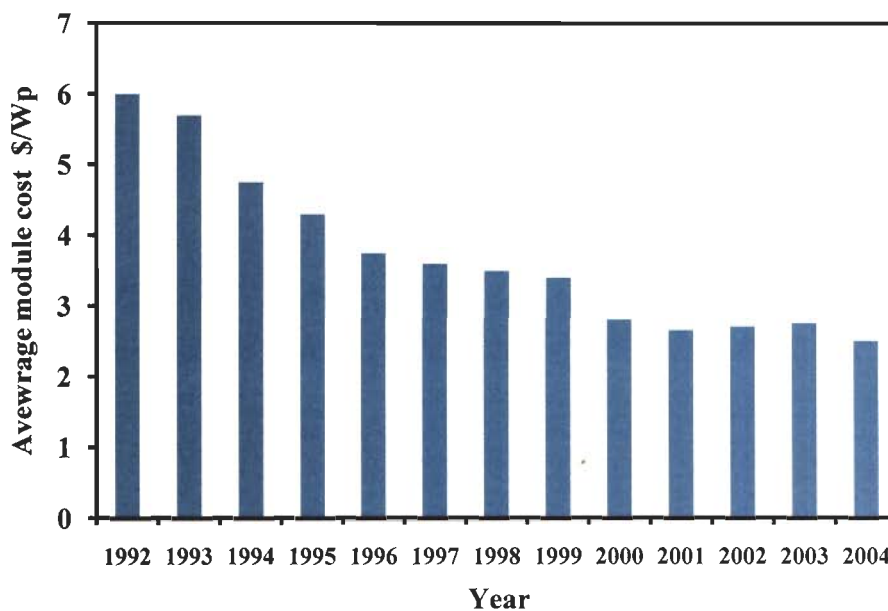


Figure 1.4: The average manufacturing cost of Si solar modules in the time range from 1992 to 2004 [118]

Thin film solar cells are preferable over the bulk single crystal Si technology for their low cost and design flexibility. Understanding and development in fabrication of thin films have triggered the research in thin film solar cell structures. Since 1990, amorphous Si and polycrystalline thin film solar cell efficiency have improved appreciably. The efficiency for amorphous Si has been reported 12% in the lab and 7% for commercial cells [202]. In 1992, the University of South Florida fabricated thin film $\text{SnO}_2/\text{CdS}/\text{CdTe}$ cell of 15.8% efficiency [21]. In 2002, the NREL (National Renewable Energy Laboratory) CdTe team have modified the CdTe device structure and fabricated a $\text{Cd}_2\text{SnO}_4/\text{Zn}_2\text{SnO}_4/\text{CdS}/\text{CdTe}$ thin-film solar cell of highest recorded 16.4% efficiency [35].

1.4.2 Thin Film Solar Cell Structure

In principle, a solar cell is a junction device obtained by placing two electronically dissimilar materials together with a thin electronic barrier in between, to separate charge carriers. However, efficient devices must ensure high conversion efficiency of solar photons generally AM1.5 (appendix A1.4) and high collection efficiency of excited charge carriers (appendix A1.5).

Thin film solar cell is a device made of different layers (figure 1.5). These layers can be deposited with different techniques on a substrate and have particular functions in

the device (appendix A1.6). Solar cells can be grown in the “substrate” or “superstrate” configurations (figure 1.5). The latter is the commonly used structure for transparent conducting electrode cells.

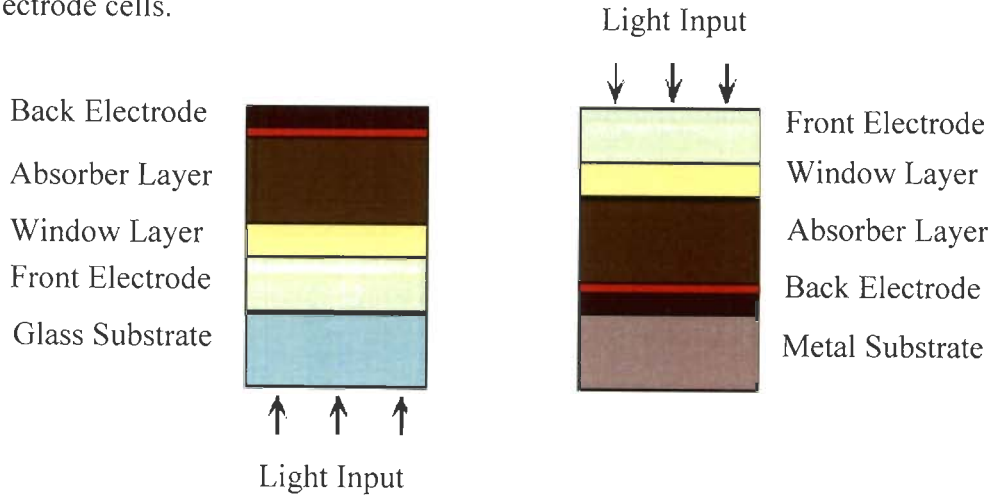


Figure 1.5: Schematic of thin film solar cell (a) Superstrate approach and (b) Substrate approach [35]

Almost all CdTe/CdS-based solar cells [1] have the so called “superstrate” configuration shown in figure 1.5(a). In this arrangement, the light is incident on a glass sheet, and the layer stack is deposited on its reverse side. Firstly a transparent conductive oxide (TCO) is deposited, and this acts as an *n-type* conductive contact for the *n*-CdS of the *p*-CdTe/CdS junction [158]. Typically the TCO’s are indium tin oxide (ITO), zinc oxide (ZnO) or tin oxide (SnO₂), or a multi-layer stack composed of these materials. The CdS is usually known as the “window layer” since light transmitted by it, is absorbed by the “absorber”, i.e. the CdTe itself. There is a well known loss (section 1.4.2 for more details) in CdTe/CdS cells arising from the fact that blue (and shorter wavelength) light absorbed by the CdS does not generate photo carriers [123]. Most absorption takes place in the highly absorbing CdTe (appendix A1.5). The uppermost part of the structure in the diagram (i.e. the dark side) is the contact to the CdTe. It is technologically more convenient that the contact is the last layer to be deposited and hence this can be done at low temperatures so as to afford some control over diffusion of impurities.

1.4.3 Zn_{1-x}Cd_xS as Window Layer

The polycrystalline CdS layer is *n-type* doped (as CdS invariably is), and therefore provides one half of the *p-n* junction. Being a wide band gap semiconductor ($E_g \sim 2.4$ eV at 300 K) it is transparent down to wavelengths of around 515 nm [178], and so is referred to as the window layer. An improvement in the properties of CdS/CdTe solar cell

is expected if $Zn_{1-x}Cd_xS$ solid solution films are used in place of the CdS alone. In hetero-junction solar cells, the part of the cell which serves as a window should have the highest forbidden gap possible and at the same time should have a very low resistivity. $Zn_{1-x}Cd_xS$ films, should be more suitable than CdS for hetero-junction solar cells because of their higher forbidden gap. The major limitation is resistivity of the $Zn_{1-x}Cd_xS$ films which increases rapidly with decreasing x . Yin *et al.* have suggested that for only values of $x > 0.8$, it is possible to reduce this resistivity even by *ex-situ* heat treatments [217].

1.5 OBJECTIVES OF THE STUDY

A very few research reports have been published on $Zn_{1-x}Cd_xS$ nanostructures. There is still much science that needs to be explored and improved. Thus, there exist urge need of understanding the ternary $Zn_{1-x}Cd_xS$ system, because of their potential applications in optoelectronic devices. It will be discussed in next chapter that the main direction of current development of $Zn_{1-x}Cd_xS$ nanostructures is based on the complex chemical routes and synthesis at elevated temperature. These drawbacks limit the use of such nanostructures for real device applications.

In the scope of this work, a single step low temperature (280 K) synthesis procedure is facilitated for the preparation of $Zn_{1-x}Cd_xS$ nanoparticles. Pulsed laser deposition technique was employed to synthesize the $Zn_{1-x}Cd_xS$ nanocrystalline thin films. Use of $Zn_{1-x}Cd_xS$ film for applications (involving two different physical phenomena) such as light emission and photovoltaic effect has been tested and demonstrated. In particular the following objectives are considered for the present study.

- Engineer reactions to synthesize nanoparticles from solutions of a host material of II-VI group semiconductors with less hazardous method,
- To quantify the doping concentration in the host lattice,
- Minimization of lattice mismatch between dopant and the host lattice to increase the extent of doping level,
- Development of nanocrystalline $Zn_{1-x}Cd_xS$ and TM doped $Zn_{1-x}Cd_xS$ coatings on optically transparent substrates by pulsed laser deposition technique,
- To study the effect of deposition parameters on the optical & structural properties of the synthesized films,
- To investigate the core-shell nanostructures for enhanced light emission from these nanostructures,

- To fabricate the photovoltaic device with $Zn_{1-x}Cd_xS$ as window layer and to test the device performance with variation in device fabrication parameters.

1.6 THE AUTHOR'S CONTRIBUTIONS

By elaborating this thesis it is considered that authors gained some contributions, which are produced in the following paragraphs:

In the first chapter the author's contributions are:

- An overview of various phenomenon considered in the present research work such as types of nanostructures, nano size effect, various applications of nanostructures in optoelectronics have been presented;
- Identification of composition tunable $Zn_{1-x}Cd_xS$ ternary semiconductor which can be utilized for both optoelectronic applications: light emission and photovoltaic;
- Identification of suitable dopant such as manganese (Mn) which can transfer the recombination route from surface states to Mn^{2+} induced states and produces orange emission; and can be incorporated in $Zn_{1-x}Cd_xS$ ternary semiconductor;
- Identification of the design methods for light emission enhancement;
- As a low cost alternatives to Si based solar cell, an understanding and development of CdTe based thin film solar cell has gained; and
- Finding the particular working case of $Zn_{1-x}Cd_xS/CdTe$ thin film solar cell, based on the conjecture that higher energy band gap semiconductor results into better photo conversion efficiencies.

In the second chapter the author's contributions are:

- On the basis of a critical literature survey, the high temperature processing and use of organic ligands were identified as major cause for poor light emission from existing nanostructures;
- Identification of the preparation procedures for $Zn_{1-x}Cd_xS$ nanostructures via both: solution and vapour routes. Previous published reports are compared and it is identified that though solution routes are low cost methods, they lack in the stoichiometry when compared to vapor routes;
- An efficient route is identified to coat the nanostructures with higher band gap material for the enhanced light emission; and

- Identification of efficiency limiting mechanisms in CdTe based thin film solar cell: window layer thickness and crystallinity were identified as major obstacles in obtaining high photo conversion efficiency.

In the third chapter the author's contributions are

- Detailed understanding of various preparation and characterization tools utilized in this study.

In the fourth chapter the author's contributions are

- Implementing the low temperature, and less hazardous co-precipitation technique for the preparation of $Zn_{1-x}Cd_xS$ nanoparticles;
- Detailed understanding of particle size distribution, error analysis of the obtained results;
- Ensuring the preserved stoichiometry in $Zn_{1-x}Cd_xS$ nanoparticles; demonstration of both: the quantum confinement and the composition effect, obtaining composition tunability; and
- Identification of near band and defect assisted emission mechanisms for the light emission in UV, blue and green spectral regions.

In the fifth chapter the author's contributions are

- Implementing the pulsed laser deposition technique for the preparation of $Zn_{1-x}Cd_xS$ nanocrystalline thin films for their use in optoelectronic devices;
- Identification of deposition parameters which provides control on surface roughness, % transmittance, crystal structure, and particle size of the $Zn_{1-x}Cd_xS$ nanocrystalline thin films;
- Identification of the mechanism responsible for structural transition in $Zn_{1-x}Cd_xS$ nanocrystalline thin films; and

In the sixth chapter the author's contributions are

- Establishing the method to confiscate the difficulty in dopant incorporation into $Zn_{1-x}Cd_xS$ nanostructures;
- Building the core-shell and nano-composite nanostructures for enhanced light emission;
- Comparing the light emission from core to the core-shell nanostructures; and
- Identification of theoretical model for effective surface passivation.

In the seventh chapter the author's contributions are

- Establishing a test for the uniform coverage of the device quality $\text{Zn}_{1-x}\text{Cd}_x\text{S}$ nanocrystalline thin films;
- Fabricating thin film solar device structure;
- Determining the photo conversion efficiencies with experiments related with both: variation in cell fabrication parameter and in $\text{Zn}_{1-x}\text{Cd}_x\text{S}$ window layer processing parameters; and
- Identifying the efficiency limiting mechanisms of $\text{Zn}_{1-x}\text{Cd}_x\text{S}/\text{CdTe}$ solar cell.

1.7 ORGANIZATION OF THE THESIS

To meet the above objectives, the present study is organized as follows:

Chapter 1 presents the world of nanostructures in a glance. Concepts relevant for the study of semiconductor nanoparticles and nanocrystalline thin films are briefly reviewed. Two important optoelectronic applications of II-VI $\text{Zn}_{1-x}\text{Cd}_x\text{S}$ ternary semiconductor namely, light emission and photovoltaics are outlined. A brief introduction is provided for the TM doped $\text{Zn}_{1-x}\text{Cd}_x\text{S}$ nanostructures for their use in light emitting devices. The other potential application of $\text{Zn}_{1-x}\text{Cd}_x\text{S}$ ternary semiconductor in photovoltaic devices is described in section 1.4. This chapter also presents the objectives and the layout of the thesis.

The literature relevant to the use of $\text{Zn}_{1-x}\text{Cd}_x\text{S}$ layer for light emitting and photovoltaic applications are reviewed in chapter 2. This chapter also presents the properties of the material systems investigated in this thesis. Different methods that have been employed for the preparation of $\text{Zn}_{1-x}\text{Cd}_x\text{S}$ nanostructures by various groups have also been discussed.

Chapter 3 consists of two sections. In the first section, synthesis strategies and methodologies for the preparation of $\text{Zn}_{1-x}\text{Cd}_x\text{S}$ nanoparticles and nanocrystalline thin films are presented. Co-precipitation technique and pulsed laser deposition techniques are used for the synthesis of nanoparticles and nanocrystalline films respectively. The other section presents the various characterization techniques that have been utilized in this study.

Chapter 4 presents the study of preparation and properties of $\text{Zn}_{1-x}\text{Cd}_x\text{S}$ nanoparticles with varying mole fraction. Various characterization techniques were employed to investigate the as-prepared $\text{Zn}_{1-x}\text{Cd}_x\text{S}$ ternary semiconductor nanoparticles.

Chapter 5 presents the synthesis of $Zn_{1-x}Cd_xS$ nanocrystalline thin films by pulsed laser deposition technique. Deposition parameters for the preparation of the $Zn_{1-x}Cd_xS$ nanocrystalline thin films have been optimized.

Chapter 6 entails the experiments in two parts. First part is related to the preparation of Mn^{2+} doped $Zn_{1-x}Cd_xS$ nanoparticles. Mn^{2+} doped $Zn_{1-x}Cd_xS$ nanoparticles are synthesized by adopting suitable modifications in the preparation methods. The relationship of emission properties of nanostructures to the mole fraction and doping amount is explored. Core-shell nanostructures have also been prepared for light enhancement from Mn^{2+} doped $Zn_{1-x}Cd_xS$ nanoparticles. The second part of this chapter present the results on the Mn^{2+} doped $Zn_{1-x}Cd_xS$ nanocrystalline thin films. $Zn_{1-x}Cd_xS$ /ZnS nanocomposites have also been investigated for enhanced light emission. The main aim of this study is to enhance the light emission from these nanostructures for their use in light emitting applications.

Chapter 7 is again bifurcated in two sections. The first section is related with the testing of uniform coverage of the $Zn_{1-x}Cd_xS$ layer on ITO substrate. The other section of this chapter deals with the PV device fabrication and characterization with $Zn_{1-x}Cd_xS$ as window layer.

Chapter 8 summarises the main findings of the present work and provides framework for future investigations.

CHAPTER 2

LITERATURE REVIEW

2.1 $\text{Zn}_{1-x}\text{Cd}_x\text{S}$ TERNARY SYSTEM

Quantization of band gap in CdS {bulk $E_g = 2.42$ eV (~ 510 nm)} has been well established experimentally [127] as well as by theoretical studies [16, 167]. The size quantization in CdS is generally used to achieve emission across the visible spectrum. ZnS has a band gap of 3.6 eV (~ 340 nm), which emits in blue-green spectral region. The ZnS related blue-green emission arises from the defect states [77]. Compared to size dependent properties of nanostructures, less attention has been given to tune their properties by varying their constituent composition. Also, these binary systems do not work well for the short wavelength spectral region from 420 to 510 nm, which is of special interest for the preparation of nanostructures-based blue LEDs and white light generation [12]. $\text{Zn}_{1-x}\text{Cd}_x\text{S}$ nanostructures are an alternative to these binary compounds for the light emission in visible spectrum. The light in visible spectrum can be achieved by composition tunability in such nanostructures.

On the other hand, the use of $\text{Zn}_{1-x}\text{Cd}_x\text{S}$ ternary semiconductor in place of CdS for photovoltaic applications provides two fold benefits. It allows more photons to pass through the absorber layer (with increased band gap via diffusion of Zn into the CdS), and hence, generate more carriers. Also, with increased band gap, larger diffusion potential is expected [217].

This chapter consists of two sections. First part (section 2.2) presents the physical and structural properties of ZnS and CdS binary semiconductors. This section also outlines the various applications of these two II-VI group semiconductors. In the second part (section 2.3 and 2.4), a review of the work carried out so far by various research groups is presented.

2.2 BINARY CONSTITUENTS

This section reviews the properties and band structure of the binary constituent (ZnS and CdS) which forms the $\text{Zn}_{1-x}\text{Cd}_x\text{S}$ ternary semiconductor.

2.2.1 Zinc Sulphide (ZnS)

Light emission from ZnS was first observed by a French chemist Théodore Sidot in 1866. His findings were presented by the renowned chemist A. E. Becquerel who was involved in the research on luminescence and phosphorescence [208]. The present renaissance of ZnS research started in the mid 1990s. Current interest is based around the potential to grow epitaxial layers, nanowires, or nanoparticles of ZnS for various potential applications such as [204];

- a highly luminescent material (when doped with transition metals or rare earth ions), with applications in display screens of computer monitors, CRT, fluorescent lamps, X-ray detectors, LED etc.,
- a potential candidate for the window layer of thin film solar cell,
- a diluted or ferromagnetic material (doped with Fe, Co, Ni, V or similar elements) for semiconductor spintronics.

2.2.1.1 Crystal structure and physical properties of ZnS

ZnS is white to yellow coloured crystal. It is typically found in the more stable cubic zincblende (ZB) structure. The hexagonal structure is found both in a synthetic material and as the mineral wurtzite (W) [206]. Both zincblende and wurtzite are intrinsic, wide energy band gap semiconductors. The zincblende structure has a bulk energy band gap of 3.68 eV at 300 K whereas the wurtzite form has a bulk energy band gap of 3.90 eV. Transition from the zincblende to wurtzite structure occurs at ~ 1020 °C in bulk ZnS [182].

In the zincblende structure, the space lattice is face centered cubic (FCC). There are two such FCC lattices which are separated by one quarter of the body diagonal of the unit cube. One lattice is occupied by Zn atoms, the other by S atoms. Each atom has 4 nearest neighbours of the opposite kind and is bound to these 4 atoms which are arranged at the corners of the surrounding tetrahedron (figure 2.1(a)). The bonding is typically covalent. The zincblende structure, like rocksalt structure, has the same face-centered cubic symmetry and reduced Brillouin zone as shown in figure 2.1(b). There is also an absence of a center of inversion. The various properties of ZnS are summarized in Table 2.1.

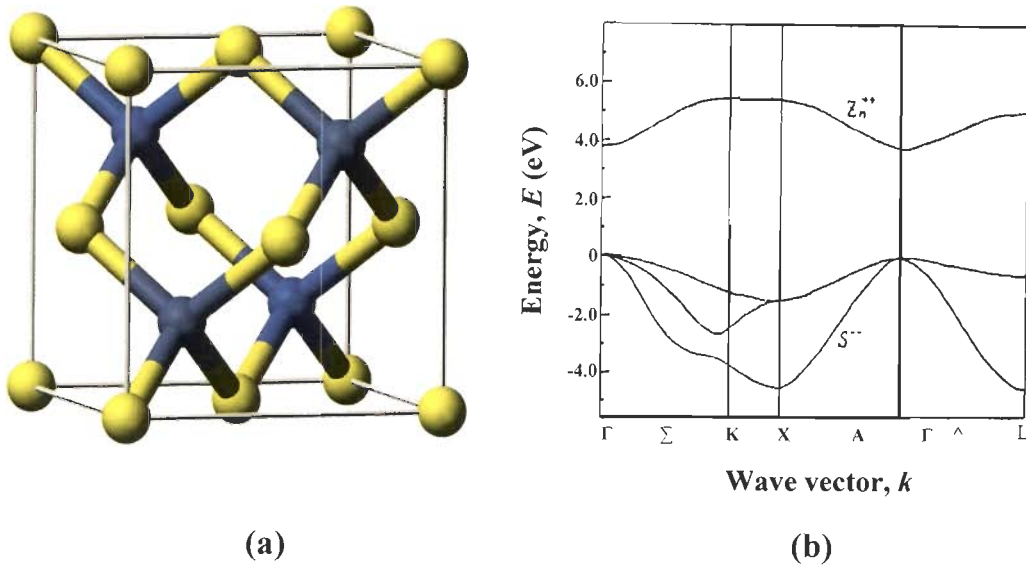


Figure 2.1: ZnS crystal structures: (a) Zinc Blende crystal structure (Zn²⁺: Gray spheres and S²⁻: Yellow spheres) [204] and (b) E-k diagram of ZnS in zincblende structure [177]

2.2.2 Cadmium Sulphide (CdS)

CdS is a direct band gap II-VI group semiconductor and has many applications such as

- Increased conductivity with light irradiation [169] (leading to uses as a photoresistor),
- when combined with a *p*-type semiconductor it forms the core component of thin film solar cell [35],
- when doped with "activator" and "co-activators" it luminesces under electron beam excitation (cathodoluminescence) [60].

2.2.2.1 Crystal structure and physical properties of CdS

Cadmium sulfide is yellow in colour. It has two crystal forms; the more stable hexagonal wurtzite structure (figure 2.2(a)) (found in the mineral Greenockite) and the cubic zincblende structure (found in the mineral Hawleyite). There is also a high pressure form having NaCl rock-salt like structure [169]. The various properties of CdS are summarized in Table 2.1. The reduced Brillouin zone of CdS in wurtzite structure is shown in figure 2.2(b).

Table 2.1: Properties of ZnS and CdS at room temperature [20, 24, 49, 51, 60, 76, 82, 103, 107, 110, 112, 134, 149, 163, 169, 176, 178, 181, 209, 213]

| Properties | ZnS | CdS |
|--|---------------------------|---|
| Crystal structure | ZB/W | ZB/W |
| Energy band gap (eV) ZB/W | 3.68/3.90 | 2.35/2.42 |
| dE_g/dP ($\times 10^{-3}$ eV/GPa) ZB | 63 | -5.7 |
| Melting point ($^{\circ}$ C) ZB | 1668 | 1750 |
| Density (gm.cm^{-3}) ZB | 4.11 | 4.87 |
| Electron and hole effective mass (m_e & m_h) | $0.25 m_0, 0.51 m_0$ | $0.19 m_0, 0.8 m_0$ |
| Dielectric constant (ϵ) | $5.2 \epsilon_0$ | $5.7 \epsilon_0$ |
| Ionic radii ($^{+2}$ state) (\AA) | 0.97 | 0.88 |
| Lattice constant a_0 (nm) ZB | 0.541 | 0.582 |
| Lattice constant (nm) W $a_0 = b_0$ c_0 c_0/a_0 | 0.3811 0.6234 1.636 | 0.4135 0.6749 1.632 |
| Symmetry ZB/W | C6me/F43m | C6me/F43m |
| Electron affinity χ (eV) | 3.9 | 4.79 |
| Work function Φ (eV) | 6.7 | 4.7 |
| Co-ordination geometry | Tetrahedral | Tetrahedral |
| Refractive index (ZB) | 2.368 | 2.529 |
| Solubility constant (K_{sp}) | 2×10^{-25} | 1.0×10^{-27} |
| Heat of formation (KJ/mol) | -206.53 ± 4.03 (ZB) | -147.65 ± 4.28 (ZB) -148.79 ± 4.13 (W) |

ZB: Zinblende; W: Wurtzite

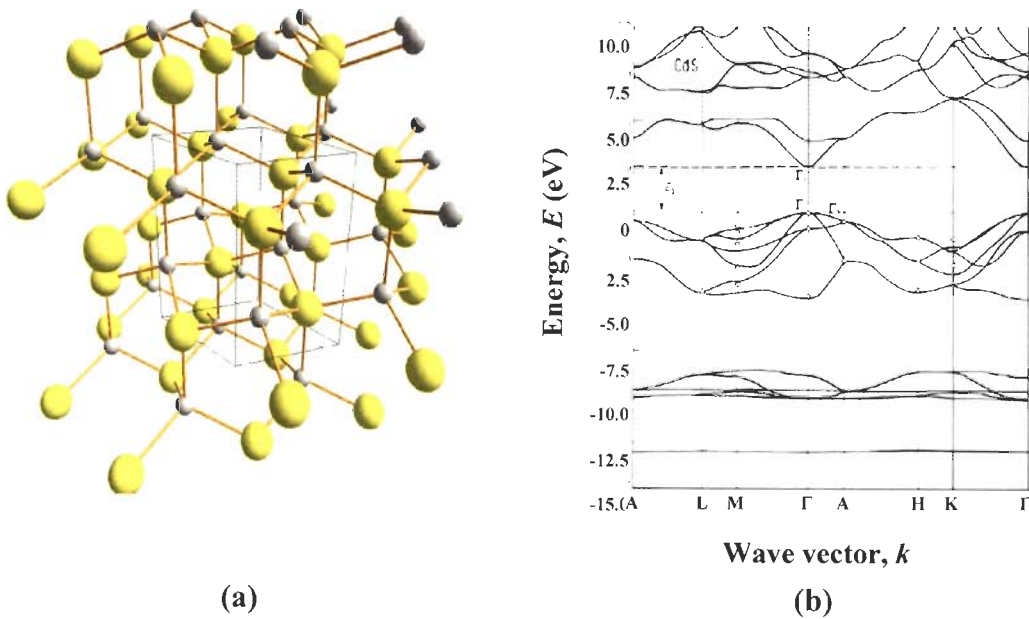


Figure 2.2: CdS crystal structures: (a) Wurtzite crystal structure (Cd^{2+} : Gray spheres and S^{2-} : Yellow spheres) and (b) E - k diagram of CdS in wurtzite structure [68]

2.3 RECENT DEVELOPMENTS IN $\text{Zn}_{1-x}\text{Cd}_x\text{S}$ NANOSTRUCTURES

A review on advances in the synthesis of $\text{Zn}_{1-x}\text{Cd}_x\text{S}$ nanostructures is presented, in the fundamental understanding of the mechanisms that control doping, and in the creation of highly crystalline films.

A research on $\text{Zn}_{1-x}\text{Cd}_x\text{S}$ nanostructures have come into light very recently since 2001 when Kulkarni *et al.* investigated the nanoparticles of CdS, $\text{Cd}_{0.75}\text{Zn}_{0.5}\text{S}$, $\text{Cd}_{0.25}\text{Zn}_{0.75}\text{S}$, and ZnS [95].

With the current protocols of high-temperature organo-metallic methods, the best reported PL efficiency of over 50 % is limited to the emission wavelengths above 520 nm for relatively large nanoparticles [78, 127, 146, 152, 153, 155, 188, 223].

Very small nanoparticles remain very difficult to be passivated and exhibit a broad size distribution. Furthermore, the tuning of physical properties by changing the particle size could cause problems in many applications, in particular, if unstable small particles are used [221, 222].

The potential application of $\text{Zn}_{1-x}\text{Cd}_x\text{S}$ nanoparticles also relies on the ability to fabricate them in the compact layer geometry such as nanocrystalline thin films. $\text{Zn}_{1-x}\text{Cd}_x\text{S}$ films for optical and microelectronic device applications could be successfully realized only if thorough insight is gained with regard to achieve the formation of desired microstructures through appropriate process controls.

Chynoweth *et al.* made an attempt to synthesize the $Zn_{1-x}Cd_xS$ films via spray deposition back in 1980 [37]. But they could not incorporate Zn into CdS lattice at mole fractions higher than 0.3.

Recently the growth technique, which can be mainly categorized into vapour route [210] and solution route, have been attempted to have better control on size, stoichiometry, and crystallinity.

Vapour route, such as thermal evaporation of CdS and ZnS powders onto silicon substrates pre-coated with gold as catalyst at reaction temperature of 900 °C results in the formation of nanoribbons of Cu doped $Zn_{1-x}Cd_xS$ [112]. Nien *et al.* have also synthesized the Cu, and Cl doped $Zn_{1-x}Cd_xS$ nanoparticles via solid state reaction at temperatures as high as 900 °C [136].

In contrast, solution routes used to synthesize $Zn_{1-x}Cd_xS$ nanostructures are summarized in Table 2.2.

The high temperature processing involved in vapour routes limits the use of such nanostructures for practical device applications. The solution route results in un-reacted species and degrades the subsequent device performance. The better choice for the preparation of $Zn_{1-x}Cd_xS$ nanostructures would be to identify the vapour based deposition technique with lower processing temperature.

2.3.1 Doped $Zn_{1-x}Cd_xS$ Nanostructures

Tuning the band gap can further be achieved by doping suitable ions. Since, impurities can be used to alter the properties of nanoscale materials in desirable and controllable ways, doped nanostructures can address key problems in applications from solar cells to imaging.

Dopants in nanostructures lead to phenomenon not found in the bulk because their electronic states are confined to a small volume. For example, *n* or *p*-type dopants can auto-ionize without thermal activation [138].

The conduction of carriers in bulk semiconductors is limited mainly by scattering from defects, in nanocrystalline films it is controlled by the communication between crystallites. Norris *et al.* proposed that to obtain superior properties from nanostructures [138], neighbouring nanoparticles should be uniform in size to have resonant electronic states. In addition, they should be closely spaced to ensure their quantum-mechanical overlap.

2.3.2 Mn²⁺ Doped Zn_{1-x}Cd_xS Nanostructures

Mn²⁺ doping in wide band gap semiconductors has resulted in high luminescence quantum efficiency owing to ${}^4T_1 \rightarrow {}^6A_1$ emission occurring at ~ 580 nm [17, 42, 100, 184].

The first report on doped semiconductor nanostructure date back to 1983 when trace amounts of Mn²⁺ was accidentally incorporated into ZnS colloids and their luminescence was studied [165]. After about eight years, the work on doped nanoparticles took off in full swing when the three dimensionally confined diluted magnetic semiconductors of Zn_{1-x}Mn_xS were synthesized in a glass matrix. Mn²⁺ luminescence was reported from Zn_{1-x}Mn_xS nanoparticles [165, 184]. Bhargava *et al.* reported in 1994 that Mn²⁺ doped ZnS nanoparticles exhibit high emission intensities and short radiative lifetimes as compared to bulk materials [17]. Due to such different properties Mn²⁺ doped ZnS were categorized as a new class of luminescent materials. This triggered the research activity in the area of doped semiconducting nanostructures, especially of ZnS:Mn. Mn²⁺ doped CdS nanoparticles have also been investigated, although to a lesser extent than ZnS.

It has proven persistently difficult to incorporate a sizable amount of manganese into such nanoparticles hosts, in spite of high solubility of dopant in the same bulk host. To explain this, few suggestions have been put forward by various research groups. Nag *et al.* suggested that the doped Mn²⁺ ion in nanoparticles such as CdSe is invariably in an energetically unfavourable state, preferring to be ejected to the surface of nanoparticles [129].

Levy *et al.* showed in their study that the rejection of Mn²⁺ from the host nanoparticles within this mechanism is also facilitated by an increase in temperature [100]. Their group observed that an increase in the reaction temperature anneals out the Mn²⁺ impurities, a phenomenon known as self-annealing.

The general inability to dope Mn ion in semiconductor host, therefore require a critical investigation.

Table 2.2: Synthesis of Zn_{1-x}Cd_xS nanostructures by solution route

| S. No. | Synthesis Method | Precursor(s) | Temperature | Type of Nanostructure | References |
|--------|--------------------------|---|-------------------------------------|---------------------------|------------|
| 1. | Photochemical Deposition | CdSO ₄ , ZnSO ₄ , and Na ₂ S ₂ O ₃ | Post deposition annealing at 400 °C | Nanocrystalline thin film | [73] |
| 2. | Colloidal Solution | CdO, ZnO, Olic acid, and 1-octadecene | 310 °C | Nanoparticles | [129] |
| 3. | Reverse Micelle | Cd(CH ₃ COO) ₂ ·2H ₂ O, Zn(CH ₃ COO) ₂ , Na ₂ S, Dioctyl sulfosuccinate, sodium salt (AOT), heptane and n-dodecanethiol | RT | Nanoparticles | [91] |
| 4. | Colloidal Solution | CdO, ZnO, 1-octadecene | 310 °C | Nanoparticles | [221, 222] |
| 5. | Chemical Bath Deposition | Cd(CH ₃ COO) ₂ ·2H ₂ O, Zn(CH ₃ COO) ₂ and thiourea | 55 - 85 °C | Nanocrystalline thin film | [81] |

2.3.3 Core-Shell Nanostructures

A lot of emission is lost due to radiationless recombination of the electron and hole at the nanostructure surface where so called “dangling bonds” acts as electron traps. The judicious choice of a passivating agent can improve the size-dependent band-edge luminescence efficiency, while preserving the processability [117]. Unfortunately, passivation by means of organic molecules is often incomplete or reversible, exposing some regions of the surface to degradation effects such as photo-oxidation [6, 89]. Chemical degradation of the ligand molecule itself or their exchanges with other ligands also lead to unstable nanostructures [89].

Hexadecylamine coated ZnSe nanoparticles were prepared by Lomascolo group by the approach of multiple injections of precursors [108]. However organic shell material suffers degradation with time and therefore imposes a time constraint. Graf *et al.* demonstrated a general method to coat various colloidal particles (gold colloids, silver colloids, boehmite rods, gibbsite platelets positively or negatively charged polystyrene, etc.) with silica [69]. They functionalized the surface of colloids using polyvinylpyrrolidone (PVP), which is an amphiphilic nonionic polymer. This method can be used for a variety of colloids and it is fast but they required a surface functionalizer which is an organic binder and could suffer from degradation with time.

It is also possible to make certain shell particles without functionalizing core particle with approach, known as controlled precipitation. In this strategy, the synthesis of shell particles can be carried out in the presence of cores. The core particles act as nuclei and hydrolyzed shell material gets condensed on these cores forming shells [139]. Jiang *et al.* have synthesized the ZnS:Mn/ZnO core shell nanoparticles by utilizing the above approach [83]. However their system suffers the hetero-step that has been formed between ZnS and ZnO semiconductors and could be responsible for comparatively lower emission intensities obtained in their work.

More efficient route is to coat the nanostructure with higher band gap and of similar group material. A stringent requirement for the epitaxial growth of several monolayers of one material on top of another is a low lattice mismatch between the two materials. If this requirement is not met, strain accumulates in the growing layer, and eventually may be released through the formation of misfit dislocations, degrading the optical properties of the system [46]. Similar approach is adopted in our work with the use of II-VI group semiconductors both as core and shell materials and is presented in Chapter 6.

Ethayaraja *et al.* synthesized the CdS/ZnS core-shell nanoparticles. Their group presented very unique approach for the estimation of shell thickness [56]. They make use of particle size difference between the core and the core-shell nanostructures to estimate the shell thickness. In particular the similar approach has also been adopted in this work for the estimation of shell thickness.

Taneja *et al.* adopted the method for the in-situ surface passivation of nanocrystalline films by terminating the surface dangling bonds of CdS with hydrogen [189]. Li *et al.* synthesized ZnO/Er₂O₃ core-shell nanostructures by pulsed laser deposition technique. Their group obtained an enhancement in the emission intensity by depositing a thin Er₂O₃ layer onto the fabricated ZnO nanorod surface [102].

2.4 Zn_{1-x}Cd_xS NANOCRYSTALLINE FILMS AS WINDOW LAYER IN CdTe SOLAR CELL

A rare literature is available till date on the use of Zn_{1-x}Cd_xS as window layer in CdTe solar cell. Extreme difficulty in preserving the stoichiometry in such films could be responsible for the lack of work carried out in this area. The many-fold advantages (see section 1.4 for detail) of using Zn_{1-x}Cd_xS thin films in place of CdS put a major thrust in this area.

Yin *et al.* studied the effect of deposition temperature of Zn_{1-x}Cd_xS layer prepared by spray pyrolysis technique [217]. However, their research was in a very early stage to make a meaningful comment.

Chou *et al.* and Arora *et al.* have identified the efficiency limited mechanisms associated with CdTe/CdS solar cell. They found high degree of interface states at CdS/CdTe interface and absorption in CdS films as major efficiency limiting mechanism [12, 36]. The former limitation could be rectified by *ex-situ* heat treatment of CdS layer in hydrogen environment. Hydrogenation removes oxygen (which acts as recombination centre) from CdS and thereby reduces the interface effects. The other efficiency limiting mechanism is related to the CdS film thickness. Thinner CdS films improves low wavelength quantum efficiency, however there is a technological limit on reducing the CdS films below 100 nm, as it leads to very poor film quality [36]. With an alternative approach the lower wavelength quantum efficiency can be increased by the use of higher band gap material. Zn_{1-x}Cd_xS films can be used in place of CdS without the need of reduction in film thickness down to 50 nm.

Wu *et al.* investigated the benefits of introducing a buffer layer of Zn_2SnO_4 (ZTO) between the CdS and two different TCOs, SnO_2 and Cd_2ZnO_4 (CTO). It was found that ZTO improved the performance significantly [211]. The cells were examined by X-ray photoelectron spectroscopy (XPS) and secondary-ion mass spectroscopy (SIMS), showing that ZTO intermixed with the CdS film at annealing temperature of 550-650 °C in argon atmosphere. They had to utilize the *ex-situ* high temperature processing, which is not suitable for soda lime glass substrate. The inter-diffusion between CdS and ZTO may lead to several beneficial effects: a) The diffusion of Zn into the CdS film increases its band gap, allowing more photons to pass through to the absorber layer, and hence, generate more carriers and b) ZTO improves the adhesion of the films to the substrate even after a severe CdCl_2 treatment.

Krishnakumar *et al.* prepared the double layer structured CdS/CdTe cells [94]. Though the approach was unique but their study was in lack of characterization evidences and therefore raises a question mark on the reproducibility of results.

In view of the above discussion, replacing CdS by $\text{Zn}_{1-x}\text{Cd}_x\text{S}$ in CdTe/CdS solar cell requires a critical investigation of structural, morphological and optical properties of $\text{Zn}_{1-x}\text{Cd}_x\text{S}$ layer as it subsequently affects the device performance.

CHAPTER 3

EXPERIMENTAL TECHNIQUES

3.1 GENERAL

The choice of a particular synthesis technique is dictated by the specific characteristics of nanostructures required for a study or application of interest. Some of the important aspects that need to be taken into consideration are the particle size distribution, presence of a surface passivation layer, whether a thin film or a colloid is required etc. While wet-chemical techniques are very useful for the synthesis of highly mono-dispersed, nanoparticles in large quantities, the production of densely packed, uniform, nanocrystalline thin films required for device fabrication is not feasible with these methods.

This chapter describes the experimental techniques that are used in this work for the fabrication, processing and characterizing of nanostructures, starting with the nanoparticles synthesis techniques (Section 3.2.1). Following that, in section 3.2.2, a detailed description of the deposition techniques for the synthesis of thin films used for device fabrication are presented. Analytical techniques for characterization of the prepared nanostructures are described in section 3.3.

3.2 SYNTHESIS TECHNIQUES

The synthesis of nanostructures can be accomplished through “*bottom up*” or “*top down*” approaches [67]. In the bottom up synthesis approach, small building blocks are assembled into larger structures, e.g. chemical synthesis and physical vapor deposition techniques. In the top down approach larger objects are modified to give small features e. g. lithographic patterning. Synthesis techniques used in this work follow bottom up approach.

3.2.1 Nanoparticles Synthesis Techniques

As discussed in the previous chapter (section 2.3), very few attempts have been made to synthesize the $Zn_{1-x}Cd_xS$ nanoparticles. Organo-metallic precursors [150], micro-emulsion methods [141], high energy ball milling [125], etc. have been developed or modified for the synthesis of nanoparticles. However all these methods require complex precursor solutions and employed very high temperature processing step (~ 500 °C)

accompanied by long heating times. Such elevated and prolonged heating results in irregularly shaped aggregated particles. It is important to synthesis nanoparticles by wet chemical techniques that can produce particles having controlled characteristics such as morphology, composition and size for achieving light emitting characteristics. In this work co-precipitation technique is adopted as particle size, and composition can be well controlled with ease by variation of precursor concentration, reaction time, reaction temperature etc.

3.2.1.1 Co-precipitation technique

Co-precipitation technique is a wet chemical bottom up approach. When the precipitation technique contains only one or two element, it is relatively straightforward. In more complicated systems such as ternary and/or quaternary, as multiple species must be precipitated simultaneously, the process is called co-precipitation technique. It has the following characteristics:

- Products of precipitation reactions are generally sparingly soluble species formed under conditions of supersaturation,
- Such conditions dictate that nucleation will be the key step in the precipitation process and that a large number of small particles will be formed followed by growth.

Generally, those chemical reactions are chosen which results in products with low solubilities, such that the solution quickly reaches a supersaturated condition. A simple addition reaction for the formation of electrolyte A_xB_y could be expressed as



The equilibrium relationship between the product and its reactants is expressed as the solubility product constant, K_{sp} :

$$K_{sp} = (a_A)^x (a_B)^y \quad (3.2)$$

where a_A and a_B are the activities of the cation A and anion B in aqueous solution.

Knowing the solubility product of a salt, it is possible to predict whether on mixing the solution of its ions, a precipitate will be formed or not. For precipitation to occur, its ionic product (Q_{sp}) should exceed solubility product [212].

3.2.1.2 Controlled co-precipitation technique

Core-shell nanoparticles are synthesized by a slight modification of this approach, known as controlled precipitation [139]. Synthesis of shell particles can be carried out in the presence of cores. The core particles act as nuclei and hydrolyzed shell material gets condensed on these cores forming shells. Reactant concentrations and the amount of added core particles play an important role in deciding the shell thickness.

3.2.2 Thin Film Deposition Technique

Thin films are thin material layers ranging from fractions of a nanometer to several micrometers in thickness and its formation starts with nucleation followed by coalescence and subsequent thickness growth, all stages of which can be influenced by deposition parameters in all the physical vapor deposition (PVD) technique.

In PVD, the synthesis of thin films is usually carried out from the same material and its purity depends on the starting materials, base vacuum, and purity of the ambient gas atmosphere [28, 214] On the other hand, in chemical deposition technique, some unreacted chemicals and products other than the desired one are often left behind after the deposition of coatings. There are wide varieties of deposition techniques available, few of them are shown in Table 3.1 along with their properties.

3.2.2.1 Pulsed laser deposition technique

Pulsed laser deposition (PLD) is a physical vapor deposition process, carried out in a vacuum system. Several features make PLD particularly attractive for complex material film growth. These include:

- Stoichiometric transfer of material from the target to the substrate,
- Compatibility with background pressures ranging from ultrahigh vacuum to 1 torr.

For low laser fluences and/or low absorption at the laser wavelength, the laser pulse would simply heat the target, with ejected flux due to thermal evaporation of target species. As the laser fluence is increased, an ablation threshold is reached where laser energy absorption is higher than that needed for evaporation. The ablation threshold is dependent on the absorption coefficient of the material and is thus wavelength dependent. At still higher fluences, absorption by the ablated species occurs, resulting in the formation of plasma at the target surface, which is not dependent on the vapor pressures of the constituent cations, resulting in stoichiometric transfer of material [74].

Table 3.1: Various thin film deposition techniques

| Mode of Deposition | Variety of Deposition Technique | Properties |
|------------------------------------|--|--|
| Physical Vapor Deposition (PVD) | Evaporation <ul style="list-style-type: none"> • Thermal Evaporation • E-beam Evaporation Pulsed Laser Deposition <ul style="list-style-type: none"> • Nanosecond laser deposition • Femtosecond laser deposition Sputtering <ul style="list-style-type: none"> • DC Sputtering • RF Sputtering Reactive PVD | <ul style="list-style-type: none"> - Expensive as it requires vacuum pumps. - Highly uniform nanocrystalline thin films |
| Chemical Vapor Deposition (CVD) | Low pressure CVD (LPCVD) Plasma-Enhanced PVD(PECVD) Metal Organic CVD(MOCVD) | <ul style="list-style-type: none"> - Expensive as vacuum is required. - Uniform nanocrystalline thin films |
| Thermal Spray | Flame Spraying (FLSP) Plasma Spraying (PLSP) Electric Arc Spraying (EASP) High-velocity Oxy Fuel (HVOF) | <ul style="list-style-type: none"> - Thermal spraying processes produce dust and fume. Therefore, adequate extraction or ventilation to remove this dust and fume from the working environment should be provided - Suitable for large area and complex geometry |
| Sol Gel Deposition | Dip Coating Spin Coating | <ul style="list-style-type: none"> - Low cost alternatives - Lack of uniform density, composition and thickness. |

Figure 3.1 is a schematic of the PLD process. A pulsed laser is focused onto a target of the material to be deposited. For sufficiently high laser energy density, each laser pulse vaporizes or ablates a small amount of the material creating a plasma plume. The ablated material is ejected from the target in a highly forward-directed plume. The ablation plume provides the material flux for film growth. The PLD set up used for the present work is shown in plate 3.1. PLD technique is used in this work for the deposition of undoped, manganese doped and nanocomposite $Zn_{1-x}Cd_xS$ thin films.

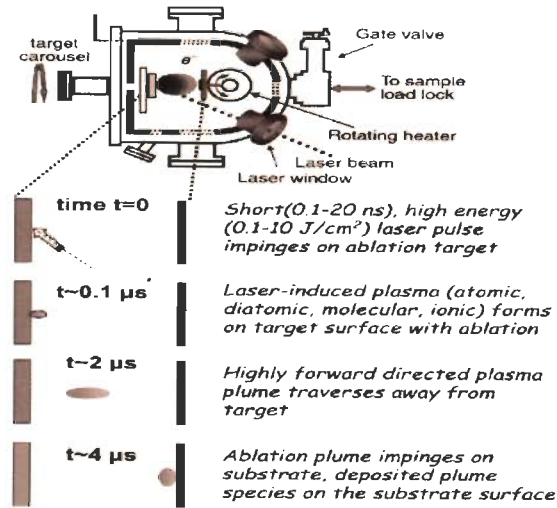


Figure 3.1: Schematic of the PLD process [74]

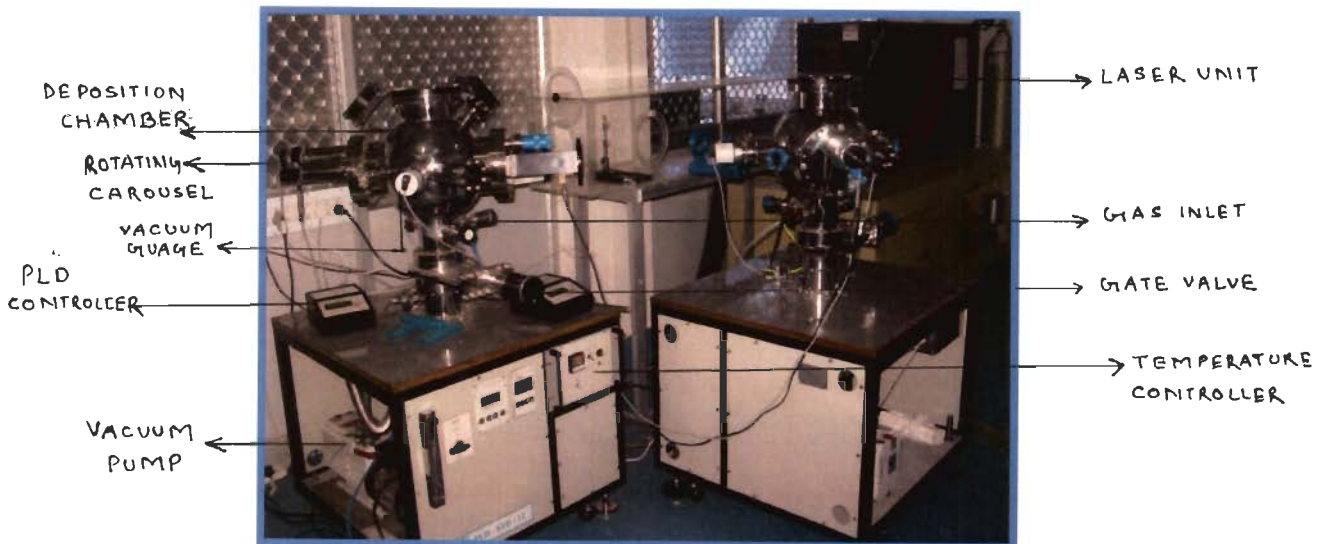


Plate 3.1: PLD unit set up in Nano Science Laboratory

3.2.2.2 Thermal evaporation technique

Thermal evaporation is also a PVD technique. It is the most effective method to deposit materials with low melting points [191]. The vacuum thermal evaporation

deposition technique (shown in figure 3.2) consists of a heating unit for the evaporation of the material to be deposited. The material vapor finally condenses in form of thin film on the cold/heated substrate surface and also on the vacuum chamber walls. Usually low pressures are used, about 10^{-6} or 10^{-5} torr, to avoid reaction between the vapor and atmosphere. At these low pressures, mean free path of vapor atoms is of the same order as the vacuum chamber dimensions. Therefore, these particles travel in straight lines from the evaporation source towards the substrate. Thermal evaporation was used to deposit four materials in this work: CdTe, CdCl₂, In and Au.

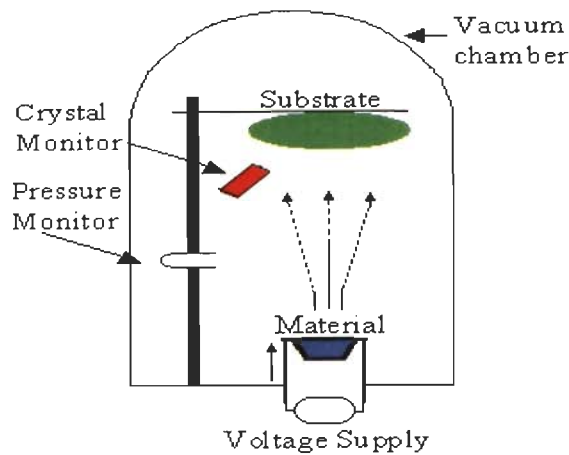


Figure 3.2: Schematic of thermal evaporation deposition [198]

3.3 CHARACTERIZATION TECHNIQUES

3.3.1 X-ray Diffraction (XRD)

XRD is a versatile, non-destructive technique that reveals detailed information about the chemical composition and crystallographic structure of a crystalline material.

3.3.1.1 Basic principle

Figure 3.3 shows the basic principles of X-ray diffraction. In this figure, a parallel beam of X-rays strikes the crystal where the atoms are placed on two parallel planes (a and b) which are separated by a distance of d (inter atomic space). The parallel X-ray beams on the left impinge onto the planes at an angle of θ and the atoms scatter the X-ray beams in all directions. If the detector is placed at an angle of θ on the right, then only when the path difference between the two reflected beams 1' and 2' is an integral number of wavelengths, the beam constructively interfere and the signal at the detector will be a maximum. Mathematically this is expressed by the following equation [43]:

$$2d \sin \theta = n\lambda \quad (3.3)$$

where, d is the spacing between two adjacent atomic planes, θ is the angle between the atomic plane and the X-rays, n is the order of diffraction maximum, and λ is the wavelength of the X-rays.

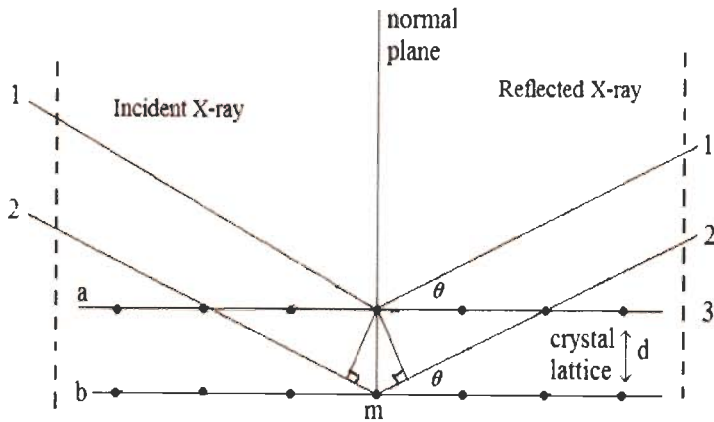


Figure 3.3: Diffraction of X-ray by a single crystal material [43]

3.3.1.2 Working principle

Figure 3.4 shows the working principle of the XRD in practice. The crystallized film is placed onto a rotating sample holder inside the chamber of the diffractometer. The incoming X-ray beams strikes the rotating material from the left while keeping the X-ray source stationary. When the sample holder rotates to a particular angle so that “Bragg” equation has been satisfied, the X-ray receiver (on the right hand) receives a strong diffraction of X-ray beam. By rotating the material, a pattern of diffraction peaks can be obtained. The position and geometric shapes of these peaks are related to the crystal structures in the material.

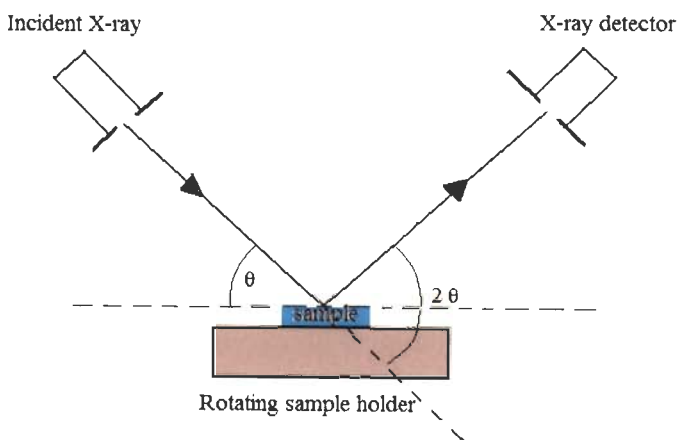


Figure 3.4: Working principles of a XRD



Plate 3.2: Photograph of XRD (Bruker AXS, D8 Advance)

3.3.1.3 XRD in practice

In this work, the crystal phases of the thin films and nanoparticles are characterized by using a Bruker (AXS, D8 Advance) X-ray diffractometer. The XRD was operated at 40 kV and 30 mA which employs CuK_α radiation with a wavelength of 1.5402 Å. The X-ray data was collected over a suitable range with a step size of 0.02° . The XRD set up used for the present work is shown in plate 3.2.

3.3.1.4 Particle/grain size

The XRD pattern can also provide the information about the material's microstructures such as particle/grain size. The grain size of a crystallized material is usually related with the width (B) of an X-ray diffraction peak (figure 3.5). The peak width (B) is measured from the diffraction peak where its intensity is at half of its maximum intensity [43]. Therefore, it is called the full width of half maximum (FWHM).

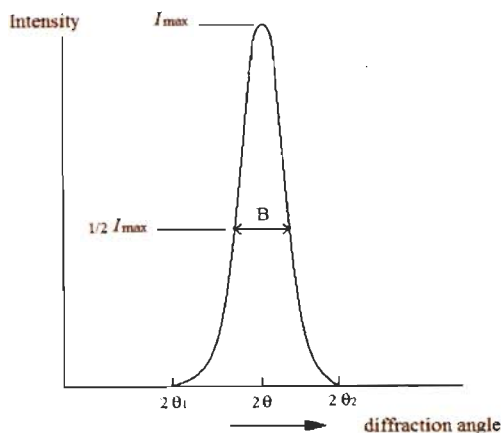


Figure 3.5: Effect of grain size on X-ray diffraction peak [43]

The measured FWHM can be mathematically converted to the grain size of the nanostructures by using “Scherrer” equation.

$$d_p = \frac{0.9 \lambda}{B \cos \theta} \quad (3.4)$$

where d_p is the average grain size, λ is the wavelength of the incoming X-ray beam (1.5402 Å in this case), B is the width of the diffraction peak in radius, θ is the position of the diffraction peak.

3.3.1.5 Lattice constant

Lattice constant of the system under investigation can be determined by making use of equation (3.3). For zincblende and wurtzite structures, the interplanar spacing and lattice constant are related by the equations (3.5) & (3.6) respectively,

$$\frac{1}{d^2} = \frac{h^2 + k^2 + l^2}{a^2} \quad (3.5)$$

$$\frac{1}{d^2} = \frac{4}{3} \left(\frac{h^2 + hk + k^2}{a^2} \right) + \frac{l^2}{c^2} \quad (3.6)$$

3.3.1.6 Texture coefficient

The texture coefficients, TC of the thin films as a function of deposition parameters can also be calculated from their respective XRD peaks using the following formula [79]

$$TC_{hkl} = \frac{I_{hkl}}{\sum_{i=1}^n h_i k_i l_i} \quad (3.7)$$

where, h, k, l are planes and i is the positive integers, n is number of orientations in XRD pattern.

3.3.2 Field Emission Scanning Electron Microscope (FE-SEM)

The Field Emission Scanning Electron Microscope (FE-SEM) produces a 2-D surface image of a material with exceptionally high resolution ~ 3-4 nm.

3.3.2.1 Working principle

A high energy beam of electrons (emitted via field emission) is focused on to the surface of the sample and the interaction between the sample atoms and electron beam causes the emission of various particles including secondary electrons, X-rays, and backscattered electrons (figure 3.6(a)). The emitted electrons are attracted through the anode and pass through electromagnetic lenses (condenser lens) which are then focused on the sample by the objective lens. A metal coil wire is placed within the object lens. This coil is used to produce a control magnetic field so that the electron beam is deflected back and forth as parallel lines to create a grid of rectangular lines over the area of interest on the sample [59]. The image of the scanned area is synchronized with the coil of the SEM. Therefore, the relative position of the feature can be displayed on a screen. Figure 3.6(b) shows the schematic of the process flow diagram.

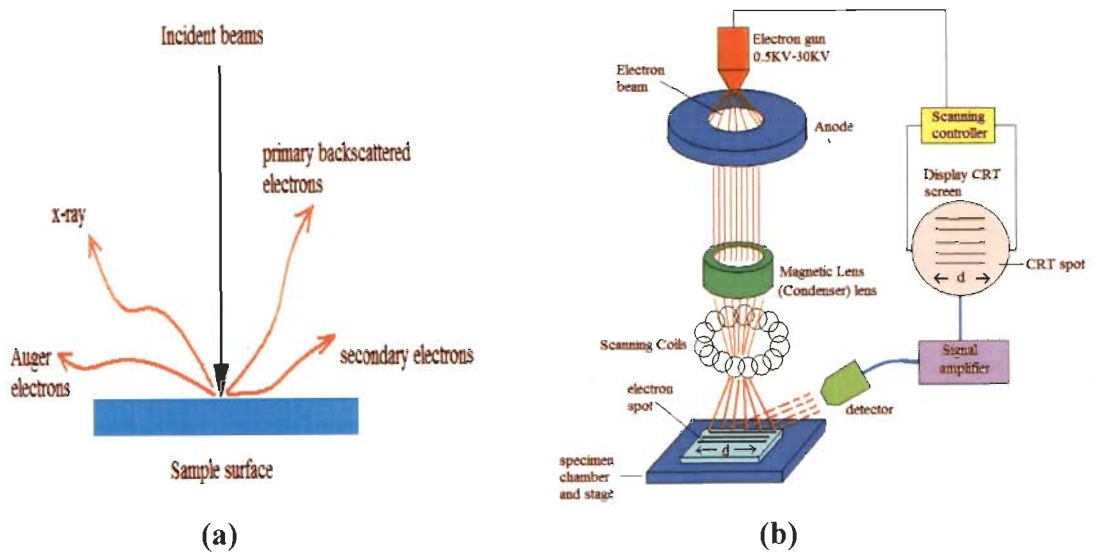


Figure 3.6: (a) The emission of various particles including secondary electrons, X-ray, and backscattered electrons and (b) Schematic diagram of the FE-SEM [59]

3.3.2.2 FE-SEM in practice

In this work, the surface morphology of the samples is studied by using a (FEI, Quanta 200F) FE-SEM. The FE-SEM set up used for the present work is shown in plate 3.3. The samples are attached to a sticky conducting carbon stub carrier and placed into the vacuum chamber of the FE-SEM. To optimize the image resolution, the FE-SEM is operated at 20 kV. The images of the thin film surface have been collected at different magnifications. A scale bar was displayed on each FE-SEM image to measure the grain size of the thin film.



Plate 3.3.: Photograph of FE-SEM (FEI Quanta 200F)

3.3.2.3 Composition analysis

The attachment of FE-SEM such as energy dispersive spectroscopy (EDS) is used for obtaining the chemical composition. An EDS spectrum normally displays peaks corresponding to the energy levels for which the most X-rays had been received. Each of these peaks is unique to an atom, and therefore corresponds to a single element. Higher the intensity of a peak in a spectrum, higher is the concentration of the corresponding element in the specimen. In this work the spectrum has been collected for 500 seconds.

3.3.3 Atomic Force Microscopy (AFM)

The Atomic Force Microscope (AFM) is a very high-resolution (0.01 nm) scanning probe microscope. AFM technique is based on the measurement of different forces (magnetic, attractive, repulsive, Van-der Waals and electron static [19]) between a moving tip and sample surface. By measuring the interaction force via a soft cantilever while the probe is scanning across the surface of the sample, a 3-D image of the surface can be obtained.

3.3.3.1 Working principle

The basic set up of an AFM is shown in figure 3.7. A small tip at the front of the soft cantilever is used to scan the sample surface [19]. The specimen's rough surface forces the tip to move, echoing the specimen's terrain. The deflection of the cantilever is measured and the height of the tip above the sample surface is maintained by the use of a laser diode feedback system and a vertical piezo micro-positioning stage.

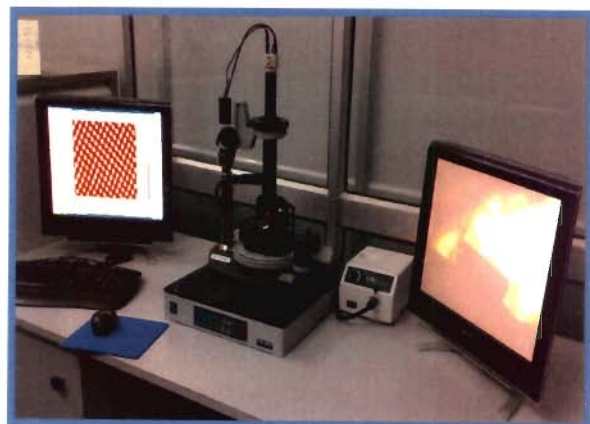
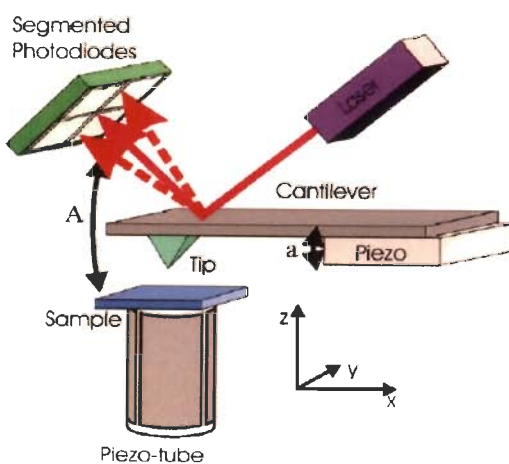


Figure 3.7: The working principles of the AFM [19]

Plate 3.4: Photograph of atomic force microscope (NT-MDT, Ntegra)

3.3.3.2 AFM in practice

In this work, a “NT-MDT, NTEGRA AFM” is used to study the surface roughness of the thin films. The AFM was operated in semi-contact mode. The probing tip scans through the sample surface with a constant force (constant force mode). The AFM set up used for the present work is shown in plate 3.4.

3.3.4 Transmission Electron Microscope (TEM)

The transmission electron microscope (TEM) operates on the same basic principles as the optical (light) microscope but uses electrons instead of light. The shorter wavelength of electrons (200 KV electrons have a wavelength of 0.025 Å) makes it possible to get a high-resolution (0.2 nm).

3.3.4.1 Working principle

A schematic diagram of a TEM is shown in figure 3.8. With an electron gun, an electron beam is formed, which is accelerated by an electric field formed by a voltage difference of, typically, 200 kV and this beam is focused to a small, thin, coherent beam by the use of condenser lenses 1 and 2. The first lens defines the "spot size" of the final spot that strikes the sample and the second lens changes the size of the spot on the sample from a wide dispersed spot to a pinpoint beam. When the focused electron beam strikes on the sample and traversed through it, the objective lens focus it to form an intermediate image. This intermediate image is in turn magnified by a projector lens(es) to form a magnified final image [207]. The TEM set up used for the present work is shown in plate 3.5.

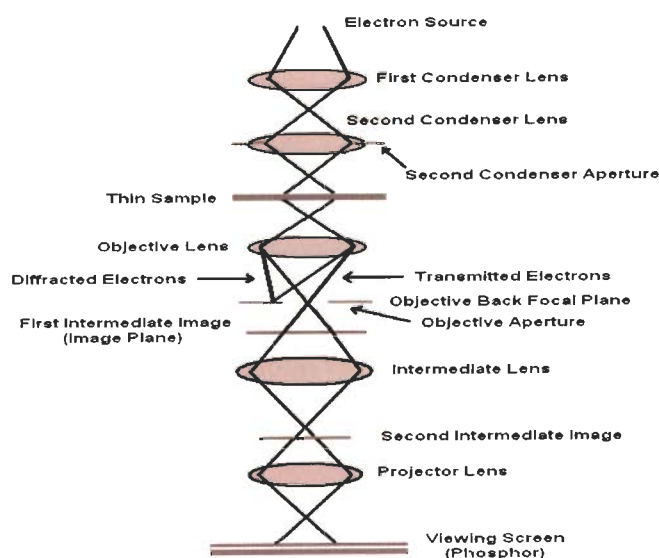


Figure 3.8: Schematic diagram of a TEM [207]

Plate 3.5: Photograph of TEM

(FEI, Tecnai 20)

3.3.4.2 Modes of operation

- **Image mode**

In image mode, intermediate aperture is removed and only objective aperture is used. When the objective aperture is positioned in the back focal plane (the flat plane at right angles to the optical axis onto which a lens will focus an image) to pass only the transmitted (undiffracted) electrons of incident electron beam and block the diffracted electrons, a bright field image is formed. When the objective aperture is positioned in the back focal plane to pass only some diffracted electrons of incident electron beam, a dark field image is formed.

- **Selected Area Electron Diffraction (SAED) mode**

In diffraction mode, objective aperture is removed and only intermediate aperture is used which passes the diffraction pattern of a selected region. The diffraction pattern that is always present in the back focal plane of the objective is brought into focus by the objective lens or in other words, intermediate lens is focused on back focal plane. Individual spots are seen when the specimen is a single crystal, while for polycrystalline material, concentric rings are observed.

3.3.4.3 Lattice spacing determination

For a single crystal, the diffraction spots from planes which are equivalent by symmetry are placed symmetrically around the central [70]. Interplanar distance, d can be calculated from the expression

$$R_{TEM}d = L\lambda \quad (3.8)$$

where, λ is the wavelength of the electron beam (0.025 Å for 200 kV), R_{TEM} is the distance of a particular spot from the central bright spot and L is the distance between the specimen and the diffraction plane, known as the camera lens constant.

3.3.4.4 TEM in practice

Transmission Electron Microscope (FEI, Tecnai 20) is used for the present work. TEM Samples were prepared by adding a drop of very dilute solution of the nanoparticles dispersed in a suitable solvent (isopropyl alcohol in our case) onto a carbon coated copper grid and subsequent evaporation of the solvent. The grids were then dried under vacuum

for an hour or so before characterizing the samples. It was not possible to prepare the thin film samples via standard TEM sample preparation route [59] in our case, as that requires very good adherence between substrate and film. An alternative and innovative sample preparation process was employed, where a transparent film was deposited with 200 laser shots on the TEM grid at desired deposition parameters. The as deposited grids were used as TEM samples.

3.3.5 UV-Vis Absorption Spectrophotometer

UV-visible spectroscopy investigates the interactions between ultraviolet or visible electromagnetic radiation and matter.

3.3.5.1 Basic principle

A schematic of a typical UV-Vis spectrophotometer is shown in figure 3.9. A beam of light from a visible and/or UV light source (Deuterium Gas Filled Lamp for UV-Range, 200-350 nm and a Tungsten Filament Lamp for the visible to near IR range, 350-1100 nm) is separated into its component wavelengths by diffraction grating. Each monochromatic beam in turn is split into two equal intensity beams by a half-mirrored device. One beam, the sample beam, passes through the sample being studied while the other beam passes through the reference. The intensity of the reference beam, which should have suffered little or no light absorption, is defined as I_0 . The intensity of the sample beam is defined as I . If the sample absorbs light, then I is less than I_0 , and transmittance can be defined as $T = I/I_0$ or absorbance as $A = \log I_0/I$. The wavelength of maximum absorbance is a characteristic value [29].

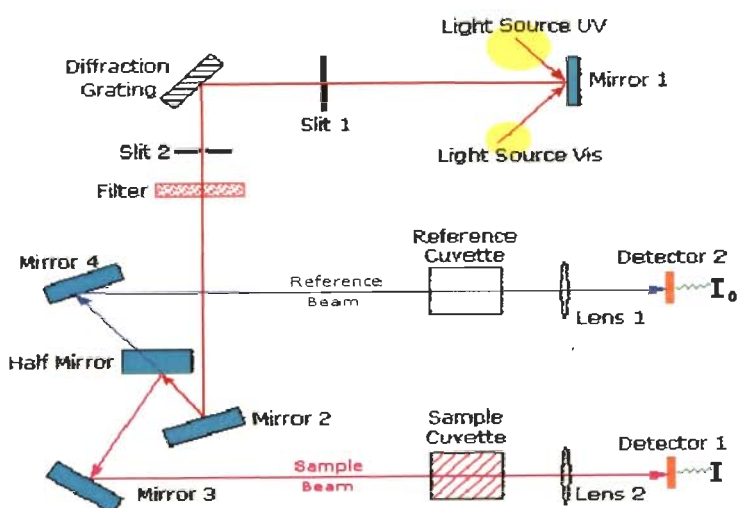


Figure 3.9: Schematic of a UV-Vis spectrophotometer [29]

3.3.5.2 Energy band gap determination

Tauc relation [190] is used for the determination of the energy band gap of semiconductors and is given by

$$\alpha h\nu = A(h\nu - E_g)^n \quad (3.9)$$

where α is the absorption coefficient, A is a constant, h is Planck's constant, ν is the photon frequency, E_g is the energy band-gap and n is $\frac{1}{2}$ for direct semiconductor. An extrapolation of the linear region of a plot of $(\alpha h\nu)^2$ on the y-axis versus photon energy $(h\nu)$ on the x-axis gives the value of the energy band gap E_g since $E_g = h\nu$ when $(\alpha h\nu)^2 = 0$.

3.3.5.3 Refractive index determination

For a partially transparent thin film it is possible to determine the refractive index by measuring the transmission of light through it. Figure 3.10 (a) shows a thin film with refractive index n , bounded by two transparent media with refractive indices, n_0 and n_1 .

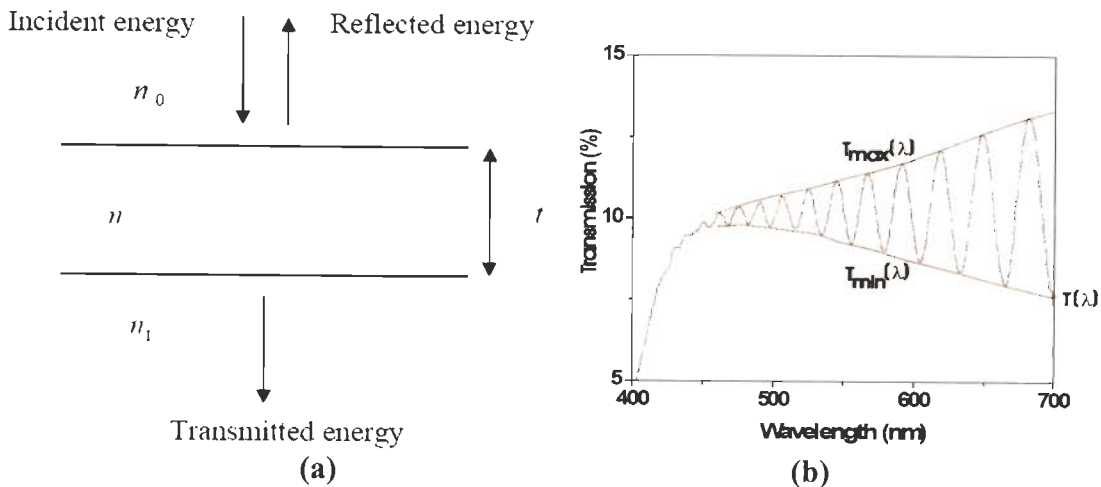


Figure 3.10: (a) Reflection and transmission of light by a thin film and (b) Transmission spectrum for a thin ZnO film [116]

Manifacier method is adopted in this work to calculate the refractive index [116], and is given by

$$n = [N + N^2 - n_0^2 n_1^2]^{1/2} \quad (3.11)$$

where

$$N = \frac{n_0^2 + n_1^2}{2} + 2n_0 n_1 \frac{T_{\max} - T_{\min}}{T_{\max} T_{\min}} \quad (3.12)$$

where T_{\min} and T_{\max} are continuous function of λ through $n(\lambda)$. These functions which are the envelopes of the maxima $T_{\max}(\lambda)$ and the minima $T_{\min}(\lambda)$ in the transmission spectrum are shown in figure 3.10 (b).

3.3.5.4 Film thickness determination

The thickness, t of the film can be calculated from two maxima or minima and is given by [116]

$$t = \frac{M \lambda_1 \lambda_2}{2(n(\lambda_1)\lambda_2 - n(\lambda_2)\lambda_1)} \quad (3.13)$$

where M is the number of oscillations between the two extrema ($M = 1$ between two consecutive maxima or minima); $\lambda_1, n(\lambda_1)$ and $\lambda_2, n(\lambda_2)$ are the corresponding wavelengths and indices of refraction.

3.3.5.5 UV-Vis in practice

UV-Vis Spectrophotometer (Varian, Cary 5000) is used for the present work. The UV-Vis set up used for the present work is shown in plate 3.6. For recording the absorption spectra of the nanoparticles, the samples were dispersed in suitable solvents such as propanol and loaded in quartz cuvettes. A blank cuvette containing only the solvent was used as a reference. For obtaining the absorption characteristics of all the samples, at first the transmittance (T) at different wavelengths (λ) are measured and then absorbance (α) at the corresponding wavelengths λ are calculated using the Beer-Lambert's relation [29]

$$\alpha = \frac{1}{y} \ln \left(\frac{1}{T} \right) \quad (3.14)$$

where y is the path length in cm. In our case the path length considered was 1 cm. In case of nanocrystalline thin films the substrate material was used as the reference sample.



Plate 3.6: Photograph of UV-Vis spectrophotometer (Varian, Cary 5000)

3.3.6 *J-V* Characterization

The *J-V* measurements were carried out in this work by applying a voltage across the device terminals using a Keithley 2400 source meter, which also measured the resultant current. The *J-V* data were fed into a Labview programme in order to determine the basic PV working parameters i.e. η , FF , V_{oc} and J_{sc} . The *J-V* measurements have done in both dark and under light. For light measurement solar simulator is used. Solar simulator (also artificial sun) is an apparatus that replicates the solar spectrum and is used for testing solar energy conversion devices. The ASTM E927-05 standard ((2010) ASTM E927-10: Standard Specification for Solar Simulation for Terrestrial Photovoltaic Testing) is a common specification for solar simulators used for photovoltaic testing.

3.3.6.1 Solar simulator in practice

A Sceintech, SS150W, Newport 91150V (standard cell) solar simulator was used to provide the AM1.5 illumination for light measurements (appendix A1.4 for more details). The Solar simulator set up used for the present work is shown in plate 3.7.



Plate 3.7: Photograph of solar simulator (Sceintech, SS150W)

3.3.7 Photoluminescence (PL) Spectrophotometer

Luminescence is, in some ways, the inverse process to absorption. A simple two-level atomic system shift to the excited state after photons of appropriate frequency is absorbed. This atomic system can return to the ground state by spontaneous emission of photons. This de-excitation process is called luminescence. However, the absorption of light is only one of the multiple mechanisms by which a system can be excited. In a

general sense, luminescence is the emission of light from a system that is excited by some form of energy. If the luminescence is due to light excitation then it is called photoluminescence. A spectrophotometer is an analytical instrument used to measure and record the fluorescence of a sample [66].

3.3.7.1 Basic principle

A schematic of PL spectrophotometer is shown in figure 3.11. The excitation source consists of the light source and a monochromator, which selects a specific wavelength range from the incoming light (monochromator can be replaced by a filter). Light emitted from the sample is analyzed by a monochromator equipped with a light detector. The light detector transforms the photons into electrical signals. After the signals are amplified, they are recorded, and provide spectral data in the form of digitized electrical signals [133].

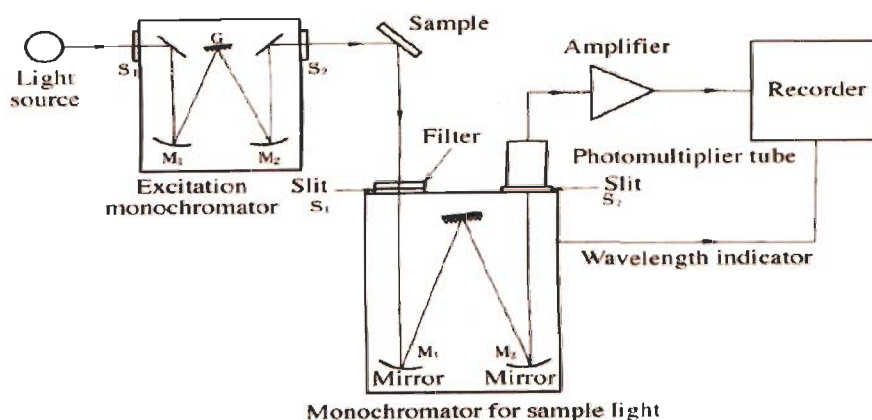


Figure 3.11: Schematic of a photoluminescence spectrophotometer [133]

3.3.7.2 PL in practice

PL spectrophotometer (HITACHI, F-2500) is used for the present work. The PL set up used for the present work is shown in plate 3.8. The emission spectrum is obtained by plotting the relationship between the wavelength and the intensity of the emitted light from a sample excited by an excitation of constant energy. On the other hand the excitation spectrum is obtained by observing changes in the emitted light intensity at a set wavelength while varying the excitation energy.



Plate 3.8: Photograph of PL measurement (HITACHI, F-2500)

3.3.8 Superconducting Quantum Interference Device (SQUID) Magnetometer

Superconducting quantum interference device (SQUID) is the most sensitive detector of magnetic flux. It consists of a superconducting ring interrupted with either one or two Josephson junctions [44, 84].

SQUID comprises of two main sections; SQUID assembly and the electronic control system. The probe contains a high precision temperature control system, allowing measurements from 1.9 to 400 K with an accuracy of 0.01 K. The superconducting magnet system which provides reversible field operation up to ± 7 Tesla uses an oscillatory technique to minimize magnetic drift immediately following field changes. The sample handling system (sample translator and sample transport) allows automatic sample measurements and position calibrations using a microstepping controller having a positioning resolution of 0.0003 cm. The dewar consists of an inner liquid helium reservoir and outer liquid nitrogen jacket, to reduce excessive liquid helium boil off. Liquid helium system provides refrigeration for the superconducting detection system and magnet, as well provides the operation down to 1.9 K.

3.3.8.1 SQUID in practice

Quantum Design SQUID (MPMS XL) magnetometer has been used in the present study to measure the magnetic properties of manganese doped nanoparticles. The SQUID set up used for the present work is shown in plate 3.9. The probe contains a high precision temperature control system, allowing measurements from 1.9 to 400 K with an accuracy of 0.01 K.



Plate 3.9: Photograph of SQUID quantum design (MPMS XL)

3.3.9 Electron Probe Micro Analyzer (EPMA)

Electron probe micro analyzer (EPMA) is an analytical tool used to non-destructively determine the chemical composition of small volumes of solid materials. It works similarly to a scanning electron microscope. The sample is bombarded with an electron beam, emitting x-rays at wavelengths characteristic to the elements being analyzed. This enables the abundances of elements present within small sample volumes (typically 10-30 cubic micrometers or less) to be determined. The concentrations of elements from boron to plutonium can be measured at levels as low as 100 parts per million (ppm) [200].

3.3.9.1 EPMA in practice

Cameca, SX100 has been used in present study to measure the manganese concentration. It can accurately measure elemental concentrations of approximately 10 ppm. The EPMA set up used for the present work is shown in plate 3.10.



Plate 3.10: Photograph of EPMA, (Cameca, SX100)

CHAPTER 4**Zn_{1-x}Cd_xS NANOPARTICLES: COMPOSITION TUNABILITY,
PARTICLE SIZING & LIGHT EMISSION**

4.1 GENERAL

Very small nanoparticles (diameter < 2 nm) with a band-edge emission in the blue spectral region remain very difficult to be passivated. Such nanoparticles exhibit broad size distribution and low emission intensity, also discussed earlier in section 2.3 [220]. In an effort we synthesized the Zn_{1-x}Cd_xS nanoparticles. This system is less toxic compared to CdS but is less investigated. Also no size selective methods or control of kinetics is necessary to exactly control the size. Emission of different colours can be obtained by varying cadmium concentration instead of controlling particle size. In ternary Zn_{1-x}Cd_xS nanoparticles this can be obtained with different cadmium concentration independent of particle size. The goal is to directly synthesize Zn_{1-x}Cd_xS nanoparticles with a relatively narrow size distribution in aqueous system.

In this chapter, a cost effective chemical route is employed for the preparation of uniform and luminescent Zn_{1-x}Cd_xS nanoparticles. A co-precipitation technique utilizing zinc, cadmium and sulphur precursors is explored for synthesizing Zn_{1-x}Cd_xS nanoparticles due to its relatively low synthesis temperature and low cost. A systematic study investigates the effects of mole fraction (*x*) on the preparation and light emission properties of Zn_{1-x}Cd_xS nanoparticles. A detailed particle size investigation and studies on the optical properties is carried out, to obtain a well characterized system apt to be used in light emitting applications.

4.2 CHAPTER PREFACE

This chapter presents the effects of variation in mole fraction on the structural, morphological and emission properties of Zn_{1-x}Cd_xS nanoparticles. The experiments are described in section 4.3. The results of the crystal structure and particle size with mole fraction are presented in sections 4.4.1, and 4.4.2 respectively. Constituent elemental analysis is shown in section 4.5. Quantum confinement and composition effects in Zn_{1-x}Cd_xS nanoparticles are discussed in section 4.6. Emission properties of Zn_{1-x}Cd_xS nanoparticles are shown in section 4.6. Section 4.7 presents summary of the results obtained in this study.

4.3 SYNTHESIS DETAILS

Zn_{1-x}Cd_xS nanoparticles have been prepared in the laboratory at 280 K using co-precipitation technique. Mole fraction (x) in the nanoparticles has been controlled by adjusting the cadmium to zinc weight ratio.

4.3.1 Chemicals

Zinc nitrate hexahydrate [Zn(NO₃)₂·6H₂O] (99.999%) and cadmium nitrate tetrahydrate [(Cd(NO₃)₂·4H₂O)] (99. %) were used as zinc, and cadmium source respectively along with sodium sulphide [(Na₂S·9H₂O)] (99.99%) as sulfur source. Chemicals were procured from Sigma-Aldrich. All chemicals were used without further purification.

4.3.2 Procedure

For a typical synthesis of Zn_{0.9}Cd_{0.1}S nanoparticles, 0.5 M zinc nitrate hexahydrate, 0.05 M cadmium nitrate tetra-hydrate and 0.5 M sodium sulphide nona-hydrate were taken to maintain the stoichiometry of the nanoparticles. Zinc nitrate and cadmium nitrate aqueous solutions were thoroughly mixed and kept at 280 K using thermostat. The Na₂S solution was then added to the mixture with a dripping speed of 10 drops/minute. Uniform magnetic stirring is provided for the better atomic diffusion during the length of the reaction. A series of samples NP-1 to NP-7 were prepared with mole fraction (x) varying from: 0.1 to 0.9. The resulting nanoparticles were washed with methanol and further isolated by centrifugation and decantation. The precipitates were dried in hot air oven at 323 K. Final products were then obtained by crushing dried precipitate using pestle mortar. Standard synthesis conditions for synthesizing the Zn_{1-x}Cd_xS nanoparticles are shown in Table 4.1.

Table 4.1: Standard conditions used in this study for synthesis of Zn_{1-x}Cd_xS nanoparticles

| Sample | Mole fraction (x) | Synthesis precursors Molarity (M) | | | Reaction temperature (K) |
|--------|-------------------|--------------------------------------|-------------------------------|------------------------------|--------------------------|
| | | Zinc nitrate hexa-hydrate | Cadmium nitrate tetra-hydrate | Sodium sulphide nona-hydrate | |
| NP-1 | 0.1 | 0.5 | 0.05 | 0.5 | 280 |
| NP-2 | 0.2 | 0.5 | 0.1 | 0.5 | 280 |
| NP-3 | 0.3 | 0.5 | 0.15 | 0.5 | 280 |
| NP-4 | 0.4 | 0.5 | 0.2 | 0.5 | 280 |
| NP-5 | 0.5 | 0.5 | 0.25 | 0.5 | 280 |
| NP-6 | 0.75 | 0.5 | 0.375 | 0.5 | 280 |
| NP-7 | 0.9 | 0.5 | 0.45 | 0.5 | 280 |

An experimental set up used in this study for the synthesis of the Zn_{1-x}Cd_xS nanoparticles is shown in figure 4.1.

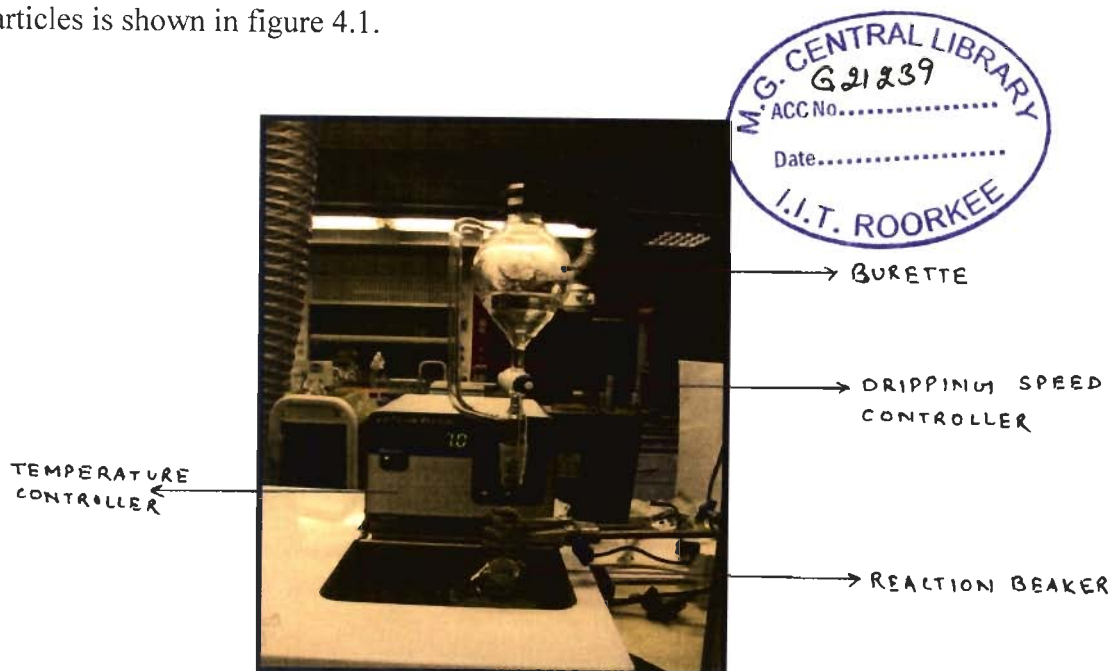


Figure 4.1: Reaction set up for the synthesis of nanoparticles

4.4 RESULTS & DISCUSSION

Variation in mole fraction results in compositional tunability. Effects of composition and quantum confinement on the emission properties of Zn_{1-x}Cd_xS nanoparticles have been investigated via PL and UV-Vis measurements. Particle size and morphology of Zn_{1-x}Cd_xS were investigated via combination of TEM, FESEM, and XRD. The results are discussed in the following sections.

4.4.1 Structural Properties of Zn_{1-x}Cd_xS Nanoparticles

Co-precipitation conditions of this study are described in Table 4.1. Figure 4.2 shows the XRD patterns of the Zn_{1-x}Cd_xS nanoparticles, namely NP-1 to NP-7 with mole fraction, x , as 0.1, 0.2, 0.3, 0.4, 0.5, 0.75, and 0.9 respectively. Vertical bars (a) and (b) in figure 4.2 corresponds to XRD peak position for (111) orientation for CdS (JCPDS # 800019) and ZnS (JCPDS # 800020) zincblende structure respectively. Broad diffraction peaks in all patterns are in accordance with the characteristics of nano-sized materials. XRD of the nanoparticles reveals a zincblende structure of the nanoparticles over the considered composition range (figure 4.2). The characteristic XRD patterns of the nanoparticles exhibit three prominent peaks, which are indexed to the scattering from (111), (220), and (311) planes respectively. Above result is consistent with the results that ZnS exist in cubic structure at low temperature reported by [110]. In 2005, Lu *et al.* synthesized the Mn²⁺ doped ZnS nanoparticles via chemical precipitation method at room temperature using Zn(CH₃COO)₂·2H₂O, Mn(CH₃COO)₂·4H₂O, and Na₂S·9H₂O as starting materials [109]. Their synthesis procedure also includes passivating agents with carboxylic functional groups such as 3-methacryloxypropyl trimethoxysilane and tween 80 for surface passivation of these nanoparticles. They indeed observed a zincblende crystal structure of as-synthesized ZnS prepared at room temperature.

Figure 4.2 shows that the diffraction peaks gradually shifts to a lower angle from sample NP-1 (28.46°) to NP-7 (26.6°). This shift towards lower angle is believed to result from the incorporation of cadmium ions into the ZnS lattice, and the larger ionic radius of Cd²⁺ as compared to that of Zn²⁺ (Table 2.1). This gradual shift suggests ternary formation. Continuous peak shifting of the nanoparticles also rule out phase separation or separated nucleation of CdS or ZnS nanoparticles. Interplaner spacing of these nanoparticles from XRD spectra (figure 4.2) is calculated by using equation (3.3), chapter 3. The variation of diffraction angles (2θ) with x and the corresponding d -spacing in the whole series of samples is shown in Table 4.2.

Singh [178] have reported in their handbook of compound semiconductors, that semiconductor alloys (solid solutions) have been proposed to obey Vegard's law, revealing the linear relationship between the lattice constant and composition as follows by equation (4.1):

$$a_{A_{1-x}B_xC}^0(x) = (1-x)a_{AC}^0 + xa_{BC}^0 \quad (4.1)$$

where $a_{A_{1-x}B_xC}^0$ is the natural constant of the ternary form $A_{1-x}B_xC$ and a_{AC}^0 and a_{BC}^0 are the natural constants of the binaries AC and BC respectively, and x is the mole fraction of binary BC .

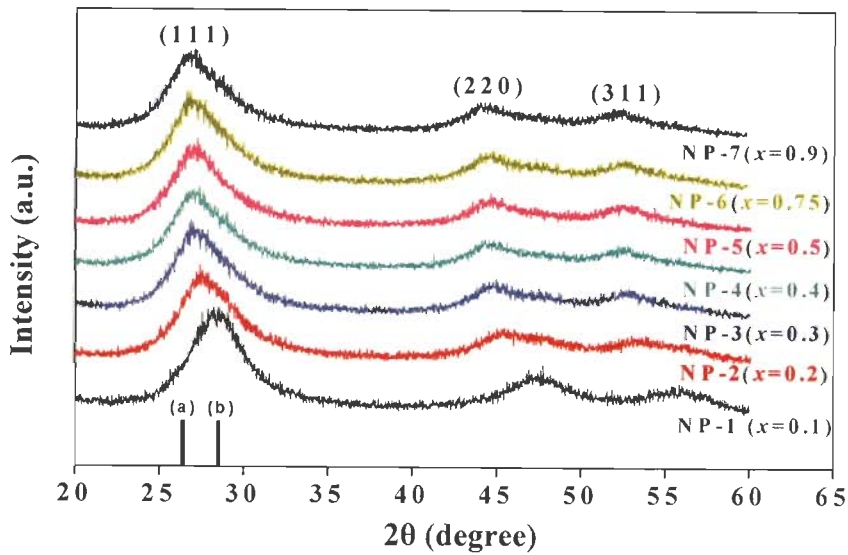


Figure 4.2: XRD patterns of Zn_{1-x}Cd_xS nanoparticles with mole fractions, x as 0.1, 0.2, 0.3, 0.4, 0.5, 0.75, and 0.9

Figure 4.3 shows the ideal lattice constant (equation 4.1) as a function of x with triangle data points (theoretical data points), where cubic $a_{ZnS}^0 = 5.345 \text{ \AA}$ and $a_{CdS}^0 = 5.820 \text{ \AA}$ (Table 2.1, chapter 2). The square shaped data points (experimental data points) are calculated by XRD pattern as shown in figure 4.2 (using equation (3.5), chapter 3) and are shown in figure 4.3. Figure 4.3 shows that the lattice parameter a measured from the XRD patterns of the Zn_{1-x}Cd_xS nanoparticles exhibits a nearly linear relationship with increasing cadmium concentration. A gradual increase in the lattice constant is observed as the mole fraction (x) increases. A close agreement exists between observed (via XRD) and the computed (via Vegard's law) lattice constant values for all the samples. This in turn indicates that the compositions of the ternary semiconductor nanoparticles are very close to the mixing molar ratio of the starting materials of ZnS and CdS.

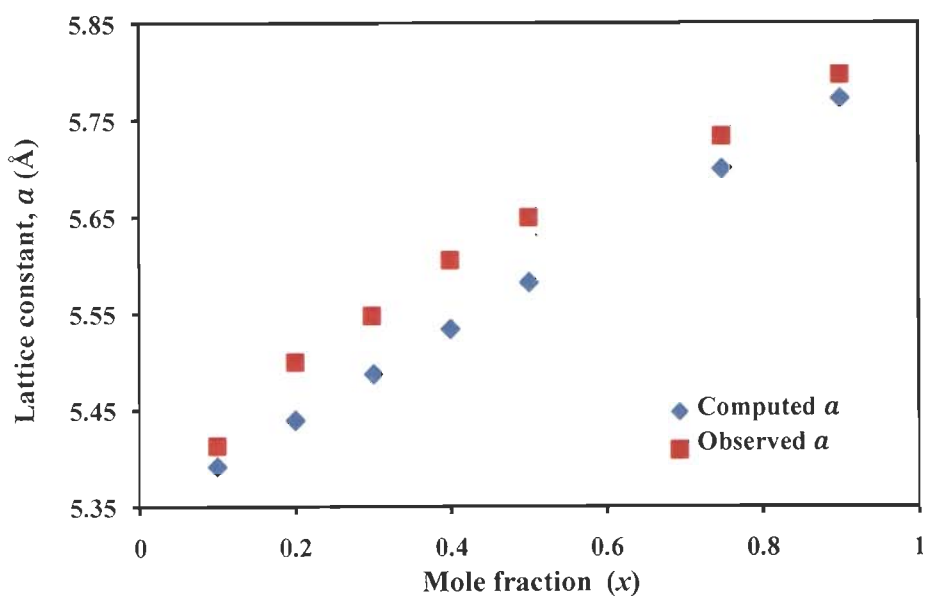


Figure 4.3: Lattice constants of Zn_{1-x}Cd_xS nanoparticles with mole fractions, x as 0.1, 0.2, 0.3, 0.4, 0.5, 0.75, and 0.9 in zincblende structure for (111) orientation

Figure 4.4 shows the $\pm 5\%$ error plot between computed (via Vegard's law) and observed (via XRD) lattice constant. It is clearly seen that the difference between these two values lies within the $\pm 5\%$ experimental error. This result shows that computed and observed lattice constant are in close agreement with each other; follow ternary rules, and provides the confidence that as-prepared nanoparticles can be used for the fabrication of nanocrystalline thin films.

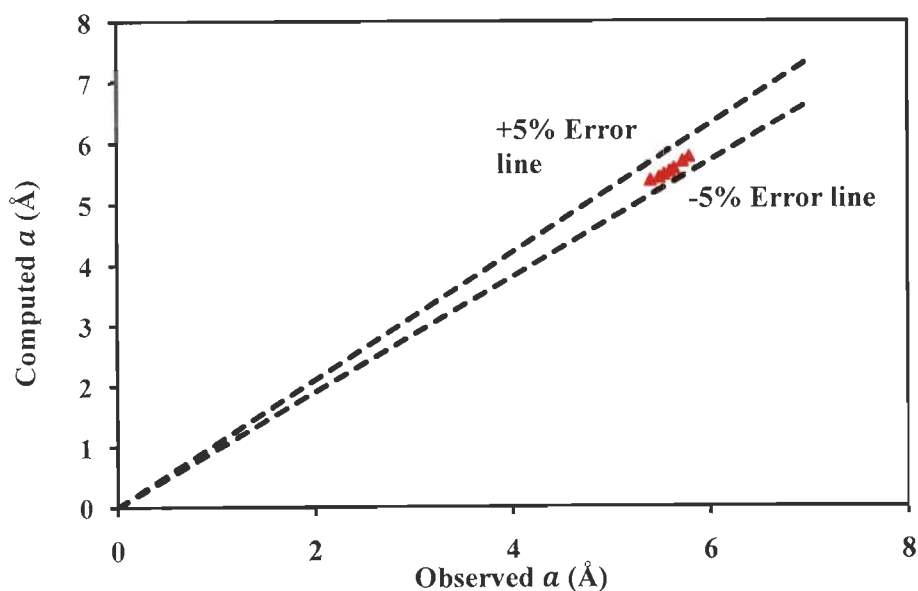


Figure 4.4: Error plot between observed and computed lattice constants of Zn_{1-x}Cd_xS nanoparticles

4.4.2 Particle Sizing

One of the goals of this work is to synthesize nanoparticles with a narrow size distribution. The particle size effect at quantum confinement regime is not used for the emission of different wavelengths [90, 104, 219], Instead emission of different wavelengths is achieved by variation of the mole fraction. Thus an absolute control of the particle size is not necessary in this work. However, the synthesized particles needs to be distributed uniformly in size and therefore should be investigated for their particle size. Since a lot of particle size measurements methods come to their detection limits for particles in the size region below 10 nm, different methods were used to get a correct image of the particle size. Nanoparticles size was measured by transmission electron microscopy (TEM) and X-ray diffraction (XRD) techniques.

4.4.2.1 Transmission electron microscopy

To estimate the average particle size of Zn_{1-x}Cd_xS nanoparticles transmission electron microscope (TEM) is used. Specimen preparation procedure for TEM imaging is described in chapter 3, section 3.3.5. Figure 4.5(a), 4.5(c) and 4.5(d) shows the TEM images for NP-5 (x as 0.5), NP-3 (x as 0.3), and NP-1 (x as 0.1) samples, respectively. TEM images of the obtained Zn_{1-x}Cd_xS nanoparticles reveal uniform spherical nanoparticles. All samples across the different compositions of Zn_{1-x}Cd_xS show TEM image with nearly spherical particles, with average particle size as 3.6 nm. Figure 4.5(b) shows the selected area electron diffraction (SAED) pattern of sample NP-5 (x as 0.5). This SAED pattern is the characteristic of a cubic phase and the rings are indexed as (111), (220) and (311) orientations. Insets of figure 4.5(c) and 4.5(d) also show the zincblende SAED patterns of NP-3 and NP-1 respectively.

One representative phase contrast image of nanoparticle of the sample is shown in the inset of figure 4.5(a). Continuous lattice fringes reveal the crystalline nature of the nanoparticle without any observable defect. Peng *et al.* have shown that the contrast of image depends on the electron scattering [148]. In their work they synthesized the CdSe/CdS core shell particles, and provide the evidence for the shell structure from the TEM image contrast. They suggested that in TEM, contrast depends on the electron scattering power of the object forming the image. The electron scattering power in turn depends on the electron density inside the object. Hence, for similar lattice parameters CdS is expected to show less contrast than CdSe since it has fewer electrons per unit cell [148]. Thus, for similar lattice parameters, ZnS is expected to exhibit lower contrast

compared to CdS, since it has fewer electrons per unit cell. We do not observe any stepwise change in the contrast across the diameter of the nanoparticle; this suggests a random distribution of cations, instead of any heterostructured nanoparticle or a phase separation within the single nanoparticle. This provides additional support to the conclusions based on XRD results. For a homogenous $Zn_{1-x}Cd_xS$, lattice parameters vary linearly with “ x ” [221, 222], and in comparison of the obtained $d_{111} = 3.25 \text{ \AA}$ (equation (3.7), chapter 3) with those of CdS and ZnS gives $x = 0.54$, which is essentially the same as that obtained by Vegard’s law within experimental uncertainties, establishing the internal consistency between independent measurements.

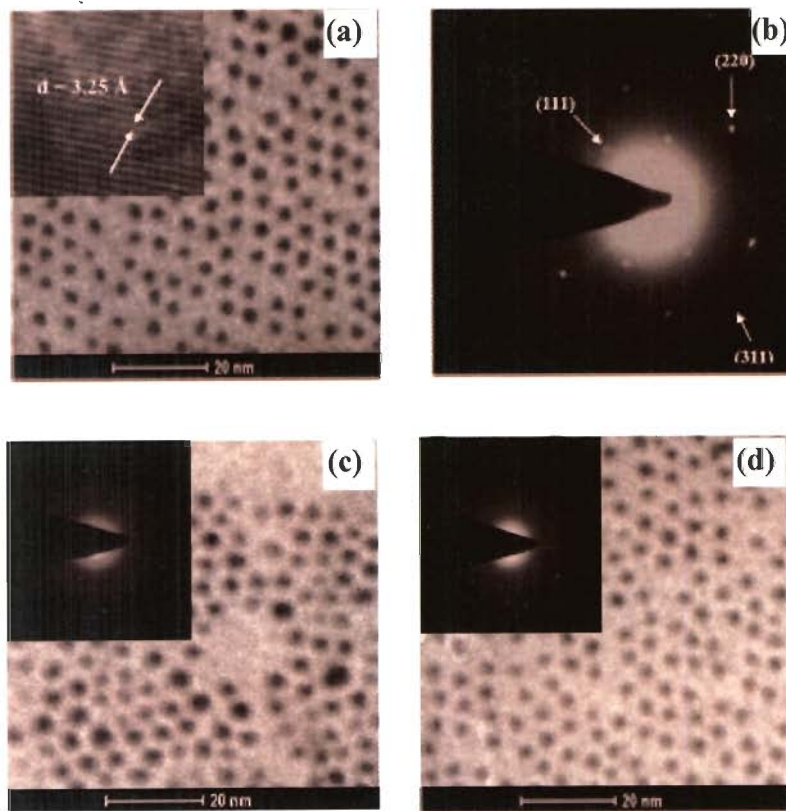


Figure 4.5 (a) TEM image of $Zn_{0.5}Cd_{0.5}S$ nanoparticles (sample NP-5); Inset: lattice fringes, (b) corresponding SAED pattern, (c) TEM image of sample $Zn_{0.7}Cd_{0.3}S$ (sample NP-3); Inset: corresponding SAED pattern, and (d) TEM image of sample $Zn_{0.9}Cd_{0.1}S$ (sample NP-1); Inset: corresponding SAED pattern

As-prepared $Zn_{1-x}Cd_xS$ nanoparticles have narrow size distributions with a relative standard deviation of 12-15% without any size sorting (appendix A2). Figure 4.6 shows the size distribution histograms of samples $Zn_{0.5}Cd_{0.5}S$ (sample NP-5), $Zn_{0.7}Cd_{0.3}S$ (sample NP-3), and $Zn_{0.9}Cd_{0.1}S$ (sample NP-1).

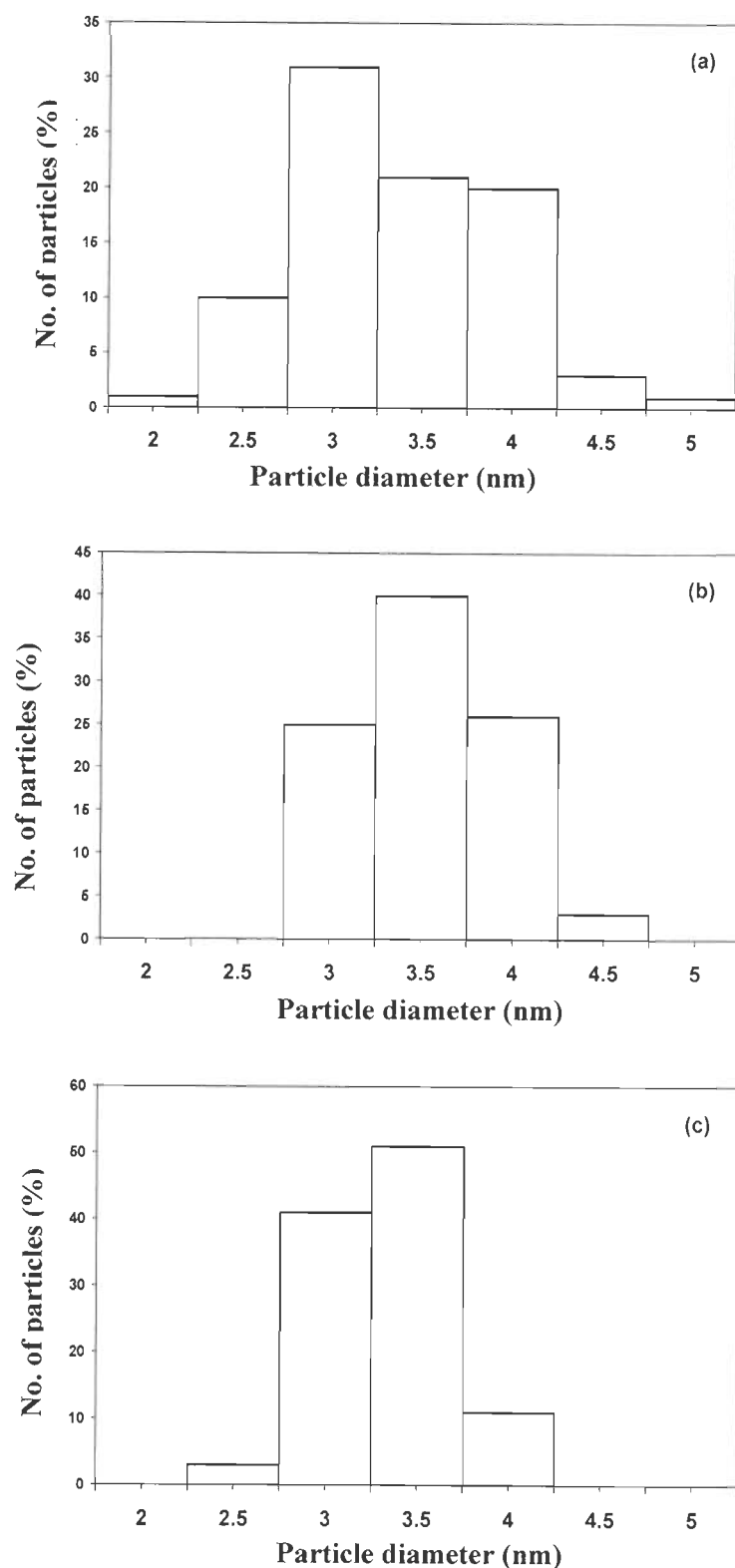


Figure 4.6: Histograms of (a) $Zn_{0.5}Cd_{0.5}S$ (sample NP-5), (b) $Zn_{0.7}Cd_{0.3}S$ (sample NP-3), and (c) $Zn_{0.9}Cd_{0.1}S$ (sample NP-1) nanoparticles; corresponding to TEM images (a), (c), and (d) respectively in figure. 4.5

4.4.2.2 X-ray diffraction technique

The peak broadening of x-ray patterns can be used to calculate the crystallite size with Scherrer's equation as given in section 3.3.1, chapter 3. Scherrer's analysis of the XRD peak broadening suggests average particle size of ~3.6 nm. The calculated particle sizes for samples NP-1 to NP-7 are shown in Table 4.2. The average particle size obtained from XRD patterns are in agreement with the average particle size obtained from TEM images.

Table 4.2: Sample composition (x), crystal structure, particle size, excitation wavelength, and emission wavelength of Zn_{1-x}Cd_xS nanoparticles characterized in this study

| Sample | Mole Fraction (x) | 2 θ^a (°) | d-spacing ^a (Å) | d_p^a (nm) | Ex ^b (nm) | Em ^c (nm) |
|--------|-------------------|------------------|----------------------------|--------------|----------------------|----------------------|
| NP-1 | 0.1 | 28.46 | 3.126 | 3.46 | 325 | 357 |
| NP-2 | 0.2 | 28.02 | 3.181 | 3.49 | 330 | 359 |
| NP-3 | 0.3 | 27.81 | 3.204 | 3.54 | 350 | 372 |
| NP-4 | 0.4 | 27.58 | 3.238 | 3.66 | 350 | 373 |
| NP-5 | 0.5 | 27.14 | 3.282 | 3.78 | 350 | 378 |
| NP-6 | 0.75 | 27.00 | 3.291 | 3.61 | 350 | 380 |
| NP-7 | 0.9 | 26.6 | 3.347 | 3.48 | 350 | 390 |

^a (111), ^b Excitation wavelength, ^c Emission wavelength (self activated band)

4.5 SURFACE MORPHOLOGY & COMPOSITIONAL ANALYSIS

Figure 4.7 illustrates surface morphology of the as-prepared sample NP-6 (x as 0.75). All the samples show similar morphologies; therefore only sample NP-6 is selected for illustration. The images clearly show that the particles are spherical in nature. This is in agreement with nanoparticles shape obtained from TEM. Overall particle size (~ 50 nm) shown by FESEM is much higher as compared with the TEM (~ 3.6 nm). This was because of the fact that TEM gave images of ultrasonicated solution at higher accelerating voltage (200 kV) while FESEM showed agglomeration of particles at lower accelerating voltages (5-20 kV). Since the images show that there are agglomerates, FE-SEM images have not been accounted for particle sizing. Figure 4.7(a) shows the surface morphology at low magnification (x 50k). With increasing magnification the images show the well

defined group of particles. However, with FE-SEM, it was not possible to resolve nanoparticles even at magnification of x 600k (figure 4.7(d)).

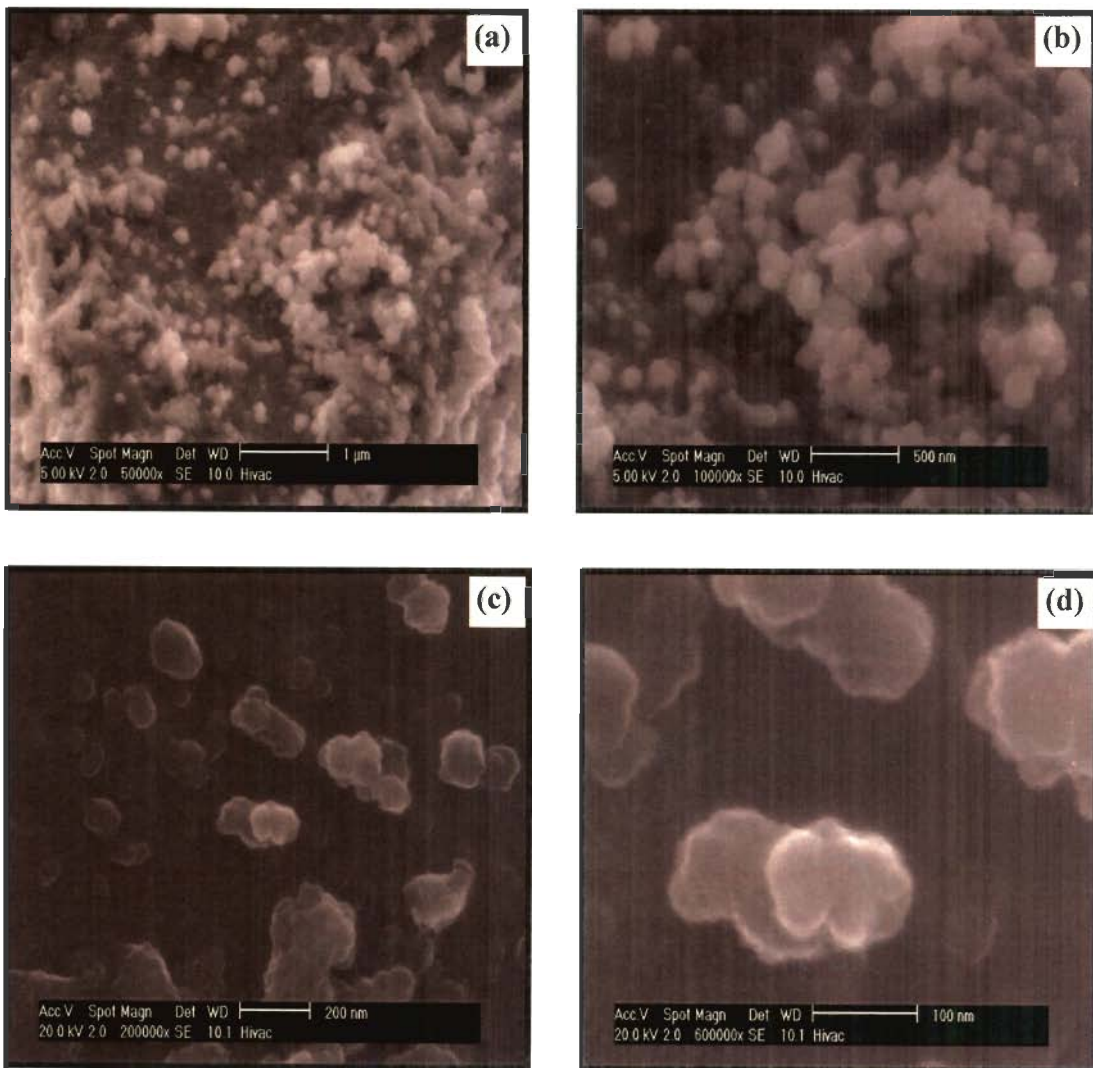


Figure 4.7: FE-SEM images of $Zn_{0.25}Cd_{0.75}S$ nanoparticles (sample NP-6) at magnification of (a) x 50k, (b) x 100k, (c) x 200k, and (d) x 600k

Compositional analysis of $Zn_{1-x}Cd_xS$ nanoparticles is carried out by using EDS attached with FE-SEM. Figure 4.8(a), (b) and, (c) shows the EDS spectrum of three samples $Zn_{0.9}Cd_{0.1}S$ (sample NP-1), $Zn_{0.5}Cd_{0.5}S$ (sample NP-5), and $Zn_{0.1}Cd_{0.9}S$ (sample NP-7) respectively. Increase in cadmium peak intensity with increasing mole fraction clearly shows the well maintained stoichiometry during the particle nucleation and growth process. Inset in figure 4.8(a), (b), and, (c) shows the corresponding at % of the constituent elements.

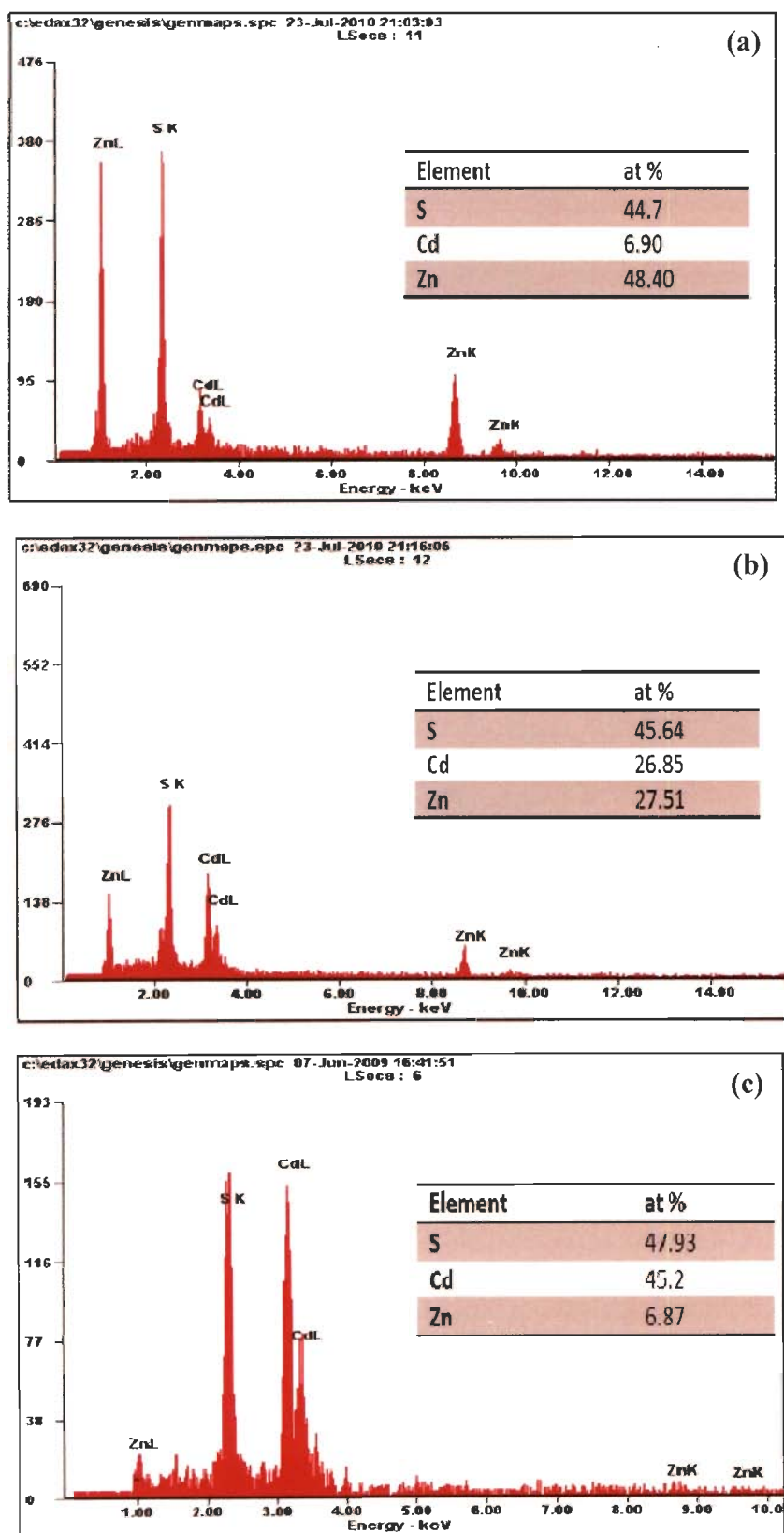


Figure 4.8: EDS spectrum of samples (a) Zn_{0.9}Cd_{0.1}S (sample NP-1), (b) Zn_{0.5}Cd_{0.5}S (sample NP-5), and (c) Zn_{0.1}Cd_{0.9}S (sample NP-7); Inset shows at % of the constituent elements

4.6 COMPOSITION DEPENDENT ENERGY BAND GAP DETERMINATION OF Zn_{1-x}Cd_xS NANOPARTICLES

The absorption spectra of Zn_{1-x}Cd_xS nanoparticles with variation in mole fraction are shown in appendix A3.2. Tauc relation (equation (3.9), chapter 3) has been applied to obtain the energy band gap values from the absorption spectra. Figure 4.9 shows the plot of $(ah\nu)^2$ with $h\nu$ of Zn_{1-x}Cd_xS nanoparticles with varying mole fraction. The red-shift in energy band gap from 3.91 to 3.1 eV, with increasing mole fraction clearly indicates the formation of ternary nanoparticles.

Figure 4.10 shows polynomial fit to the energy band gap values obtained by absorption measurement (figure. 4.9). A model suggested by Cohen *et al.* has been adopted to obtain the quadratic fit for the data points (appendix A2.2.) [39]. Equation (4.2) is a quadratic fit to the data points shown in figure 4.10. Regression coefficient of the trend line is very close to 1, signifies that the trend line fits very well to the experimental data points.

$$E_g(x) = 4.029 - 1.398x + 0.438x^2 ; R^2 = 0.996 \quad (4.2)$$

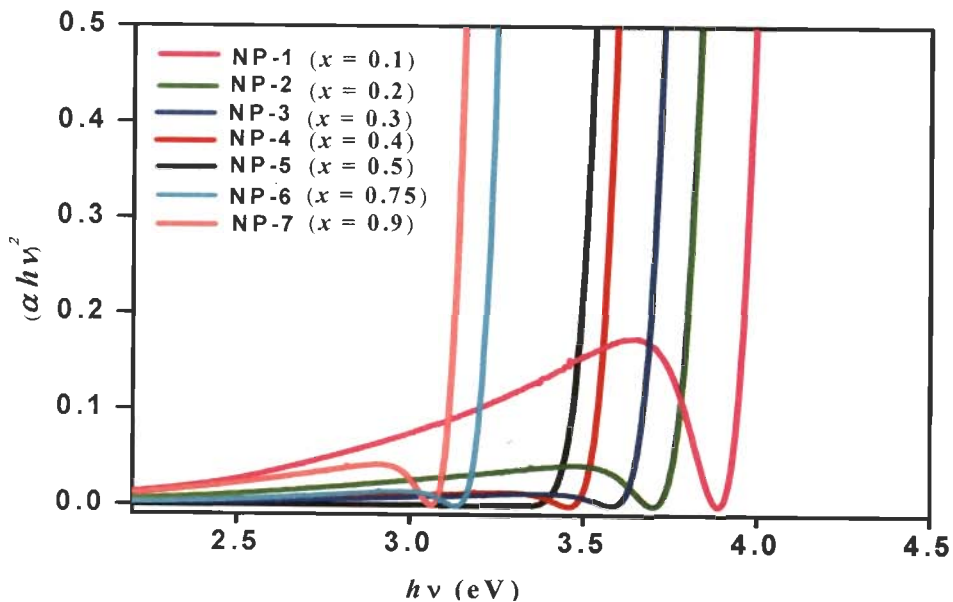


Figure 4.9: $(ah\nu)^2$ with $h\nu$ of Zn_{1-x}Cd_xS nanoparticles with mole fractions, x as 0.1, 0.2, 0.3, 0.4, 0.5, 0.75, and 0.9

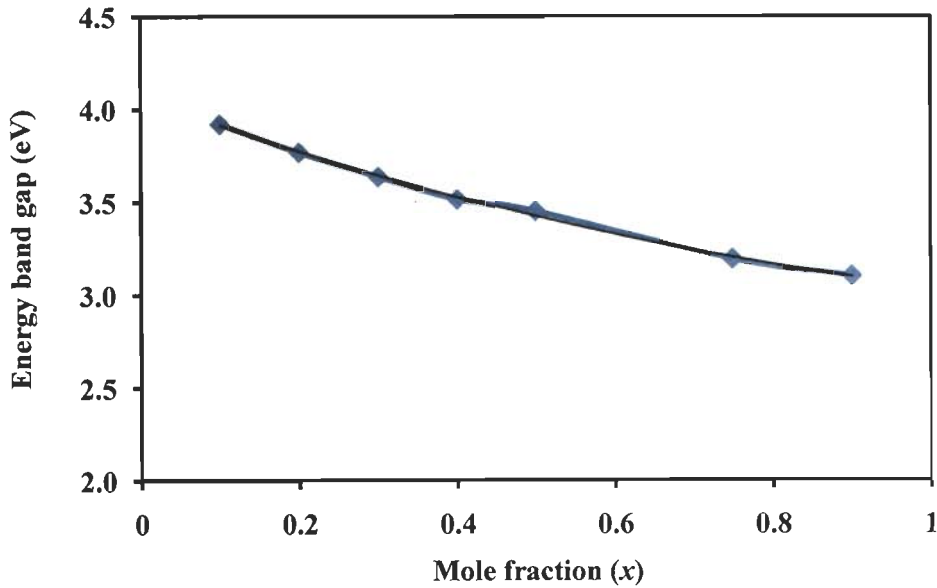


Figure 4.10: A polynomial fit to the energy band gap values of Zn_{1-x}Cd_xS nanoparticles

In case of ternary nanoparticles, the band gap energies are determined by their size and composition i.e. quantum confinement and composition effect. In bulk CdS-ZnS alloyed crystals their composition (x) dependent band gap energies ($E_g(x)$) can be expressed by the relation [178]

$$E_g(x) = E_g(\text{ZnS}) + [E_g(\text{CdS}) - E_g(\text{ZnS}) - b]x + bx^2 \quad (4.3)$$

where $E_g(\text{ZnS})$ and $E_g(\text{CdS})$ are the band gap energies for bulk ZnS and CdS (Table 2.1), respectively and b is the bowing parameter and has the value 0.61 [187] for bulk system. For Zn_{1-x}Cd_xS nanoparticles with average size of 3.6 nm (as obtained from XRD and TEM analysis), band gap energies with composition (x) can be calculated by using equation (4.3). For Zn_{1-x}Cd_xS nanoparticles the bowing parameter is the coefficient of the quadratic term of the equation (4.2) and has a value of 0.438.

The increase of the fundamental band gap of the nanoparticles due to quantum confinement effects, suggested by Brus (equation (1.1), chapter 1), is reproduced here (Brus, 1984)

$$E_g = E_g^0 + \frac{h^2}{8\mu R^2} - \frac{1.8e^2}{4\pi\epsilon R} \quad (4.4)$$

where E_g^0 is the energy band gap for the bulk material, R is the radius of the nanoparticle, $1/\mu = 1/m_e + 1/m_h$ (μ is the reduced mass; m_e and m_h being the electron and hole effective

masses respectively), ε is the dielectric constant and e is the electronic charge. Corresponding values for ZnS and CdS are outlined in Table 2.1, chapter 2. By substituting these values in equation (4.4), size dependent band gap energy relations for ZnS and CdS is derived for quantum confined structure. Corresponding equations for ZnS and CdS are:

$$E_g = E_g^0 + 2.13 R^{-2} (nm) - 0.51 R^{-1} (nm) \quad (4.5)$$

$$E_g = E_g^0 + 2.49 R^{-2} (nm) - 0.465 R^{-1} (nm) \quad (4.6)$$

With average particle size of 3.6 nm (as obtained from XRD and TEM analysis), a shift in the band gap values of 0.38 & 0.51 eV is obtained for ZnS and CdS respectively. Therefore, instead of using energy band gap value of 3.68 eV for ZnS and 2.35 eV for CdS (Table 2.1), 3.974 eV for ZnS nanoparticles and 2.87 eV for CdS nanoparticles are plugged in equation (4.3) and the resulting composition (x) dependent band gap energies of Zn_{1-x}Cd_xS nanoparticles in the quantum confinement regime can be arranged as follows:

$$E_g(x) = 3.974 - 1.7x + 0.438x^2 \quad (4.7)$$

Composition (x) dependent band gap energies of bulk Zn_{1-x}Cd_xS semiconductor can be given by substituting the corresponding bulk values (Table 2.1, chapter 2) in equation (4.3):

$$E_g(x) = 3.65 - 1.91x + 0.61x^2 \quad (4.8)$$

Figure 4.11 shows results for ternary bulk and nanoparticles as dashed (equation (4.8)) and solid lines (equation (4.7)), respectively. The shift in energy from dashed to solid line (vertical axis) clearly shows the quantum confinement effect. Energy shift at horizontal axis clearly shows the compositional tunability. Using the calculated band gap energy (solid curve) of Zn_{1-x}Cd_xS nanoparticles, actual composition of samples can be indirectly estimated (see co-ordinates of point A in figure 4.11). Figure 4.12 shows the $\pm 5\%$ error plot between computed (via equation 4.7) and observed (via UV-Vis absorption measurement) energy band gap values. The difference between these two values lies on the - 5% experimental line. An increase in error (in comparison to lattice constant error, figure 4.4) could be due to unconventional method which is adopted to obtain the bowing parameter of Zn_{1-x}Cd_xS ternary system. These results show that as-prepared nanoparticles consist both: the quantum confinement and the composition effects.

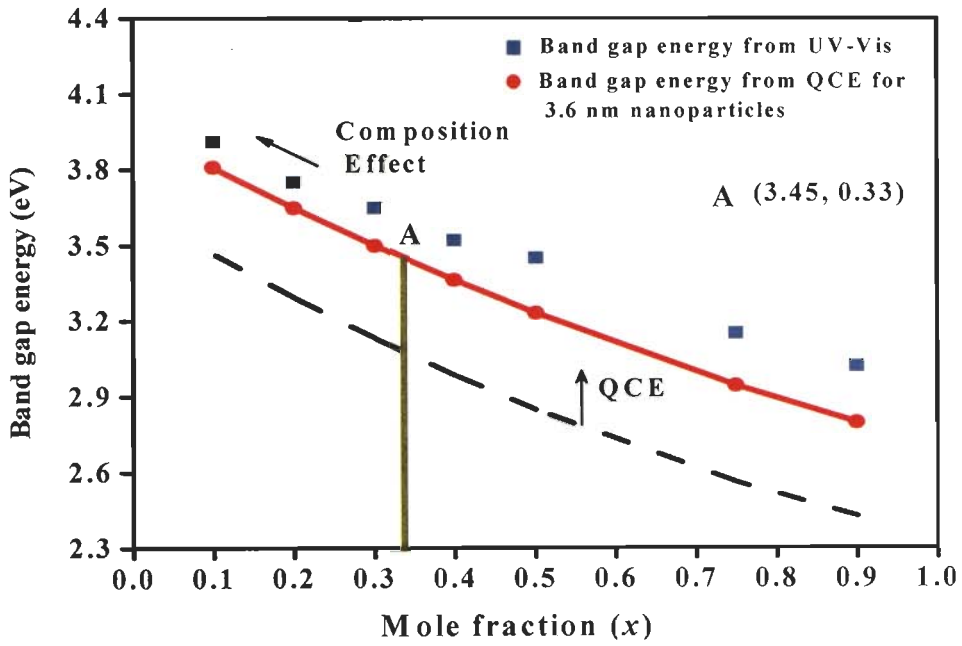


Figure 4.11: Composition dependence of calculated absorption energies of bulk crystals (dashed lines) and nanoparticles with a size of 3.6 nm (solid line)

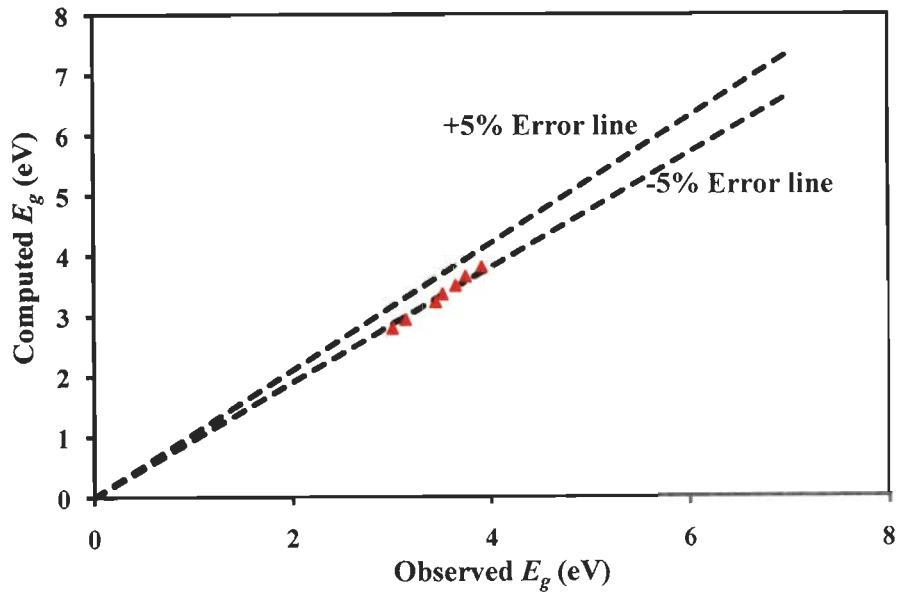


Figure 4.12: Error plot between observed and computed energy band gap value of $Zn_{1-x}Cd_xS$ nanoparticles

4.7 COMPOSITION DEPENDENT EMISSIONS FROM $Zn_{1-x}Cd_xS$ NANOPARTICLES

$Zn_{1-x}Cd_xS$ nanoparticles were characterized via photoluminescence (PL) measurement at room temperature for their light emitting properties. Excitation conditions for PL measurement must be considered carefully, because the absorption of

most materials depends on energy, the penetration depth of the incident light will depend on the excitation wavelength. Hence, different excitation energies probe different regions of the sample. Gfroerer and Mishra *et al.* have suggested that the excitation wavelength must be chosen, so as to satisfy the basic excitation energy requirement exceeding the band gap energy [66, 124]. Nanoparticles were thus excited with wavelengths fulfilling this criterion. Corresponding excitation wavelengths are shown in Table 4.2. Figure 4.13 shows the three emission bands i.e. self activated, blue and green emissions in the PL spectra. The self activated bands are due to the near band edge (NBE) transitions and results in the light emission in the ultraviolet (UV) spectral regions. Due to size quantization, NBE emission band has shifted to higher energies compared to the absorption band of bulk counterpart. NBE emission band red-shifts with increasing mole fraction (357 nm for NP-1 to 390 nm for NP-7). This red shift in the self activated band provides an additional evidence of ternary formation, in addition to the XRD, TEM and UV-Vis characterizations. NBE emission wavelengths for samples NP-1 to NP-7 are shown in Table 4.2.

Figure 4.14 shows PL emission at ~ 480 and ~ 520 nm giving rise to blue and green emission respectively. Ge *et al.* have synthesized single-crystal one-dimensional nanostructures via halide-transport chemical vapor deposition (HTCVD) process and showed the emissions from various defects levels of the zinc and sulfur vacancies. In our work, emission band at ~ 480 nm is attributed to a self-activated centre presumably formed between a zinc vacancy and a shallow donor associated with a sulfur vacancy [65]. PL peak intensity of blue emission (~ 480 nm) decreases with increase in cadmium content, and is attributed to lesser number of available zinc vacancies as those vacancies could have been occupied by the cadmium ions. Solid solution of CdS and ZnS also result in a green emission band. Karasawa *et al.*, have reported a broad peak centering at 516 nm in the PL spectrum of ZnS combined with CdS superlattice structure [88]. Yang *et al.*, reported the synthesis of cadmium doped ZnS nanometer-scale particles via coprecipitation technique [215]. Their group utilized $\text{Zn}(\text{CH}_3\text{COO})_2 \cdot 2\text{H}_2\text{O}$ and $\text{Cd}(\text{CH}_3\text{COO})_2 \cdot 2\text{H}_2\text{O}$ and thioacetamide (TAA). The reaction temperature was fixed at 80 °C. They showed that the fluorescence spectra is red shifted in the emission wavelength (ranging from 450 nm to 620 nm). Their group observed a relatively broad emission (ranging from blue to yellow). PL band at ~ 520 nm can therefore be related with the presence of cadmium ions. It can be seen from figure 4.14 that the green emission band intensity increases on the expense of blue emission band intensity.

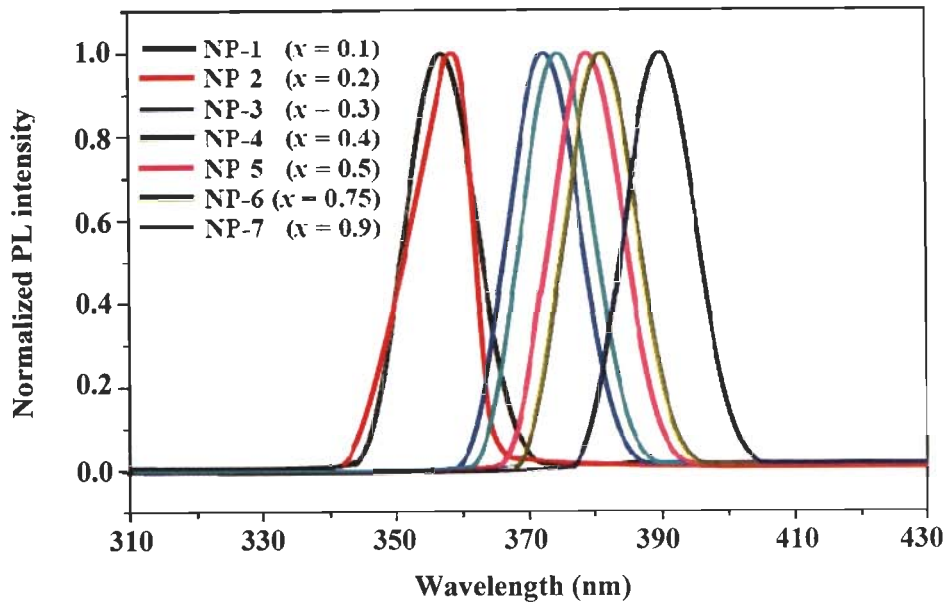


Figure 4.13: Normalized self activated PL spectra of the Zn_{1-x}Cd_xS nanoparticles with mole fraction, x as 0.1, 0.2, 0.3, 0.4, 0.5, 0.75, and 0.9

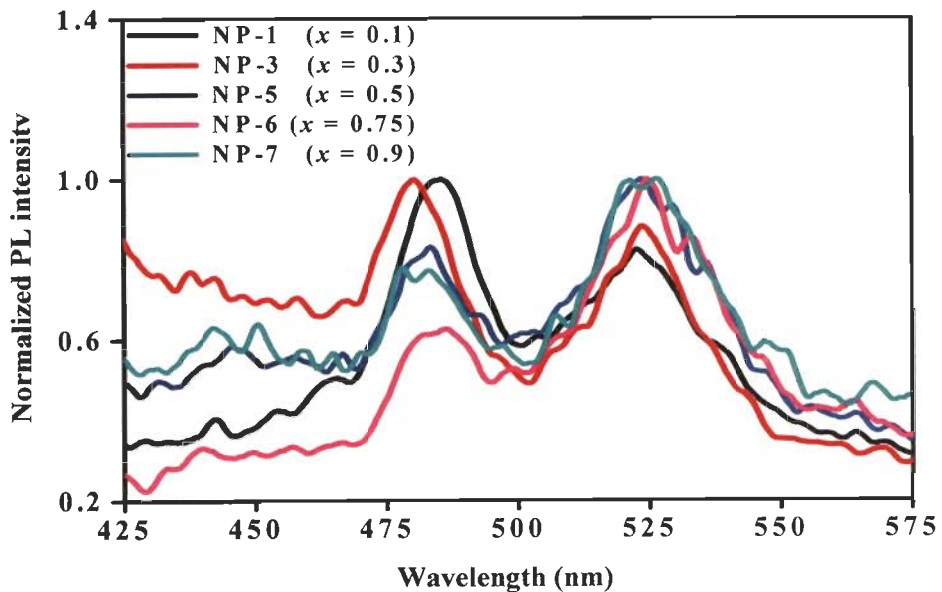


Figure 4.14: Normalized blue and green emissions in PL spectra of the Zn_{1-x}Cd_xS nanoparticles with mole fraction, x as 0.1, 0.3, 0.5, 0.75, and 0.9

Figure 4.15 shows the ratio of peak intensities of green to blue light emission ($I_{G/B}$) of some of the samples. It can be seen from figure. 4.15 that there is an increase in the $I_{G/B}$ with increase in mole fraction. This increase in $I_{G/B}$ with mole fraction signifies the improvement in the intensity of green emission over the blue emission. Green

diamond shaped points in figure 4.15 are the ratio of green to blue emission intensities, $I_{G/B}$, measured for 5 repetition runs of one particular sample, while the red diamond shaped points represents the average of these data points. The black line shows the deviation of $\pm 5\%$ from the average value. For all the samples the deviation of data points from average value is within $\pm 5\%$. This shows that PL emission is almost identical for each run and provides the consistency of our experiments.

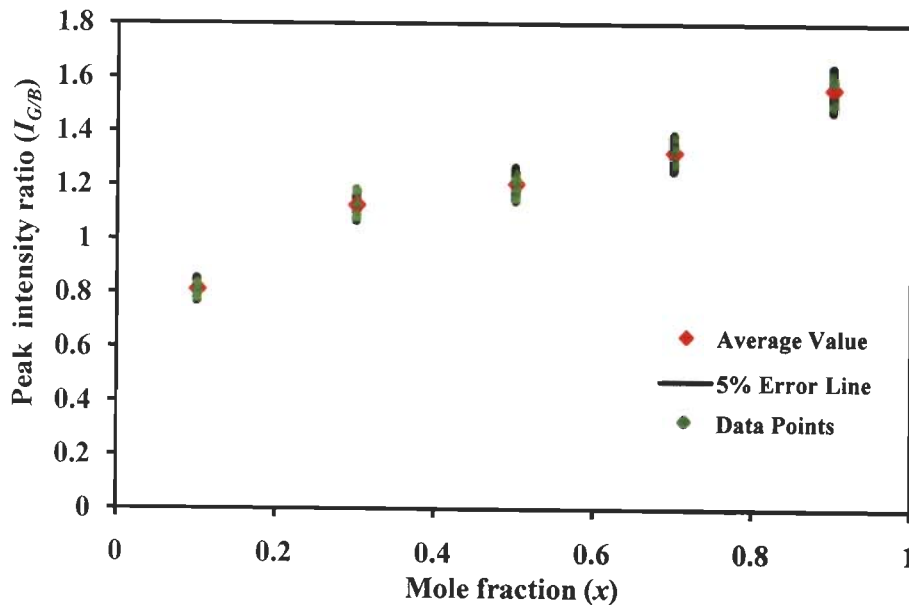


Figure 4.15: Variation of peak intensity ratio ($I_{G/B}$) with mole fraction, x as 0.1, 0.3, 0.5, 0.75, and 0.9

Figure 4.16 shows the proposed schematic energy level diagram for light emissions from $Zn_{1-x}Cd_xS$ nanoparticles. It represents the transitions from different surface states and resulting emissions.

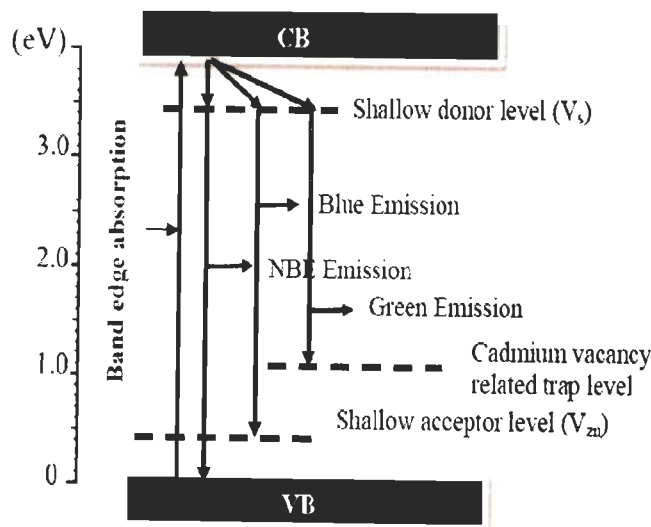


Figure 4.16: Schematic energy level diagram for transition between different levels of Zn_{1-x}Cd_xS nanoparticles

4.8 SUMMARY

This chapter provides useful information in determining the process window for the composition dependent emission properties. Low temperature synthesis of Zn_{1-x}Cd_xS nanoparticles via co-precipitation technique is carried out in aqueous medium because of its inherent advantages of being simple and environment friendly. It is found that the actual composition of the nanoparticles is very close to the mixing molar ratio of the starting materials. Both XRD and TEM show the zincblende structured Zn_{1-x}Cd_xS nanoparticles with average particle size ~ 3.6 nm. A gradual increase in the lattice constant is observed with increase in mole fraction. This trend is consistent with Vegard's law and indicates a homogeneous ternary structure. Both QCE and composition effects in Zn_{1-x}Cd_xS nanoparticles are demonstrated with the help of UV-Vis measurements. An indirect estimate of the ternary composition can be obtained with these two effects in nano-regime. PL data also confirms a systematic red-shift in quantum confined NBE emission with increase in mole fraction. Zn_{1-x}Cd_xS nanoparticles are found to emit in the blue and green visible spectral regions. The above findings provide a confidence that the as-prepared Zn_{1-x}Cd_xS nanoparticles can successfully be used for the fabrication of thin films.

CHAPTER 5

Zn_{1-x}Cd_xS NANOCRYSTALLINE THIN FILMS:
PROCESSING & CHARACTERIZATION

5.1 GENERAL

The potential application of nanocrystalline Zn_{1-x}Cd_xS films for optical and microelectronic device applications could be successfully realized only if thorough insight is gained with regard to the formation of desired microstructures through appropriate process controls. Nevertheless, they show a lower crystallinity, with respect to other semiconducting compounds; they are highly defective and their structural properties are mainly linked to the growth processes used for the layer deposition [72, 168].

Nicolau *et al.* synthesized the Zn_{1-x}Cd_xS films by the successive ionic layer adsorption and reaction process [135]. The pure zincblende phase was obtained from $x = 0$ to $x \approx 0.75$ and the pure wurtzite phase from $x \approx 0.75$ to $x = 1$. Their results however suffer from lack of stoichiometry.

Sebastian and Ocampo used the screen printing for the preparation of Zn_{1-x}Cd_xS *thick films* from a paste containing CdS and ZnCl₂ pigments [172]. Presence of CdCl₂ and ZnCl₂ phases along with ZnS were found in the screen printed films. *Ex-situ* heat treatment of these films at about 500° C transformed them into Zn_{1-x}Cd_xS films.

Gunasekaran and Ichimura studied the effect of precursor concentration on the growth of Zn_{1-x}Cd_xS films prepared by a photochemical technique for x ranging from 0 to 1. A change in surface morphology with zinc content in the alloy was observed [73]. Their experiments with Auger electron spectroscopy (AES) indicate the presence of oxygen along with sulphur, cadmium and zinc. Structure of the films was found to be a mixed phase of Zn_{1-x}Cd_xS and ZnO.

Most of the reports for the deposition of Zn_{1-x}Cd_xS films involve the chemical route. The need for a post-annealing or calcination step — commonly required in most wet chemical techniques, usually leads to coarsening of particle size, and broadening of the size distribution, in addition to undesirable chemical reactions.

Owing to the aforementioned facts, present work has been focused on the growth and characterization of Zn_{1-x}Cd_xS thin films by vapor deposition route.

5.2 CHAPTER PREFACE

This chapter presents the effects of a) the laser flux density, b) the working pressure, c) the deposition temperature, and d) the mole fraction, on structural, morphological optical and emission properties of Zn_{1-x}Cd_xS nanocrystalline thin films. Experiments are described in section 5.3. Prior to the target fabrication for PLD deposition, it was necessary to devise and test a method to check the energy band gap variation due to applied pressure. This pressure sensitivity of Zn_{1-x}Cd_xS semiconductor is outlined in Section 5.3.1. The results of the crystal structure, surface roughness, particle size, and light emission as a function of laser flux density, working pressure, deposition temperature, and mole fraction are discussed in section 5.4, 5.5, 5.6, and 5.7 respectively. Since the evidence pointed to a crystal structure change in Zn_{1-x}Cd_xS nanocrystalline thin films, physical and analytical tests are undertaken.

5.3 SYNTHESIS DETAILS

Zn_{1-x}Cd_xS films were prepared by ablating stoichiometric home-made targets (see section 5.3.1) using PLD technique. The process parameters such as laser flux density, working pressure, deposition temperature, and mole fraction were optimized. The effect of these parameters on the structural, morphological, optical and emission properties of Zn_{1-x}Cd_xS nanocrystalline thin films have been investigated.

5.3.1 Target Fabrication

For optoelectronic applications energy band gap is a key factor in determining the device performance. Energy band gap changes significantly with application of pressure [34, 173]. Cheong *et al.* have established that for relatively low pressures (~30 Kbar), the pressure dependences are linear within experimental uncertainties, and can be described by a linear pressure coefficient. Shan *et al.*, have reported the pressure-induced energy shifts of the optical transition related to the direct energy gap of CdSe crystal with application of hydrostatic forces [34]. They observed sharp, derivative-like spectral features and corresponds them to the band gap transition in CdSe which shifts linearly toward higher energy with increasing pressure [174].

This is expected since it depends sensitively on the atomic spacing which will change as pressure is applied. Thus an optimum pressure condition is derived in this work for the fabrication of Zn_{1-x}Cd_xS target by taking their band structure into account. At atmospheric pressure, the lowest conduction band minimum in ZnS and CdS is at the

central Γ point of the Brillouin zone (figure 2.1(b) and 2.2(b), chapter 2). At high pressures, the Γ minimum moves relative to the Γ_v valence band such that E_g changes at rates of 6.3×10^{-2} eV/GPa and -5.6×10^{-3} eV/GPa for ZnS and CdS respectively [26, 27].

Pressure sensitivity of semiconductor is defined in terms of pressure coefficient [34, 173]. Pressure coefficient is defined as the first derivative of the energy band gap with respect to hydrostatic pressure. Therefore pressure sensitivity can be written as dE_g/dP . With application of the pressure, energy band gap varies in accordance with above pressure coefficients i.e.

$$(E_i)_0 = (E_i) + \left(\frac{\Delta E_i}{\Delta P}\right) \Delta P \quad (5.1)$$

where ΔP is change in pressure, and E_i is energy band gap of i^{th} valley. For Zn_{1-x}Cd_xS semiconductor, i value is Γ valley and $(E_i)_0$ is energy band gap with zero pressure. $(E_i)_0$ for Zn_{1-x}Cd_xS semiconductor is obtained by applying Vegard's law (equation (4.3), chapter 4) by taking E_{gZnS} as 3.68 eV and E_{gCdS} as 2.35 eV.

Substituting energy band gap values of Zn_{1-x}Cd_xS for x as 0.1 to 0.9 (appendix A1.2) in equation (5.1) with applied pressure of 18 ton, change in energy band gap is obtained as $\sim 10^{-3}$ eV. This change in band gap does not alter the optical window and thus defines the optimum pressure range for the fabrication of Zn_{1-x}Cd_xS target. Based on the above computation Zn_{1-x}Cd_xS nanoparticles have been given a pressure of 18 ton to fabricate the PLD target. Figure 5.1(a) shows the snapshot of dye which is used in this work for pellet preparation. Figure 5.1(b), (c) and (d) shows the snapshots of the fabricated targets. These *as-fabricated* pellets are used as targets for the pulsed laser deposition.

5.3.2 Synthesis Conditions

Zn_{1-x}Cd_xS films were deposited on corning 1737 glass substrates. The substrates were cleaned by ultrasonic baths of acetone and methanol and then dried under nitrogen gas. KrF excimer pulsed laser operating at 248 nm is utilized for the deposition of Zn_{1-x}Cd_xS nanocrystalline thin films. Films were deposited in a custom designed (Excel Instruments, India) vacuum chamber. A base pressure of $< 5 \times 10^{-6}$ torr was achieved with the aid of rotary (Pfeiffer, DUO 10) and turbo molecular pump (Pfeiffer, HIPAC 300). The working pressure was varied from 1.5×10^{-2} to 200 mtorr by varying the argon gas flow rate. The target-substrate distance was varied from 20 to 50 mm. Target was rotated

at 20 rpm to preclude pit formation on its surface and also to ensure uniform ablation. Pulsed laser used for ablation was set with a pulse width of 25 ns. The pulse repetition rate was varied from 5-10 Hz.

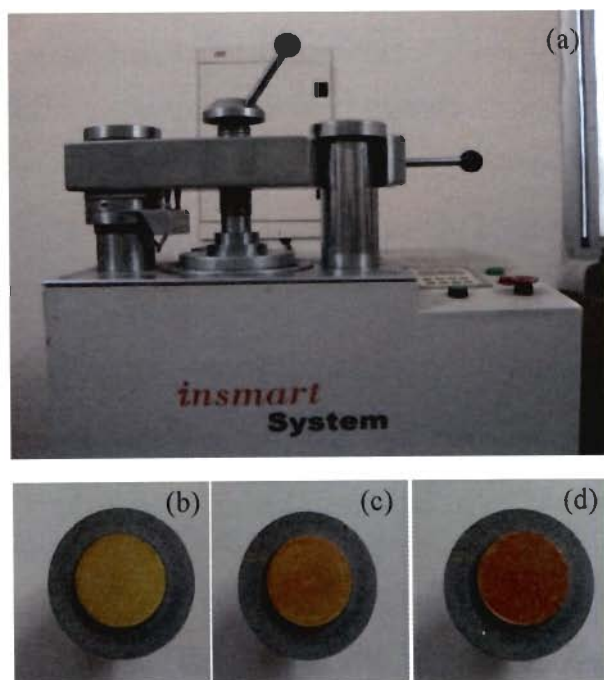


Figure 5.1: (a) Dye for pellet preparation; as-fabricated pellets in laboratory with mole fraction as: (b) 0.3, (c) 0.5, and (d) 0.7

Thirty four samples were deposited in this study to obtain well crystalline phase, minimal surface roughness and low defect density. Standard synthesis conditions for Zn_{1-x}Cd_xS films prepared in this study are shown in Table 5.1.

Samples NTF-1, NTF-2, NTF-3, and NTF-4 (Table 5.1) were deposited with target-substrate distances of 10, 20, 30, and 40 mm respectively. The target-substrate distance of 30 mm results into the deposition rate of 3 Å/sec. With increase in target-substrate distance from 30 to 40 mm results in very slow deposition rates (~ 0.5 Å/sec). With decreasing target-substrate distance (20 and 10 mm) large particles (debris etc.) starts to deposit on the film surface. Also, molecular species bombard the surface of the films with high kinetic energy that eventually results in the degradation of the film surface (Eason, 2007). The target-substrate distance was therefore kept at 30 mm in this work.

Samples NTF-5, NTF-6, and NTF-7 (Table 5.1) were deposited with pulsed repetition rates of 5, 8, and 10 Hz respectively. Since the pulse width was fixed at 25 ns, off period duty cycle for considered repetition rates lies in seconds (figure 5.2). This time

scale is large enough to release the effect of shock waves, which are of the order of μs [54, 74]. Thus no significant change occurred with varying pulse repetition rate.

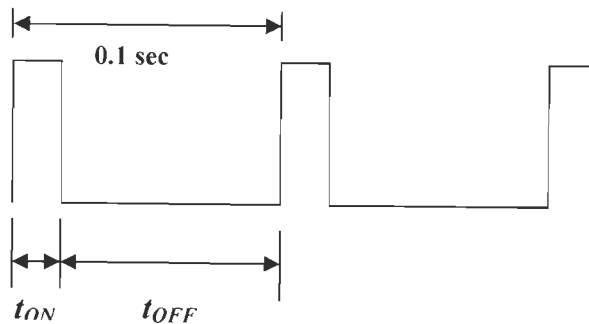


Figure 5.2: Pulsed wave for 10 Hz repetition rate with $t_{ON} = 2.5 \times 10^{-8}$ sec and $t_{OFF} = \sim 0.1$ sec

5.4 LASER FLUX DENSITY VARIATION

This section investigates the effect of laser flux density on the structural, and morphological properties of $\text{Zn}_{1-x}\text{Cd}_x\text{S}$ thin films. Samples with mole fraction “ $x = 0.9$ ” were prepared with laser flux densities of 2.5, 3.0, 3.33, 3.75, and 4.16 J/cm^2 namely NTF-8, NTF-9, NTF-10, NTF-11, and NTF-12 respectively (Table 5.1). Complete description of deposition parameters are mentioned in Table 5.1.

5.4.1 Results & Discussions

Variation in laser flux density changes the kinetic energy of plasma species. This change in kinetic energy of plasma species controls the coarsening of particles. This in turn provides regulation of surface roughness of the synthesized films. An effect of laser flux density on the surface morphology of $\text{Zn}_{0.1}\text{Cd}_{0.9}\text{S}$ films was investigated via TEM and AFM Imaging. The results obtained with varying laser flux density are discussed in the following sections.

Table 5.1: Synthesis conditions of Zn_{1-x}Cd_xS nanocrystalline thin films prepared in this study. It also contains the obtained phase

| Sample | Synthesis parameters | | | | | | Obtained phase (ZB/W) |
|--------|--------------------------------|----------------------------|---|---------------------------------|-----------------------------|-------------------|-----------------------|
| | Target-substrate distance (mm) | Pulse repetition rate (Hz) | Laser flux density (J/cm ²) | Working chamber pressure (torr) | Deposition temperature (°C) | Mole fraction (x) | |
| NTF-1 | 10 | 10 | 3.33 | 1.5 x 10 ⁻⁵ | 400 | 0.1 | ZB |
| NTF-2 | 20 | 10 | 3.33 | 1.5 x 10 ⁻⁵ | 400 | 0.1 | ZB |
| NTF-3 | 30 | 10 | 3.33 | 1.5 x 10 ⁻⁵ | 400 | 0.1 | ZB |
| NTF-4 | 40 | 10 | 3.33 | 1.5 x 10 ⁻⁵ | 400 | 0.1 | ZB |
| NTF-5 | 30 | 5 | 3.33 | 1.5 x 10 ⁻⁵ | 400 | 0.1 | ZB |
| NTF-6 | 30 | 8 | 3.33 | 1.5 x 10 ⁻⁵ | 400 | 0.1 | ZB |
| NTF-7 | 30 | 10 | 3.33 | 1.5 x 10 ⁻⁵ | 400 | 0.1 | ZB |
| NTF-8 | 30 | 10 | 2.50 | 1.5 x 10 ⁻⁵ | 400 | 0.9 | W |
| NTF-9 | 30 | 10 | 3.00 | 1.5 x 10 ⁻⁵ | 400 | 0.9 | W |
| NTF-10 | 30 | 10 | 3.33 | 1.5 x 10 ⁻⁵ | 400 | 0.9 | W |
| NTF-11 | 30 | 10 | 3.75 | 1.5 x 10 ⁻⁵ | 400 | 0.9 | W |
| NTF-12 | 30 | 10 | 4.16 | 1.5 x 10 ⁻⁵ | 400 | 0.9 | W |
| NTF-13 | 30 | 10 | 3.33 | 10 x 10 ⁻² | 400 | 0.9 | W |
| NTF-14 | 30 | 10 | 3.33 | 20 x 10 ⁻² | 400 | 0.9 | W |
| NTF-15 | 30 | 10 | 3.33 | 50 x 10 ⁻² | 400 | 0.9 | W |

| | | | | | | | |
|--------|----|----|------|----------------------|-----|------|----|
| NTF-16 | 30 | 10 | 3.33 | 10×10^{-1} | 400 | 0.9 | W |
| NTF-17 | 30 | 10 | 3.33 | 20×10^{-1} | 400 | 0.9 | W |
| NTF-18 | 30 | 10 | 3.33 | 1.5×10^{-5} | 200 | 0.1 | ZB |
| NTF-19 | 30 | 10 | 3.33 | 1.5×10^{-5} | 300 | 0.1 | ZB |
| NTF-20 | 30 | 10 | 3.33 | 1.5×10^{-5} | 500 | 0.1 | W |
| NTF-21 | 30 | 10 | 3.33 | 1.5×10^{-5} | 600 | 0.1 | W |
| NTF-22 | 30 | 10 | 3.33 | 1.5×10^{-5} | 200 | 0.3 | ZB |
| NTF-23 | 30 | 10 | 3.33 | 1.5×10^{-5} | 300 | 0.3 | ZB |
| NTF-24 | 30 | 10 | 3.33 | 1.5×10^{-5} | 400 | 0.3 | W |
| NTF-25 | 30 | 10 | 3.33 | 1.5×10^{-5} | 500 | 0.3 | W |
| NTF-26 | 30 | 10 | 3.33 | 1.5×10^{-5} | 600 | 0.3 | W |
| NTF-27 | 30 | 10 | 3.33 | 1.5×10^{-5} | 200 | 0.5 | ZB |
| NTF-28 | 30 | 10 | 3.33 | 1.5×10^{-5} | 300 | 0.5 | W |
| NTF-29 | 30 | 10 | 3.33 | 1.5×10^{-5} | 400 | 0.5 | W |
| NTF-30 | 30 | 10 | 3.33 | 1.5×10^{-5} | 500 | 0.5 | W |
| NTF-31 | 30 | 10 | 3.33 | 1.5×10^{-5} | 600 | 0.5 | W |
| NTF-32 | 30 | 10 | 3.33 | 1.5×10^{-5} | 400 | 0.2 | ZB |
| NTF-33 | 30 | 10 | 3.33 | 1.5×10^{-5} | 400 | 0.4 | W |
| NTF-34 | 30 | 10 | 3.33 | 1.5×10^{-5} | 400 | 0.75 | W |

5.4.1.1 Effect of laser flux density on structural properties

Figure 5.3 shows XRD patterns of samples NTF-8, NTF-9, NTF-10, NTF-11, and NTF-12 with laser flux densities of 2.5, 3.0, 3.33, 3.75, and 4.16 J/cm² respectively. Three diffraction peaks corresponding to (100), (002), and (111) planes of the wurtzite crystalline Zn_{0.1}Cd_{0.9}S are obtained. The interplanar spacing of Zn_{0.1}Cd_{0.9}S nanocrystalline thin films is calculated via XRD pattern for (002) reflection (equation 3.3, chapter 3) and comes out to be 3.29 Å.

It can be observed from figure 5.3 that the diffraction peaks formed at laser flux density of 2.5 J/cm², are broad and weak. With increase in laser flux density from 2.5 to 3.0 J/cm², diffraction peaks becomes less broad with enhanced diffraction intensity. With further increase in laser flux density to 3.33 J/cm², Zn_{0.1}Cd_{0.9}S diffraction peaks become more intense and sharper. It is an indication of improved crystalline quality of the films. As laser flux density is further increased to 3.75 J/cm², intensity of diffraction peaks became weaker slightly, indicating degradation in the crystallinity of the films. At laser flux density of 4.16 J/cm² there is a sharp decrease in the XRD intensity.

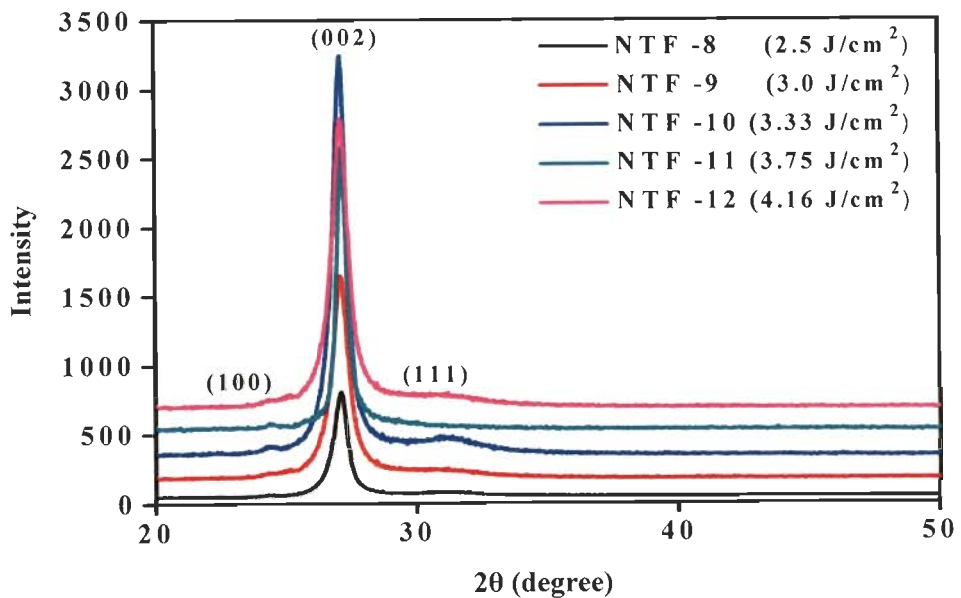


Figure 5.3: XRD patterns of Zn_{0.1}Cd_{0.9}S films corresponding to laser flux densities of 2.5, 3.0, 3.33, 3.75, and 4.16 J/cm²

To analyze the intensity changes of (002) peak, texture coefficient along (002) orientation is calculated by using equation (3.7). The same is reproduced here for (002) orientation (equation 5.2); corresponding graph is shown in figure 5.4.

$$TC = \frac{I(002)}{[I(100) + I(002) + I(111)]} \quad (5.2)$$

Texture coefficient shows a highest preferential *c*-axis orientated structure along (002) plane at laser flux density of 3.33 J/cm². Higher crystal orientation is due to reduction in the scattering of the carriers at the grain boundaries and crystal defects due to the shorter carrier path length in *c*-plane. In laser ablation processes, a large amount of ions in the plasma are present. Kinetic energy of plasma species increases with increase in the laser flux density. When plasma species reached the substrate surface, they congregated and grew as dense aggregates of independent nanoparticles with different sizes to form thin films [74]. Improvement in the crystallinity; better texture coefficient; of the films deposited at moderate laser flux density is due to sufficient atomic mobility that results in crystalline conformation. Tong *et al.* have studied the effect of laser flux density on the surface morphology of CdS films and made the similar observations [192]. Their group used the femto-second laser, requiring lesser laser incident energy to meet the equivalent laser flux densities. In this study, too high laser flux density raises kinetic energy of ions and thus, may lead to high plasma density. As the laser incident energy was increased to 4.16 J/cm², the direct bombardment of the ions led to induce a large structural disorder during film growth.

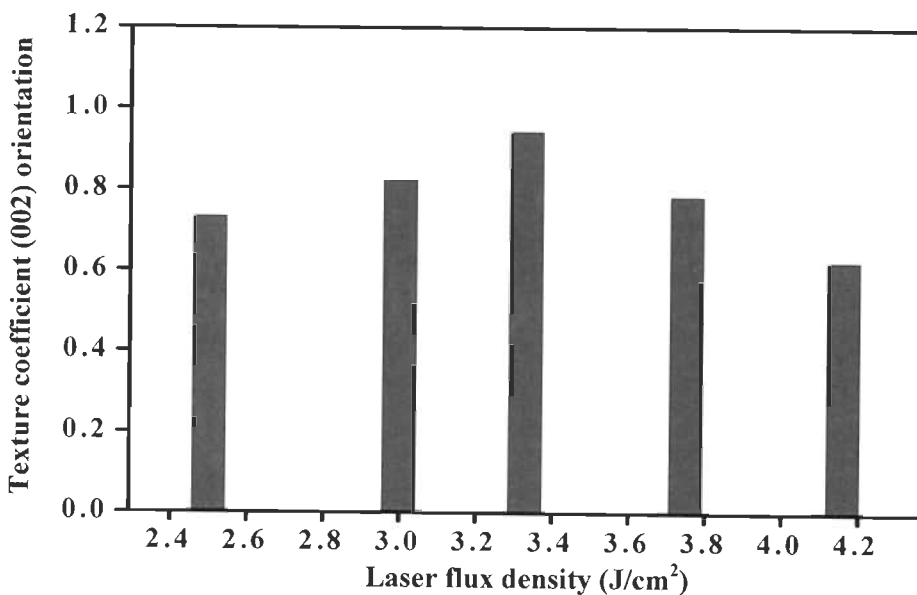


Figure 5.4: Texture coefficient of (002) orientation of Zn_{0.1}Cd_{0.9}S films corresponding to laser flux densities of 2.5, 3.0, 3.33, 3.75, and 4.16 J/cm²

5.4.1.2 Effect of laser flux density on surface morphology

Figure 5.5(a) shows TEM image of sample NTF-10 deposited at 3.33 J/cm^2 . TEM sample preparation procedure for nanocrystalline thin film is described in section 3.3.5, chapter 3. TEM image shows with nearly spherical particles with average diameter of 15 nm. Figure 5.5(b) shows the lattice lines of sample NTF-10. Interplanar distance is calculated by using equation (3.6) and is 3.293 \AA . Interplanar distance obtained from TEM matches closely with that obtained from XRD (3.29 \AA). Figure 5.5(c) shows SAED pattern characteristic of a wurtzite phase.

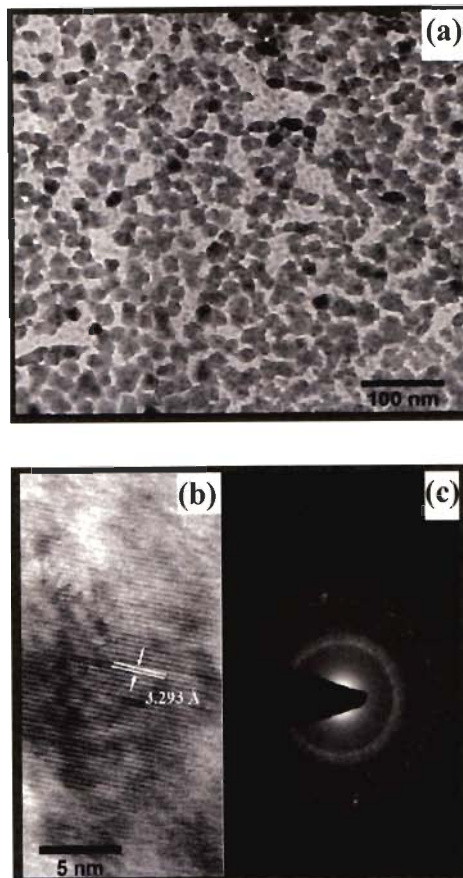


Figure 5.5: $\text{Zn}_{0.1}\text{Cd}_{0.9}\text{S}$ film (sample NTF-10) at 3.33 J/cm^2 (a) TEM image, (b) Lattice spacing, and (c) SAED pattern

Figure 5.6 shows AFM images of samples NTF-8, NTF-10, and NTF-12 corresponding to laser flux densities of 2.5 , 3.33 , and 4.16 J/cm^2 . AFM images show that the films have spherical particles. Particle size of $\sim 22 \text{ nm}$ is observed at 2.5 J/cm^2 (figure 5.6(a)). With increase in laser flux density from 2.5 to 3.33 J/cm^2 , particle size increases from 22 to 25 nm and it is relatively uniform (figure 5.6(b)). A similar particle size (25 nm) was also observed at 3.0 J/cm^2 (not shown here). It also shows narrow size distribution of particles with relative standard deviation of $5\text{-}8\%$. Increase in laser flux

density to 3.75 J/cm^2 , results in relatively large size particles of $\sim 29 \text{ nm}$ (image not shown). At laser flux density of 4.16 J/cm^2 (figure 5.6(c), the particles are bigger ($\sim 32 \text{ nm}$) and follow broad size distribution (relative standard deviation is 20-22 %).

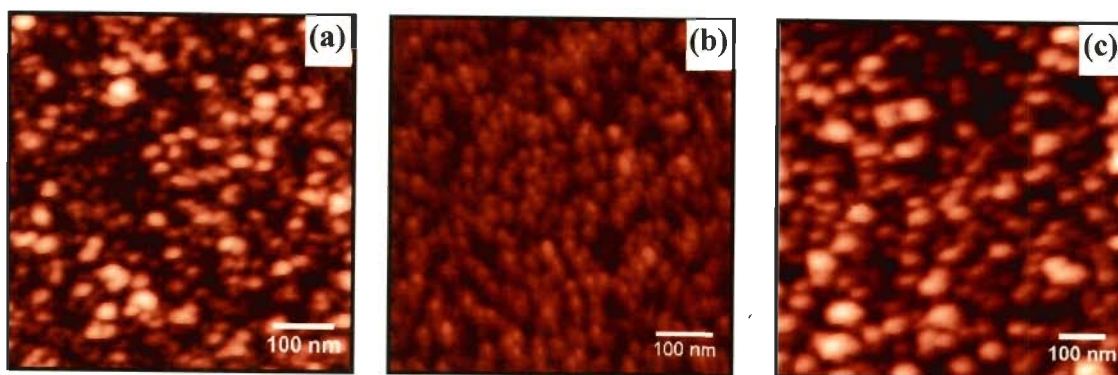


Figure 5.6: Surface morphology of Zn_{0.1}Cd_{0.9}S films corresponding to laser flux densities of (a) 2.5, (b) 3.33, and (c) 4.16 J/cm² respectively

Figure 5.7 shows the rms surface roughness with laser flux densities. Rms surface roughness of 15.4, 12.1, 8.0, 14.4, and 20.5 nm are obtained for samples NTF-8, NTF-9, NTF-10, NTF-11, and NTF-12 respectively. Green diamond shaped points in figure 5.7 are the rms surface roughness measured at five different locations of one particular sample. Red diamond shaped points represents the average of these data points. The black line shows the deviation of $\pm 5\%$ from average value. It is worthy to note that the deviation of data points from average value is small; data lies within $\pm 5\%$ line for laser flux density at 3.33 J/cm^2 . With increasing flux density, the deviation from average value increases. This trend also shows the higher non uniformity of particles, which eventually results into the increased surface roughness.

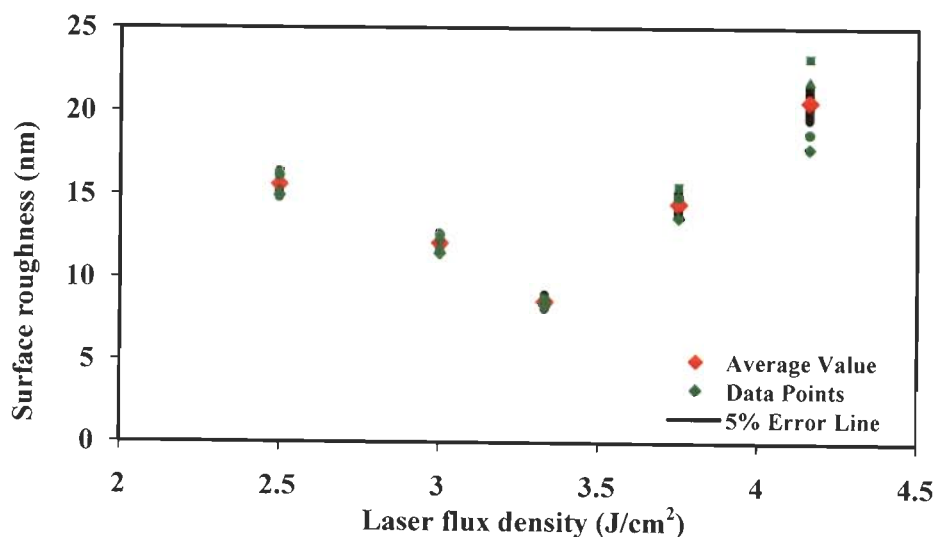


Figure 5.7: Average surface roughness of Zn_{0.1}Cd_{0.9}S films corresponding to laser flux densities of 2.5, 3.0, 3.33, 3.75, and 4.16 J/cm²

Gupta *et al.* reported that during the film growth, species (ions and neutrals) propagating with various velocities reach the surface of growing film. The higher energy component of plume was related to ions, while neutral particles can obtain their velocities by collisions with fast ions [54, 74, 99]. Plasma formed under these conditions of the laser incident flux of 4.16 J/cm², led to the ions with too high kinetic energy. The atoms on the growing films could be bombarded and sputtered by incident ions with too high kinetic energy. While, a few large size neutral particles or debris could be emitted from the target. This results in coarsening and the large non-uniformity of particle size. A destructive effect due to high energy could lead to deterioration of the growing films.

Figure 5.8 shows transmittance spectra of samples NTF-8, NTF-9, NTF-10, NTF-11, and NTF-12 at laser flux densities of 2.5, 3.0, 3.33, 3.75, and 4.16 J/cm². Sample NTF-10 shows an average transmittance of ~75% in the visible region for. Percentage transmittance reduces with increase in flux density and reaches to 60%. This reduction in transmittance at higher flux densities can be attributed to increased surface roughness.

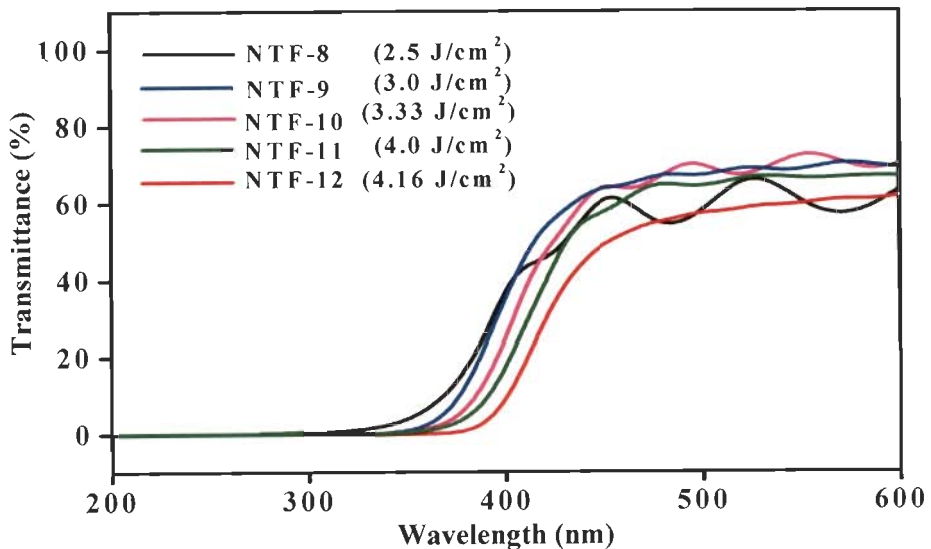


Figure 5.8: Transmittance $T(\lambda)$ of Zn_{0.1}Cd_{0.9}S films at 2.5, 3.0, 3.33, 3.75, and 4.16 J/cm²

Zn_{0.1}Cd_{0.9}S nanocrystalline thin films should possess higher transmission for their use as window layer of PV devices. It would allow more light to pass through this layer. It is worthy to note that the laser flux density also regulates the percentage transmission in these films. In this study, the ~ 75% transmission is obtained at 3.33 J/cm². At lower flux densities crystalline quality of the films degrades while the higher

flux densities results in increased surface roughness and therefore decreased the transmittance.

Transmission data is also used to obtain the refractive indices and thicknesses of the films. Refractive indices and thicknesses of the films were calculated by the method suggested by Manificier *et al.* (section 3.3.5.3 & 3.3.5.4 respectively). Thicknesses of the as-deposited films are found in the range of 460-540 nm. Refractive indices and thicknesses of samples NTF-8, NTF-9, NTF-10, NTF-11 and NTF-12 are shown in Table 5.2.

Table 5.2: Sample roughness, average particle size, refractive index and film thickness with laser flux density

| Sample | Laser flux density (J/cm ²) | Surface roughness (nm) | d_p (nm) | Refractive index | Thickness (nm) |
|--------|---|------------------------|------------|------------------|----------------|
| NTF-8 | 2.5 | 15.4 | 13.2 | 1.90 | 460 ± 20 |
| NTF-9 | 3.0 | 12.1 | 14.2 | 1.93 | 470 ± 20 |
| NTF-10 | 3.33 | 8.0 | 15.5 | 1.92 | 500 ± 20 |
| NTF-11 | 3.75 | 14.4 | 16.3 | 1.90 | 520 ± 20 |
| NTF-12 | 4.16 | 20.5 | 17.3 | 1.89 | 540 ± 20 |

5.5 PARTICLE SIZE VARIATION

Particle size of nanocrystalline thin films can be varied by varying the chamber working pressure. It can be varied by varying argon gas flow rate, keeping other deposition parameters identical. By doing so, systematic control on the particle size can be obtained [28]. Five samples namely NTF-13, NTF-14, NTF-15, NTF-16, and NTF-17 were prepared with working pressures of 10, 20, 50, 100, and 200 mtorr respectively (Table 5.1). Figure 5.9 shows AFM images of some selective samples NTF-13, NTF-15, and NTF-17 at working pressures of 10, 50 and 200 mtorr respectively.

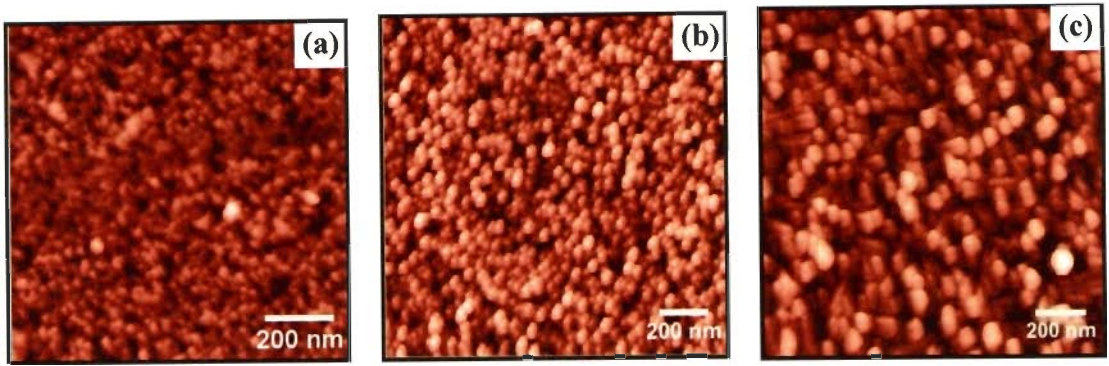


Figure 5.9: AFM images of Zn_{0.1}Cd_{0.9}S films corresponding to working pressures of (a) 10, (b) 50, and (c) 200 mtorr respectively

Particle size increases from 18 to 80 nm (~ 4.5 times) with increase in working pressures from 10 to 200 mtorr. Increase in particle size with pressure can be explained by the relationship of the mean free path, λ_{mfp} (cm), with working pressure of the gas and is given by

$$\lambda_{mfp} = 2.330 \times 10^{-20} \frac{T}{(P\delta_m^2)} \quad (5.3)$$

where, T (K) is the temperature, P (Torr) is the pressure and δ_m (cm) is the molecular diameter of the gas [28, 31, 113]. In this work, argon (atomic diameter 1.76 Å) has been used as the working gas [28]. Since working pressure is inversely proportional to mean free path (equation (5.3)), the ablated atoms undergo a large number of collisions when the chamber pressure is high and have a higher probability of agglomeration. Thus particle size increases even before arriving at the substrate surface. Chandra *et al.* have reported the effect of sputtering gas diameter on the particle size. They observed an increase in particle size with increasing inert gas molecule diameter. This study is in corroboration of the above findings; increase in working pressure increases the particle size. Variation of mean free path and particle size with increasing working pressure is shown in figure 5.10. Sample NTF-10 (deposited at 1.5×10^{-5} torr) has also been added for the comparison. Figure 5.10 clearly shows that there is ~ 5 fold increase in particle size when working pressure increases from 1.5×10^{-2} to 200 m torr.

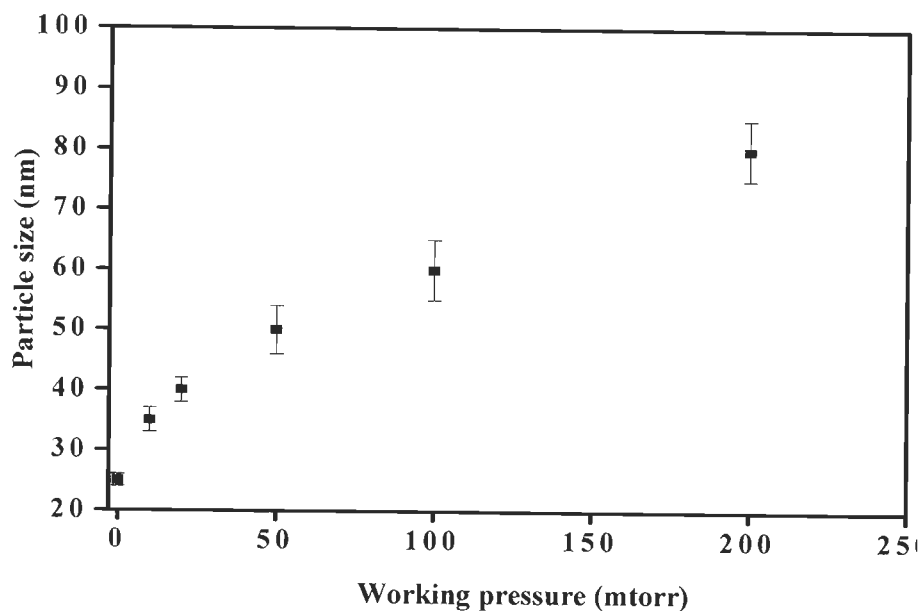


Figure 5.10: Variation of particle size of Zn_{0.1}Cd_{0.9}S films with working pressures of 0.015, 10, 20, 50, 100, and 200 mtorr

Variation in particle size and mean free path with working pressures are presented in Table 5.3.

Table 5.3: Working pressure, mean free path, and corresponding particle sizes as observed from AFM

| Sample | Working pressure (mtorr) | Mean free path (cm) | Particle size (nm) |
|--------|--------------------------|---------------------|--------------------|
| NTF-10 | 1.5×10^{-2} | 3375 | 25 ± 1 |
| NTF-13 | 10 | 5.06 | 35 ± 2 |
| NTF-14 | 20 | 2.53 | 40 ± 2 |
| NTF-15 | 50 | 1.01 | 50 ± 3 |
| NTF-16 | 100 | 0.506 | 60 ± 5 |
| NTF-17 | 200 | 0.253 | 80 ± 5 |

5.6 DEPOSITION TEMPERATURE VARIATION

This section investigates the effect of deposition temperature (T_s) on the crystal structure of Zn_{1-x}Cd_xS (x as 0.1, 0.3, and 0.5) thin films. Deposition temperature was varied from 200 to 600 °C in steps of 100 °C. Three series of samples namely NTF-18, NTF-19, NTF-2, NTF-20, and NTF-21 with mole fraction as 0.1; NTF-22, NTF-23, NTF-24, NTF-25, and NTF-26 with mole fraction as 0.3; and NTF-27, NTF-28, NTF-29, NTF-

30, and NTF-31 with mole fraction as 0.5 were deposited. Complete description of deposition parameters are mentioned in Table 5.1.

5.6.1 Results & Discussions

Variation in deposition temperature results into the phase transition of Zn_{1-x}Cd_xS nanostructures. It is established that phase transition temperature depends on both: the deposition temperature and the mole fraction. Results obtained with varying deposition temperature are discussed in the following sections.

5.6.1.1 Effect of deposition temperature on crystal structure

Figure 5.11 shows the XRD spectra of samples NTF-18, NTF-19, NTF-2, NTF-20, and NTF-21 deposited at 200, 300, 400, 500, and 600 °C respectively. XRD peaks of (111) orientation of all samples are positioned at 28.5° (this peak position is consistent with Zn_{0.9}Cd_{0.1}S nanoparticles). Figure 5.11 shows the zincblende phase of samples NTF-18, NTF-19 and NTF-2 ($T_s \leq 400$ °C) with (111) orientation as highest intensity peak. With increase in deposition temperature from 400 to 500 °C, crystal structure changes from zincblende to wurtzite. The wurtzite structure in figure 5.11 is characterized via (100) and (002) orientations emerging along with (111) orientation [143, 144].

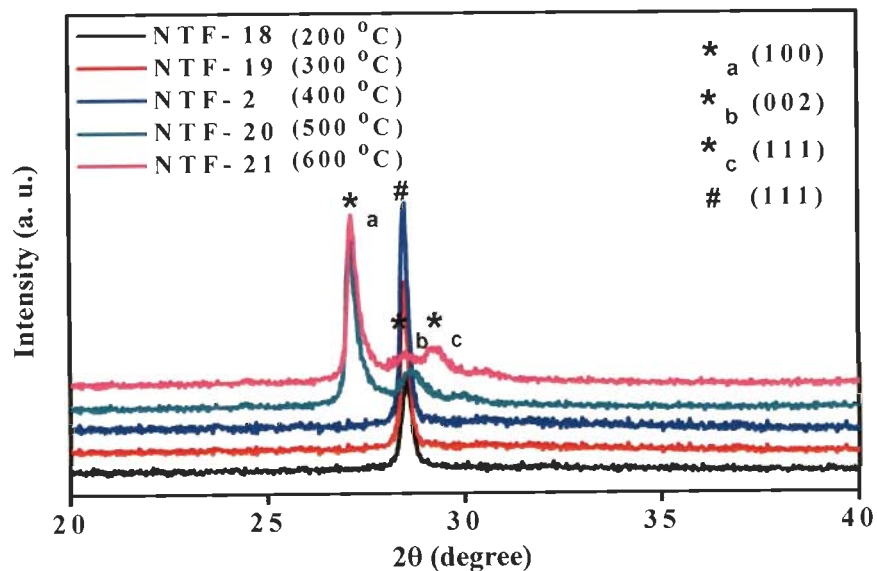


Figure 5.11: X-ray diffraction spectra of Zn_{0.9}Cd_{0.1}S films corresponding to deposition temperatures of 200, 300, 400, 500, and 600 °C

(* Orientations for wurtzite structure, # Orientation for zincblende structure)

Effect of deposition temperature on phase transition in Zn_{1-x}Cd_xS films has been further investigated with increased mole fraction. Five samples namely NTF-22, NTF-23, NTF-24, NTF-25, and NTF-26 were prepared at 200, 300, 400, 500, and 600 °C respectively with mole fraction as 0.3. Figure 5.12 shows the XRD spectra of samples NTF-22, NTF-23, NTF-24, NTF-25, and NTF-26. Zn_{0.7}Cd_{0.3}S films retained the zincblende structure with (111) dominant orientation up to deposition temperature of 300 °C (figure 5.12). The XRD peak at $x = 0.3$ is found to be positioned at 27.14° (this peak position is consistent with Zn_{0.7}Cd_{0.3}S nanoparticles). With increase in deposition temperature from 300 °C, lattice structure changes from zincblende to wurtzite (characterized via (100) and (002) orientations). It is important to note that the phase transition in Zn_{1-x}Cd_xS films at $x = 0.3$ occurs at a lower temperature than with 0.1.

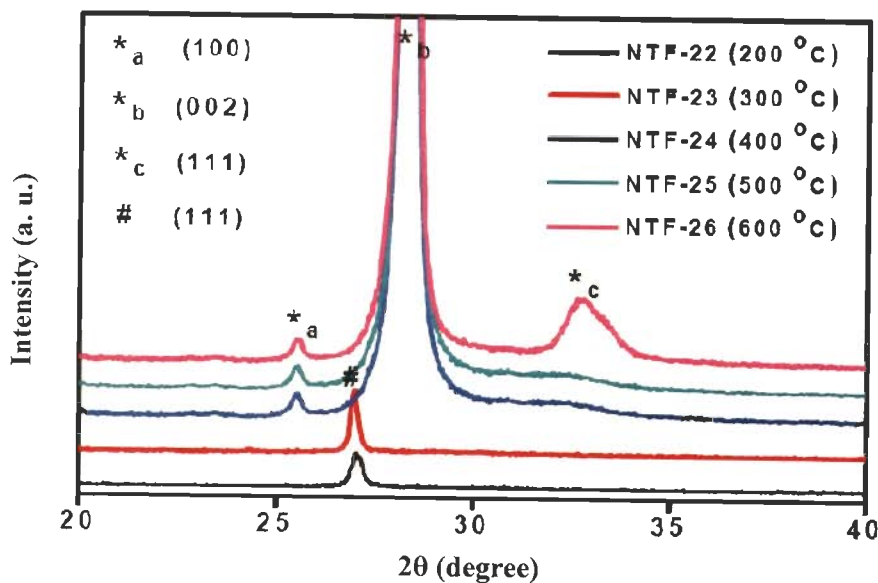


Figure 5.12: X-ray diffraction spectra of Zn_{0.7}Cd_{0.3}S films corresponding to deposition temperatures of 200, 300, 400, 500, and 600 °C

(* Orientations for wurtzite structure, # Orientation for zincblende structure)

In a continuing effort, another series of samples namely NTF-27, NTF-28, NTF-29, NTF-30, and NTF-31 at 200, 300, 400, 500, and 600 °C were prepared with x as 0.5. Figure 5.13 shows the XRD spectra of samples NTF-27, NTF-28, NTF-29, NTF-30, and NTF-31. Zn_{0.5}Cd_{0.5}S films retained the zincblende structure with (111) dominant orientation only when deposition temperature is limited to 200 °C. Further increase in deposition temperature from 200 °C results in the wurtzite structure.

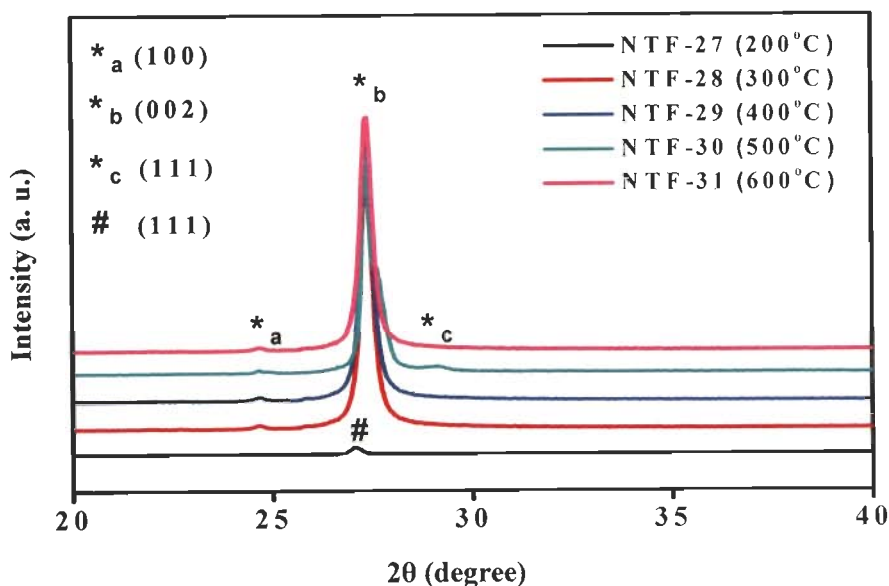


Figure 5.13: X-ray diffraction spectra of Zn_{0.5}Cd_{0.5}S films corresponding to deposition temperatures of 200, 300, 400, 500, and 600 °C

(* Orientations for wurtzite structure, # Orientation for zincblende structure)

As seen above, the structural change from zincblende to wurtzite; in Zn_{1-x}Cd_xS nanocrystalline thin films is a function of both, the deposition temperature and the mole fraction. XRD patterns of three samples NTF-20, NTF-24, and NTF-28 with mole fraction and deposition temperature (0.1, 500 °C), (0.3, 400 °C), and (0.5, 300 °C) respectively are shown in figure 5.14. From these observations it can be construed that an increased cadmium concentration results in the formation of a wurtzite phase at lower deposition temperature. These results show that cadmium concentration in ZnS lattice generates distortions which eventually produce structural changes. Since zinc and cadmium have different ionic radii (Table 2.1, chapter 2), a lattice deformation is expected when cadmium substitutes zinc. Furthermore, the addition of high cadmium concentration into ZnS lattice produces a crystal structural transition from zincblende to wurtzite at lower deposition temperature. This decrease in deposition temperature can be attributed to the difference arising from heat of formation of parent ZnS and CdS binaries. Since CdS has lower heat of formation than ZnS (Table 2.1, chapter 2), a less thermal energy needs to be supplied for the nucleation of the wurtzite phase into the parent zincblende phase.

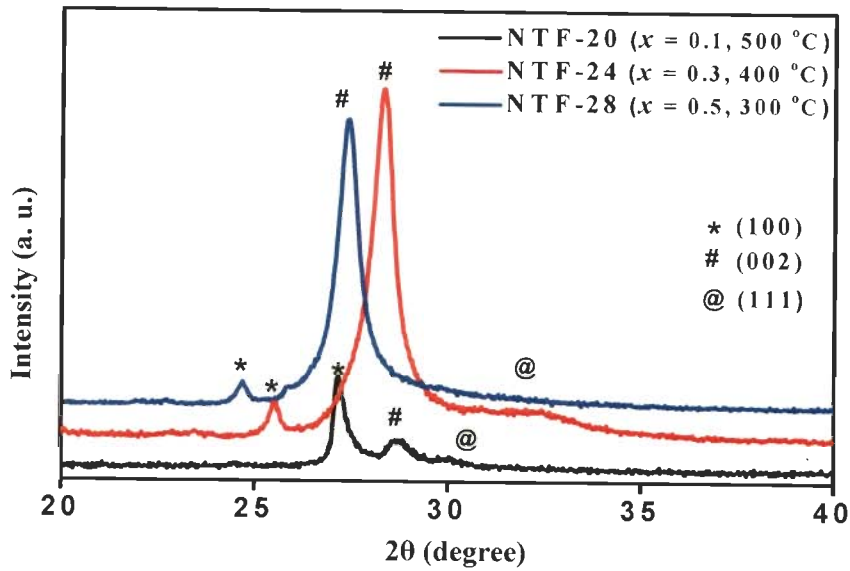


Figure 5.14: XRD patterns of three samples of $Zn_{1-x}Cd_xS$ with mole fractions and deposition temperatures of (0.1, $500^\circ C$), (0.3, $400^\circ C$), and (0.5, $300^\circ C$)

5.6.1.2 Phase transition investigation via TEM

Figure 5.15(a) shows TEM image of sample NTF-19 (x as 0.1) deposited at $300^\circ C$. It shows nearly spherical particles, with particle diameter of 20 ± 3 nm. Figure 5.15(b) shows the SAED characteristic of zincblende phase.

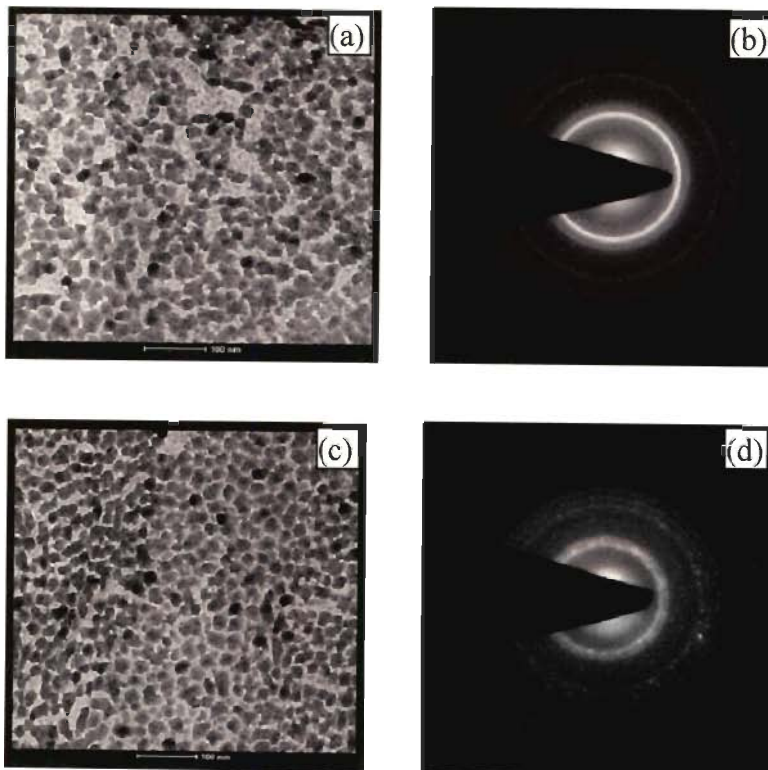


Figure 5.15: (a) TEM image of $Zn_{0.9}Cd_{0.1}S$ sample deposited at $300^\circ C$, (b) corresponding SAED pattern, (c) TEM image of $Zn_{0.9}Cd_{0.1}S$ sample deposited at $500^\circ C$, and (d) corresponding SAED pattern

Figure 5.15(c) (see above) shows the TEM image of sample NTF-20 (x as 0.1) deposited at 500 °C. Figure 5.15(d) (see above) shows the SAED pattern characteristic of wrutzite phase. Diffraction patterns clearly provide the evidence of the phase transition with increase in deposition temperature.

5.6.1.3 Effect of deposition temperature on energy band gap

Figure 5.16(a) shows transmittance spectra of samples NTF-27, NTF-28, NTF-29, NTF-30, and NTF-31 deposited at 200, 300, 400, 500 and 600 °C with mole fraction as 0.5. Transmittance of more than 70 % in the visible region is obtained for these samples.

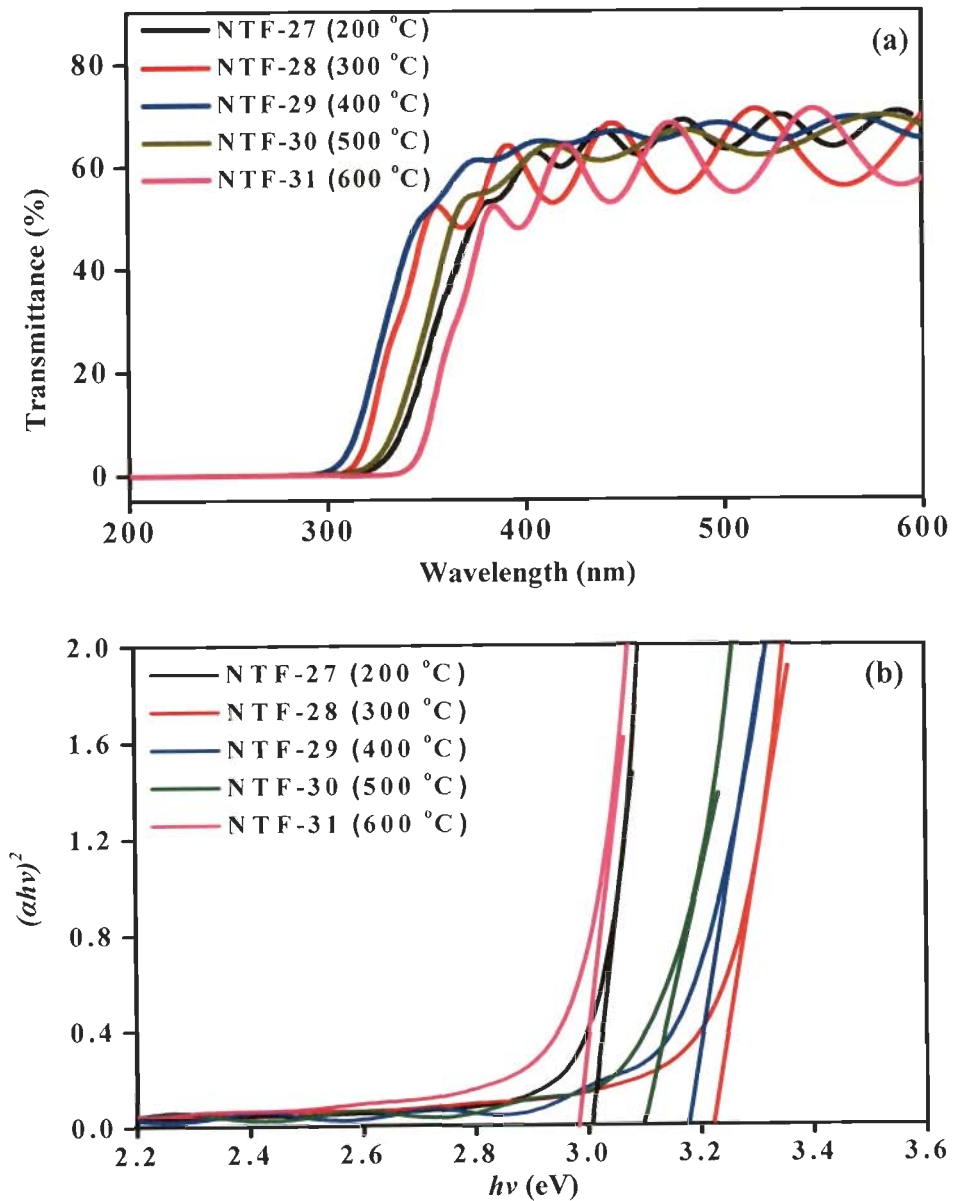


Figure 5.16: (a) Transmittance $T(\lambda)$ and (b) $(ahv)^2$ with $h\nu$ profiles of Zn_{0.5}Cd_{0.5}S films at 200, 300, 400, 500, and 600 °C

Similar transmittance is obtained for all series studied in this section. Thicknesses of the deposited films are found in the range of 500 ± 30 nm. Direct energy band gap of samples NTF-27, NTF-28, NTF-29, NTF-30, and NTF-31 were determined by making use of Tauc relation, considering n as $1/2$ (equation (3.9)) and is shown in figure 5.16(b). An extrapolation of the linear region of a plot of $(\alpha h\nu)^2$ on the y-axis versus photon energy ($h\nu$) on the x-axis gives the value of the energy band gap. As the deposition temperature increases from 200 to 600 °C the energy band gap changes from 2.95 to 3.35 eV. For $T_s > 200$ °C the traces of wurtzite phase appear in Zn_{0.5}Cd_{0.5}S films and it increases with increasing deposition temperature ($E_{gZnS} = 3.68$ and $E_{gCdS} = 2.36$ eV for the zincblende phase; $E_{gZnS} = 3.9$ eV $E_{gCdS} = 2.5$ eV for wurtzite phase) (Table 2.1, chapter 2). Subbaiah *et. al* have observed an increase in band gap of ZnS layers with increasing deposition temperatures from 473–623 K by the method of close-spaced evaporation [186].

Figure 5.17 shows the variation of energy band gaps of samples with deposition temperatures, for three different mole fractions 0.1, 0.3 and 0.5. With mole fraction as 0.3, lattice structure retains zincblende structure and E_g follows the zincblende structure band gap values for $T_s < 400$ °C. E_g decreases slightly when T_s is increased from 200 to 300 °C. This decrease in E_g is due to increased particle size at higher deposition temperature. For $T_s > 300$ °C, E_g increases sharply from 3.25 to 3.5 eV. This large change in E_g is due to lattice structure transition and E_g follows the wurtzite structure band gap values. With further increase in T_s up to 600 °C, E_g decreases and is again attributed to the increased particle size with increase in deposition temperature.

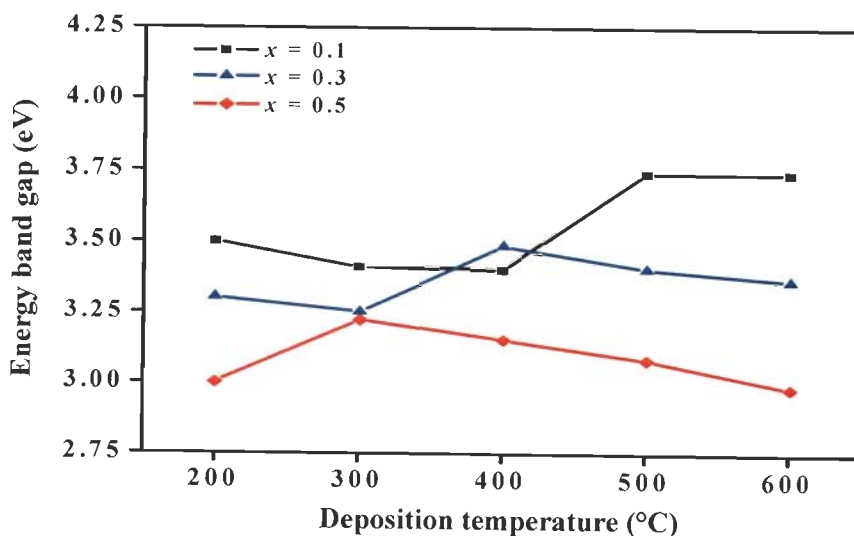


Figure 5.17: Energy band gap of Zn_{1-x}Cd_xS (x as 0.1, 0.3, and 0.5) nanocrystalline thin films at 200, 300, 400, 500 and 600 °C

Figure 5.17 also shows the energy band gap values for samples deposited with mole fraction of 0.1, and 0.5 with increasing deposition temperature. Similar trend of energy band gap values with increasing deposition temperature is observed for 0.1, and 0.5 mole fractions as well.

5.6.1.4 Effect of deposition temperature on PL emission intensity

Figure 5.18 show PL emission spectra of samples NTF-18, NTF-19, NTF-2, NTF-20, and NTF-21 deposited at 200, 300, 400, 500, and 600 °C with $x = 0.1$. Samples were excited with 350 nm wavelength. PL spectra show two emission peaks positioned at ~ 374 and ~ 429 nm. PL peak for band gap emission of Zn_{0.9}Cd_{0.1}S should appear at 356 and 343 nm for zincblende and wurtzite phase respectively (corresponding to energy band gaps of 3.47 and 3.60 eV; obtained via Vegard's law with $x = 0.3$). It is observed that PL peak slightly shifted towards higher wavelength at 374 nm and corresponds to the near band edge (NBE) emission. The emergence of the peak at 429 nm is due to the surface defects which are originating within the band gap. We can attribute the formation of this defect related emission either to dangling bonds at the semiconductor surface that give rise to electronic states within the energy band gap or to the recombination centers that is formed below the energy band gap and gives rise to surface defects.

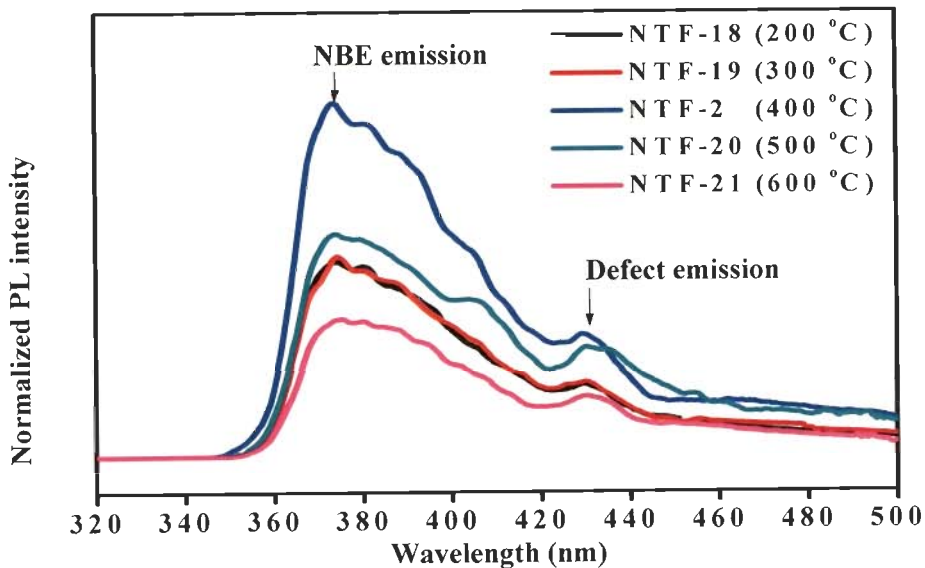


Figure 5.18: PL emission spectra of Zn_{0.9}Cd_{0.1}S films at 200, 300, 400, 500, and 600 °C

Yao *et al.* have devised a parameter which provides significant information about film crystalline quality via PL measurement. Their group suggested that the measure of quality of deposited film is the peak intensity ratio ($I_{NBE/DEF}$) between the principal bound exciton i.e. near band edge emission (NBE) and defect center luminescence [216]. Figure 5.19 shows intensity ratio, $I_{NBE/DEF}$ with deposition temperature. Since defect centre emission is generally related with complex defects or impurities, the higher $I_{NBE/DEF}$ ratio in Zn_{0.9}Cd_{0.1}S films indicates a low concentration of these crystalline defects. It is observed that $I_{NBE/DEF}$ value improves with increase in deposition temperatures. For higher deposition temperatures (> 400 °C), $I_{NBE/DEF}$ ratio decreases. This decrease in $I_{NBE/DEF}$, can be attributed to phase transition which takes place at higher temperatures. It again indicates the phase transition in Zn_{0.9}Cd_{0.1}S nanocrystalline thin film at temperatures in excess of 400 °C. This provides an additional support with the results obtained from XRD and TEM. Green diamond shaped points in figure 5.19 are the emission intensity ratio obtained at different locations of one particular sample, while the red diamond shaped points represents the average of these data points. The black line shows the deviation of $\pm 5\%$ from average value. It is worthy to note that the deviation of data points from average value is within $\pm 5\%$ error line with a slight deviation for the sample which is deposited at 600 °C.

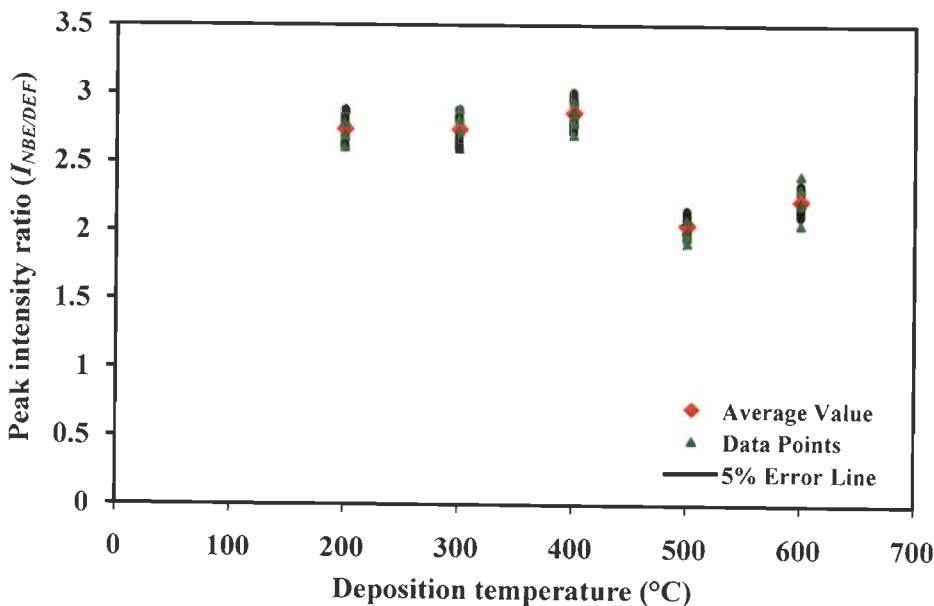


Figure 5.19: Variation of $I_{NBE/DEF}$ ratio of Zn_{0.9}Cd_{0.1}S films corresponding to deposition temperatures of 200, 300, 400, 500, and 600 °C

5.7 MOLE FRACTION VARIATION

This section investigates the samples deposited with varying mole fraction. Laser flux density and deposition temperature were kept constant at 3.33 J/cm² and 400 °C respectively. A series of samples with mole fractions as 0.1, 0.2, 0.3, 0.4, 0.5, 0.75, and 0.9 namely NTF-2, NTF-32, NTF-24, NTF-33, NTF-29, NTF-34, and NTF-10 respectively is prepared. Complete description of deposition parameters are mentioned in Table 5.1.

5.7.1 Results & Discussions

As seen in section 5.6, the phase transition in Zn_{1-x}Cd_xS nanocrystalline thin films is due to both: the mole fraction and the deposition temperature. This is again verified by covering the entire composition range. Variation in mole fraction provides the data reliability by comparing the energy band gaps obtained via two different characterization techniques. Results obtained with varying mole fraction are discussed in the following sections.

5.7.1.1 Effect of mole fraction on structural properties

Figure 5.20 shows XRD patterns of samples NTF-2, NTF-32, NTF-24, NTF-33, NTF-29, NTF-34, and NTF-10 at mole fractions 0.1, 0.2, 0.3, 0.4, 0.5, 0.75, and 0.9 respectively deposited at 400 °C. XRD pattern of ZnS film is also added for the comparison. Diffraction peaks of sample NTF-2 (*x* as 0.1) shifted to a lower angle from 28.7 to 28.56° from the zincblende structure of ZnS film.

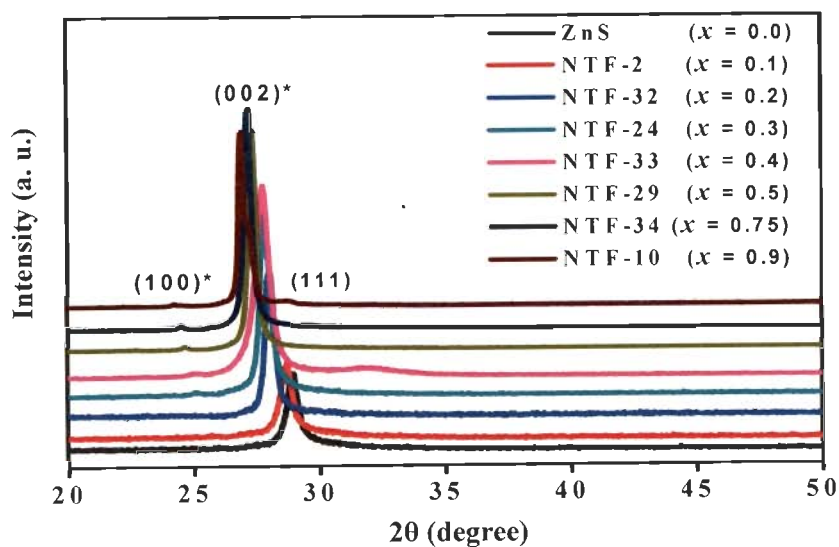


Figure 5.20: XRD spectra of Zn_{1-x}Cd_xS films with mole fractions 0, 0.1, 0.2, 0.3, 0.4, 0.5, 0.75, and 0.9

* Orientations for hexagonal structure

It can also be remarked that higher the x , more the diffraction peak feature shifts towards lower angle. This gradual shift confirms the preservice of stoichiometry in the deposited films. It can further be seen that for the sample deposited with mole fractions, $x = 0.1$ and 0.2 , have zincblende structure characterized by (111) orientation. Increase in $x > 0.2$ changes the crystal structure to wrutzite, with two dominant (002) and (100) orientations (as discussed earlier in section 5.6.1).

Figure 5.21 shows ideal lattice constants as a function of mole fraction in both zincblende and wrutzite structure (lines (1)-(3)) of Zn_{1-x}Cd_xS ternary semiconductor (appendix A1.3). Square data points in figure 5.21 corresponds to lattice constants with varying mole fraction both in zincblende and wrutzite structure obtained from XRD data (figure 5.20). It is observed from figure 5.21 that for $x \leq 0.2$ the experimentally calculated lattice constants closely matches with the zincblende lattice constant values. Further increase in x brings the experimental lattice values closer to hexagonal ones. This clearly suggests that increase in mole fraction above 0.2 changes the structure of Zn_{1-x}Cd_xS nanocrystalline thin films from zincblende to wrutzite. From the close agreement between observed (via XRD) and computed lattice constants (via Vegard's law) it can be concluded there is a change in phase transformation temperature with mole fraction in nanocrystalline Zn_{1-x}Cd_xS thin films. Table 5.4 presents the change in d -spacing with x for the whole series of samples calculated using the XRD data.

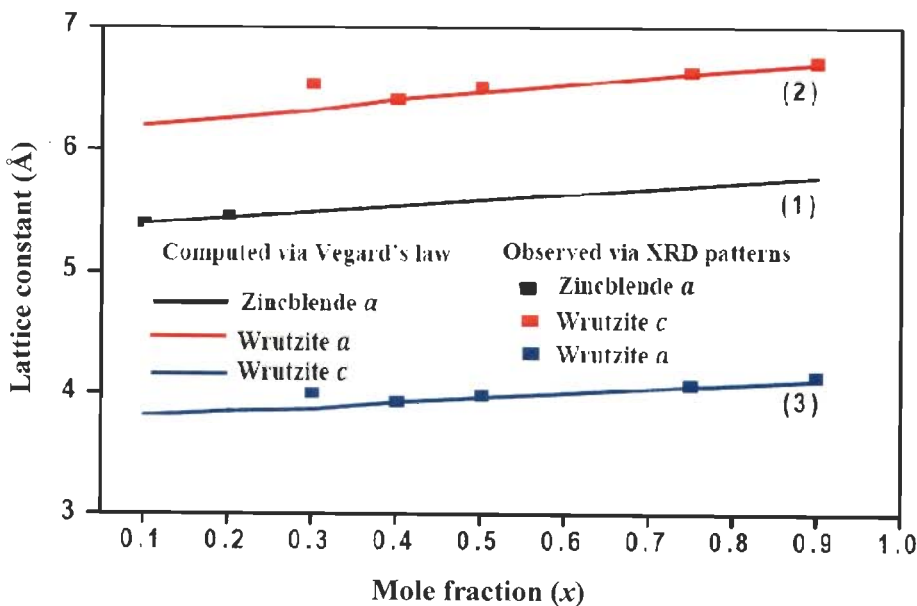


Figure 5.21: Lattice constants of Zn_{1-x}Cd_xS films with varying mole fraction deposited at 400 °C both in zincblende and wrutzite structure

Figure 5.22 shows $\pm 5\%$ error plot between computed (via Vegard's law) and observed (via XRD) lattice constant. It can be clearly seen that the difference between these two values lies within the $\pm 5\%$ error lines. This result shows that the lattice constant follow ternary rules. This close agreement also shows that the deposition parameters optimized in this work successfully preserved the stoichiometry of target material into the nanocrystalline thin films.

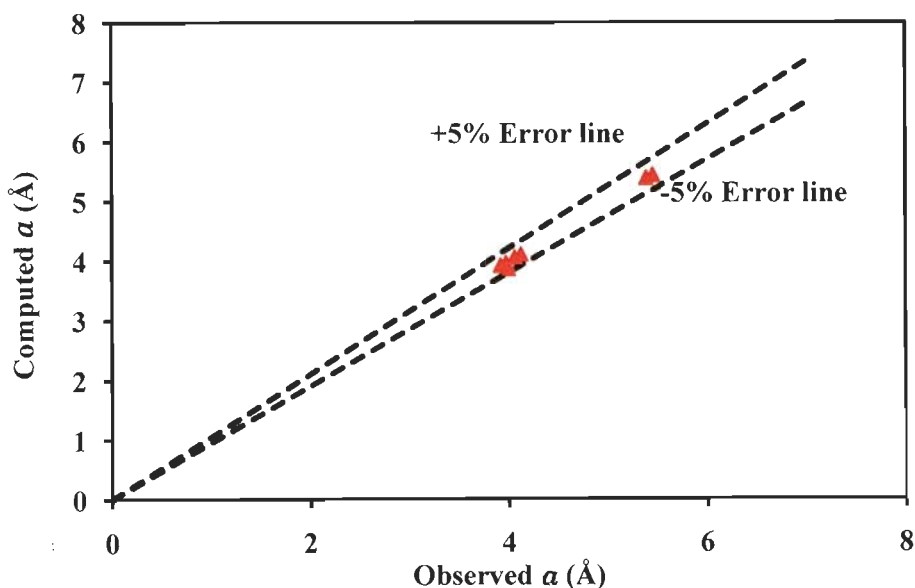


Figure 5.22: Error plot between observed and computed lattice constants of $Zn_{1-x}Cd_xS$ films with varying mole fraction

5.7.1.2 Effect of mole fraction on energy band gap

Transmittance spectra of samples NTF-2, NTF-32, NTF-24, NTF-33, NTF-29, NTF-34, and NTF-10 with mole fractions 0.1, 0.2, 0.3, 0.4, 0.5, 0.75, and 0.9 respectively are shown in figure 5.23. It shows an average percentage transmittance of $\sim 75\%$. There is a systematic red shift in the transmittance edge with increasing mole fraction. Transmittance edge shifts from 363 to 493 nm when mole fraction increases from 0.1 to 0.9.

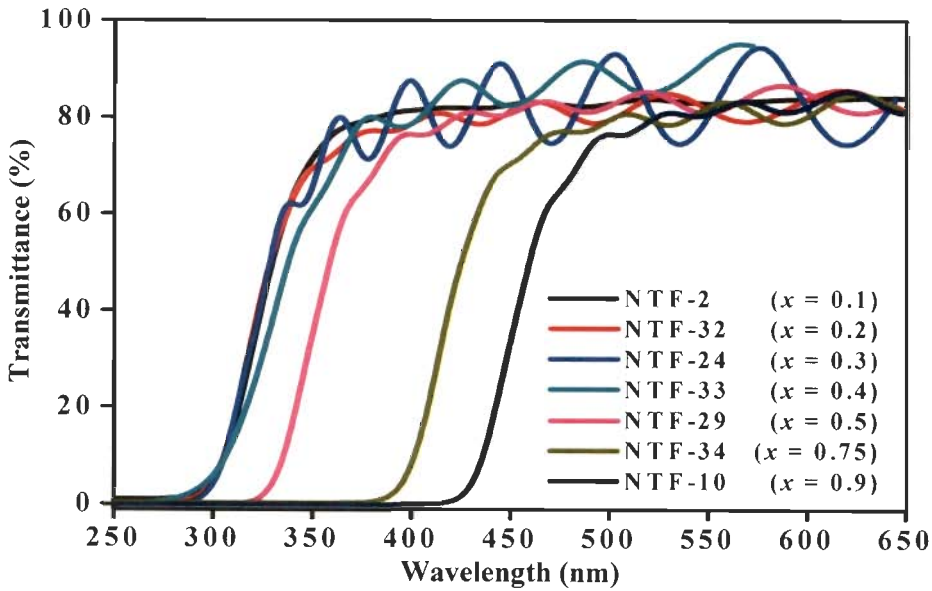


Figure 5.23: Transmittance $T(\lambda)$ of Zn_{1-x}Cd_xS films with mole fractions 0.1, 0.2, 0.3, 0.4, 0.5, 0.75, and 0.9

Figure 5.24 shows the energy band gaps obtained from transmittance (figure 5.20) spectra by applying the Tauc relation (equation 3.9, chapter 3). It can be seen from figure 5.24 that energy band gap first increases due to the phase transition. Thereafter, for higher x , structure remains in wurtzite phase and energy band gap follow the Vegard's law. Thus with increasing x , from 0.3 to 0.8, energy band gap decreases.

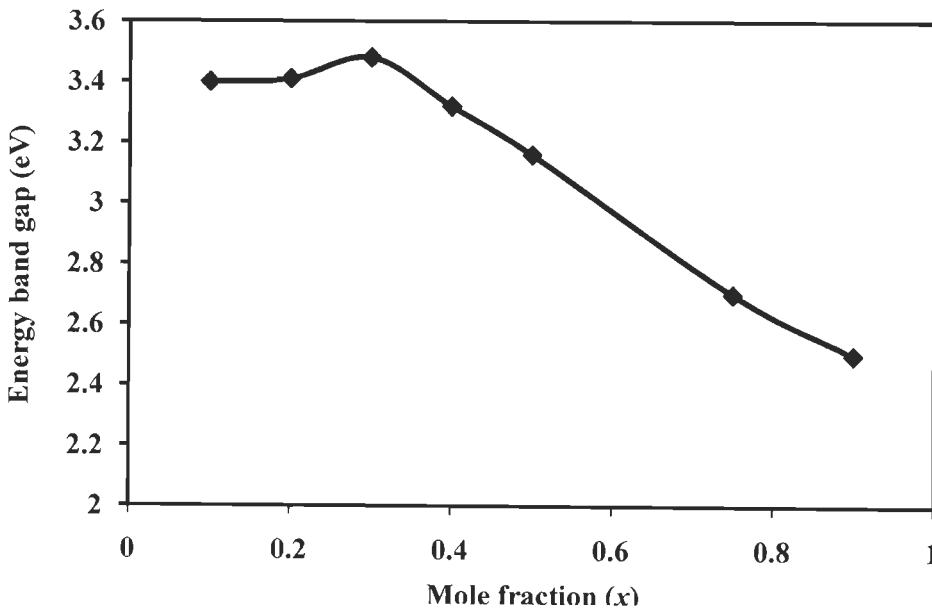


Figure 5.24: Energy band gap of Zn_{1-x}Cd_xS films with mole fractions 0.1, 0.2, 0.3, 0.4, 0.5, 0.75, and 0.9

5.7.1.3 Effect of mole fraction on PL emission intensity

Figure 5.25 shows two typical PL emission spectra with mole fractions 0.4 and 0.5 at 400 °C. Similar emission spectra's are obtained for all samples, with only change in the NBE peak position. Both spectra in figure 5.25 exhibit a near band emission at 416 and 424 nm. Both spectra also exhibit a feature due to defect related emission in addition to NBE peak. Table 5.4 presents the NBE wavelength with mole fraction, x .

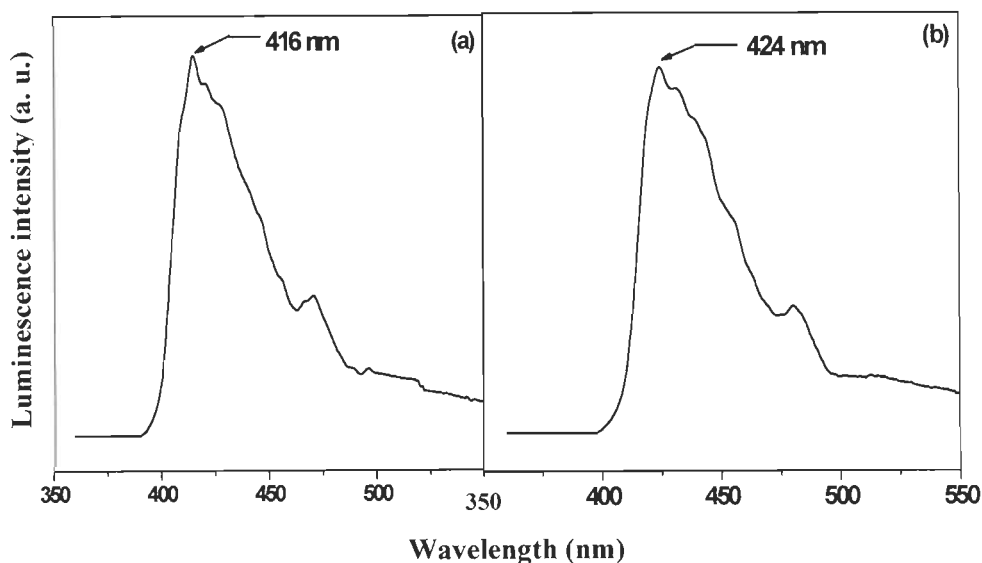


Figure 5.25: PL spectra at 300 K: (a) Zn_{0.6}Cd_{0.4}S and (b) Zn_{0.5}Cd_{0.5}S films at 400°C

Table 5.4: Sample composition, crystal structure, emission wavelengths, and binding energy of Zn_{1-x}Cd_xS thin films deposited at substrate temperature of 400 °C

| Mole Fraction (x) | 2 θ (°) | d-spacing (Å) | NBE wavelength (nm) | Binding energy (meV) |
|-------------------|----------------|---------------|---------------------|----------------------|
| 0.1 | 28.56 | 3.110 | 387 | 34.30 |
| 0.2 | 28.07 | 3.150 | 398 | 33.60 |
| 0.3 | 27.85 | 3.198 | 405 | 32.90 |
| 0.4 | 27.75 | 3.204 | 416 | 32.20 |
| 0.5 | 27.33 | 3.248 | 424 | 31.50 |
| 0.75 | 27.15 | 3.281 | 480 | 29.75 |
| 0.9 | 27.01 | 3.297 | 510 | 28.70 |

Figure 5.26 is a plot of the NBE peak energy position with mole fraction. The solid curve is the quadratic fit to the data going through the known end points given by the equation

$$E_{peak} = 3221 - 364.8x - 570x^2 \text{ meV}; R^2 = 0.997 \quad (5.4)$$

The quadratic term in equation (5.4) is correlated with the bowing of E_g [178].

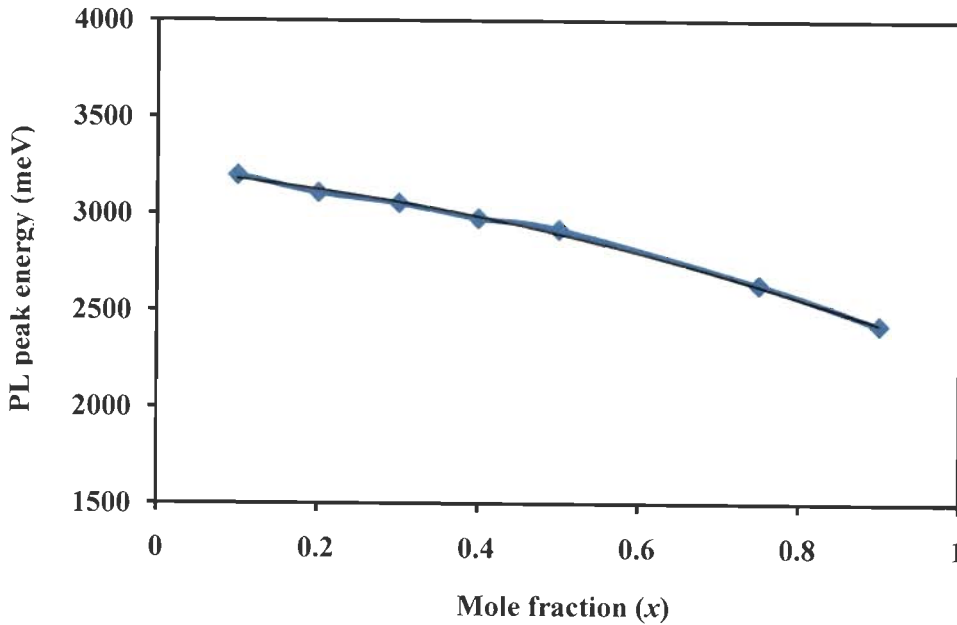


Figure 5.26: PL NBE peak energy positions of Zn_{1-x}Cd_xS films

Shinoya and Yin, have suggested that energy band gap can also be obtained with the help of PL measurements [177]. Energy band gap is obtained when PL excitonic transition energies are added to the binding energies (equation 5.5).

$$E_g = E_{peak} + E_{BE} \quad (5.5)$$

Vegard's law can be applied to obtain binding energies of Zn_{1-x}Cd_xS ternary semiconductor. Ueda *et al.* reported the binding energy (E_{BE}) of 35 and 28 meV for ZnS and CdS binaries respectively [193]. Binding energies in meV calculated via Vegard's law with mole fraction are shown in Table 5.4. Adding binding energies to equation (5.4) in accordance with equation (5.5), band gap energies with mole fraction are obtained. Figure 5.27 shows the energy band gap values with mole fraction obtained via PL measurements.

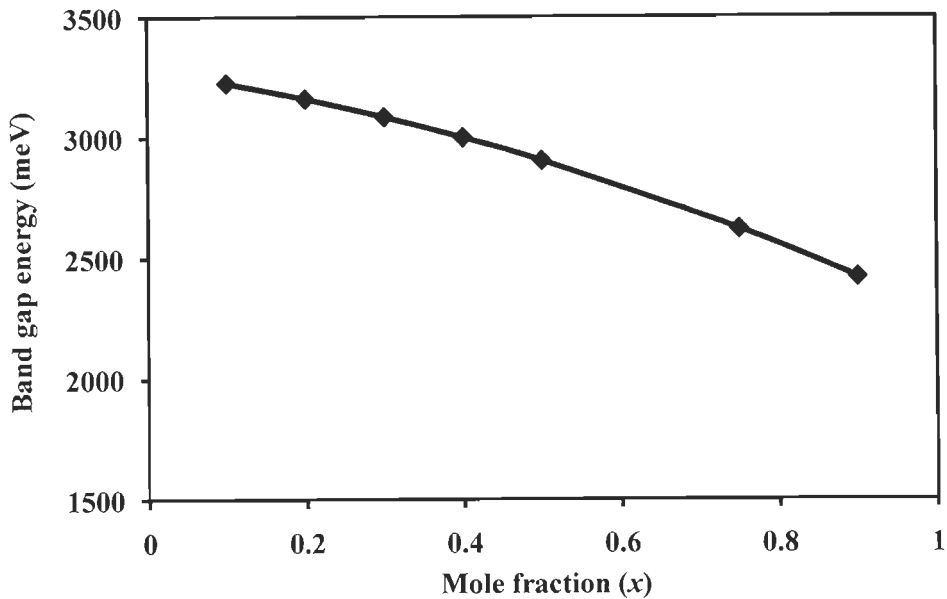


Figure 5.27: Plot of energy band gaps of Zn_{1-x}Cd_xS films obtained via PL measurements

Figure 5.28 shows $\pm 5\%$ error plot between energy band gaps obtained via absorption and PL measurements. It can be seen that the difference between these two lies within $\pm 5\%$ error lines. However, there are few data points where the difference exceeds this error limit. This can be attributed to the bowing, which seems to affect the band gap energies in the middle of composition range. Nevertheless, these results provide the validity of data which have been analyzed from two different characterization techniques.

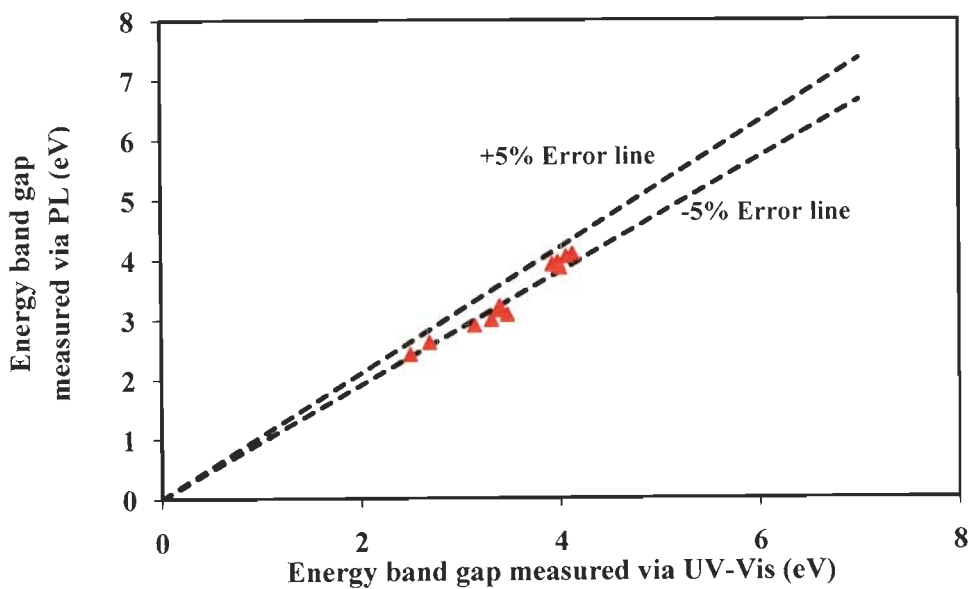


Figure 5.28: Error plot between band gap energies of Zn_{1-x}Cd_xS films obtained via absorption and PL measurement

5.8 SUMMARY

This chapter provides a process window for nanocrystalline Zn_{1-x}Cd_xS thin films. *In-house* nanoparticles were used as the target material for the film deposition and were given an optimal pressure of 18 ton to fabricate the target. The crystallinity, and the surface roughness of Zn_{1-x}Cd_xS thin films were found to depend on the laser flux density. The optimal incident energy in this work was determined as 3.33 J/cm². A control on the particle size of the nanocrystalline films was obtained by varying the working pressure. Particle size increases ~ 4.5 times of its original value (15 nm) when working pressure increases from 1.5x 10⁻² to 200 mtorr. A structural phase transformation from zincblende to wurtzite is observed in Zn_{1-x}Cd_xS nanocrystalline thin films. It is established that the transformation temperature decreases with increase in mole fraction. Thus deposition temperature along with the mole fraction provides the control on the lattice structure. Compositional homogeneity of the as-deposited films was checked by Vegard's law. The close agreement between the obtained and the computed lattice constants (within ± 5 %) confirmed the stoichiometric deposition. Light emission data is being validated via PL and absorbance measurement. The above finding provides well regulated/controlled properties of the as-deposited Zn_{1-x}Cd_xS nanocrystalline thin films.

CHAPTER 6

Zn_{1-x}Cd_xS:Mn NANOSTRUCTURES FOR LIGHT EMISSION

6.1 GENERAL

In previous chapters, the main efforts have been focused on the preparation of Zn_{1-x}Cd_xS nanostructures by varying their constituent composition. The emitted radiations from these nanostructures are obtained in the visible and UV region. The visible (blue and green) emission was obtained due to defects/vacancies related traps while the UV emission originates from near band edge transition. It is discussed earlier in section 1.3, chapter 1, that selective light emission, independent of defect states, can be obtained by the incorporation of luminescence activator such as manganese in the suitable host.

The issues such as dopant incorporation and homogeneity have been identified as the major obstacles for the advancement in the field of selective light emission. Dalpian and Chelikowsky suggested that the doped Mn²⁺ ion in nanostructures such as CdSe is invariably an energetically unfavorable state, preferring to be ejected to the surface of nanostructures [47]. It was also suggested that the rejection of Mn²⁺ from the semiconducting host is facilitated by an increase in the temperature. Levy *et al.* described the process of dopants self annealing, which results into the out diffusion of impurities due to higher reaction temperature [100]. Nag *et al.* established that an increase in reaction temperature anneals out the Mn²⁺ dopants due to self-annealing [130].

From the above discussion it can be suggested that (i) it is difficult to dope Mn²⁺ in II-VI semiconductors (ii) a relatively higher doping may be achieved with a lower reaction temperature [129].

In the present study, an approach has been devised to increase the dopant (Mn²⁺) incorporation in the host (Zn_{1-x}Cd_xS), leading to Zn_{1-x}Cd_xS:Mn nanostructured system. It is suggested that difficulty in dopant incorporation arises from the difference in the lattice constants of the host and the dopant. Nag *et al.* reported that mismatch between the substituent dopant and the substituted cation, would cause a significant amount of strain in the nanoparticle lattice. The strain fields generated in the lattice are necessarily long range, much longer than typical nanoparticle dimensions; it tends to relieve itself by ejecting the dopant to the surface of nanoparticles [129].

Since lattice constant of MnS lie in between CdS and ZnS (Table 2.1, chapter 2) [48], tuning the average lattice constant of the host Zn_{1-x}Cd_xS nanostructures, with different values of “x” provides motivating way to enhance the dopant incorporation.

In addition to the above discussed approach, an attempt has also been made to increase the luminescence intensity via two different approaches. In one the dopant concentration is varied by variation in manganese precursor concentration. The other is related with the change in the design of nanostructures via preparation of core-shell/nanocomposite structures. Core-shell/nanocomposite structures effectively passivate the surface states and leads to the enhanced light emission.

6.2 CHAPTER PREFACE

Section 6.3 presents the synthesis conditions for the preparation of Mn²⁺ doped Zn_{1-x}Cd_xS nanoparticles. Section 6.4 presents the variation in mole fraction for the minimization of lattice constant mismatch between the host and the dopant. Section 6.4 also presents the manganese concentration variation at the optimized host conditions. The objective of these experiments is to enhance the light emission. Section 6.5 discussed the substitution of Mn²⁺ ion into Zn_{1-x}Cd_xS nanoparticles with the aid of SQUID magnetometer. This section is followed by the preparation of Zn_{1-x}Cd_xS:Mn/ZnS core-shell nanoparticles and the relevant study is presented in section 6.6.

Section 6.7 presents the preparation of Mn²⁺ doped Zn_{1-x}Cd_xS nanocrystalline thin films. Light emission from Zn_{1-x}Cd_xS:Mn/ZnS nano-composites is discussed in section 6.8.

6.3 SYNTHESIS DETAILS

Manganese doped Zn_{1-x}Cd_xS nanoparticles were synthesized in the laboratory at 280 K using co-precipitation technique.

6.3.1 Chemicals

Zinc nitrate hexahydrate [(Zn(NO₃)₂·6H₂O)] (99.999%), cadmium nitrate tetrahydrate [(Cd(NO₃)₂·4H₂O)] (99.0%) and manganese nitrate hydrate [(Zn(NO₃)₂·xH₂O)] (99.99%) were used as zinc, cadmium, and manganese source respectively along with sodium sulphide nonahydrate [(Na₂S·9H₂O)] (99.99%) as sulfur source. Chemicals were procured from Sigma-Aldrich. All chemicals were used without further purification.

6.3.2 Synthesis Procedure

Synthesis procedure is similar to as outlined in chapter 4, section 4.2.2. The only change is the addition of manganese precursor to the mixture of zinc and cadmium precursor as the agent of manganese dopant.

In a typical synthesis, zinc, cadmium and manganese precursor aqueous solutions were thoroughly mixed and kept at 280 K using thermostat. The Na₂S solution was then added to the mixture with a dripping speed of 10 drops/minute. Uniform magnetic stirring is provided for the better atomic diffusion during the length of the reaction. The resulting nanoparticles were washed with methanol and further isolated by centrifugation and decantation. The precipitates were dried in hot air oven at 323 K. Final products were obtained by crushing dried precipitate using pestle mortar.

6.3.3 Synthesis Conditions

In one set of experiment manganese doped Zn_{1-x}Cd_xS nanoparticles were prepared with variation in mole fraction. In other set of experiment, mole fraction, *x* is kept constant at 0.45 and manganese concentration varies from 1 to 10 mol% with respect to zinc precursor concentration. Standard synthesis conditions of Mn²⁺ doped Zn_{1-x}Cd_xS nanoparticles are shown in Table 6.1.

Table 6.1: Standard synthesis conditions of Mn²⁺ doped Zn_{1-x}Cd_xS nanoparticles. It also contains the synthesis parameters for core-shell nanoparticles

| Mn ²⁺ doped Zn _{1-x} Cd _x S nanoparticles | | | | | | | Shell formation | | |
|--|-------------------|--------------------------|------------------------------|-----------------------------|-------------------------------|--------------------------|--------------------------|-----------------------------|---------------------------|
| Sample | Mole fraction (x) | Synthesis precursors | | | | Reaction temperature (K) | Precursor volume (ml) | | Shell to core ratio (s/c) |
| | | Molarity (M) | | | | | Zinc nitrate hexahydrate | Sodium sulphide nonahydrate | |
| | | Zinc nitrate hexahydrate | Cadmium nitrate tetrahydrate | Sodium sulphide nonahydrate | Manganese nitrate hexahydrate | | | | |
| MNP-1 | --- | 0.5 | --- | 0.5 | 0.005 | 280 | --- | --- | --- |
| MNP-2 | 0.1 | 0.5 | 0.050 | 0.5 | 0.005 | 280 | --- | --- | --- |
| MNP-3 | 0.25 | 0.5 | 0.125 | 0.5 | 0.005 | 280 | --- | --- | --- |
| MNP-4 | 0.45 | 0.5 | 0.225 | 0.5 | 0.005 | 280 | --- | --- | --- |
| MNP-5 | 0.75 | 0.5 | 0.375 | 0.5 | 0.005 | 280 | --- | --- | --- |
| MNP-6 | 0.45 | 0.5 | 0.225 | 0.5 | --- | 280 | --- | --- | --- |
| MNP-7 | --- | 0.5 | --- | 0.5 | 0.010 | 280 | --- | --- | --- |
| MNP-8 | --- | 0.5 | --- | 0.5 | 0.015 | 280 | --- | --- | --- |
| MNP-9 | --- | 0.5 | --- | 0.5 | 0.025 | 280 | --- | --- | --- |
| MNP-10 | --- | 0.5 | --- | 0.5 | 0.050 | 280 | --- | --- | --- |
| MNP-11 | 0.1 | 0.5 | 0.050 | 0.5 | 0.010 | 280 | --- | --- | --- |

| | | | | | | | | | |
|--------|------|-----|-------|-----|-------|-----|-----|-----|------|
| MNP-12 | 0.1 | 0.5 | 0.050 | 0.5 | 0.015 | 280 | --- | --- | --- |
| MNP-13 | 0.1 | 0.5 | 0.050 | 0.5 | 0.025 | 280 | --- | --- | --- |
| MNP-14 | 0.1 | 0.5 | 0.050 | 0.5 | 0.050 | 280 | --- | --- | --- |
| MNP-15 | 0.25 | 0.5 | 0.125 | 0.5 | 0.010 | 280 | --- | --- | --- |
| MNP-16 | 0.25 | 0.5 | 0.125 | 0.5 | 0.015 | 280 | --- | --- | --- |
| MNP-17 | 0.25 | 0.5 | 0.125 | 0.5 | 0.025 | 280 | --- | --- | --- |
| MNP-18 | 0.25 | 0.5 | 0.125 | 0.5 | 0.050 | 280 | --- | --- | --- |
| MNP-19 | 0.45 | 0.5 | 0.225 | 0.5 | 0.010 | 280 | --- | --- | --- |
| MNP-20 | 0.45 | 0.5 | 0.225 | 0.5 | 0.015 | 280 | --- | --- | --- |
| MNP-21 | 0.45 | 0.5 | 0.225 | 0.5 | 0.025 | 280 | --- | --- | --- |
| MNP-22 | 0.45 | 0.5 | 0.225 | 0.5 | 0.050 | 280 | --- | --- | --- |
| MNP-23 | 0.75 | 0.5 | 0.375 | 0.5 | 0.010 | 280 | --- | --- | --- |
| MNP-24 | 0.75 | 0.5 | 0.375 | 0.5 | 0.015 | 280 | --- | --- | --- |
| MNP-25 | 0.75 | 0.5 | 0.375 | 0.5 | 0.025 | 280 | --- | --- | --- |
| MNP-26 | 0.75 | 0.5 | 0.375 | 0.5 | 0.050 | 280 | --- | --- | --- |
| MNP-27 | 0.45 | 0.5 | 0.225 | 0.5 | 0.025 | 280 | 5 | 5 | 0.05 |
| MNP-28 | 0.45 | 0.5 | 0.225 | 0.5 | 0.025 | 280 | 10 | 10 | 0.1 |
| MNP-29 | 0.45 | 0.5 | 0.225 | 0.5 | 0.025 | 280 | 20 | 20 | 0.2 |
| MNP-30 | 0.45 | 0.5 | 0.225 | 0.5 | 0.025 | 280 | 50 | 50 | 0.5 |
| MNP-31 | 0.45 | 0.5 | 0.225 | 0.5 | 0.025 | 280 | 100 | 100 | 1.0 |

6.4 TUNING OF HOST LATTICE FOR DOPANT INCORPORATION

Figure 6.1 shows XRD patterns of Mn²⁺ doped Zn_{1-x}Cd_xS nanoparticles namely MNP-1, MNP-2, MNP-3, MNP-4, and MNP-5 at mole fractions 0.0, 0.1, 0.25, 0.45 and 0.75 respectively. Figure 6.1 shows the zincblende crystal structure for all considered samples. The red, black and blue vertical bars in figure 6.1 shows the standard zincblende patterns for bulk CdS (JCPDS # 800019), ZnS (JCPDS # 800020) and MnS (JCPDS # 721534) respectively. It is seen from figure 6.1 that the obtained diffraction peaks do not match with any of these three diffraction patterns. It suggests the formation of Mn²⁺ doped Zn_{1-x}Cd_xS nanoparticles. It also suggests that there does not exist separate ZnS, CdS or MnS phase. Figure 6.1 shows that there is a continuous XRD peak shift to a lower angle with increased mole fractions. This systematic diffraction peak shift is in agreement with our previous results (chapter 4, section 4.3.1), proving consistency of the independent experiments.

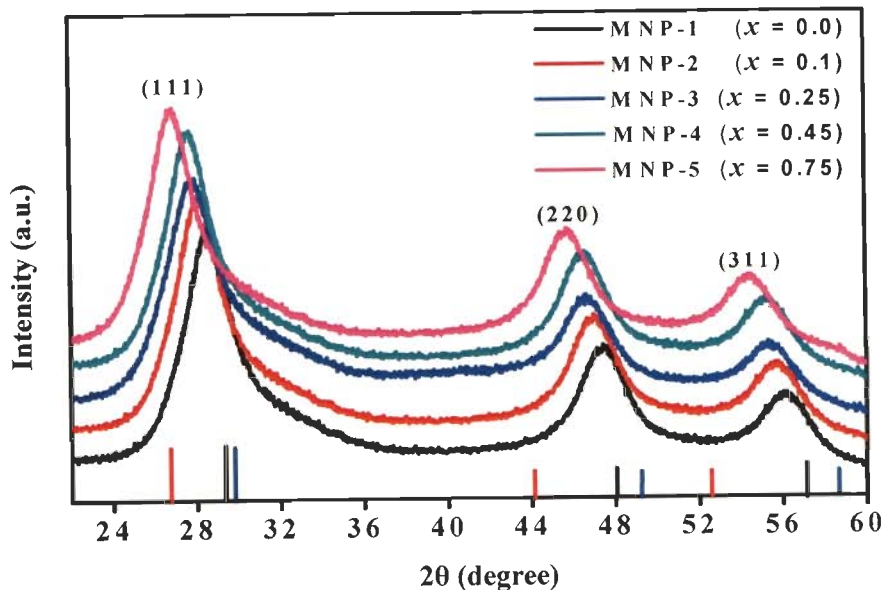


Figure 6.1: XRD patterns of Mn²⁺ (1 mol%) doped Zn_{1-x}Cd_xS nanoparticles at mole fractions, x as 0, 0.1, 0.25, 0.45, and 0.75

Vertical bars corresponds to JCPDF positions of (a) ZnS, black color bar (#800020) (b) CdS, red color bar (#800019) (c) MnS, blue color bar (#401288)

Table 6.2 presents the changing diffraction angles (2θ) with x and the corresponding d -spacing of samples.

Table 6.2: Mole fraction (x), crystal structure, and interplanar spacing of Mn²⁺ (1 mol%) doped Zn_{1-x}Cd_xS nanoparticles

| Sample | x | $2\theta^a$ ($^\circ$) | d -spacing ^a (\AA) |
|--------|------|-----------------------------|---|
| MNP-1 | 0 | 28.56 | 3.126 |
| MNP-2 | 0.1 | 28.28 | 3.181 |
| MNP-3 | 0.25 | 27.90 | 3.194 |
| MNP-4 | 0.45 | 27.74 | 3.212 |
| MNP-5 | 0.75 | 26.90 | 3.311 |

^a(111) orientation,

Figure 6.2 shows the PL emission spectra of samples MNP-1, MNP-2, MNP-3, MNP-4, and MNP-5 at mole fractions 0.0, 0.1, 0.25, 0.45 and 0.75 respectively. It shows the PL emission band at ~ 480 nm giving rise to blue emission. The blue emission can be attributed to a self-activated centre presumably formed between a zinc vacancy and a shallow donor associated with a sulfur vacancy [166]. Figure 6.2 also shows the characteristic orange emission of manganese at ~ 585 nm. This orange emission is due to the transition of carriers from manganese incurred excited states (4T_1) to the ground state (6A_1), i.e. $^4T_1 \rightarrow ^6A_1$ transition [17]. It is important to note that PL emission spectra do not show the green emission band, which was earlier present in undoped Zn_{1-x}Cd_xS nanoparticles. The green emission is the defect assisted emission and was attributed to the transition from the donor level associated with sulfur vacancies and acceptor level associated with cadmium vacancies. Absence of green emission in Mn²⁺ doped Zn_{1-x}Cd_xS nanoparticles suggests an efficient transfer of carriers from donor level to the Mn²⁺ incurred excited level.

Figure 6.2 shows that the intensity of orange emission, first increases with increase in mole fraction (figure 6.2) and it attains the maximum intensity of $\sim 1.1 \times 10^5$ at $x = 0.45$. Thereafter emission intensity decreases with increase in mole fraction. Figure 6.3 shows the plot of maximum PL intensity for the characteristic emission at ~ 585 nm with increasing mole fraction. It clearly shows that the orange emission intensity is highest at $x = 0.45$.

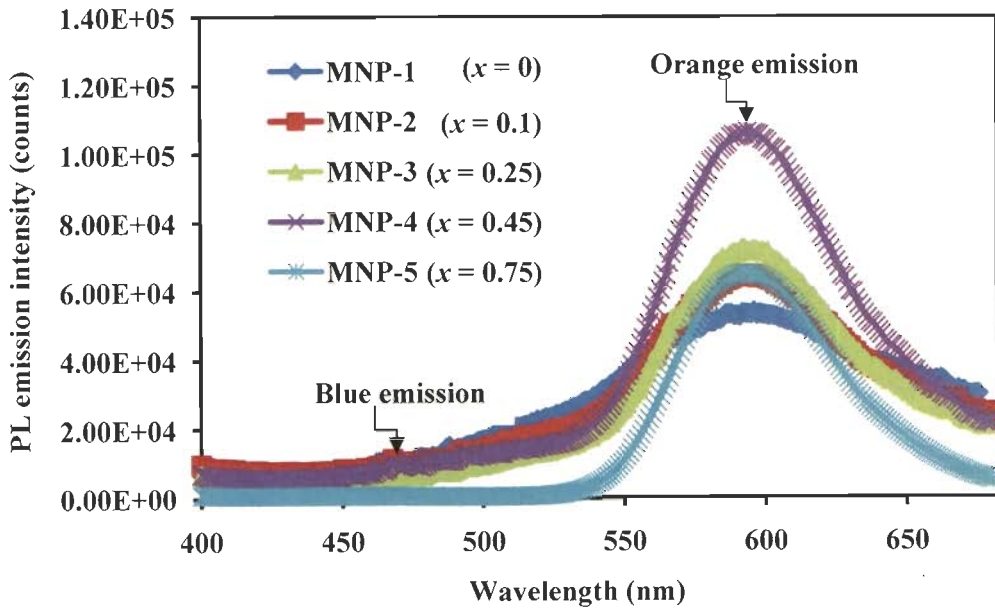


Figure 6.2: PL emission spectra of Mn^{2+} (1 mol%) doped $Zn_{1-x}Cd_xS$ nanoparticles at mole fractions, x as 0, 0.1, 0.25, 0.45, and 0.75

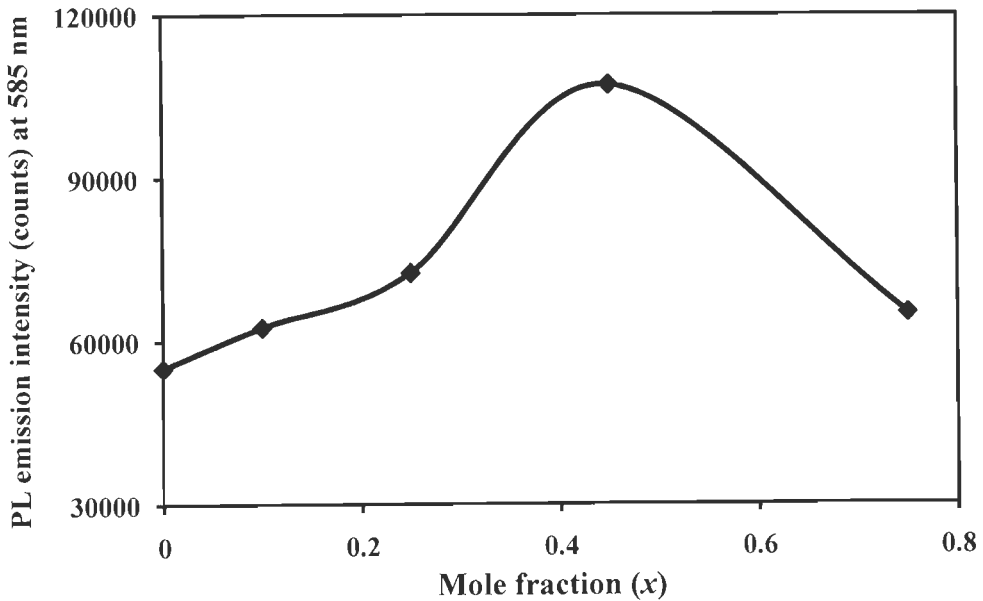


Figure 6.3: Plot of maximum PL intensity at ~ 585 nm of Mn^{2+} (1 mol%) doped $Zn_{1-x}Cd_xS$ nanoparticles with mole fraction

The reason for the difference in characteristic emission intensity with mole fraction is attributed to the difference in the lattice constants of MnS and $Zn_{1-x}Cd_xS$. Table 6.3 shows the lattice constant values accepted in this work from either by the literature or have been calculated by Vegard's law.

Table 6.3: Lattice constant from references and those obtained from XRD patterns for (111) orientation in zincblende structure

| Compound | Lattice constant (Å) | References | Lattice constant (Å) |
|---|----------------------|--|---|
| MnS | 5.559 | [48] | |
| Zn _{1-x} Cd _x S (calculated via Vegard's law) (Table A1.3, appendix A1) | | [178] $a_{ZnS}^0 = 5.345 \text{ Å}$ (PDF# 800020) $a_{CdS}^0 = 5.820 \text{ Å}$ (PDF # 010647) $a_{A_{1-x}B_xC}(x) = (1-x)a_{AC}^0 + xa_{BC}^0$ | Zn _{1-x} Cd _x S (obtained from XRD pattern) (equation (3.5), chapter 3) |
| $x = 0.10$ | 5.392 | | 5.509 |
| $x = 0.25$ | 5.463 | | 5.532 |
| $x = 0.45$ | 5.559 | | 5.565 |
| $x = 0.75$ | 5.701 | | 5.745 |

Figure 6.4 shows $\pm 5\%$ error plot between computed (via Vegard's law) and observed (via XRD) lattice constant for Mn²⁺ doped Zn_{1-x}Cd_xS nanoparticles. It can be clearly seen from figure 6.4 that the difference between these two lies within $\pm 5\%$ error. This study provides the confidence that the lattice constants obtained in this work can further be used for the determination of percentage lattice mismatch between the host and the dopant.

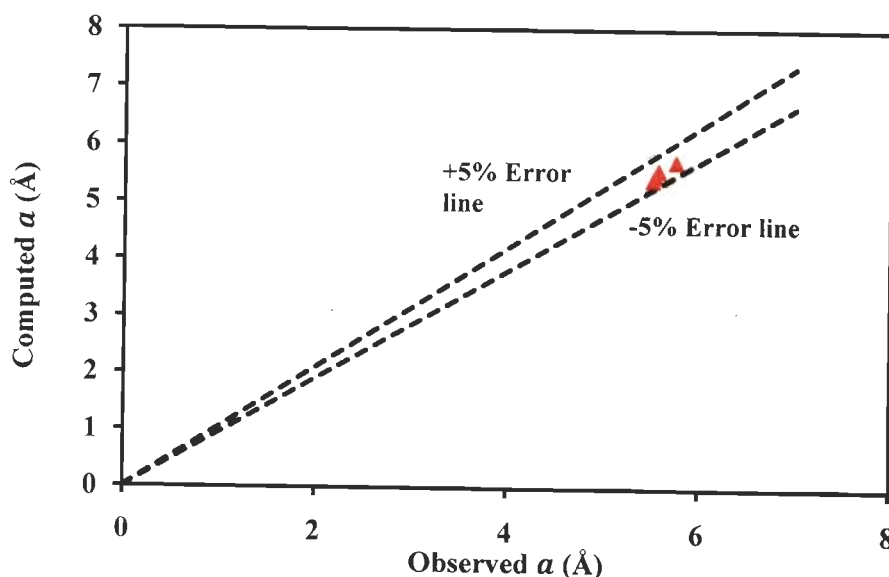


Figure 6.4: $\pm 5\%$ error plot between computed and observed lattice constants

The percentage difference in lattice constants of MnS and Zn_{1-x}Cd_xS with lattice constant x is calculated from the corresponding d_{111} interplanar spacing (equation (3.5), chapter 3) and is given as follows:

$$\% \text{ difference in lattice constant} = (a^{\text{host}} - a^{\text{MnS}}) / a^{\text{host}} * 100 \quad (6.1)$$

Figure 6.5 shows the percentage difference of the lattice constants of MnS and the host Zn_{1-x}Cd_xS with mole fraction as 0.1, 0.25, 0.45, and 0.75 respectively. The lattice mismatch is minimal $\sim 0.1\%$ at mole fraction of $x = 0.45$. With change in mole fraction from $x = 0.45$, PL emission intensity decreases systematically with increasing compressive as well as tensile mismatches. The evident maximum of orange emission peak at $x = 0.45$ in figure 6.3 can therefore be attributed to minimal lattice mismatch between Zn_{1-x}Cd_xS with MnS.

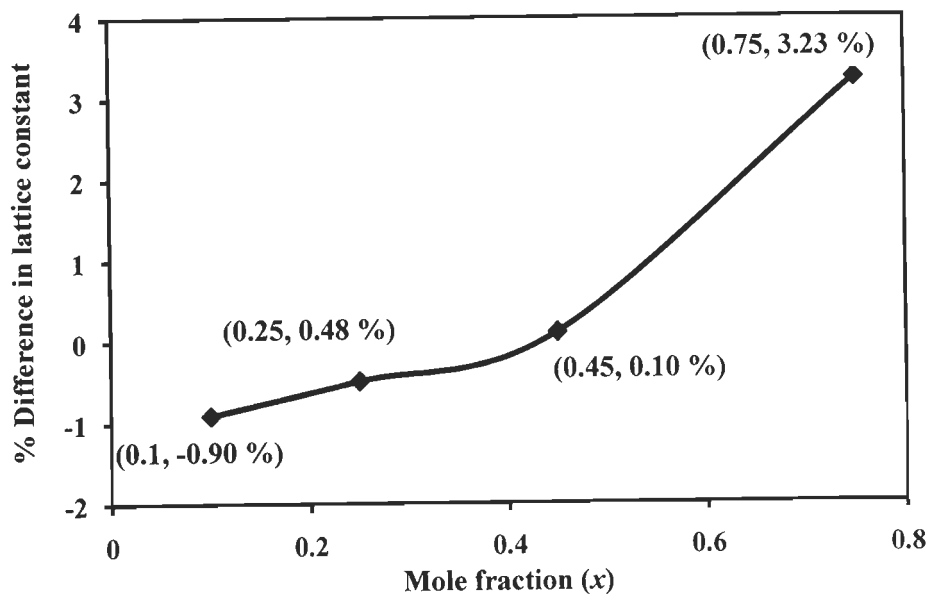


Figure 6.5: The plot of % difference of lattice mismatch of MnS and Zn_{1-x}Cd_xS with mole fraction

In order to probe the ability to dope such nanoparticles at low temperature further experiments were carried out. Mn²⁺ precursor concentrations were varied in the reaction mixture for every composition (x) of the Zn_{1-x}Cd_xS nanoparticles. Figure 6.6 shows the XRD patterns of the Mn²⁺ doped and undoped Zn_{1-x}Cd_xS nanoparticles for a given “ x ” are identical. It suggests independence of the nanoparticle size and crystal structure on the manganese content. The nanoparticle size was calculated using Scherrer formula, (equation 3.4, chapter 3). The size of the Zn_{0.55}Cd_{0.45}S:Mn nanoparticles calculated via

XRD at different manganese concentrations show average size of 3.6 nm. Son *et al.* suggested that the PL properties of nanoparticles can be influenced by their size [183]. Therefore the size effect is minimized in the present study. It is also worthy to note that capping agents have not been used in this study. It also prevents the effect of capping agent on the PL emission intensity, thereby allowing the investigation of doping concentration. Figure 6.6 also shows that there is no peak shift with manganese concentration.

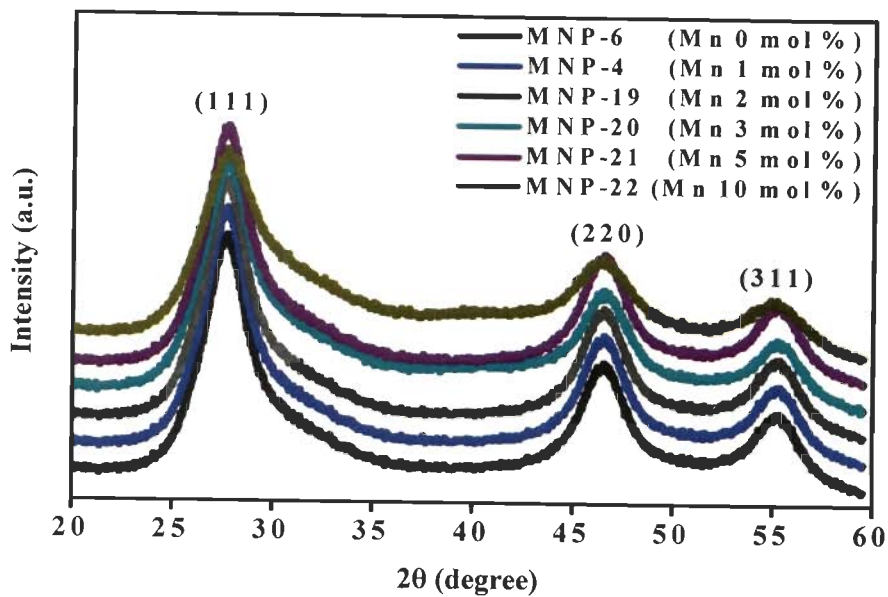


Figure 6.6: XRD patterns of Mn^{2+} doped $Zn_{0.55}Cd_{0.45}S$ nanoparticles with varying manganese concentrations of 0, 1, 2, 3, 5, and 10 mol%

Figure 6.7 shows the mole percentage of manganese obtained by EPMA in the prepared nanoparticles with respect to the manganese precursor with different values of x . These results show the increase in the incorporation of manganese in nanoparticles of all compositions with increasing manganese precursor concentrations. However, the manganese incorporation remains consistently low ($< 1.5\%$) for pure ZnS nanoparticles (attributed to highest lattice mismatch with MnS). The maximum manganese incorporation is obtained at $x = 0.45$ for all precursor concentrations. It is due to the minimal lattice mismatch between the dopant and the host. These results establish a pronounced dependence of the extent of manganese doping on the nanoparticle composition, x .

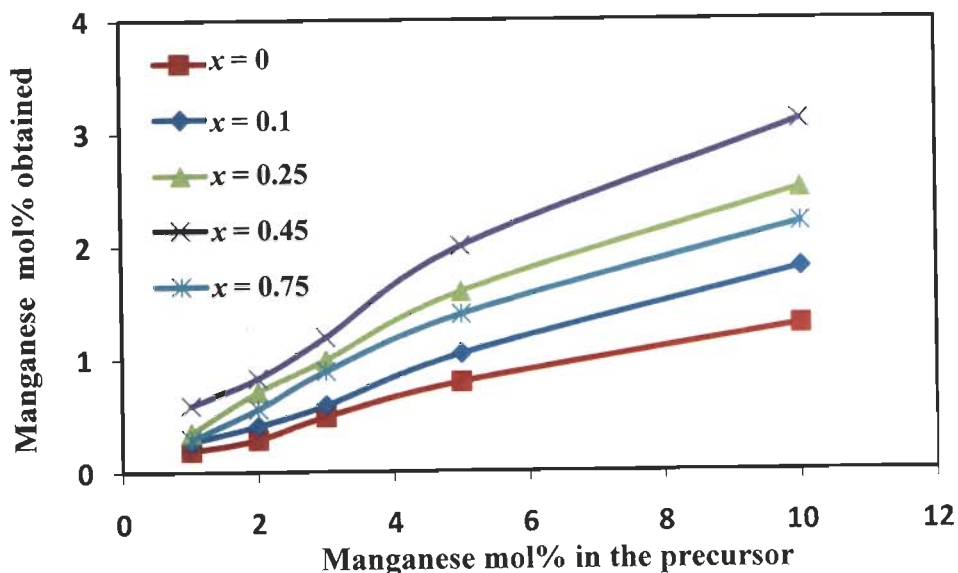


Figure 6.7: Manganese mol% in synthesized MNPs with manganese precursor

Figure 6.8 shows the photo luminescence excitation (PLE) spectrum of Mn²⁺ doped Zn_{0.55}Cd_{0.45}S nanoparticles measured at room temperature. Manganese concentration was kept constant at 5 mol%. PLE spectrum was obtained by monitoring the characteristic orange emission of Mn²⁺ at 585 nm, while keeping the excitation wavelength fixed at 350 nm. The maximum of excitation peak by Mn²⁺ emission is centered at 350 nm, which can be attributed to the excitation from host. In addition to the host excitation, several other peaks labeled as (1) to (6) are also obtained in the excitation spectrum. Similar results were obtained theoretically and experimentally by Tanabe and Sugano [177] and by Peng *et al.* [146]. According to the results in these literatures, these absorption peaks in the PLE spectra can be attributed to the intra-configurational transitions of the 3d⁵ multiplet states of Mn²⁺. The obtained peaks in figure 6.8 can therefore be attributed to the transitions of ⁶A₁(6S)–⁴T₁(4G), ⁶A₁(6S)–⁴T₂(4G), ⁶A₁(6S)–⁴A₁(4G), ⁴E(4G), ⁶A₁(6S)–⁴T₂(4D), and ⁶A₁(6S)–⁴E(4D) in the order of increasing energy. With variation in doping concentrations, excitation peak positions remain almost unchanged. It also shows that the doping concentration does not influence the multiplet energies of Mn²⁺.

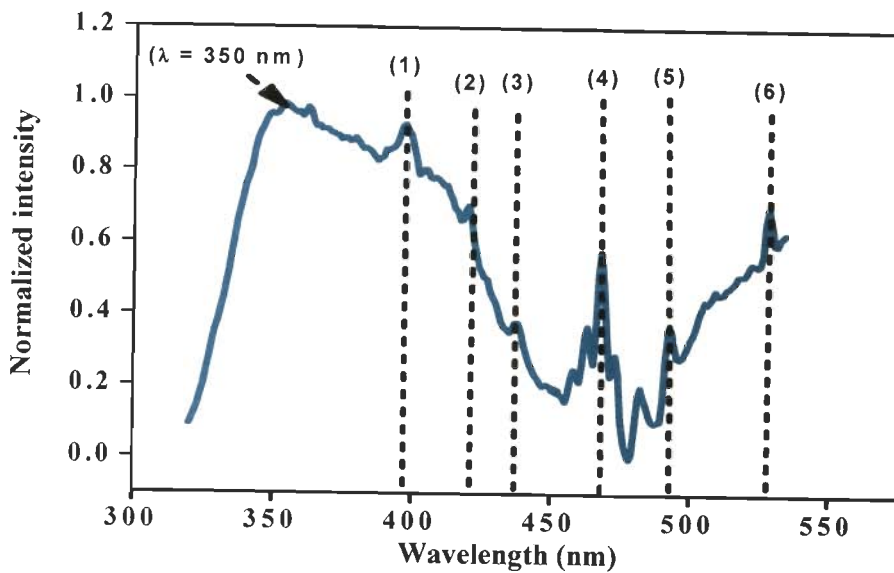


Figure 6.8: PLE spectrum of Mn^{2+} (5 mol%) doped $Zn_{0.55}Cd_{0.45}S$ nanoparticles

Figure 6.9 shows the PL emission spectra of samples MNP-4, MNP-19, MNP-20, MNP-21, and MNP-22 corresponding to manganese concentrations of 1, 2, 3, 5, and 10 mol% respectively. Figure 6.9 shows both the characteristic (orange) and defect related (blue) emissions. It is also seen from figure 6.9, that a very weak blue emission is obtained. Figure 6.9 shows that the orange emission intensity varies with variation in manganese concentration. It increases first when manganese concentrations are increased from 1 to 5 mol% and thereafter it decrease at manganese 10 mol%. It is also observed that with variation in Mn^{2+} concentration, the peak position of the Mn^{2+} related characteristic emission (~ 585 nm) remains unchanged.

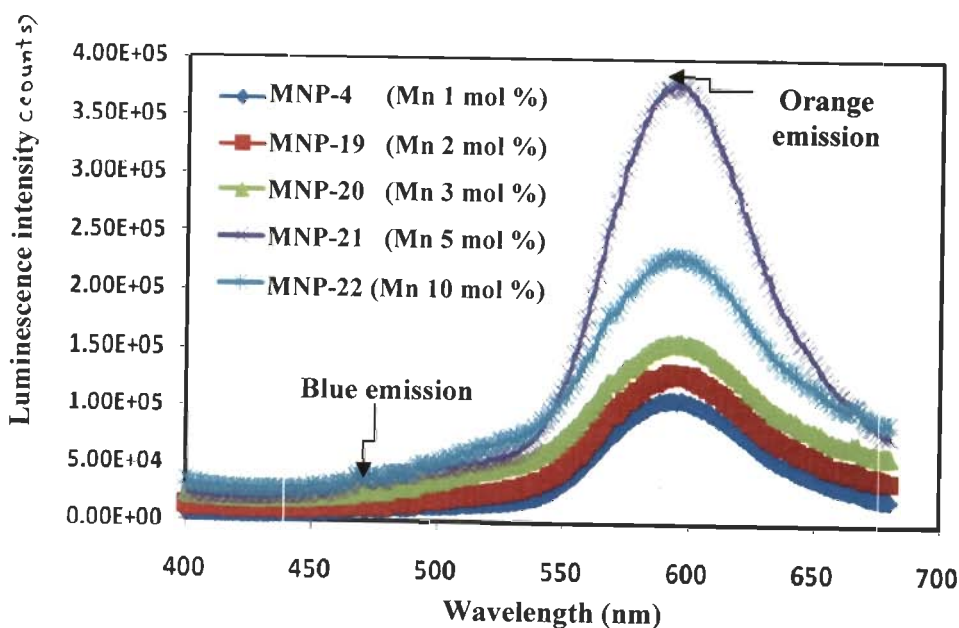


Figure 6.9: PL emission spectra of Mn^{2+} doped $Zn_{0.55}Cd_{0.45}S$ nanoparticles at Mn^{2+} concentrations of 1, 2, 3, 5, and 10 mol%

Figure 6.10(a) shows the orange emission intensity with variation in manganese concentration at $x = 0.45$. The emission intensity $\sim 1.0 \times 10^5$ is obtained at 1 mol%. The maximum emission intensity of $\sim 3.7 \times 10^5$ is obtained at 5 mol% manganese concentration. The orange emission intensity increases by a factor of ~ 3.7 with increase in manganese precursor concentration from 1 to 5 mol%. The behavior of the emission intensity with the manganese concentration shows an interesting feature. It increases first with increasing manganese content, reaches a maximum, then decreases. A possibility proposed in literature is so called concentration quenching. It will be shown in section 6.5, that the Mn^{2+} is homogeneously distributed, so that concentration quenching can be excluded in this work. The decrease in emission intensity at higher manganese concentration can be explained either by a preferred adsorption of the Mn^{2+} at the particle surface or by formation of separate MnS particles at higher manganese concentrations.

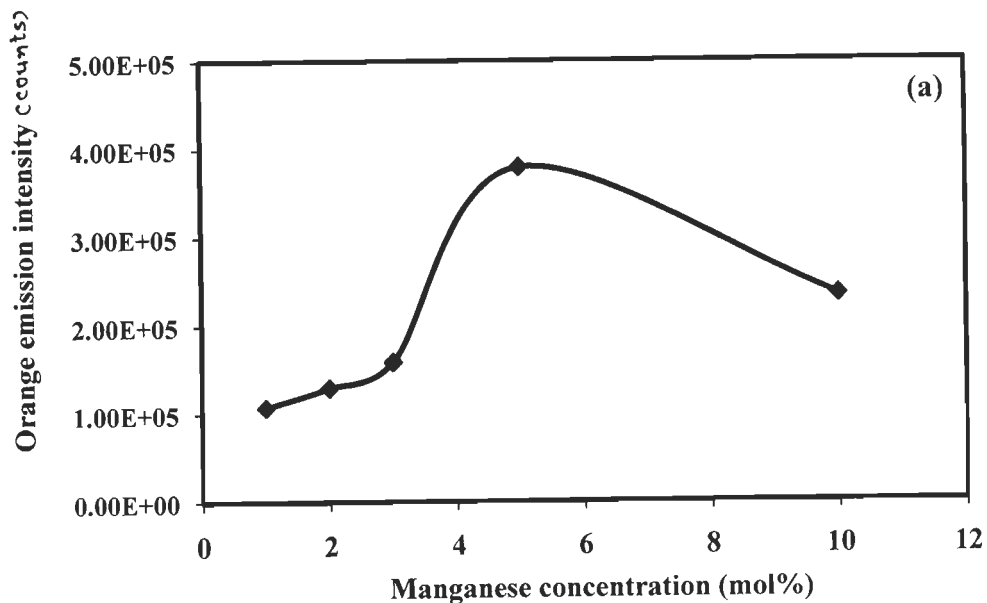


Figure 6.10: (a) Plot of orange emission intensity with manganese concentrations of 1, 2, 3, 5, and 10 mol%

Figure 6.10(b) shows the ratio of PL intensities of the orange emission of Mn^{2+} to the blue emission, ($I_{O/B}$) of the host lattice with variation in manganese concentration. Intensity ratio increases with the increase of Mn^{2+} precursor concentration (up to 5 mol%), suggesting that the intensity from the Mn^{2+} emission has a substantial enhancement due to the increase of Mn^{2+} ions as the effective luminescent centers. While it suggests that the intensity from the defect emission has slow increase. At Mn^{2+} precursor concentration of 10 mol%, intensity ratio decreases. This result strengthens our

hypothesis that there is an efficient transfer of carriers from donor defect states to the Mn²⁺ incurred states, which eventually leads to the reduction in the defect assisted emissions.

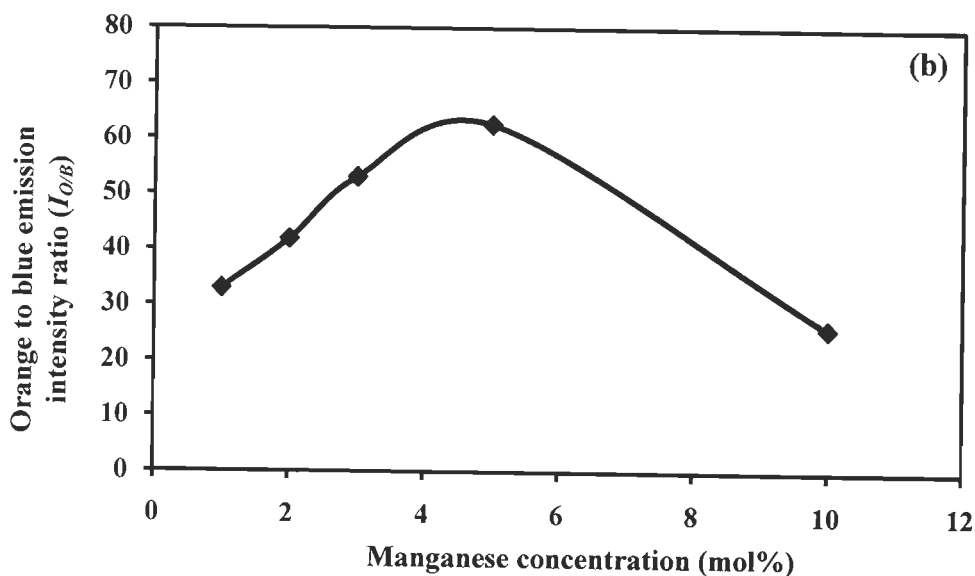


Figure 6.10: (b) Plot of $I_{O/B}$ with manganese concentrations as 1, 2, 3, 5, and 10 mol%

Emission spectrum at 5 mol% manganese doped sample in the present study is entirely dominated by the orange emission ($I_{O/B} \sim 60$). The excitation process generates an electron-hole pair across the band gap of the nanoparticle host (3.55 eV, obtained via absorbance measurement, appendix A3). The present results make it evident that there is a more efficient energy transfer of the excitation from the host to the doped manganese site compared to that of the defect states. It suggests a strong coupling between the manganese d levels and the host states. The energy transfer is also unlikely to occur directly from the semiconductor band states to the low-lying Mn d -states.

It had been theoretically calculated that the Mn²⁺ acceptor energy level in ZnS is 0.88 eV above the maximum of VB [106]. Hence the energy levels of Mn²⁺ 4T_1 and 6A_1 can be located in the energy band gap of Zn_{0.55}Cd_{0.45}S nanoparticles. A schematic energy level diagram of Mn²⁺ doped Zn_{0.55}Cd_{0.45}S nanoparticles is shown in figure 6.11. This diagram presents the various recombination routes and therefore obtained emissions in Mn²⁺ doped Zn_{0.55}Cd_{0.45}S nanoparticles.

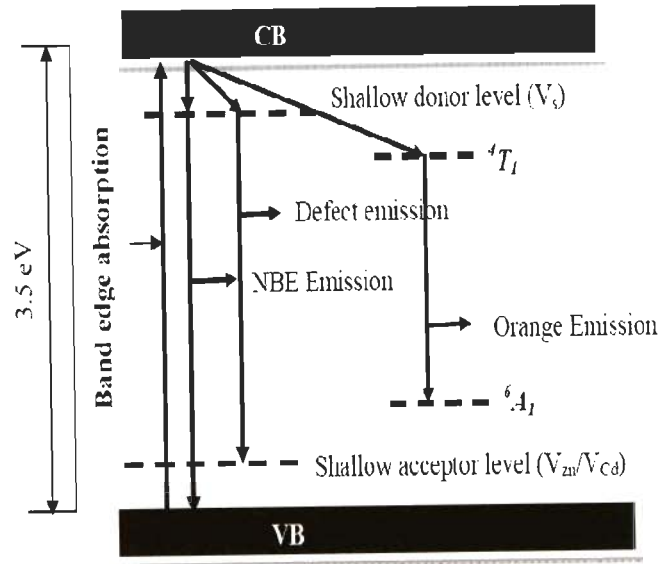


Figure 6.11: Schematic energy level diagram of transitions between host and Mn²⁺ related energy levels

6.5 Mn²⁺ HOMOGENOUS SUBSTITUTION VERIFICATION

In order to validate the argument of the homogeneity of dopant inside the nanoparticles, magnetic measurements were conducted. The magnetization properties of samples MNP-4, MNP-19, MNP-20, MNP-21 and MNP-22 corresponding to manganese concentration of 1, 2, 3, 5 and 10 mol% at $x = 0.45$ were investigated by a SQUID magnetometer. Figure 6.12(a) shows the field-dependent magnetizations of samples at manganese concentrations of 1, 2, 3, 5 and 10 mol% measured at 5 K. The curves show no hysteresis and no remanence, indicating the absence of ferromagnetism in all samples [18, 30, 44]. It can be observed from figure 6.12(a) that the magnetic moment (M) increases with increase in external field (H), typical feature of paramagnetic behavior. According to Langevin model of paramagnetism [44], it is a system where localized non-interacting electronic magnetic moments on the atomic sites are randomly oriented as a result of their thermal energy. Figure 6.12 shows that for the same magnetic field H , magnetization M increases with increases in manganese concentration. This systematic increase in magnetic moment with varying concentration showed the homogenous distribution of manganese. For the sake of comparison, field-dependent moment of undoped sample was taken at 5 K and is shown in figure 6.12(a). The pure Zn_{0.55}Cd_{0.45}S sample exhibited, as expected, a diamagnetic behavior. Field dependent magnetization (M - H) curves of sample MNP-21 (5 mol% manganese) at 5, 50, 100, and 300 K are

shown in figure 6.12(b). There is a systematic decrease in the magnetic moment with increasing temperature. At temperatures ≥ 200 K a diamagnetic behavior is observed.

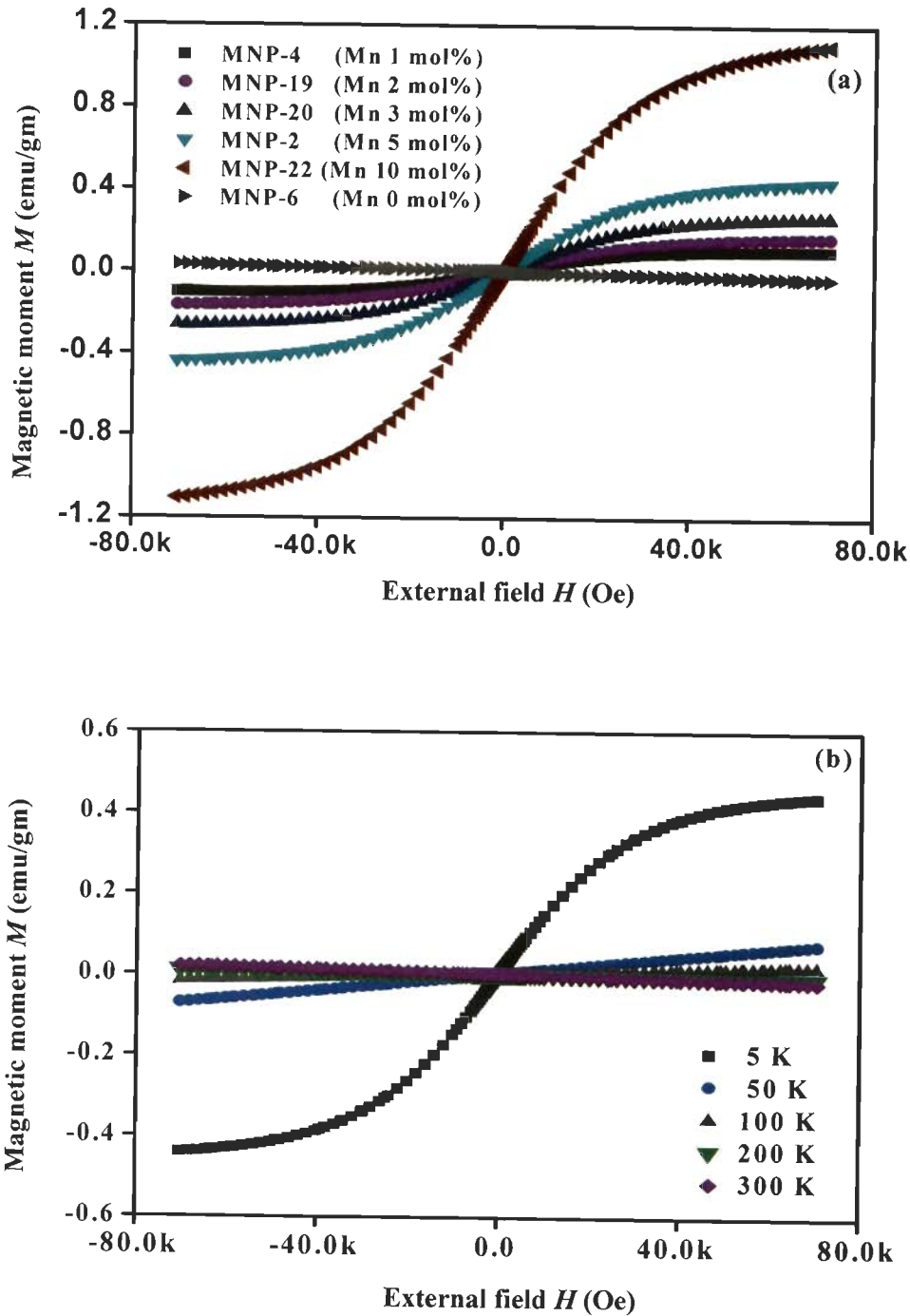


Figure 6.12: Magnetic moment with applied magnetic field of Mn²⁺ doped Zn_{0.55}Cd_{0.45}S nanoparticles (a) At 5 K with Mn²⁺ concentrations as 0, 1, 2, 3, 5, and 10 mol% and (b) At 5, 50, 100, 200, and 300 K of Mn²⁺ (5 mol%, sample MNP-21)

6.6 CORE-SHELL NANOPARTICLES

The high surface-to-volume ratio of nanoparticles suggests that the surface properties are of great importance when studying relevant optical properties such as emission. Since a large portion of the atoms are located on or near the surface of the nanoparticles, the surface properties have significant effects on their optical properties. The surface states are likely to trap electrons and/or holes and induce the non-radiative recombination of these charge carriers. These non-radiative recombinations are undesirable as they evolve heat which in turn reduces the emission output. It is due to these reasons that, the surface modification of semiconductor nanoparticles is an important issue.

In an early study of electroluminescence from CdSe nanoparticle/polymer composites, Dabbousi *et al.* found the I - V characteristics of a tunnel junction which they attributed to band offsets at the nanoparticle/polymer interface [45, 46]. Instead the insulating layer formed at junction might be due to the trioctylphosphine oxide (TOPO) passivation layer. Kos *et al.* pointed that by using chemically grown nanoparticles in electroluminescent applications, the carrier injection is inhibited by the organic surfactants bound to the surface [92]. Brovelli *et al.* also suggested that the passivation layer and the conductive organic polymers used for carrier injection, limit the carrier mobility and results in poorer device performance [22]. Other investigations of nanoparticle/semiconductor polymer light emitting devices (LEDs) did not consider the effect of the passivation layers on carrier transport [38, 40].

The performance of conducting polymer/nanoparticles composite LEDs may be improved when these insulating capping layers are eliminated by the use of inorganic semiconductor core-shell nanoparticles produced by controlled co-precipitation technique. Semiconductor nanoparticles capped by a wider band gap semiconductor have shown to exhibit enhanced band-edge luminescence up to one order of magnitude compared to surfactant covered unshelled nanoparticles [64, 78].

In particular the present approach has been taken from the work of Jiang *et al.* where they prepared ZnS:Mn/ZnO nanoparticles via controlled co-precipitation technique [83]. In this study Zn_{0.55}Cd_{0.45}S/ZnS core-shell nanoparticles are prepared for improving the light emission from nanoparticles. The use of ZnS for shell coating has fourfold advantages:

- (i) it is of the II-VI semiconductor group,
- (ii) it is an organic compound which does not suffers from the organic material limitations,
- (iii) slight modification in the current preparation approach facilitate the use of this material with ease, and
- (iv) is of higher energy band gap than core nanoparticles and thus can effectively passivates the core structure.

6.6.1 Synthesis of Core-Shell Nanoparticles

Core formation

Zinc nitrate hexahydrate, cadmium nitrate tetrahydrate, manganese nitrate hexahydrate and sodium sulphide nonahydrate were used as starting materials. In a typical reaction, ($\text{Cd}^{2+} + \text{Zn}^{2+} + \text{Mn}^{2+}$) and S^{2-} containing aqueous solutions were prepared by dissolving their respective salt in DI water. Appropriate molar amounts of salts were taken to maintain the mole fraction x , as 0.45, so as to have minimal lattice mismatch between the host and dopant. The solution concentration of manganese in $\text{Zn}_{0.55}\text{Cd}_{0.45}\text{S}:\text{Mn}$ nanoparticles is fixed at optimized precursor concentration of 5 mol%. Resulting precipitates were filtered off and washed several times in distilled water and acetone. The precipitates were dried in hot air oven at 323 K. The as prepared nanoparticles are referred to as core nanoparticles.

Shell formation

For the ZnS shell coating on core nanoparticles the precipitation reaction of zinc nitrate hexahydrate and sodium sulphide nonahydrate was employed. In a typical reaction 0.5 gm of core nanoparticles were dissolved in 200 ml distilled water and subjected to an ultrasonic bath for 1 hr. This stock solution is then mixed thoroughly with the appropriate amount of 0.5 M aqueous zinc nitrate solution (say 50 ml). The equal volume (50 ml) of sodium sulphide of 0.5 M aqueous solution was supplied at a very slow rate of ~ 2 ml/min. The resulting precipitates were dealt with as the same procedure as for core nanoparticles. A series of samples MNP-27, MNP-28, MNP-29, MNP-30 and MNP-31 were prepared with shell-to-core (s/c) ratio of 0.05, 0.1, 0.2, 0.5 and 1 respectively. Detailed synthesis conditions are presented in Table 6.1.

6.6.2 Effect of s/c Ratio on the Structural Properties of $Zn_{0.55}Cd_{0.45}S:Mn/ZnS$ Core-Shell Nanoparticles

Figure 6.13 shows the XRD patterns of core-shell nanoparticles with increasing s/c ratio. XRD pattern of core nanoparticles (sample MNP-21) is also shown in figure 6.13. The vertical bars, a and b in figure 6.13 denote the peak positions of (111) orientation of zincblende structured $Zn_{0.55}Cd_{0.45}S$ and ZnS nanoparticles respectively. The position of vertical bar b is well established and is taken from the JCPDS (PDF# 800020). The (111) diffraction peak of $Zn_{0.55}Cd_{0.45}S$ nanoparticles shifted to lower angle (from 28.6 to 27.74°) in comparison to the ZnS. Figure 6.13 shows that the sample with s/c ratio of 0.05, has dominant (111) orientation at peak position of a. In addition to the above peak, the other peak which is positioned at b emerges. With increase in s/c ratio the intensity of peak positioned at b increases while the intensity of the peak positioned at a starts to diminish. This trend followed for s/c ratio of 0.2. With increase in s/c ratio from 0.2 to 0.1, the peak positioned at b has grown as dominant (111) orientation (samples MNP-30 and MNP-31). At this s/c ratio, the peak positioned at a disappears. Thereafter no change was found in the XRD spectra. This systematic change in the XRD spectra suggests that there is a coating of shell material (ZnS) over the core nanoparticles. The variation in both: the peak position and the peak intensity with s/c ratio also suggest that shell thickness increases with increase in s/c ratio.

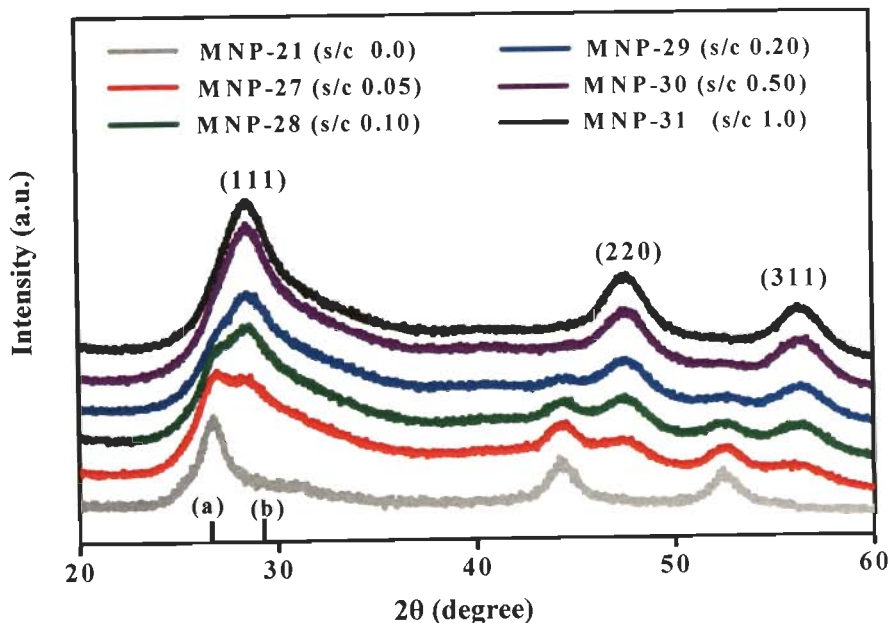


Figure 6.13: XRD patterns of $Zn_{0.55}Cd_{0.45}S:Mn$ (5 mol%)/ZnS nanoparticles at s/c ratios of 0, 0.05, 0.1, 0.2, 0.5, and 1

Figure 6.14 shows the peak intensities of XRD peak at position a and b. The histograms clearly show that there is an systematic increase in the intensity of the peak positioned at b with increase in s/c ratio. This also suggests that the shell thickness increases with s/c ratio and supports the formation of core-shell nanoparticles.

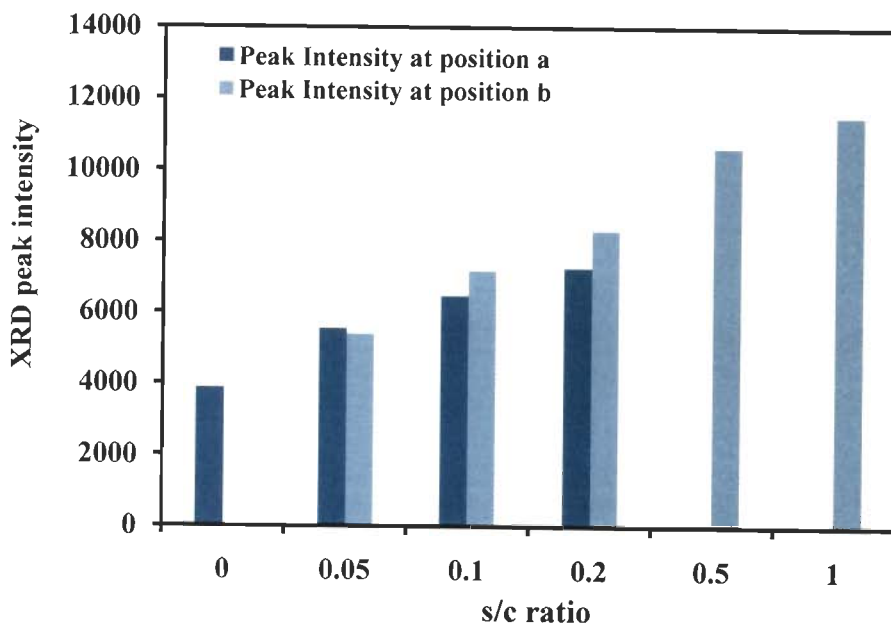


Figure 6.14: Peak intensity variation of Zn_{0.55}Cd_{0.45}S:Mn (5 mol%)/ZnS nanoparticles at s/c ratios of 0, 0.05, 0.1, 0.2, 0.5, and 1

6.6.3 Effect of s/c Ratio on Absorption Band Edge of Zn_{0.55}Cd_{0.45}S:Mn/ZnS Core-Shell Nanoparticles

Figure 6.15 shows UV-Vis absorption spectra of as-prepared Zn_{0.55}Cd_{0.45}S:Mn/ZnS core-shell nanoparticles, with s/c ratio varying from 0.05 to 1. Figure 6.15 also shows the UV-Vis spectra of core (Zn_{0.55}Cd_{0.45}S:Mn) nanoparticles. For all considered s/c ratios, the peak positions of core-shell spectra are found to be red-shifted compared to the core nanoparticles. The peak positions also red shifts with increasing s/c ratio. This red-shift of core-shell nanoparticles with respect to core nanoparticles suggests an increase in the overall nanoparticles diameter. The increased particle diameter is attributed to the growth of ZnS shell around the core nanoparticles. Similar observations of red shift during shell growth have also been reported in other core-shell systems. Cao *et al.* reported the preparation of core-shell ZnS:Mn/ZnS nanoparticles. Their group observed a red-shift in the absorption spectra of core-shell with increasing shell thickness [25].

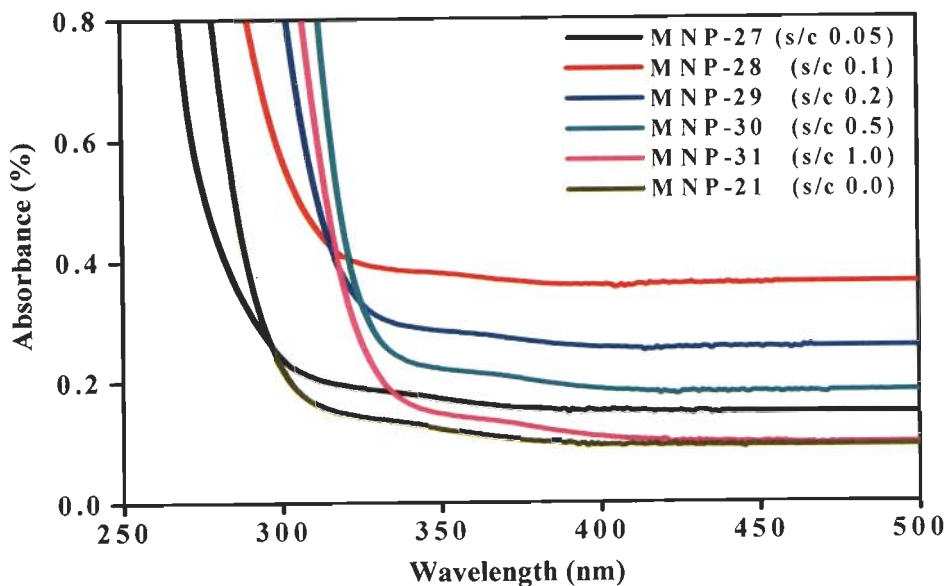


Figure 6.15: Absorption spectra of $Zn_{0.55}Cd_{0.45}S:Mn$ (5 mol%)/ZnS nanoparticles corresponding to s/c ratio of 0, 0.05, 0.1, 0.2, 0.5, and 1

Figure 6.16 shows the variation of particle size with s/c ratio varying from 0.05 to 1. The recorded absorption spectra of nanoparticles have also been used to determine the particle diameter of the core nanoparticles and core-shell nanoparticles (see appendix A3 for particle size calculation). It is seen from figure 6.16 that the particle size increases with increase in s/c ratio and is almost identical ~ 4.7 nm for s/c ratios of 0.5 and 1.

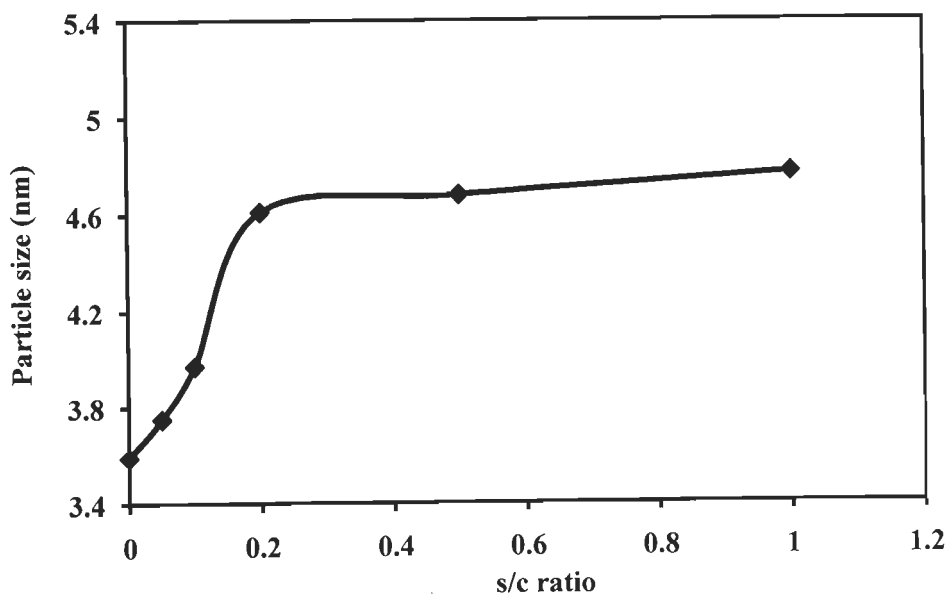


Figure 6.16: Variation in particle size of $Zn_{0.55}Cd_{0.45}S:Mn$ (5 mol%)/ZnS nanoparticles with s/c ratio

6.6.4 Shell Thickness Determination of Zn_{0.55}Cd_{0.45}S:Mn/ZnS Core-Shell Particles

The absorption spectra of nanoparticles are also used to determine the shell thickness of the core-shell nanoparticles. The shell thickness of nanoparticles can be calculated from their absorption spectrum, if it is assumed that whole nanoparticles consist of only Zn_{0.55}Cd_{0.45}S. This assumption can be taken in a view that the shell thickness is very small in comparison to the core nanoparticles diameter [33]. Using the size difference between the core and core-shell nanoparticles the thickness of ZnS shell could be estimated. Shell thickness with increasing s/c ratio is plotted in figure 6.17. Shell thickness of 0.59 nm is estimated at s/c ratio of 1. Table 6.4 presents the shell thickness with s/c ratio varying from 0.05 to 1.

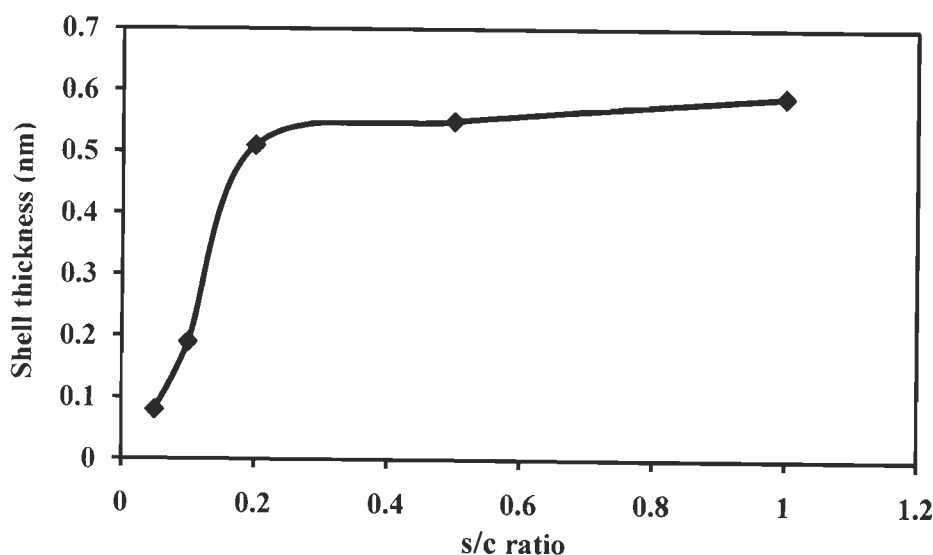


Figure 6.17: Variation in shell thickness of Zn_{0.55}Cd_{0.45}S:Mn(5 mol%)/ZnS nanoparticles with s/c ratio

Table 6.4: XRD peak positions, particle size via UV-Vis, and shell thickness of Zn_{0.55}Cd_{0.45}S:Mn/ZnS core-shell nanoparticles

| Sample | s/c ratio | 2θ (°) | Particle size d _{UV-Vis} (nm) | Shell thickness (nm) |
|--------|-----------|---|--|----------------------|
| MNP-21 | --- | 27.74 ^a | 3.59 | ---- |
| MNP-27 | 0.05 | 27.74 ^a , 28.60 ^b | 3.75 | 0.08 |
| MNP-28 | 0.1 | 27.74 ^a , 28.60 ^b | 3.97 | 0.19 |
| MNP-29 | 0.2 | 28.60 ^b | 4.61 | 0.51 |
| MNP-30 | 0.5 | 28.60 ^b | 4.68 | 0.54 |
| MNP-31 | 1.0 | 28.60 ^b | 4.77 | 0.59 |

^a vertical bar positioned at a in figure 6.13, ^b vertical bar positioned at b in figure 6.13

6.6.5 PL Enhancement in Zn_{0.55}Cd_{0.45}S:Mn/ZnS Core-Shell Nanoparticles

Fig. 6.18 shows the PL emission spectra of as-prepared Zn_{0.55}Cd_{0.45}S:Mn/ZnS core shell nanoparticles, with varying s/c ratio from 0.05 to 1. The PL emission spectra were taken at an excitation wavelength of 350 nm. It can be seen from figure 6.18 that a dramatic distinction in orange emission intensity of core-shell nanoparticles (with identical optical density) is obtained. With increase in s/c ratio the orange emission intensity increases. It reaches to a maximum of $\sim 5.6 \times 10^6$ at s/c ratio of 0.5. Further increase in s/c ratio results in the reduction in orange emission intensity. The PL emission spectra also showed an increase in defect assisted emissions at higher s/c ratios. It is previously established that at s/c ratio of 1, the ZnS shell has grown completely. It is important to note that the emissions from undoped Zn_{1-x}Cd_xS nanoparticles are either defect assisted or by the near band edge. Thus increased shell thickness i.e. increased ZnS can results in the defect emissions from ZnS. In the view of above discussion, the reduction in the emission intensity at s/c ratio of 1, can be attributed the ZnS related defect assisted emissions.

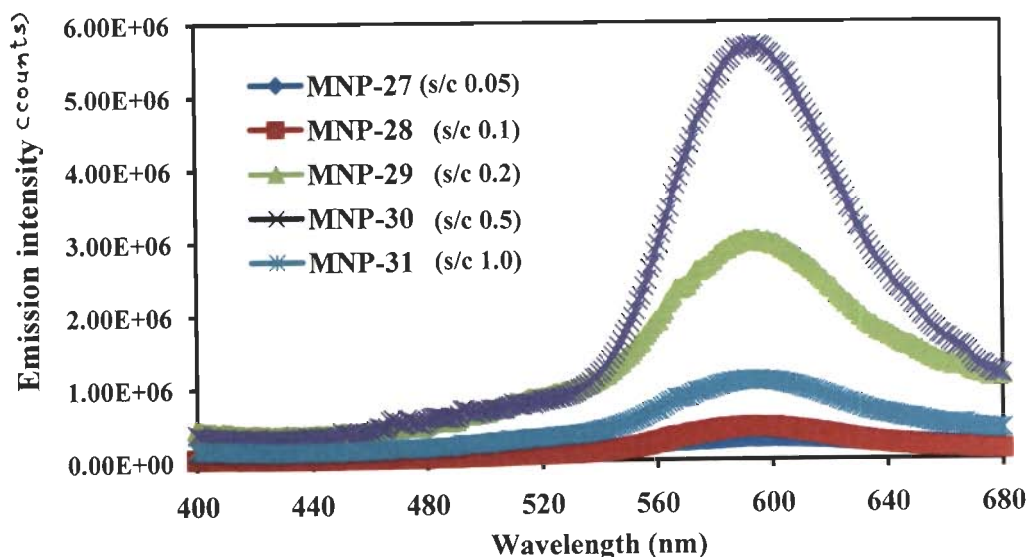


Figure 6.18: PL emission spectra of Zn_{0.55}Cd_{0.45}S:Mn (5 mol%)/ZnS nanoparticles with varying s/c ratio

Figure 6.19 shows the emission intensity ratio ($I_{s/c}$) of core-shell to core nanoparticle at ~ 585 nm. Maximum increase in PL intensity obtained in this work is ~ 15 times higher than the emission obtained from the core nanoparticles, and is obtained at s/c ratio of 0.5. Further increase in s/c ratio reduces the orange emission intensity drastically and is attributed, as discussed in previous paragraph, to the emergence of ZnS related defect emissions.

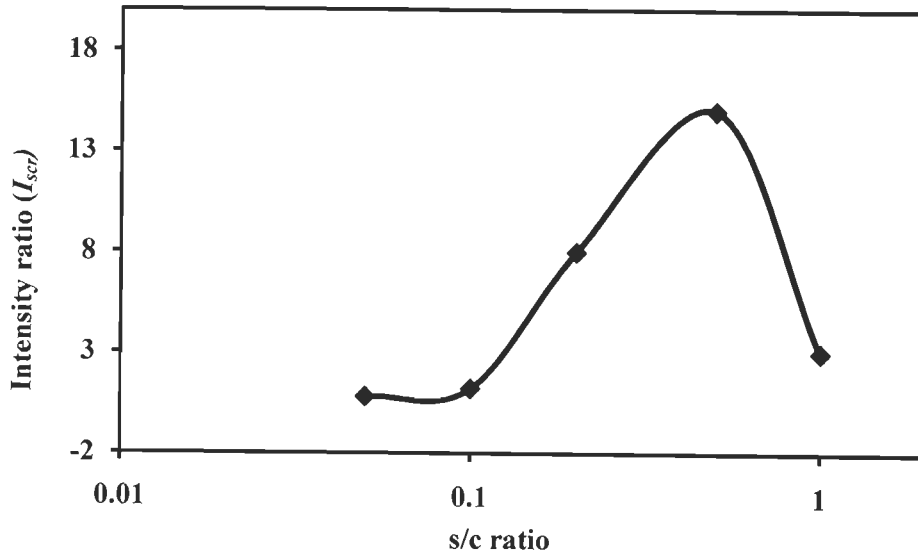


Figure 6.19: Plot of I_{scr} of Zn_{0.55}Cd_{0.45}S:Mn (5 mol%)/ZnS nanoparticles with s/c ratio

6.7 Mn²⁺ DOPED Zn_{0.55}Cd_{0.45}S NANOCRYSTALLINE THIN FILMS

The nanocrystalline thin films, due to their narrow photoluminescence (PL), are expected to provide sharpness in electroluminescence (EL) spectrum of light emitting diodes. The emission intensity strongly depends on the:

- (i) crystallinity,
- (ii) the nature of the luminescence center,
- (iii) its co-ordination in the crystal lattice and,
- (iv) dopant concentration.

Out of the above four identified issues, the nature and co-ordination of dopant has been established in the previous experiments. Therefore there is need to investigate the crystallinity and issues related with out-diffusion of impurities during deposition.

Like most of the luminescent materials ZnS:Mn shows a reduction in the photoluminescence due to concentration quenching of Mn²⁺ ions (~ 1 mol%) [170]. This concentration quenching is explained by the migration of the excitation among the centers and finally to a non-radiative or to a red or infrared emitting center. It is assumed that an excited Mn center can transfer energy to an unexcited one through a resonant non-radiative transfer process via trap in the form of red, infrared or non-radiative centers. The energy loss to a trap depends on the probability of finding a trap near the path of excitation.

In one approach, it is attempted that this energy loss can be decreased by the growth technique itself by decreasing the concentration of defects. While on the other hand, use of passivation layer is expected to decrease the defect density which in turn will reduce the energy loss.

In the view of above framework, the nanocrystalline Mn²⁺ doped Zn_{0.55}Cd_{0.45}S thin films are prepared. Higher crystallinity of the films is ensured by the optimized process parameters. The deposition parameters of Zn_{1-x}Cd_xS nanocrystalline thin films have already been optimized and related study is presented in chapter 5. Use of the previously optimized deposition parameters results in the highly crystalline Mn²⁺ doped Zn_{0.55}Cd_{0.45}S nanocrystalline thin films. Therefore the identical deposition parameters have been used in this study as well.

6.7.1 Preface

The following section presents the preparation method and emission properties of manganese doped nanocrystalline films at previously optimized deposition parameters. In this study, manganese doped Zn_{0.55}Cd_{0.45}S films were fabricated on Corning 1737 glass substrates by PLD technique. Purpose of this study is to get the crystalline films and to investigate the effect of manganese concentration on the light emission properties of the deposited films. In particular section 6.7.3 investigates the effect of manganese concentration on the structural, optical and emission properties. A series of samples with mole fraction “ $x = 0.45$ ” were prepared with manganese concentration of 1, 2, 3, 5, and 10 mol% namely MNTF-2, MNTF-3, MNTF-4, MNTF-5, and MNTF-6 respectively. Other synthesis parameters related with deposition are mentioned in Table 6.5.

Section 6.9 presents the nanocomposites of Zn_{0.55}Cd_{0.45}S:Mn/ZnS. A use of ZnS layer decreases the defect density which in turn will increase the emission intensity. In composite structure a top ZnS layer is deposited on pre-deposited Zn_{0.55}Cd_{0.45}S:Mn thin films. The film thickness is kept constant at 500 ± 20 nm by fixed number of 15,000 laser shots.

6.7.2 Synthesis Details

In the present work, Zn_{1-x}Cd_xS films with varying manganese concentration are deposited by PLD technique on Corning 1737 glass substrates by ablating stoichiometric home-made targets. Targets for laser ablation were obtained by applying uni-axial hydrostatic pressure ~ 18-20 tons (as optimized previously in section 5.2.1, chapter 5) on

manganese doped Zn_{1-x}Cd_xS particles prepared by a co-precipitation method (section 6.3). Depositions were carried out with a KrF excimer laser (Lambda Physik) operating at 248 nm in a custom designed vacuum chamber (Excel Instruments, India). Chamber was maintained at base vacuum of 5×10^{-6} torr with the aid of rotary and turbo molecular pump. The target-substrate distance was maintained at 30 mm. The target was rotated at 20 rpm to preclude pit formation on the target surface and to ensure uniform ablation of the target. Pulsed laser used for ablation was set with a pulse width of 25 ns with a repetition rate of 10 Hz. Deposition parameters were kept constant at previously optimized parameters. The laser flux density, the working pressure, and the deposition temperature were kept constant at 3.33 J/cm², 1.5×10^{-5} torr and 200 °C respectively. Standard synthesis conditions for manganese doped Zn_{1-x}Cd_xS films fabricated in this study are shown in Table 6.5.

Nanocomposites of Zn_{0.55}Cd_{0.45}S:Mn/ZnS were also prepared at identical deposition parameters. Synthesis parameters of nanocomposites are shown in Table 6.5.

Table 6.5: Synthesis conditions of Mn²⁺ doped Zn_{0.55}Cd_{0.45}S nanocrystalline thin films and their nanocomposites

| Sample | Synthesis parameters | | | | | | ZnS top layer |
|---------|-----------------------|---|-----------------------------------|-----------------------------|-------------------|----------------|-----------------------|
| | Number of laser shots | Laser flux density (J/cm ²) | Working pressure of Ar gas (torr) | Deposition temperature (°C) | Mole fraction (x) | Manganese mol% | Number of laser shots |
| MNTF-1 | 15000 | 3.33 | 1.5 x 10 ⁻⁵ | 200 | 0.45 | --- | --- |
| MNTF-2 | 15000 | 3.33 | 1.5 x 10 ⁻⁵ | 200 | 0.45 | 1 | --- |
| MNTF-3 | 15000 | 3.33 | 1.5 x 10 ⁻⁵ | 200 | 0.45 | 2 | --- |
| MNTF-4 | 15000 | 3.33 | 1.5 x 10 ⁻⁵ | 200 | 0.45 | 3 | --- |
| MNTF-5 | 15000 | 3.33 | 1.5 x 10 ⁻⁵ | 200 | 0.45 | 5 | --- |
| MNTF-6 | 15000 | 3.33 | 1.5 x 10 ⁻⁵ | 200 | 0.45 | 10 | --- |
| MNTF-7 | 12000 | 3.33 | 1.5 x 10 ⁻⁵ | 200 | 0.45 | 5 | 3000 |
| MNTF-8 | 11000 | 3.33 | 1.5 x 10 ⁻⁵ | 200 | 0.45 | 5 | 4000 |
| MNTF-9 | 10000 | 3.33 | 1.5 x 10 ⁻⁵ | 200 | 0.45 | 5 | 5000 |
| MNTF-10 | 9000 | 3.33 | 1.5 x 10 ⁻⁵ | 200 | 0.45 | 5 | 6000 |

6.7.3 Results & Discussion

Figure 6.20 shows the XRD patterns of samples MNTF-2, MNTF-3, MNTF-4, MNTF-5, and MNTF-6 corresponding to manganese concentrations of 1, 2, 3, 5, and 10 mol%. Three diffraction peaks corresponding to (111), (220), and (311) orientations of the zincblende crystalline structure with reflections positioned at $2\theta = 27.7^\circ$, 48.67° and 56.31° respectively are obtained. It is previously established (chapter 5), that at deposition temperature of 200°C and mole fractions of 0.5, results in the zincblende structure. Deposition temperature is therefore kept at 200°C , so that the lattice remains in zincblende structure and emission from the nanocrystalline thin films can be compared with manganese doped nanoparticles. Figure 6.20 shows the pulsed laser ablated films consist of narrow peak, suggesting the higher crystalline quality. Figure 6.20 also shows that there is no peak shift with increase in manganese concentration, suggesting that there is no change in the lattice constants of the films with variation in manganese concentration.

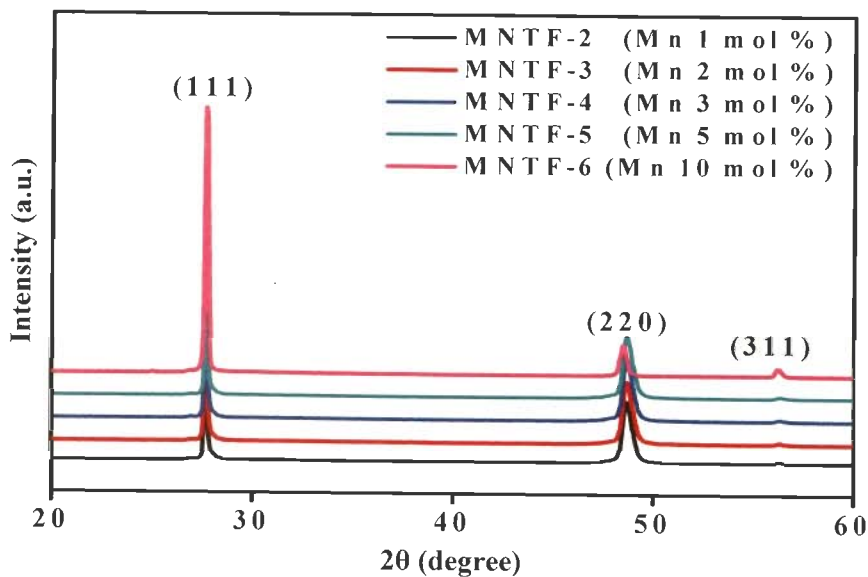


Figure 6.20: XRD patterns of Mn^{2+} doped $Zn_{0.55}Cd_{0.45}S$ films at Mn^{2+} concentrations of 1, 2, 3, 5, and 10 mol%

Figure 6.21 shows the transmittance spectra of samples MNTF-2, MNTF-3, MNTF-4, MNTF-5, and MNTF-6 deposited at manganese concentrations of 1, 2, 3, 5, and 10 mol%. Transmittance of $\sim 70\%$ in the visible region is obtained from these thin films. Thicknesses of the deposited films are found to be 500 ± 20 nm.

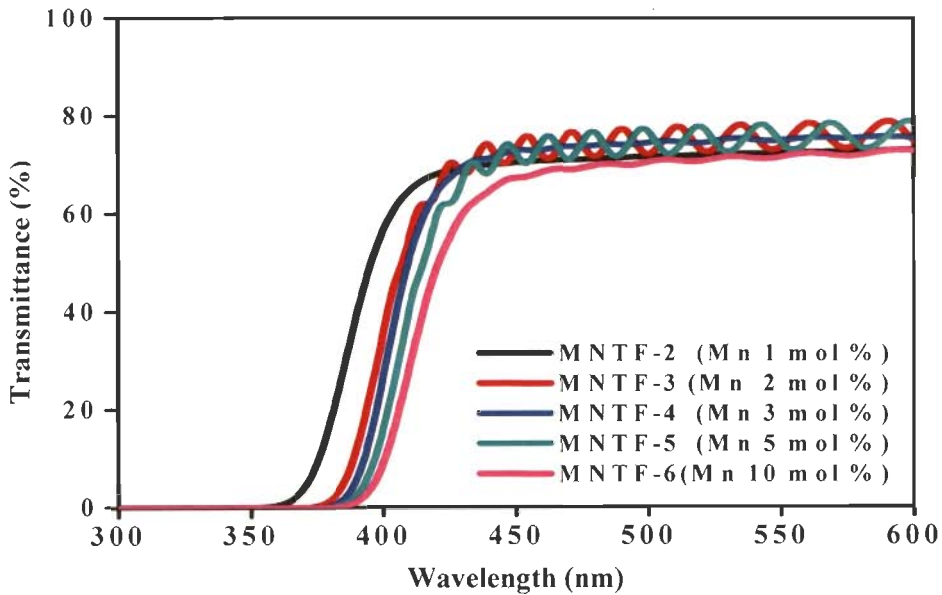


Figure 6.21: Transmittance $T(\lambda)$ of Mn^{2+} doped $Zn_{0.55}Cd_{0.45}S$ films at Mn^{2+} concentrations of 1, 2, 3, 5, and 10 mol%

Figure 6.22 shows the PL emission spectra of samples MNTF-1, MNTF-2, MNTF-3, MNTF-4, MNTF-5, and MNTF-6 corresponding to Mn^{2+} concentrations of 0, 1, 2, 3, 5, and 10 mol%. PL emission at ~ 450 nm is a blue emission and is due to defect emissions. Figure 6.22 shows the orange emission at ~ 585 nm and is attributed to the ${}^4T_1 \rightarrow {}^6A_1$ transition of manganese. PL emission spectrum of sample MNTF-1 (undoped) is also shown in figure 6.22. The emission spectrum of undoped sample is dominated entirely by the defect emissions. For manganese concentration of 1 mol% (sample MNTF-2), there is an emergence of characteristic emission. However, the intensity of orange emission is lower in comparison to defect assisted emission. With increase in manganese concentration orange emission enhances and defect related emission decreases. This trend continued to manganese concentrations ≤ 5 mol% (sample MNTF-5). For manganese concentrations > 5 mol% results in the reduction in orange emission intensity.

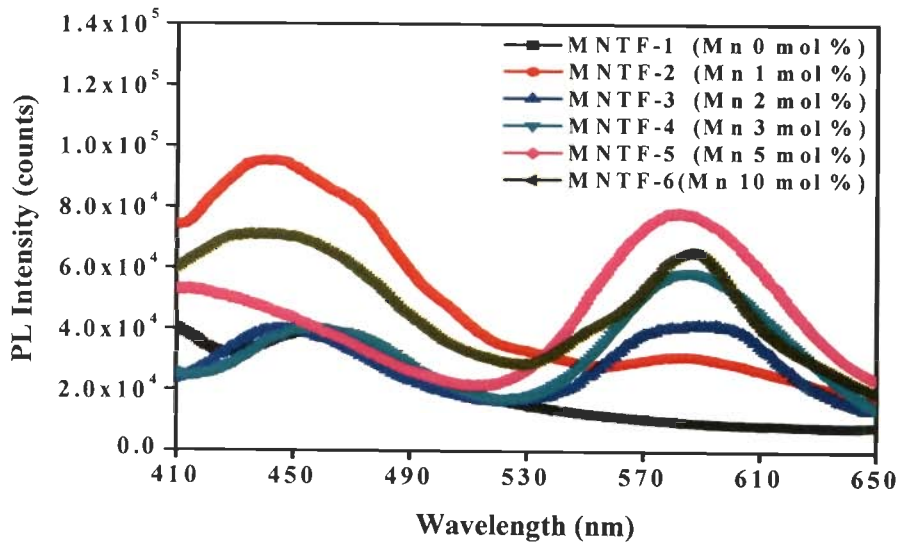


Figure 6.22: PL emission spectra of Mn²⁺ doped Zn_{0.55}Cd_{0.45}S films at Mn²⁺ concentrations of 0, 1, 2, 3, 5, and 10 mol%

Figure 6.23 shows the bar chart of intensities for defect and characteristic emissions of Mn²⁺ doped Zn_{0.55}Cd_{0.45}S films. It can be seen from figure 6.23 that defect assisted emissions dominates for the entire composition range. It suggests that nanocrystalline films have higher defects. Defect emission was highest at 1 mol% manganese. Thereafter, defect emission intensities are comparable for manganese concentrations varying from 2-5 mol%. The defect emission increases further for concentrations > 5 mol%. Characteristic emission intensity decreases and that of defect emission increases at 10 mol%. This decrease in intensity is attributed to the nucleation of separate MnS phase, and is also discussed earlier in section 6.4.

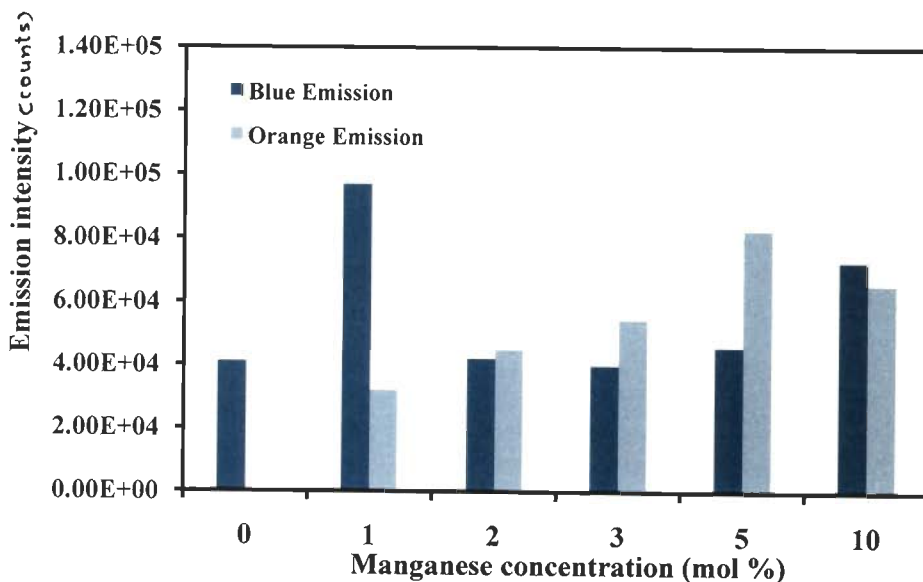


Figure 6.23: Peak intensity variation of blue and orange emission of Mn²⁺ doped Zn_{0.55}Cd_{0.45}S films at Mn²⁺ concentrations of 0, 1, 2, 3, 5, and 10 mol%

Figure 6.24 shows the plot of maximum PL intensities of characteristic emission at ~ 585 nm with variation in manganese concentrations. The maximum orange emission intensity $\sim 8 \times 10^4$ is obtained from nanocrystalline thin films. The obtained emission intensity from nanocrystalline thin films is lowered by a factor of ~ 5 when compared to Mn²⁺ doped Zn_{0.55}Cd_{0.45}S nanoparticles.

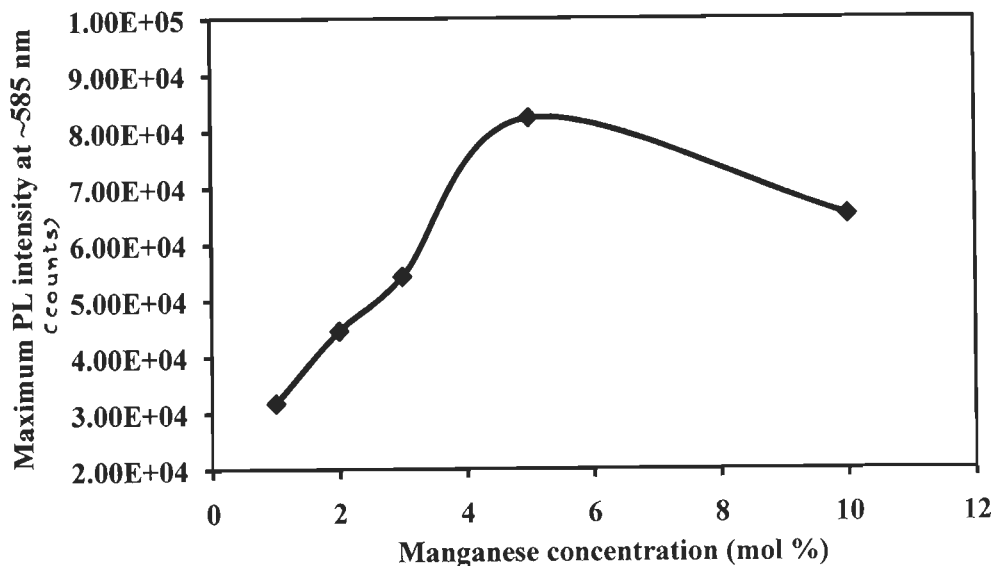


Figure 6.24: The plot of maximum PL intensity for at ~ 585 nm of Mn²⁺ doped Zn_{0.55}Cd_{0.45}S films at Mn²⁺ concentrations of 0, 1, 2, 3, 5, and 10 mol%

6.8 Zn_{0.55}Cd_{0.45}S:Mn/ZnS NANOCOMPOSITE FILMS

Nanocomposite film is constituted of two semiconductors Zn_{0.55}Cd_{0.45}S:Mn and ZnS, and it is shown that the larger energy band gap component of nanocomposite effectively passivates the smaller band gap component. Taneja *et al.* and Vasa *et al.* reported the surface passivation of pure CdS films via chemical passivation by a prolonged *in-situ* exposure to H₂+N₂ gas mixture [189, 196]. Their group further reported that chemical passivation is not much effective and a coating of higher energy band gap material is needed to effectively passivate the surface [14]. They showed that the photoluminescence emitted from a two-component quantum dot ensemble on a thin film is significantly higher than that achieved from chemical passivation.

In this study ZnS top layer thickness has been varied and its effect on light emission properties is investigated. Results are discussed in section 6.9.2. A series of samples with ZnS top layer thickness corresponding to laser shots of 3000, 4000, 5000, and 6000 were prepared (sample MNTF-7, MNTF-8, MNTF-9, and MNTF-10). The total

film thicknesses of the nanocomposites were kept constant by the fixed 15000 laser shots. Complete description of the synthesis parameters are mentioned in table 6.5.

6.9 RESULTS & DISCUSSION

ZnS top layer of $Zn_{0.55}Cd_{0.45}S:Mn/ZnS$ nanocomposites results in the enhanced emission intensity. The effect of varying top layer thickness on the emission intensity has been investigated. The results obtained with varying top layer thickness are discussed in the following sections.

6.9.1 Structural Characterization

Figure 6.25 shows the XRD pattern of $Zn_{0.55}Cd_{0.45}S:Mn/ZnS$ nanocomposite grown on corning 1737 glass substrates. The x-ray diffraction spectra of the pulsed laser ablated nanocomposite show a single broader peak, which could arise from a superposition of the stronger diffraction lines of $Zn_{0.55}Cd_{0.45}S:Mn$ and ZnS.

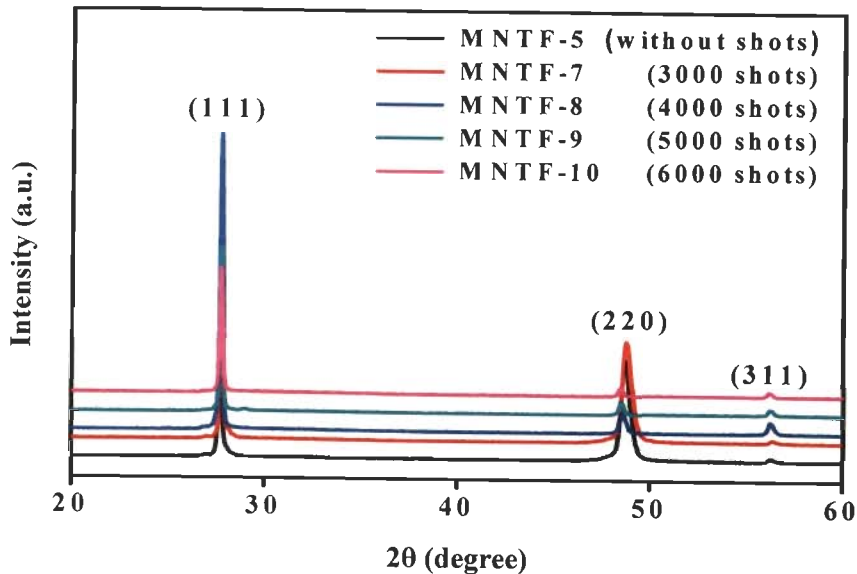


Figure 6.25: XRD patterns of $Zn_{0.55}Cd_{0.45}S:Mn/ZnS$ films at 0, 3000, 4000, 5000, and 6000 laser shots

Figure 6.26 shows transmittance spectra of the samples MNTF-7, MNTF-8, MNTF-9, and MNTF-10 prepared at 3000, 4000, 5000, and 6000 laser shots. Transmission spectrum of $Zn_{0.55}Cd_{0.45}S:Mn$ is also shown in figure 6.26. Transmittance of ~70% in the visible region is obtained for these samples. Transmittance spectra clearly show the difference in the absorption edge upon ZnS coating. Absorption wavelength of the nanocomposite has blue-shifted with respect to $Zn_{0.55}Cd_{0.45}S:Mn$ films. This result is

contrary to the observed red-shift in the absorption spectrum of the core-shell nanoparticles. It suggests that the ZnS coating does not affect the particle size of the films. The observed blue-shift in the absorption spectrum can therefore be due to the ZnS coating, clearly demonstrating the successful formation of nano-composites.

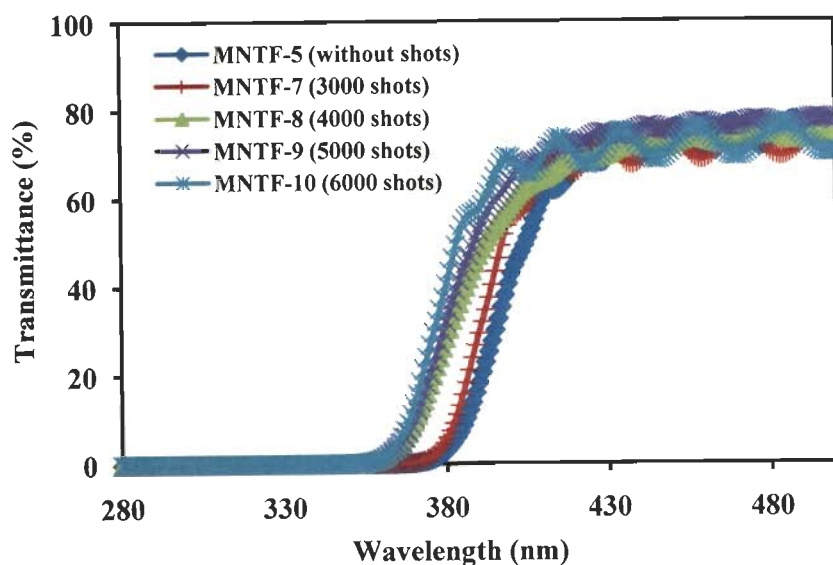


Figure 6.26: Transmittance $T(\lambda)$ of $Zn_{0.55}Cd_{0.45}S:Mn/ZnS$ films corresponding to laser shots of 0, 3000, 4000, 5000, and 6000

6.9.2 PL Enhancement in $Zn_{0.55}Cd_{0.45}S:Mn/ZnS$ Nanocomposite

PL of the nanocomposite was measured at room temperature to investigate its emission properties. Figure 6.27 shows PL emission spectra of samples MNTF-5, MNTF-7, MNTF-8, MNTF-9, and MNTF-10. It can be seen from figure 6.27 that the nanocomposite exhibits a distinct enhanced PL emission. The most dominant feature is the reduction in the FWHM of the orange emission peak. FWHM decreases from ~ 60 nm (without ZnS coating) to ~ 18 nm (4000 laser shots), and is accompanied by an intensity increase. The maximum emission intensity $\sim 1.1 \times 10^5$ is obtained at 4000 laser shots. With shell coating, surface defect emission was significantly eliminated due to the effective surface passivation by the ZnS outer shell. Fraction of manganese ions sitting on or near the surface could be internalized by an additional ZnS outer shell. Unlike the internal manganese ion, the surface manganese ion possesses inhomogeneous, disordered environments induced by a high density of surface defects, and its radiative transition is readily quenched. However, the internalized manganese ion is at a distance from the surface of the structure, and its radiative transition becomes less disturbed by the surface defects, leading to the enhanced luminescence. With increase in laser shots (increasing

ZnS top layer thickness), defect related emission starts to dominate (sample MNTF-9 and MNTF-10). This defect related emission can again be attributed to ZnS emissions, and is discussed earlier in section 6.6.5.

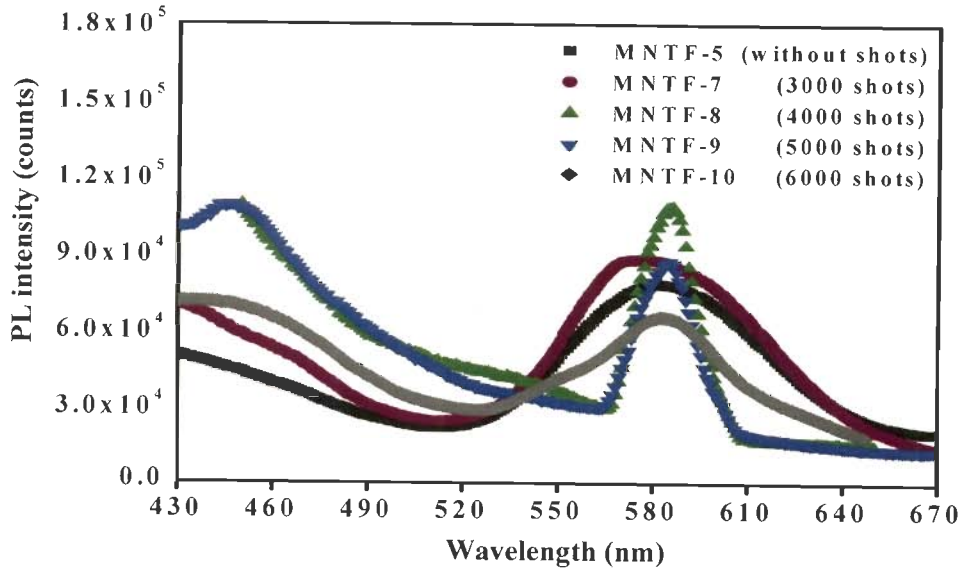


Figure 6.27: PL emission spectra of $Zn_{0.55}Cd_{0.45}S:Mn/ZnS$ films with ZnS top layer laser shots of 0, 3000, 4000, 5000, and 6000

Figure 6.28 shows the orange emission intensities ratio ($I_{top/c}$) of nanocomposite to core layer. Increase in PL intensity obtained in this work is ~ 1.4 times higher than the emission obtained from the core $Zn_{0.55}Cd_{0.45}S:Mn$ films. The PL enhancement in core-shell nanoparticle was increased by a factor of ~ 15 , whereas in nanocomposite films it enhances only by a ~ 1.4 .

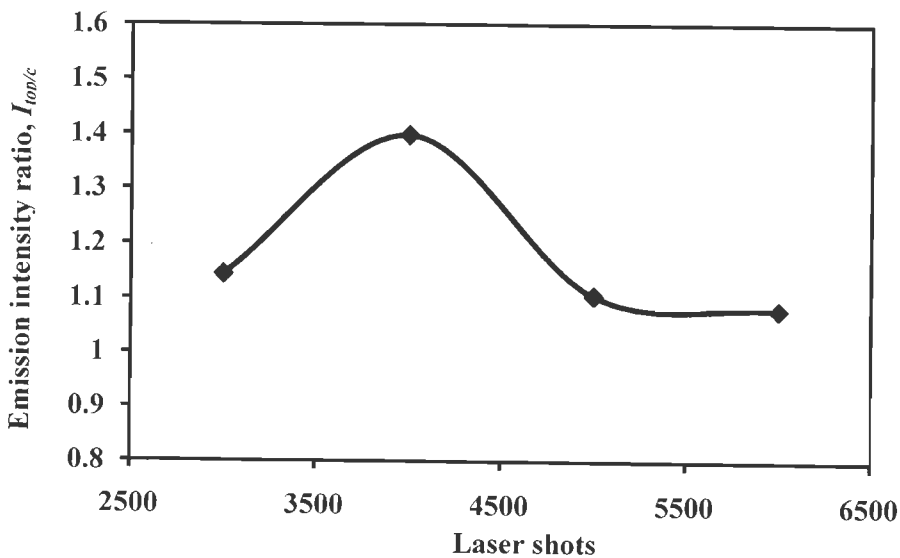


Figure 6.28: Plot of $I_{top/c}$ with ZnS top layer variation of $Zn_{0.55}Cd_{0.45}S:Mn/ZnS$ films corresponding to laser shots of 0, 3000, 4000, 5000, and 6000

Li *et al.* suggested that the type-I (straddling) structure effectively confines the carriers of the core layer by depositing a higher energy band gap material onto the lower band gap material [102]. The obtained PL enhancement in this work can be explained by the formation of a type-I (straddling) nanostructure [218]. Based on the electron affinity model [9] the schematic energy band diagram of Zn_{0.55}Cd_{0.45}S:Mn/ZnS nanocomposite structure is shown in figure 6.29. The electron affinity (χ_{ZnS}) of ZnS is 3.9 eV (Table 2.1, chapter 2) and that of Zn_{0.55}Cd_{0.45}S:Mn is calculated as 4.305 eV using Vegard's law (χ_{CdS} is 4.8 eV; χ_{ZnS} is 3.9 eV) (Table 2.1, chapter 2). These values have been taken in an assumption that the manganese incorporation does not alter the energy band gap of host nanocrystalline thin films. Figure 6.29(a) shows the schematic of type-I heterostructure. Figure 6.29(b) shows the line diagram of core and nanocomposite. The electron affinity of core is higher than those of ZnS shell. Consequently, these two semiconductors form type-I structure as shown in figure 6.29(c). This structure confines the carriers since the higher band gap of the shell material provides effective surface passivation, which enhances the emission intensity.

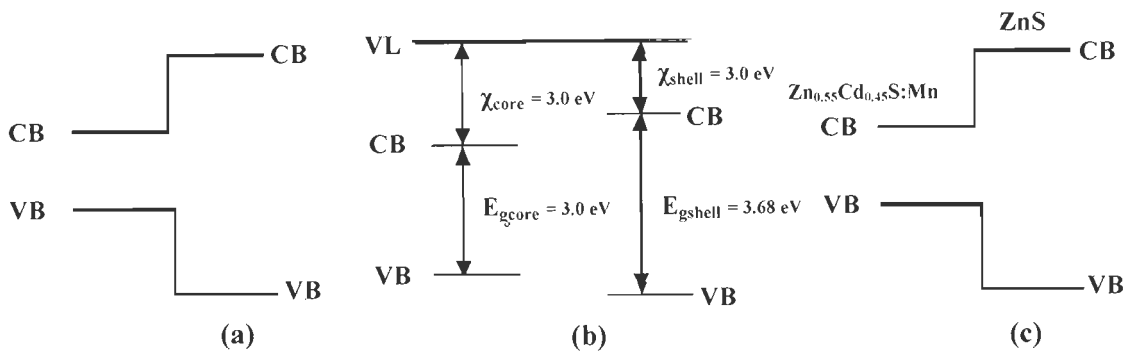


Figure 6.29: (a) Schematic of type-I (straddling) structure, (b) Electron affinity model of system under consideration, and (c) Schematic of as-formed type-I (straddling) structure of Zn_{0.55}Cd_{0.45}S:Mn/ZnS nanocomposite

6.10 SUMMARY

The successful incorporation of dopant (characterized via orange emission) inside the host nanostructure is established in this work. The lattice mismatch minimization between MnS and Zn_{1-x}Cd_xS allows a substantially larger amount of manganese incorporation in the host lattice. Maximum of characteristic peak emission was obtained at mole fraction, $x = 0.45$, with 0.10% lattice mismatch. PL intensities ratio of the orange

emission of Mn²⁺ to the blue emission of the host lattice attains the maximum of ~ 60 at Mn²⁺ precursor concentration of 5 mol%. Preparation of core-shell nanostructures leads to PL enhancement by a factor of ~ 15 when coated with ZnS shell of 0.55 nm. The emission intensities of nanocrystalline films are found to be of poorer quality than their counterpart (nanoparticles). The emission enhancement in nanocomposite Zn_{0.55}Cd_{0.45}S:Mn/ZnS was increased by a factor of ~1.4 with coating of ZnS top layer. Emission enhancement in nanostructures is explained by the formation of type I hetero-junction, based on their electron affinity model.

CHAPTER 7

DEVICE APPLICATION OF $Zn_{1-x}Cd_xS$ NANOSTRUCTURED
THIN FILMS FOR PHOTOVOLTAIC

7.1 INTRODUCTION

The average solar radiation reaching the earth surface is very rich in photons with energies ranging from 1.4 – 3.0 eV [187, 224]. In CdTe solar cells CdS is popularly used as a window material and as an *n*-type hetero-junction partner to *p*-CdTe. The energy band gaps of CdTe and CdS are 1.5 and 2.4 eV [Table 2.1, chapter 2; Table A4.1, Appendix A4.1], respectively. Thus photons with energies within this range can reach CdTe layer, where they contribute to the cell's photocurrent. The absorption coefficients of II-VI compounds in the spectrum window are high [2], about 10^4 - 10^5 cm^{-1} . Thus, the carrier generation by higher energy photons in the *n*-CdS layer takes place at the surface far away from the depletion region where the generated carriers can be collected. As a result, these carriers are often lost to surface recombination current. This current increases the dark current and consequently reduces the useful current delivered by the cell to a load. Thus if CdS could be replaced by a higher energy band gap material it will allow more photons to pass, and should result in higher efficiencies.

Nakamura *et al.* showed in their study of CdS/CdTe cells, reducing the thickness of CdS layer to less than 100 nm reduces the absorption. The reduced absorption in CdS layer can minimize the surface recombination current [131]. However, at this thickness cell appear to be inefficient due to increase in the shunting probability. Below 70 nm, there is a general degradation [5] in the cell performance owing to considerable increase in shunt resistance.

It should have, therefore, been more appropriate to use a thick layer of ZnS films with 3.7 eV energy band gap as a window layer, but there are several drawbacks associated with the use of ZnS:

- (i) it is highly resistive and can significantly increase the cell's series resistance,
- (ii) the lattice mismatch between ZnS and CdTe is $\sim 30\%$, making it a poorer hetero-junction partner to CdTe compared to CdS [140], also discussed earlier in chapter 1.

Thus in the present scenario it can be framed that ZnS/CdTe alone is not suitable for the thin film solar cell structures. The arguments above then make $Zn_{1-x}Cd_xS/CdTe$ structure an attractive window/absorber structure. This structure can provide twofold benefits:

- (i) it can maintain the traditional CdS/CdTe contact and,
- (ii) at the same time can improve the short wavelength spectral response of the cell, without compromising the transport properties, the series and the shunt resistances of the cell.

In view of the above discussion, $Zn_{1-x}Cd_xS$ layer with mole fraction, “ $x = 0.9$ ” is used as window layer in CdTe based solar cell.

7.1.1 Framework of the Work

A novel method for testing the uniform coverage of the CdS layer has been suggested by Alamri *et al.* and Alturkestani [5, 8]. In their work they tested the coverage of CdS films over variety of substrate in terms of TCO layer i.e. ITO and SnO_2 coated glass and manufacturer. A similar approach is used in this study to test the uniform coverage of the $Zn_{0.1}Cd_{0.9}S$ nanocrystalline thin films deposited on ITO substrate.

Fabrication of high efficiency cells requires that the CdTe grain sizes should be greater than 1 μm . The higher grain size avoids significant bulk recombination, larger interface state density, and high resistance. However, CdTe films have typically small grains, and short minority carrier lifetime and high resistivity due to many grain boundaries [97]. Kampmann and Lincot suggested a method known as $CdCl_2$ treatment (also referred as “*activation step*”), which they utilized to enhance the grain size and density of the CdTe film [87].

This treatment is undertaken by applying $CdCl_2$ on the back surface of the CdTe layer prior to heat- treatment. The application of $CdCl_2$ can be done either i) covering the CdTe sample with a saturated $CdCl_2$ /methanol solution, or ii) evaporating a $CdCl_2$ thin film [15, 145]. Although the exact role of this treatment is not clear, various research groups have suggested that it affects the cell in several ways:

- (i) Alamri suggested that the type conversion such as *p*-doping in the material takes place (from intrinsic to *p* type) [5],
- (ii) Hussain suggested that the $CdCl_2$ treatment induces the Cl related acceptor levels in CdTe which leads to the *p*-type behaviour in CdTe [80].

- (iii) Romeo *et al.* reported that $CdCl_2$ treatment enhances the CdTe recrystallization, leading to better efficiencies [160],
- (iv) Compann *et al.* and McCandless *et al.* showed that $CdCl_2$ treatment not only helps in recrystallization it also leads to the CdTe/CdS intermixing (inter-diffusion) [41, 121]
- (v) Paulson and Dutta, suggested that inter-diffusion reduces interface state density at CdTe/CdS interface [145].

The aim of $CdCl_2$ treatment is to diffuse chlorine into the CdTe and its effectiveness depends on the annealing conditions (e.g. time, temperature and atmosphere) [137]. Moreover, these conditions must be optimized for CdTe deposited by different methods e.g. different grain size can be obtained via different deposition techniques. Gupta *et al.* optimized the $CdCl_2$ treatment for sputtered CdTe/CdS cells with various CdTe thicknesses [75]. The treatment of all cells was performed in $CdCl_2$ vapour at $T \sim 390$ °C for various time durations. While the optimum annealing time was ~ 30 minutes for a cell with 2.3 μm thick CdTe, only 10 minutes gave the best efficiency when the CdTe thickness was reduced to 0.87 μm . $CdCl_2$ treatment requirement may differ based on the nature of CdTe (i.e. thickness in this case). Major *et al.* have shown that insufficient treatment of $CdCl_2$ creates a buried junction [115] whereas over treatment may delaminate the films from the substrate. Hence, optimizing the $CdCl_2$ treatment conditions for CdTe cells is necessary to achieve good performance.

The solar cell performance is gauged via four basic parameters: (a) short circuit current density, J_{sc} in A/cm^2 , (b) open circuit voltage V_{oc} in volts, (c) fill factor, FF (%), (d) photo conversion efficiency, η (%) (see appendix A4.2 for detailed description of solar cell parameters).

The crystalline quality and compactness of CdS layer are important parameters which influences the performance of CdTe/CdS solar cells. The thickness of the CdS layer can strongly affect the device performance. Rose *et al.* have shown that devices with CdS layer of 60 nm typically have lower open circuit voltages [162]. While, devices with CdS thicknesses over 100 nm have reduced photocurrent due to absorption in the CdS and lower V_{oc} due to inferior CdS from the latter stages of chemical bath deposition (CBD) growth. CdS thickness may also produce changes in the CdTe surface morphology [161]. The deposition temperature of window layer also affects the cell efficiency by variation the crystalline quality of the window layer [57]. Nanograins may enhance the formation

of an inter-diffused layer at the CdTe/CdS interface which can influence the junction transport properties. In a continuing effort the $CdCl_2$ treatment parameters, $Zn_{0.1}Cd_{0.9}S$ film thickness, and deposition temperature have been varied and their effect on solar parameters have been investigated.

7.2 CHAPTER PREFACE

This chapter presents two studies: the first part (section 7.3) is concerned with the interface between $Zn_{0.1}Cd_{0.9}S$ and transparent conducting oxide (TCO) layer. To investigate the interface properties, post heat treatments of the TCO prior to the growth of $Zn_{0.1}Cd_{0.9}S$ layer were studied. In particular, a method suggested by Alamri *et al.* and Alturkestani, is applied to test the uniform coverage of the $Zn_{0.1}Cd_{0.9}S$ layer and is presented in section 7.3.2 [5, 8].

In the second part of this chapter (section 7.4), the work has been extended to the fabrication of full device structures and their photovoltaic device performance have been investigated. The application, role and optimization of the activation step of CdTe cells (i.e. $CdCl_2$ treatment) are presented in Section 7.5. The effect of $CdCl_2$ treatment on the PV performance of the cells is discussed in section 7.5.3. It is known that for any given window layer ($Zn_{0.1}Cd_{0.9}S$ in our case) processing conditions, the outcomes depend on the processing parameter. Both the intrinsic properties of the layers (e.g. surface morphology) and the processing procedure (e.g. post-heat treatment) may affect these layers significantly which in turn affect the device performance. It is previously discussed in section 7.1.1 that the window layer thickness and deposition temperature directly affects the surface morphology of the subsequent layer and thus device performance. The effect of thickness and deposition temperature on the performance of the cell parameters is therefore studied. The results are discussed in sections 7.5.5 and 7.5.7 respectively.

7.3 $Zn_{0.1}Cd_{0.9}S/TCO$ INTERFACE PROPERTIES

The $Zn_{0.1}Cd_{0.9}S/TCO$ interface plays an important role in the performance of solar cells. Although the main purpose of TCO is to serve as a front electrode it can significantly affect both the growth of the $Zn_{0.1}Cd_{0.9}S$ window layer, and the junction properties. Thermal stability is an essential requirement for this layer.

Ideally the $Zn_{0.1}Cd_{0.9}S/TCO$ junction should be Ohmic. Alamri *et al.* suggested that TCO properties changes at higher processing temperatures [5]. They observed a change in the SnO_2 properties (utilized as TCO), at temperatures > 400 °C. The TCO

layer can be subjected to heat treatment either via *in-situ* (during cell fabrication process) or via post-heat treatment steps (during the cell activation process). The altered TCO properties can change the window/TCO junction from Ohmic to rectifying. This can eventually delaminate the cell performance. Thus the effect of window/TCO stack should be investigated.

For this purpose TCO, (Indium tin oxide (ITO) is used in this study) is subjected to pre-heat treatment for various durations and environments and their interface properties have been investigated.

7.3.1 TCO Pre-Heat Treatment Conditions and $Zn_{0.1}Cd_{0.9}S$ /TCO Stack Formation

TCO pre-heat treatment and contacting details for the samples studied in this section are shown in Table 7.1. $Zn_{0.1}Cd_{0.9}S$ layer was deposited by PLD technique. Synthesis details of $Zn_{0.1}Cd_{0.9}S$ layer are provided in Table 7.1. $Zn_{0.1}Cd_{0.9}S$ films were deposited on $1.5 \times 1.5 \text{ cm}^2$ area of ITO substrate. All samples were contacted with indium dot (2 mm diameter), which was applied by thermal evaporation at a pressure of $\sim 10^{-5}$ torr. Indium makes an Ohmic contact with *n-type* semiconductor [5], and is therefore chosen as a contact material. Since indium makes an Ohmic contact, any rectification behavior induced by pre-heat treatment can be credited to the $Zn_{0.1}Cd_{0.9}S$ /ITO interface. The *I-V* characteristics were measured using the Keithley sourcemeter 2400 and the results are presented in section 7.3.2.

Before analyzing the junction interface between $Zn_{0.1}Cd_{0.9}S$ /ITO, it was essential to test the coverage of the window layer. This step was necessary because the pin holes, if present in the $Zn_{0.1}Cd_{0.9}S$ layer can make direct contact between indium and ITO and resulting characteristic will be Ohmic regardless of the junction type. This might give an impression that the obtained Ohmic characteristic is due to $Zn_{0.1}Cd_{0.9}S$ /ITO interface and can be misleading.

Table 7.1: Synthesis parameters of $Zn_{0.1}Cd_{0.9}S$ /TCO stack and treatment conditions of TCO tested in this study. The table also contains the contact types and the results of the $I-V$ characteristics

| Stack | Zn _{0.1} Cd _{0.9} S layer Synthesis Parameters | | | TCO (ITO) Treatment | | | | Contact | Nature of $I-V$ curve |
|----------|--|---|--------------------------|--------------------------------|-----------------|-----------|------------|---------------------|-----------------------|
| | Deposition Temperature (°C) | Laser Flux Density (J/cm ²) | Working Pressure (mtorr) | Gas | Pressure (Torr) | Temp (°C) | Time (min) | In/Au | |
| Stack#1 | 400 | 3.33 | 200 | O ₂ | 50 | 500 | 20 | In | Ohmic |
| Stack#2 | 400 | 3.33 | 200 | O ₂ | 50 | 500 | 30 | In | Ohmic |
| Stack#3 | 400 | 3.33 | 200 | O ₂ | 50 | 500 | 40 | In | Ohmic |
| Stack#4 | 400 | 3.33 | 200 | H ₂ +N ₂ | 10+40 | 500 | 20 | In | Ohmic |
| Stack#5 | 400 | 3.33 | 200 | H ₂ +N ₂ | 10+40 | 500 | 30 | In | Ohmic |
| Stack#6 | 400 | 3.33 | 200 | H ₂ +N ₂ | 10+40 | 500 | 40 | In | Ohmic |
| Stack#7 | 400 | 3.33 | 200 | - | - | 500 | - | In | Ohmic |
| Stack#8 | 400 | 3.33 | 200 | O ₂ | 50 | 500 | 40 | Au (mask pattern a) | Ohmic/Schottky |
| Stack#9 | 400 | 3.33 | 200 | H ₂ +N ₂ | 10+40 | 500 | 40 | Au (mask pattern a) | Ohmic/Schottky |
| Stack#10 | 400 | 3.33 | 200 | O ₂ | 50 | 500 | 40 | Au (mask pattern b) | Ohmic/Schottky |
| Stack#11 | 400 | 3.33 | 200 | H ₂ +N ₂ | 10+40 | 500 | 40 | Au (mask pattern b) | Ohmic/Schottky |
| Stack#12 | --- | --- | --- | --- | --- | --- | --- | Au | Ohmic |

7.3.2 Accessing Uniform Coverage of $Zn_{0.1}Cd_{0.9}S$ Films Grown on ITO

Pinholes in the window layer can provide misleading $I-V$ curves for the $In/Zn_{0.1}Cd_{0.9}S/ITO$ stack. Patel *et al.* showed that the gold makes Schottky/rectifying contact with n -type semiconductor [142]. Au was therefore chosen as contact material to devise the continuity test of this stack. Therefore, $Au/Zn_{0.1}Cd_{0.9}S/ITO$ structure should always show Schottky characteristic even when $Zn_{0.1}Cd_{0.9}S/ITO$ junction is Ohmic (see appendix A5 for Ohmic and Schottky junctions). When pinholes in the $Zn_{0.1}Cd_{0.9}S$ layer are present, then a direct Ohmic contact will be established between the Au and the ITO, and the resulting characteristic will be Ohmic.

For this study stacks 8 to 12 were prepared with Au contact. Two types of mask patterns with 16 and 9 dots of 2 mm diameter were prepared and are shown in figure 7.1(a) & (b) respectively. Four or three lines of dots were selected so as to probe the entire deposited area of substrate. Stacks 8 and 9, were contacted with 16 dot geometry. Stacks 10 and 11 were contacted with 9 dot geometry. For each stack, the $I-V$ curves were measured.

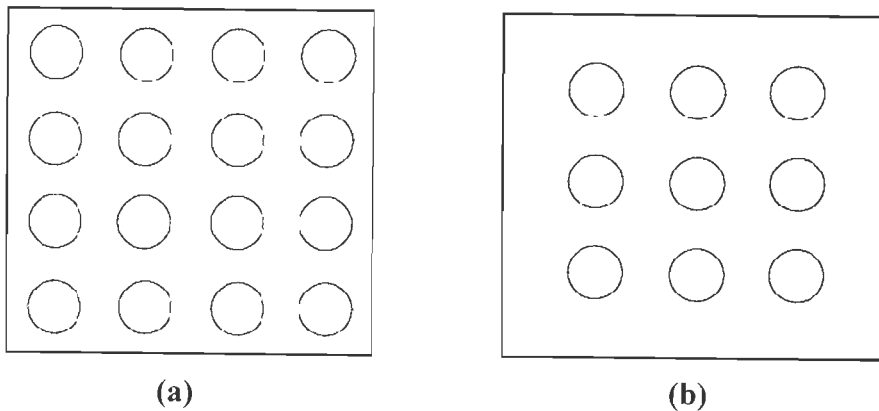


Figure 7.1: Au mask patterns: circle represents 2 mm diameter Au dots in (a) Sixteen dot geometry, and (b) Nine dot geometry

Figure 7.2 shows the typical behavior obtained from $I-V$ measurements of $Au/Zn_{0.1}Cd_{0.9}S/ITO$ stacks. For stacks 8 and 9, both Schottky and Ohmic behavior was observed. Stacks 10 and 11 showed the Schottky characteristics, except for few contacts which were on the outer edge of the mask pattern b. Figure 7.2(a) shows a typical Schottky characteristic of junction, while figure 7.2(b) shows an Ohmic characteristic. Stack 12 (Au/ITO stack) show an Ohmic behavior. Schottky characteristic shown in figure 7.2(a) can therefore be attributed to $Au/Zn_{0.1}Cd_{0.9}S$ junction. Observed Ohmic

behavior (Fig. 7.2 (b)) is therefore due to the pinholes in $Zn_{0.1}Cd_{0.9}S$ layer. Occurrence of Ohmic behavior with mask pattern a, was much higher than with b. For mask pattern a, ~30% contact showed Ohmic characteristic. For Mask pattern b, only ~ 5% contact showed Ohmic characteristic. This trend suggests that the quality of the $Zn_{0.1}Cd_{0.9}S$ films is poor at side-lines of the substrate. In general, it was found that there was an increased density of pinholes in the $Zn_{0.1}Cd_{0.9}S$ film near the substrate edge. This study suggests that this method has the ability to probe the area for the back contact deposition.

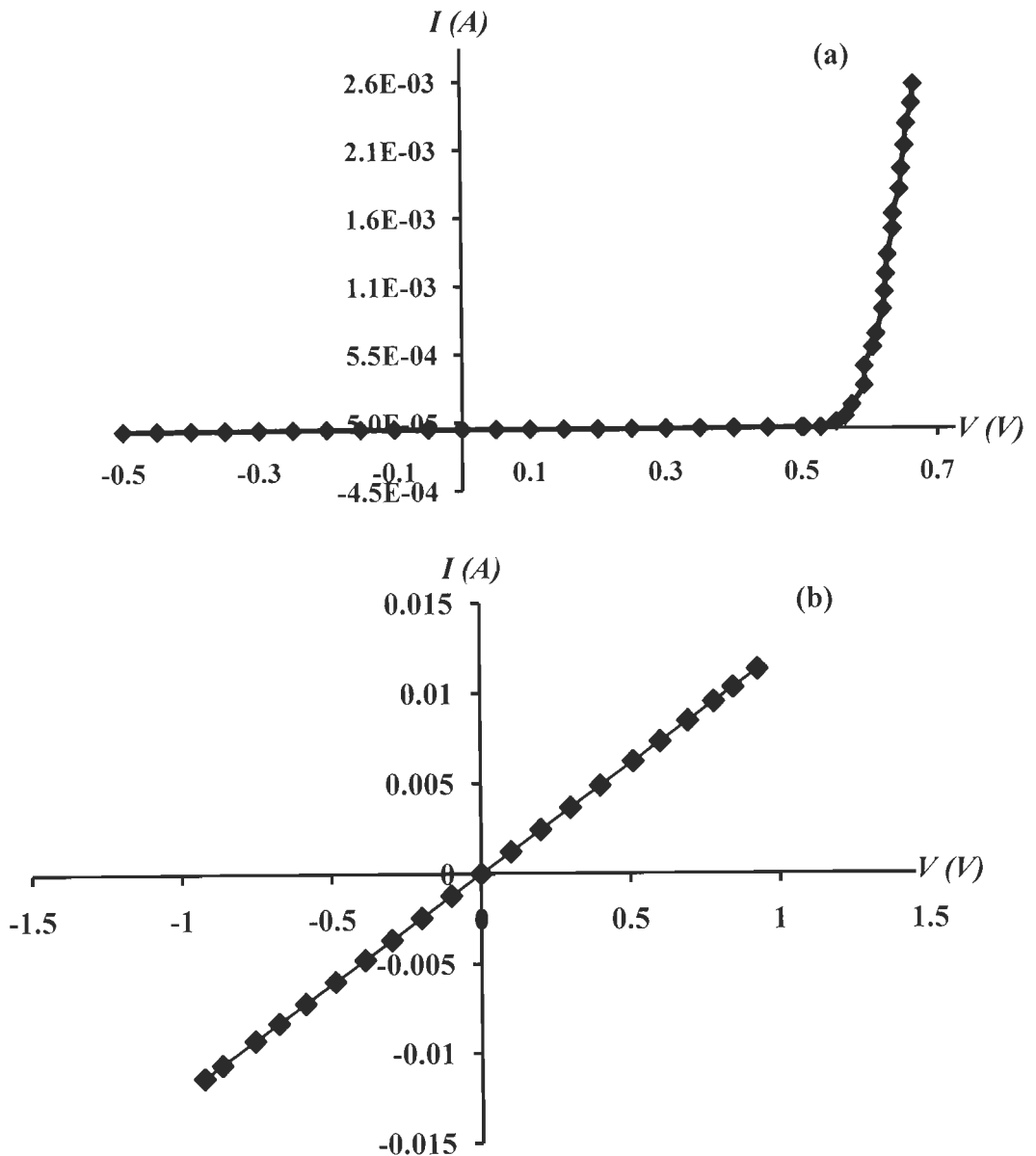


Figure 7.2: I - V curves for (a) An Au/ $Zn_{0.1}Cd_{0.9}S$ /ITO stack depicting rectifying behavior, and (b) An Au/ $Zn_{0.1}Cd_{0.9}S$ /ITO stack depicting Ohmic behavior

7.3.3 Effect of Pre-Heat Treatment of ITO Substrates

$I-V$ curves for all $Zn_{0.1}Cd_{0.9}S$ layer deposited on either as grown (stack 7) or preheat treated ITO substrate (stacks 1-3 for oxidizing; 4-6 for reducing environment) with In contacts showed an Ohmic behavior. The average resistance values for oxidizing environments were found, higher than that for reducing environment. The average resistance for oxidizing behavior was found as 95Ω with standard deviation of 2.4. The average resistance for reducing environment was found as 63Ω with standard deviation of 1.3.

It is again verified that the obtained Ohmic behavior is not due to pin holes. To carry out this testing two samples were contacted with Au. For this measurement In contact was surrounded by four gold contacts with spacing of 2 mm between In and Au contacts. $I-V$ characteristics of these Au contacts were of Schottky behavior, showing that there are no pin holes in $Zn_{0.1}Cd_{0.9}S$ layer at those areas and the observed Ohmic characteristic is purely a junction characteristic. Obtained $I-V$ characteristics for In/ $Zn_{0.1}Cd_{0.9}S$ /ITO stacks are Ohmic in nature but their resistances varied for oxidizing and reducing treatment conditions. However, the resistance values do not vary greater than $\pm 5\%$ with change in treatment time irrespective of the heat treatment environment.

This study suggests that junction properties did not get affected by the pre-heat treatment temperature range considered in this study; indeed junction preserves Ohmic characteristic.

Table 7.2 contains the reference/method for energy band gaps, work functions and electron affinities for In, $Zn_{0.1}Cd_{0.9}S$ and ITO either calculated or obtained from the literature. The purpose of this schematic is to show that $Zn_{0.1}Cd_{0.9}S$ and ITO stack forms an Ohmic junction.

Table 7.2: The references/methods for the electron affinity, work function, and energy band gaps adopted in this work for indium, Zn_{0.1}Cd_{0.9}S and ITO

| Material | Indium | Zn _{0.1} Cd _{0.9} S | ITO |
|--------------------------------|--------|---|-------|
| Electron Affinity, χ (eV) | ---- | 4.7 | 4.7 |
| References/Method | | $\chi_{ZnS} = 3.9$ eV (Table 2.1) $\chi_{CdS} = 4.79$ eV (Table 2.1) [178] Vegard's Law $\chi_{A_{1-x}B_xC}(x) = (1-x)\chi + x\chi$ | [61] |
| Work Function, Φ (eV) | 4.12 | 4.9 | 4.12 |
| References/Method | [93] | $\Phi_{ZnS} = 6.7$ eV (Table 2.1) $\Phi_{CdS} = 4.7$ eV (Table 2.1) [178] Vegard's Law $\Phi_{A_{1-x}B_xC}(x) = (1-x)\Phi + x\Phi$ | [119] |
| Energy Band Gap, E_g (eV) | ---- | 2.56 | 3.6 |
| References/Method | | $E_g = 3.90$ eV (ZnS W, Table 2.1) $E_g = 2.42$ eV (CdS W, Table 2.1) [178] Vegard's Law $E_{g_{A_{1-x}B_xC}}(x) = (1-x)E_g + xE_g$ | [63] |

Figure 7.3 shows the band structure of isolated components as determined from the knowledge of energy band gaps, work functions and electron affinities either calculated or obtained from the literature.

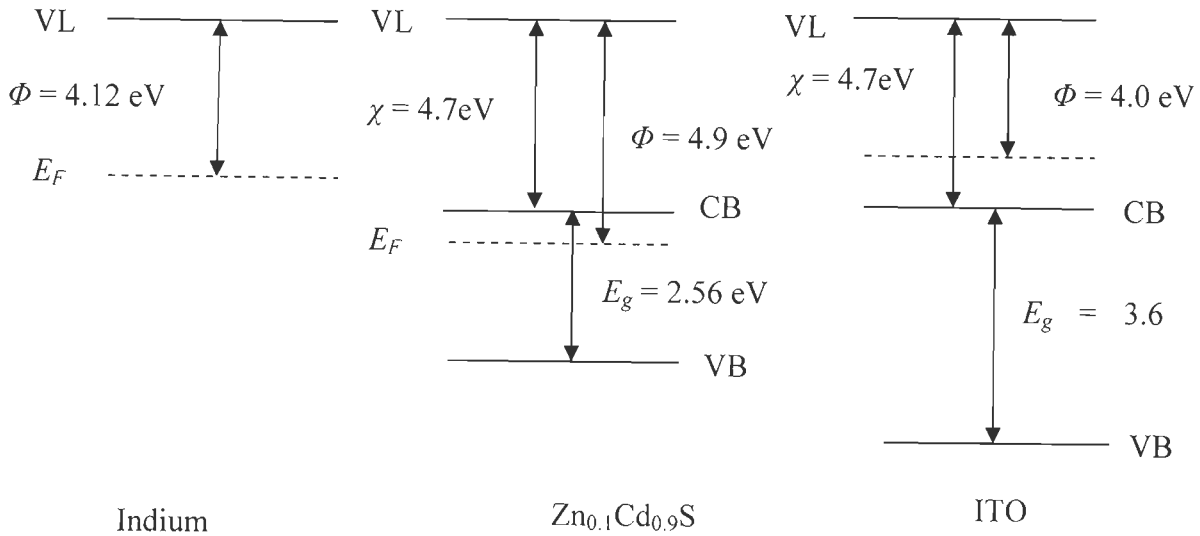


Figure 7.3: The electronic details of each layer of the stack. VL, CB, VB, E_F , E_g , χ , and Φ represents the vacuum level, conduction band, valence band, fermi energy level, energy band gap, electron affinity, and work function respectively

Using data shown in Table 7.2, a band diagram for the complete structure is drawn and is shown in figure 7.4. The energy diagram showed the Ohmic junction at $Zn_{0.1}Cd_{0.9}S$ /ITO interface, corroborating the experimental I - V characteristics. It is further established that the so-obtained Ohmic characteristic is the junction property and is not due to pinholes. This diagram dictates that the electrons may flow freely from $Zn_{0.1}Cd_{0.9}S$ into ITO (figure 7.4).

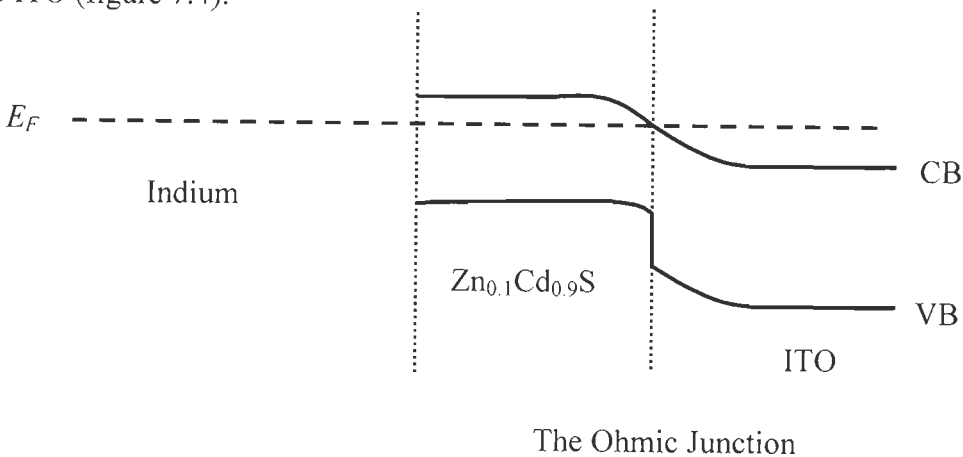


Figure 7.4: Band alignments of the In/ $Zn_{0.1}Cd_{0.9}S$ /ITO stack representing Ohmic junction

After identification of suitable area for back contact deposition, the devices were fabricated. The effect on heat treatment steps involved in the device fabrication process on window/ITO has also been investigated. It is ensured that such heat treatment did not change the properties of window/ITO stack. The following are the details of the steps that were involved in the device fabrication.

7.4 DEVICE FABRICATION STEPS

Details of the cleaning, growth and processing procedures used in this work for device fabrication are provided below. The substrates used in this work were commercially available indium-tin-oxide (ITO) coated glass.

Cleaning the TCO substrates

- Rinsing thoroughly by DI water,
- Soaking in standard laboratory grade soap solution combined with ultrasonication for 30 minutes,
- Rinsing thoroughly by DI water,
- Soaking in acetone combined with ultrasonication for 15 minutes,
- Soaking in iso-propanol combined with ultrasonication for 15 minutes, and
- Drying with N_2 .

Growth of the $Zn_{0.1}Cd_{0.9}S$ layer

$Zn_{0.1}Cd_{0.9}S$ films were grown by pulsed laser deposition technique at previously optimized deposition parameters. Summary of deposition parameters considered for device preparation are given below (see chapter 5 for more details).

- Laser Flux Density at 3.33 J/cm^2 ,
- Working Pressure of Ar gas at 200 mtorr,
- Deposition Temperature at 400°C , and
- Mole Fraction (x) at 0.9.

Typical treatment for the $Zn_{0.1}Cd_{0.9}S$ performed in the device fabrication was post-growth heat treatment in $H_2 + N_2$ atmosphere at 350°C for 2 hr.

Growth of the CdTe layer

The growth of the CdTe layer was undertaken by vacuum evaporator coater. A pellet of CdTe was prepared from commercially available CdTe powder (99.99% purity, Sigma Aldrich, UK) for the deposition of CdTe films. CdTe thin films of fixed thickness $\sim 4 \mu\text{m}$ were prepared by the vacuum evaporation technique in a vacuum better than 2×10^{-5} torr using HINDHIVAC 12 Vacuum Coating Unit (Model: 12A4DM). A tungsten boat was used as the evaporation source and the substrates were $Zn_{0.1}Cd_{0.9}S/ITO/glass$ held at 300°C , which were placed directly above the source at a distance of nearly 20 cm. The deposition rate was in the range between 3–5 $\text{\AA}/\text{s}$.

CdCl₂ treatment

- Wet CdCl₂ treatment

Conventional wet chemical CdCl₂ treatment (0.1 mol% CdCl₂ in methanol) was given to the CdTe/ $Zn_{0.1}Cd_{0.9}S/ITO/Glass$ stack. The films were immersed in the solution for 5 mins and then dried in flowing nitrogen.

- Dry CdCl₂ treatment

In this treatment a layer of CdCl₂ (100 nm thick) is deposited by the evaporation of CdCl₂ powder (Sigma Aldrich, 99.9%) in a vacuum of 7×10^{-2} mtorr at room temperature

Heat treatment

After applying the CdCl₂, all samples were heat treated in air using a tube furnace. The samples were placed on a silicon wafer held on a quartz frame. The duration of heat treatment started when the sample was put in the middle of the furnace, and ended when it was removed to the edge of the furnace tube. A range of temperatures used in this work and their effect on solar cell parameters are discussed in section 7.5.

Cleaning

Following heat treatment, all samples were washed by hot DI water to remove any excess amount of CdCl₂ left after treatment. Next, the samples were washed thoroughly by DI water prior to drying by a flow of N₂.

Preparation of the CdTe surface for back contacting

In this work standard “*bromine etch*” was used to prepare the back surface of devices for contacting. This helps to make a Te rich surface. To obtain an Ohmic back contact samples were etched in a bromine/methanol solution (250 μ L/50 mL) for 5 seconds, with timing being started from immersion in the solution. After bromine etch following cleaning steps were also applied:

- Rinsed thoroughly by DI water,
- Blowing dry with N₂.

Contact deposition

A conductive graphite paste (65.6 wt% C, 32.8 wt% HgTe, 1.6 wt% CuTe) (Agar Scientific) was applied on the surface, and the samples were heat treated for 20 min in an Ar atmosphere at 270 °C. Finally, Ag paste was applied on the graphite contact and cured at 100 °C for 1 h in air. The front contact was obtained with Ag paste and was taken from bare ITO film.

Table 7.3 summarizes the growth and treatment conditions for the samples fabricated in this study.

Table 7.3: Summary of the growth and treatment conditions of cells

| Cell | Substrate | CdCl ₂ treatment | | | | Zn _{0.1} Cd _{0.9} S growth | |
|---------|-----------|-----------------------------|----------------|------------------|------------|--|----------------|
| | | Type | Thickness (nm) | Temperature (°C) | Time (min) | Deposition temperature (°C) | Thickness (nm) |
| Cell#1 | ITO | Wet | - | 400 | 5 | 400 | 150 |
| Cell#2 | ITO | Wet | - | 425 | 5 | 400 | 150 |
| Cell#3 | ITO | Wet | - | 450 | 5 | 400 | 150 |
| Cell#4 | ITO | Wet | - | 500 | 5 | 400 | 150 |
| Cell#5 | ITO | Wet | - | 400 | 10 | 400 | 150 |
| Cell#6 | ITO | Wet | - | 425 | 10 | 400 | 150 |
| Cell#7 | ITO | Wet | - | 450 | 10 | 400 | 150 |
| Cell#8 | ITO | Wet | - | 500 | 10 | 400 | 150 |
| Cell#9 | ITO | Dry | 100 | 400 | 5 | 400 | 150 |
| Cell#10 | ITO | Dry | 100 | 425 | 5 | 400 | 150 |
| Cell#11 | ITO | Dry | 100 | 450 | 5 | 400 | 150 |
| Cell#12 | ITO | Dry | 100 | 500 | 5 | 400 | 150 |
| Cell#13 | ITO | Dry | 50 | 425 | 5 | 400 | 150 |

| | | | | | | | |
|---------|-----|-----|-----|-----|----|-----|-----|
| Cell#14 | ITO | Dry | 50 | 425 | 10 | 400 | 150 |
| Cell#15 | ITO | Dry | 100 | 425 | 10 | 400 | 150 |
| Cell#16 | ITO | Dry | 100 | 425 | 5 | 400 | 60 |
| Cell#17 | ITO | Dry | 100 | 425 | 5 | 400 | 80 |
| Cell#18 | ITO | Dry | 100 | 425 | 5 | 400 | 100 |
| Cell#19 | ITO | Dry | 100 | 425 | 5 | 400 | 200 |
| Cell#20 | ITO | Dry | 100 | 425 | 5 | 350 | 150 |
| Cell#21 | ITO | Dry | 100 | 425 | 5 | 450 | 150 |
| Cell#22 | ITO | Dry | 100 | 425 | 5 | 500 | 150 |

7.5 EFFECT OF $CdCl_2$ HEAT TREATMENT ON CELL PROPERTIES

Lee *et al.* suggested that the grain boundaries in CdTe thin films are strong electrical recombination centers [98]. Durose *et al.* and Sites *et al.* have shown in their study of CdS/CdTe solar cell that the grain boundaries also act as barriers to current transport [52, 180].

It is therefore suggested that for improved device performance grain boundaries should be minimized. This can be achieved by increasing the grain size in CdTe films. A commonly used process to enhance the grain size of CdTe film is the introduction of heat treatment after $CdCl_2$ activation step. With the application of $CdCl_2$ heat treatment the crystallographic rearrangements takes place in the CdTe layer of the cell. These crystallographic rearrangements are related to the (i) stress in the layer, (ii) effect of heat treatment, and (iii) $CdCl_2$ sintering flux.

7.5.1 Structural Properties – Recrystallization

Figure 7.5(a) & (b) shows the XRD patterns of the CdTe films heat treated at four different temperatures after wet and dry $CdCl_2$ treatment respectively. The crystal structure of as-deposited CdTe films (without $CdCl_2$ dipping treatment) is zincblende with preferential orientation of (111) positioned at $2\theta = 23.7^\circ$. Generally, it is difficult for materials of different crystal systems to form a hetero-junction. It is established in chapter five of this work, that at mole fraction, $x = 0.9$, the $Zn_{0.1}Cd_{0.9}S$ films consist wurtzite structure irrespective of the considered deposition temperature. XRD measurements of the deposited $Zn_{0.1}Cd_{0.9}S$ films (section 5.3, chapter 5) shows the wurtzite structure preferentially oriented to the (002) plane. Nakamura *et al.* suggested that the c -plane of the wurtzite structure and the (111) plane of the zincblende structure readily form the hetero-junction [131]. Therefore, the CdTe grains grow in $\langle 111 \rangle$ direction onto the $Zn_{0.1}Cd_{0.9}S$ layer gets preferentially oriented to the c -plane.

Figure 7.5(a) & (b) shows that the CdTe films heat treated with $CdCl_2$ (regardless of treatment nature), the crystal structure of the film did not change, but other peaks corresponding to (220), (311), (400), (331) and (422) planes of zincblende structure, began to appear. Emergence of these peaks show that there was loss of preferential orientation and recrystallization have taken place. With increase in heat treatment temperature, intensity of the diffraction peak of (111) plane decreases and those of other orientations increases. It is also seen from figure 7.5(a) & (b) that reduction in the

intensity of (111) orientation is more with dry $CdCl_2$ treatment than obtained with wet $CdCl_2$ treatment.

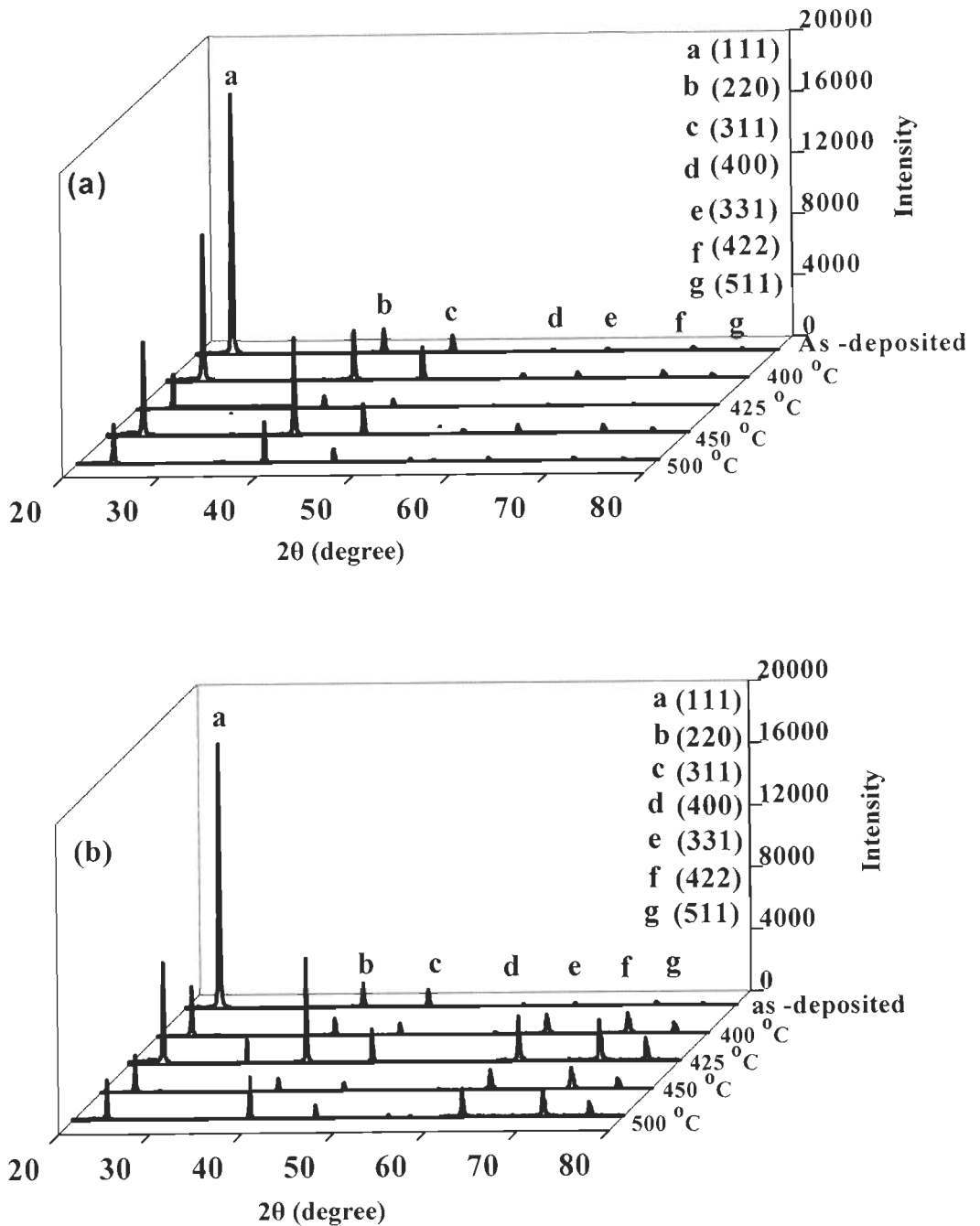


Figure 7.5: XRD patterns of CdTe films treated with (a) Wet $CdCl_2$ and (b) Dry $CdCl_2$

The texture coefficients of the orientations of CdTe films is calculated by using equation (3.7), chapter 3. Figure 7.6(a) shows the texture coefficients (TC) of all the orientations of CdTe films heat treated at 400, 425, 450 and 500 °C with wet $CdCl_2$

treatment. The texture coefficients of orientations of as-deposited CdTe film are also shown. It is clearly seen that the as deposited films are preferentially oriented to $\langle 111 \rangle$ plane. With application of heat treatment, TC of (111) plane decreases and those of other planes increases. The lowest TC of (111) plane is obtained at 450°C with wet CdCl_2 treatment. For the layers heat treated at temperatures $> 450^\circ\text{C}$, the TC of all the planes are almost constant. It suggests that the TC of CdTe planes above 450°C is independent of heat treatment temperature.

Figure 7.6(b) shows the texture coefficients (TC) of all the orientations of CdTe films heat treated at 400 , 425 , 450 and 500°C with dry CdCl_2 treatment. For dry CdCl_2 treatment, TC analysis showed that at 425°C crystal planes became randomly oriented. Figure 7.6(b) also shows that the TC of (111) plane was lower in dry CdCl_2 treatment than obtained with wet CdCl_2 treatment at any given heat treatment temperature. It suggests that the recrystallization was complete at lower temperature. The texture coefficient of (111) plane is found to be minimum at 425°C . At higher heat treatment temperatures there is a little effect on the TC of the (111) plane with dry CdCl_2 treatment. Both treatments show similar trend of texture coefficients.

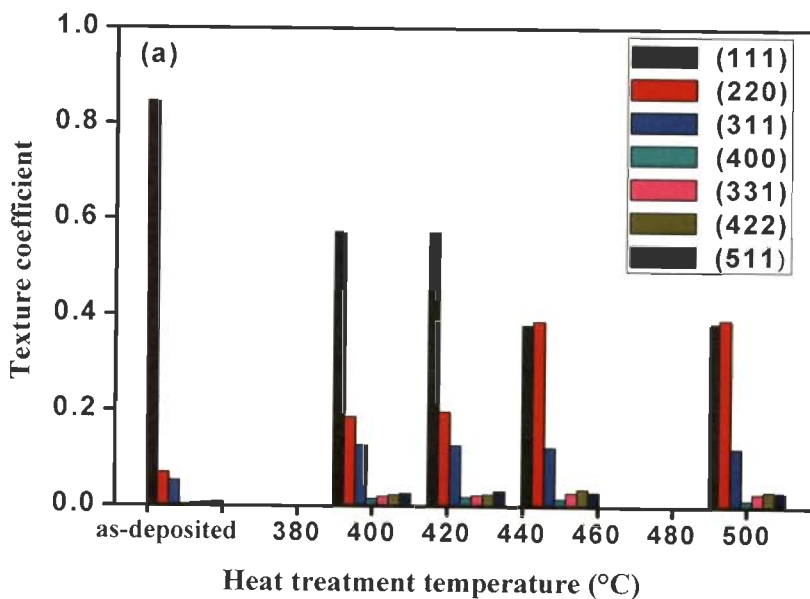


Figure 7.6(a): Texture coefficients of CdTe films with wet CdCl_2 treatment with variation in heat treatment temperature

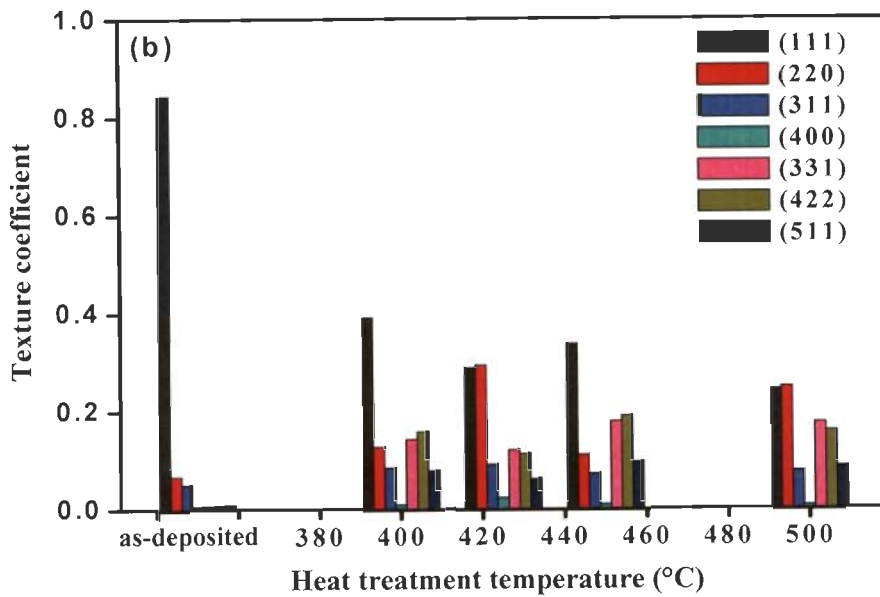


Figure 7.6(b): Texture coefficients of CdTe films at dry $CdCl_2$ treatment with variation in heat treatment temperature

XRD measurements are also used as a gauge for the intermixing and stress in the CdTe layer. As-deposited samples consist of compressive stresses due to lattice and thermal mismatch between the CdTe and underlying layer. The lattice constant of as-deposited CdTe film decreases from 6.500 to 6.478 Å (close to the CdTe bulk lattice constant $a_{CdTe}(bulk) = 6.468$ Å [126]). The decrease in the lattice constant is an indication of decrease or elimination of stress in the films. Lattice parameter may also decrease because of the intermixing of $Zn_{0.1}Cd_{0.9}S$ and CdTe layers. The $CdCl_2$ heat treatment improves the $Zn_{1-x}Cd_xS/CdTe$ junction by enhancing the inter-diffusion.

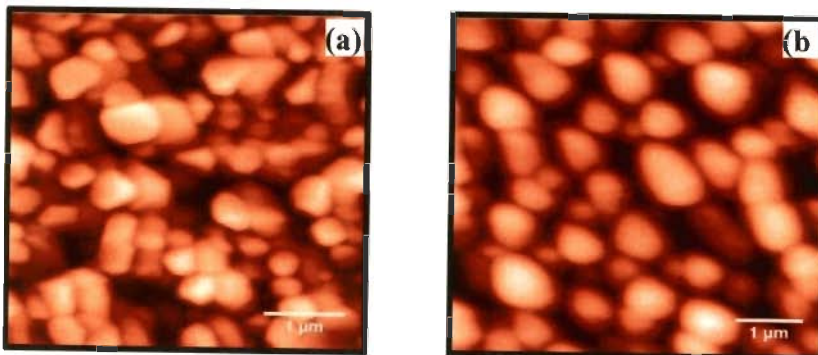
7.5.2 Surface Morphology-Grain Enhancement

Figure 7.7(a) shows AFM images of the surface of as-deposited CdTe films. As-deposited film showed a grains size of ~ 0.3 μm . The grain size in CdTe films increases with increasing heat treatment temperature due to recrystallization. Figure 7.7(b) shows AFM image of the surface of wet treated CdTe films heat treated at 450 °C. Grain size of the CdTe film heat treated at 450 °C reaches to ~ 0.8 μm with wet $CdCl_2$ treatment. The grain sizes of ~ 0.6 μm were obtained at both 400 and 425 °C for CdTe films (AFM images not shown here). This result is consistent with the study carried by Mendoza-Pérez *et al.* (2006, and 2009) [122, 123]. Their group suggested that the heat treatment

induces a sintering mechanism within the CdTe films that act to decrease inter-grain pore size and increases average grain size. Romeo *et al.* suggested that the creations of new grains are the results of disintegration of some larger grains. They attributed this to the relaxation of excessive strain in the lattice [160]. Their group further suggested that the coalescence of small grains into bigger ones is caused by the $CdCl_2$ sintering flux and by the high temperature [160]. Efficiency of the CdTe solar cells is improved by larger grain sized structure as it leads to the reduction in charge carrier trapping in grain boundaries. At heat treatment temperature of $\sim 500^\circ C$ grain size remains almost constant. It is due to the fact that $CdCl_2$ acts as sintering agent which vaporized at temperature $> 490^\circ C$ [159]. This temperature is the eutectic temperature between $CdCl_2$ and CdTe. The rms surface roughness of 40 nm at $450^\circ C$ was obtained for wet treated samples.

Figure 7.7(c), 7.7(d), 7.7(e), and 7.7(f) shows AFM images of the surface of CdTe films heat treated at 400, 425, 450, and $500^\circ C$ respectively with dry $CdCl_2$ treatment. Significant grain growth has been observed with dry $CdCl_2$ treatment when compared to as-deposited and wet treated cells. Grain size of $\sim 2.0 \mu m$ is obtained at $400^\circ C$. This growth further continued and grain size reaches to $\sim 3.5 \mu m$ at $425^\circ C$. Thereafter grain size remains almost constant with increase in heat treatment temperature. The surface roughness increases from 20 to 32 nm when treatment temperature increases from 425 to $500^\circ C$ for dry $CdCl_2$ treatment. The rms surface roughness was lower for dry treated cells compared to wet treated cells at all considered heat treatment temperatures.

The present results indicate that the amount of chlorine does play an important role in grain growth. A smaller amount of chlorine implies less stress in the films, and slower recrystallization process. For wet $CdCl_2$ treated samples there was a small amount of residual chlorine on the samples during the heat treatment. Since temperature is responsible for recrystallization, increase in heat treatment temperature results into the increased average grain size irrespective of the treatment type.



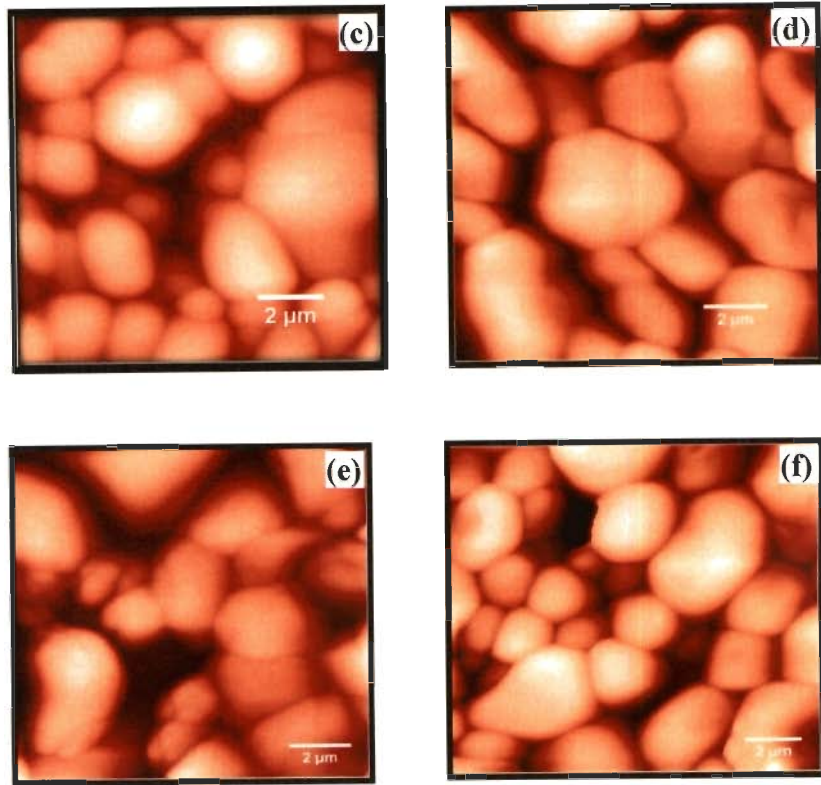


Figure 7.7: AFM images of CdTe films: (a) as-deposited, (b) wet $CdCl_2$ treated at $450\text{ }^\circ\text{C}$, and (c)-(f) dry $CdCl_2$ treated at $400\text{-}500\text{ }^\circ\text{C}$.

Figure 7.8(a) shows the optical transmittance of CdTe films annealed at four different temperatures with dry $CdCl_2$ treatments. For the optical measurements CdTe films were deposited on ITO/Glass substrate only. The abrupt absorption edge $\sim 800\text{ nm}$, corresponding to CdTe energy band gap is observed. Transmittance edge shifts to longer wavelength at higher heat treatment temperatures. This shift in the transmittance edge can be attributed to increase in grain sizes which is due to increase in heat treatment temperatures. Average transmittance also reduces with increase in the heat treatment temperature. Figure 7.8(b) shows the average percentage transmission at absorption wavelength of both the wet and dry treated samples. Samples treated with dry $CdCl_2$ treatment were found to have lower average transmittance for all heat treatment temperatures compared to wet $CdCl_2$ treatment.

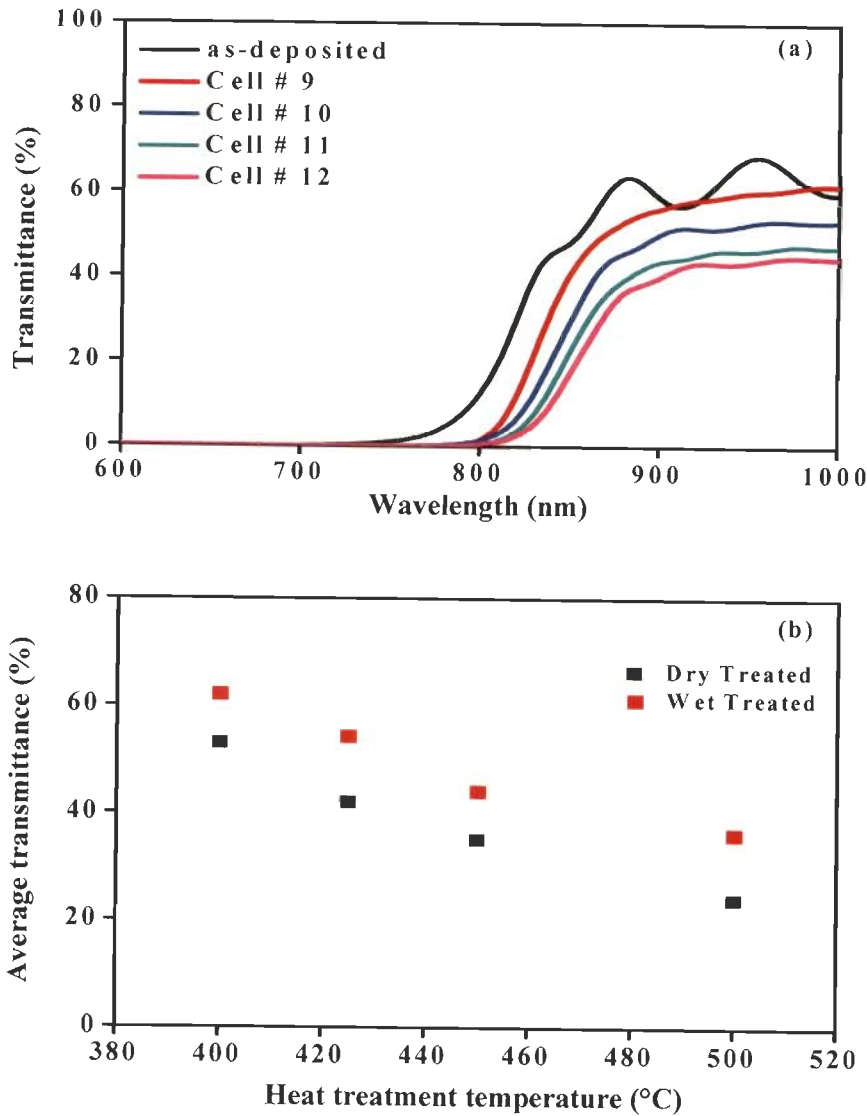


Figure 7.8: (a) Transmittance of CdTe films with temperature for dry $CdCl_2$ treatment and (b) Average transmittance of CdTe films for both wet and dry $CdCl_2$ treatment

7.5.3 Solar Cell Performance with $CdCl_2$ Treatment

The $CdCl_2$ treatment improves the structural and morphological properties of the CdTe layer such as recrystallization, interdiffusion and grain growth, as discussed in previous section. It eventually results in a significant increase in photo conversion efficiency (η). The average of three cells has been taken for identical processing conditions. The photo conversion efficiencies of cells fabricated with as-deposited CdTe layer had very poor efficiencies ($\eta < 1\%$).

7.5.3.1 Wet $CdCl_2$ treatment

Figure 7.9(a), (b), (c) and (d) shows the effect of variation in heat treatment temperature on photo conversion efficiency (η), fill factor (FF), short circuit current density (J_{sc}) and open circuit voltage (V_{oc}) in wet $CdCl_2$ treatment. With wet $CdCl_2$ treatment, several dipping parameters were varied, such as solution concentration, treatment time. However, no significant difference in cell efficiency with the variation of solution concentration or treatment time was observed. The photo conversion efficiency, η remains almost constant at $\sim 2.4\%$ with increase in heat treatment temperature from 400 to 425 °C. Higher photo conversion efficiency of 3.1% is obtained at 450 °C. The increase in η at 450 °C is attributed to the increased grain size of the CdTe film. It however, rapidly reduces at 500 °C and reaches to 1.65%. Figure 7.9(b) shows that the fill factor (FF) follows the similar trend (as of photo conversion efficiency) with variation in heat treatment temperature. The maximum $FF \sim 38\%$ is obtained at 450 °C. Figure 7.9(c) shows that the short circuit density (J_{sc}) remains low (11.5 mA/cm^2) for the heat treatment temperatures ≤ 425 °C. J_{sc} increases from 11.5 to 13 mA/cm^2 when heat treatment temperature from 425 to 450 °C. This increase in J_{sc} might be due to higher conductivity of the window/absorber layer. It is shown in section 7.5.4, that the series resistance of the wet treated cells decreases when heat treatment temperatures increases from 425 to 450 °C. It suggests the low recombination of carriers at 450 °C, which in turn increases the photo conversion efficiencies. Thereafter, J_{sc} decreases to 10 mA/cm^2 at 500 °C. It can also be seen from figure 7.9 (d), that the open circuit voltage, (V_{oc}) has decreased substantially at 500 °C. V_{oc} decreases from 617 to 535 mV with increase in heat treatment temperature from 450 to 500 °C. The reason for the relatively low efficiency is low values of V_{oc} and J_{sc} probably caused by the small grain size of these films and consequent increase in grain boundary area. Diffusion of impurities such as sodium from soda lime glass substrate to TCO layer can also responsible for the deterioration of cell performance at elevated temperatures. The best performing cell with wet $CdCl_2$ treatment was obtained at 450 °C and had an efficiency of 3.1%.

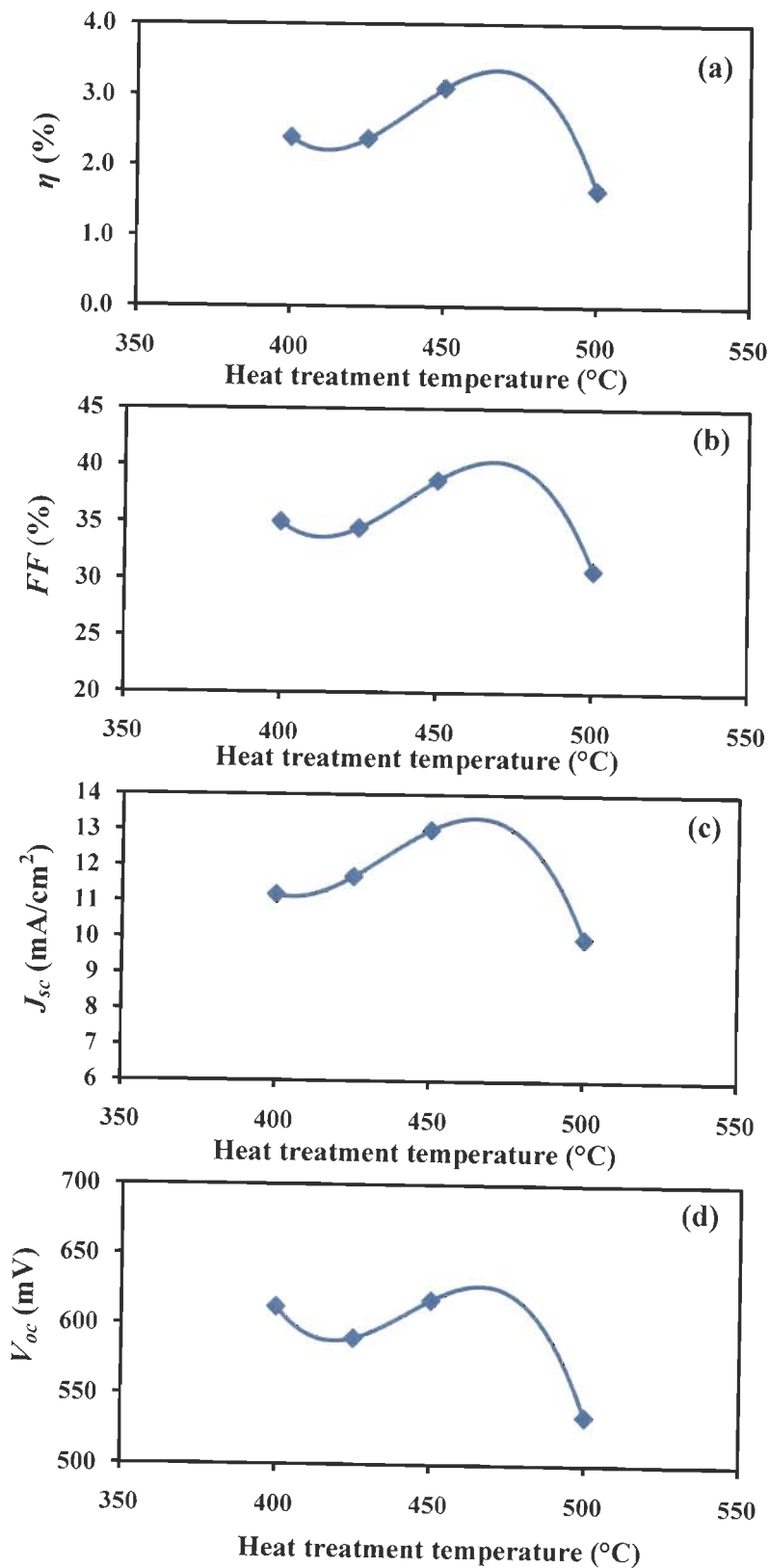


Figure 7.9: Cell parameters of the CdTe/Zn_{0.1}Cd_{0.9}S/ITO/Glass device with wet CdCl₂ treatment: (a) photo conversion efficiency, η (%) (b) fill factor, FF (%) (c) short circuit density, J_{sc} (mA/cm²) and (d) open circuit voltage, V_{oc} (mV)

7.5.3.2 Dry $CdCl_2$ treatment

Figure 7.10(a), (b), (c) and (d) shows the effect of variation in heat treatment temperature on photo conversion efficiency (η), fill factor (FF), short circuit current density (J_{sc}) and open circuit voltage (V_{oc}) in dry $CdCl_2$ treatment. V_{oc} and J_{sc} improves with increase in heat treatment temperature from 400 to 425 °C, this in turn increases the η . The efficiency increase is attributed to both the enhanced grain size of CdTe films and increased inter-diffusion. The highest grain size $\sim 3.5 \mu m$ of CdTe film is obtained at 425 °C (figure 7.7). The large grain sized structure results in lesser grain boundaries which significantly reduces the carrier trapping [105]. The interdiffusion between the CdTe and $Zn_{0.1}Cd_{0.9}S$ increases with increase in heat treatment temperature. This interdiffusion can lead to the reduction in lattice mismatch between the CdTe and $Zn_{0.1}Cd_{0.9}S$ layer. Both factors results in improved η at 425 °C. Best cell in this group results in photo conversion efficiency of 5.2% at 425 °C. With increase in temperature from 425 to 450 °C, η decreases from 5.2 to 3.6%.

It is seen from AFM that heat treatments above 425 °C have little effect on the grain size. Thus grain size effect does not contribute any more to increase photo conversion efficiencies for temperatures > 425 °C. With the application of heat treatment the sulphur diffuses from $Zn_{0.1}Cd_{0.9}S$ layer to CdTe film. The sulphur diffusion increases at higher rate with increasing heat treatment temperatures. This can lead to situation where the consumption of $Zn_{0.1}Cd_{0.9}S$ by CdTe film can takes place. It reduces the lower wavelength cutoff region and can be responsible for reduced efficiencies at higher heat treatment temperatures. In addition to sulphur, sodium diffusion from glass substrate to TCO, can takes place at higher processing temperatures [171]. Diffusion of elements from different layers of device eventually results in the overall reduction in the cell performance.

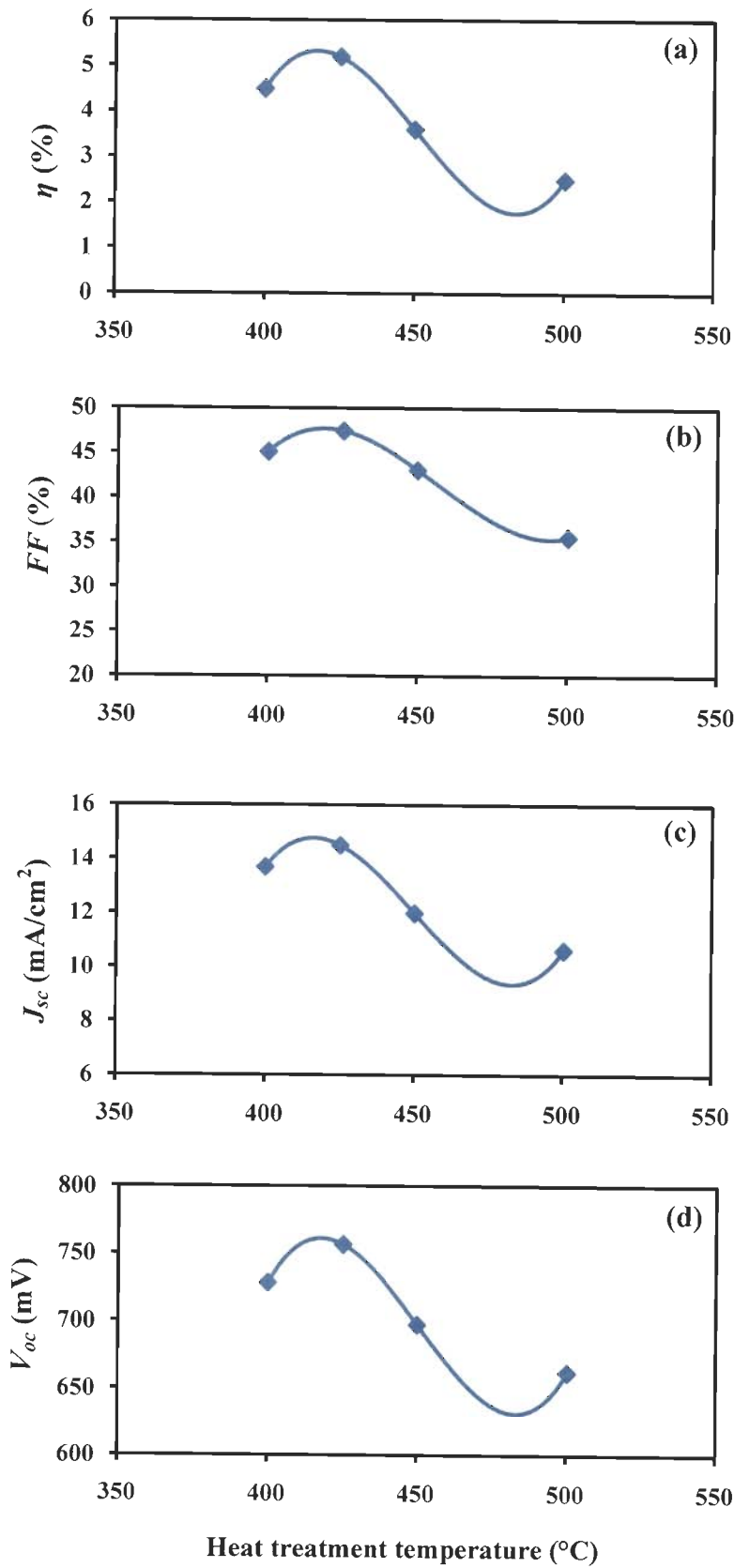


Figure 7.10: Cell parameters of the CdTe/Zn_{0.1}Cd_{0.9}S/ITO/Glass device with dry CdCl₂ treatment: (a) photo conversion efficiency, η (%) (b) fill factor, FF (%) (c) short circuit density, J_{sc} (mA/cm²) and (d) open circuit voltage, V_{oc} (mV)

In the present study, dry $CdCl_2$ treatment was found to be more effective than wet treatment. The highest efficiency (5.2% at 425 °C) in dry $CdCl_2$ treatment is obtained at lower temperature than in wet $CdCl_2$ treatment (3.1% at 450 °C). XRD studies confirmed that the dry treatment is more effective in recrystallization than the wet $CdCl_2$ treatment. It is mentioned earlier that recrystallization strongly depends upon the amount of chlorine. In the dipping process during wet $CdCl_2$ treatment, the chlorine is limited only to residual layer on the film surface. In addition, for dry treatment, cells are subjected to heat treatment for 5 minutes while for wet treatment the heat treatments were carried out for 30 minutes. Thus most of the layer is expected to evaporate away from the film in wet treatment as it is exposed for longer time and recrystallization was not effective for wet treated samples. Thus the use of dry $CdCl_2$ treatment provides two fold benefits: (i) higher efficiencies and (ii) lower processing temperature.

7.5.4 Series Resistances (R_s) of Wet and Dry Treated Cells

Series resistances of the cells are calculated by the method shown in appendix A4.3. The series resistances of cells (under illumination) with wet and dry $CdCl_2$ heat treatment temperatures are shown in Table 7.4.

Table 7.4: Series resistances of the cells with wet and dry $CdCl_2$ treatment

| Cell | Processing conditions | | |
|---------|-----------------------------|-------------|--------------------------|
| | CdCl ₂ treatment | Temperature | Series resistance, R_s |
| | wet/dry | (°C) | ($\Omega\text{-cm}^2$) |
| Cell#1 | wet | 400 | 23.5 |
| Cell#2 | wet | 425 | 23.0 |
| Cell#3 | wet | 450 | 24.0 |
| Cell#4 | wet | 500 | 45.0 |
| Cell#9 | dry | 400 | 13.0 |
| Cell#10 | dry | 425 | 5.5 |
| Cell#11 | dry | 450 | 21.0 |
| Cell#12 | dry | 500 | 27.0 |

The minimum series resistance of 5.5 and 24 $\Omega\text{-cm}^2$ at 425 and 450 $^\circ\text{C}$ are extracted for dry and wet treated cells respectively. For wet CdCl_2 treatment, the series resistance does not vary appreciably and remains at $\sim 24 \Omega\text{-cm}^2$ for treatment temperatures $\leq 450 \text{ }^\circ\text{C}$. However, it shoots to 45 $\Omega\text{-cm}^2$ at 500 $^\circ\text{C}$ and is responsible for the degradation in cell efficiency. For dry CdCl_2 treatment, series resistance decreases from 13 to 5 $\Omega\text{-cm}^2$, when treatment temperature increases from 400 to 425 $^\circ\text{C}$. The decreased series resistance shows that there is decrease in recombination current of the cell which results in the photo conversion efficiency of 5.2%. It is due to higher grain size and the reduction of the defects, which causes carrier trapping in CdTe films. The higher obtained efficiency is also attributed to the improvement in V_{oc} . The V_{oc} increases with higher uniformity of device layers (lesser shunting probability). Further increase in heat treatment temperature to 450 $^\circ\text{C}$ results in the higher series resistances (21 $\Omega\text{-cm}^2$) and thereby resulting in overall efficiency degradation. Lee *et al.* have observed similar behavior of series resistance for as-deposited and methanol CdCl_2 dipped CdS/CdTe cells with variation in heat treatment temperature [98]. Low values of fill factor (for both dry and wet treatment) shown in figure 7.9 and 7.10 indicates that the series resistances of these cells are contributing to poorer cell performance. Figure 7.11 shows the series resistances of the wet and dry CdCl_2 treated cells. It shows that the series resistance for wet treated cells are always higher than dry treated cells at any given heat treatment temperature.

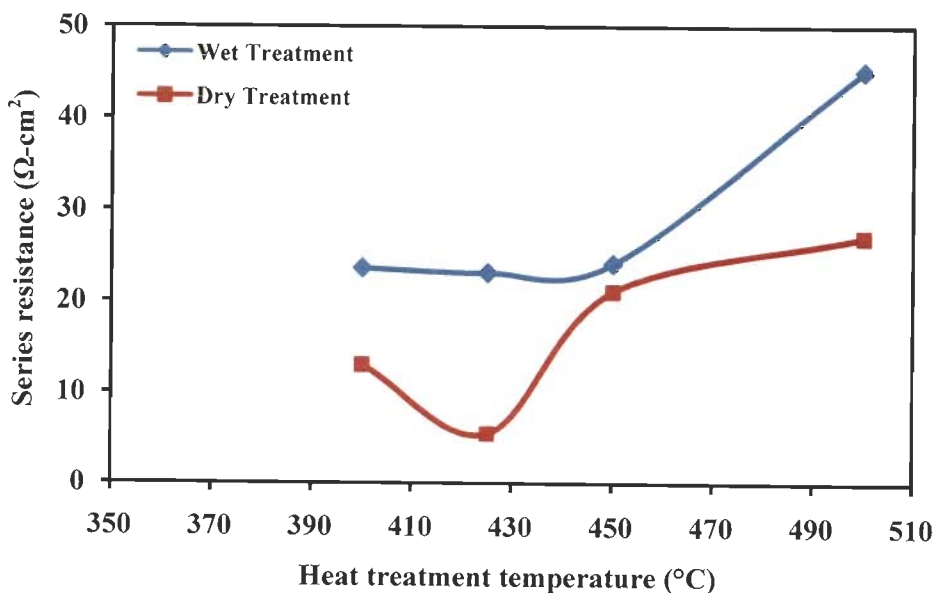


Figure 7.11: Series resistance of the CdTe/ $Zn_{0.1}Cd_{0.9}S$ /ITO/Glass device structure with wet and dry CdCl_2 treatment

7.5.5 Effect of $Zn_{0.1}Cd_{0.9}S$ Film Thickness on Cell Parameters

Depending on the thickness of the window layer some of the light above the energy band gap can still pass through to the CdTe giving additional current to the device. The reduction of layer thickness is then important to gain more photons in CdTe, but on the other hand the uniform coverage of the TCO and the consumption of layer into CdTe impose the processing limit on the reduction in film thickness of window layer.

This section investigates the effect of $Zn_{0.1}Cd_{0.9}S$ film thickness on solar cell parameters. Film thickness was varied by varying the number of laser shots. Five samples at $Zn_{0.1}Cd_{0.9}S$ film thicknesses of 60, 80, 100, 150, 200 nm were deposited. Since the film thickness is of few nanometers, the transmittance spectra did not showed the fringes in the spectra. Therefore, in this study it was not possible to calculate the film thickness by the Manificier method. Thickness of the films was measured by step profilometer (Ambius Tec., XP 200) with $\pm 5\%$ accuracy. Deposition parameters of $Zn_{0.1}Cd_{0.9}S$ films are shown in Table 7.5. Device fabrication parameters are shown in Table 7.3.

Table 7.5: Deposition parameters of the $Zn_{0.1}Cd_{0.9}S$ film with variation in film thickness

| Cell | Laser shots | Thickness (nm) | Laser flux density (J/cm^2) | Deposition temperature ($^{\circ}C$) | Mole fraction (x) | Base pressure (torr) | Working pressure (mtorr) |
|-----------|-------------|----------------|---------------------------------|--|-------------------|----------------------|--------------------------|
| Cell # 16 | 1200 | 60 | 3.33 | 400 | 0.9 | 5×10^{-6} | 200 |
| Cell # 17 | 1600 | 80 | 3.33 | 400 | 0.9 | 5×10^{-6} | 200 |
| Cell #18 | 2000 | 100 | 3.33 | 400 | 0.9 | 5×10^{-6} | 200 |
| Cell # 10 | 3000 | 150 | 3.33 | 400 | 0.9 | 5×10^{-6} | 200 |
| Cell #19 | 4000 | 200 | 3.33 | 400 | 0.9 | 5×10^{-6} | 200 |

Figure 7.12(a), (b), and (c) shows the AFM images of the $Zn_{0.1}Cd_{0.9}S$ films at 150, 100, and 60 nm film thickness respectively. It is established earlier in chapter 5, that working pressure at 200 mtorr during deposition results in average grain size of ~ 80 nm. $Zn_{0.1}Cd_{0.9}S$ films at 200 (AFM image not shown here) and 150 nm (figure 7.12(a)) have a smooth film surface with nearly uniform grains with grain size ~ 80 -100 nm, and is in corroboration with previous study. Figure 7.12(a) also shows that there are not any

visible pin holes. Average rms roughness ~ 4.2 nm is obtained at 150 nm film thickness. Reducing the film thickness down to 100 nm result in the relatively lesser uniform grains. Rms surface roughness of ~ 10 nm is obtained at the film thickness of 100 nm. However there are few pin holes observed in the film at this thickness. With further decrease in film thickness to 60 nm, surface roughness increases sharply and reaches to 24 nm. In addition to the increased surface roughness pin holes are clearly observed in the films.

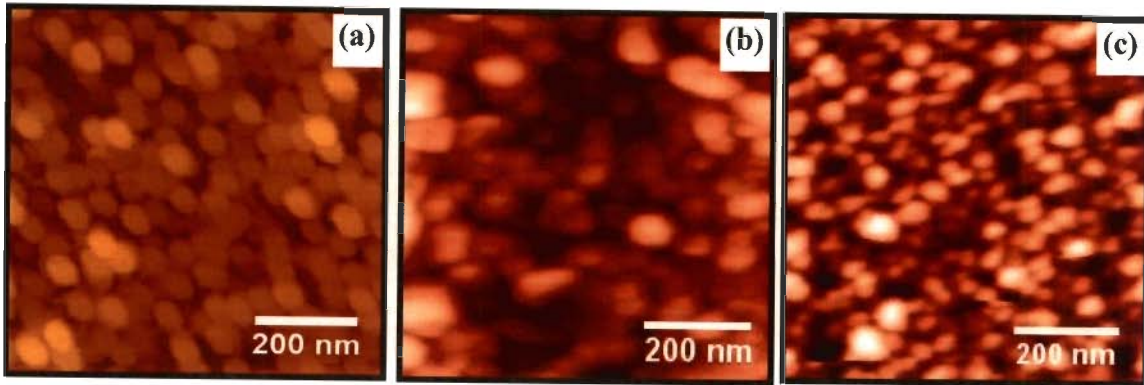


Figure 7.12: AFM image of the $Zn_{0.1}Cd_{0.9}S$ layer structure with varying film thickness: (a) 150, (b) 100, and (c) 60 nm

Figure 7.13 (a), (b), (c) and (d) shows the effect of variation in $Zn_{0.1}Cd_{0.9}S$ films thickness on photo conversion efficiency (η), fill factor (FF), short circuit current density (J_{sc}) and open circuit voltage (V_{oc}). With decreasing $Zn_{0.1}Cd_{0.9}S$ film thickness from 200 to 150 nm there is an increase in J_{sc} . This in turn increases the η from 4.8 to 5.2%. It has been previously reported that the thinner CdS films results in a better short response wavelength [58, 63, 94]. With the use of $Zn_{0.1}Cd_{0.9}S$ films instead of CdS adds one more dimension to improve the short wavelength response as it will allow high energy photons to reach the CdTe film. $Zn_{0.1}Cd_{0.9}S$ film with 100 nm film thickness leads to increase in J_{sc} accompanying a reduction in V_{oc} and FF , thereby reducing overall efficiency of the cell (3.73%). Further reduction in $Zn_{0.1}Cd_{0.9}S$ film thickness down to 80 nm, V_{oc} reduces drastically, resulting in the net decrease in photo conversion efficiency reaching to 2.45%, primarily due to reduction in V_{oc} and fill factor along with some decrease in J_{sc} . Film thickness at 60 nm, results in delaminated efficiencies ($\eta \ll 1\%$).

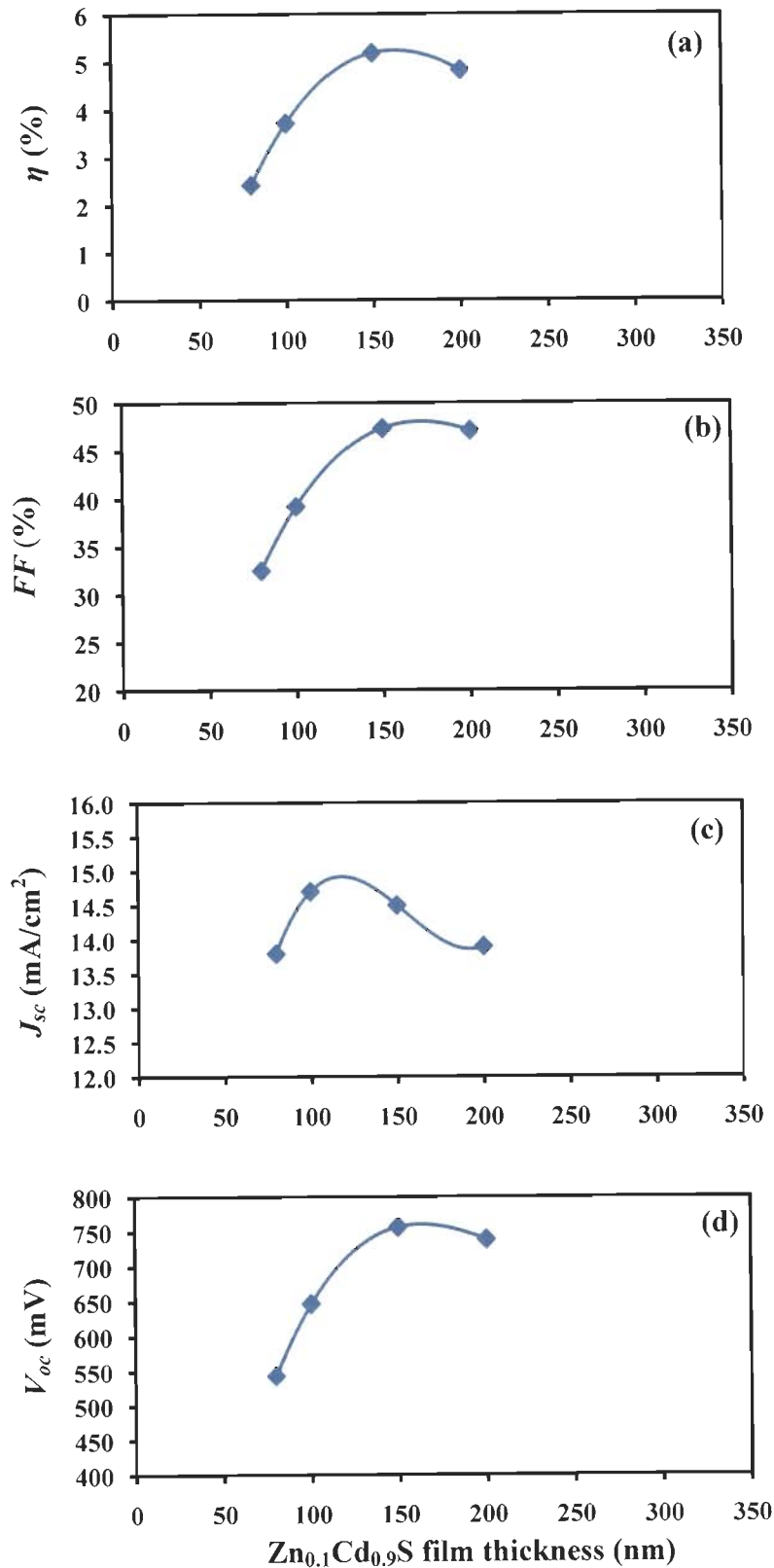


Figure 7.13: Cell parameters of the CdTe/ $Zn_{0.1}Cd_{0.9}S$ /ITO/Glass device with variation in $Zn_{0.1}Cd_{0.9}S$ film thickness: (a) photo conversion efficiency, η (%) (b) fill factor, FF (%) (c) short circuit density, J_{sc} (mA/cm^2) and (d) open circuit voltage, V_{oc} (mV)

Window layer acts like a dead layer to the photo generated carriers. Thicker films absorb more high energy photons while thinner films (< 100 nm) leads to poor cell efficiencies. With reduced film thickness, the probability of pin holes in $Zn_{0.1}Cd_{0.9}S$ film increases. Pin holes generates a direct contact between ITO and CdTe layer and are responsible for providing low shunt resistance values. Low shunt resistance values results in the decrease in V_{oc} and FF . In addition $Zn_{0.1}Cd_{0.9}S$ film is deposited on ITO substrate, which can aggravate the pin holes problem in thinner films. Ruggeberg *et al.* reported that built in voltage reduces for ITO/CdTe direct contact [164]. Sites et al, with the aid of $I-V$ simulation results have shown that V_{oc} reduces at low CdS thickness [179]. It is due to this reason that efficiency decreases at 100 nm film thickness, in spite of observed higher short circuit density.

7.5.6 Series Resistance (R_s) of Cells with Variation in $Zn_{0.1}Cd_{0.9}S$ Film Thickness

The series resistances of $Zn_{0.1}Cd_{0.9}S/CdTe$ (under illumination) solar cells with variation in $Zn_{0.1}Cd_{0.9}S$ film thickness are shown in Table 7.6.

Table 7.6: Series resistance of cells with $Zn_{0.1}Cd_{0.9}S$ film thickness

| Cell | Thickness (nm) | Series Resistance, R_s ($\Omega\text{-cm}^2$) |
|-----------|-------------------|--|
| Cell # 16 | 60 | --- |
| Cell # 17 | 80 | 22.0 |
| Cell #18 | 100 | 15.0 |
| Cell # 10 | 150 | 5.5 |
| Cell #19 | 200 | 12.0 |

Figure 7.14 shows the series resistance, R_s of the cells with variation in $Zn_{0.1}Cd_{0.9}S$ film thickness. Minimum $R_s \sim 5.5 \Omega\text{-cm}^2$ is obtained at 150 nm film thickness. Increase in film thickness to 200 nm results in the higher series resistance and is attributed to the increased bulk resistance of the $Zn_{0.1}Cd_{0.9}S$ film. Series resistance, R_s was highest $\sim 22 \Omega\text{-cm}^2$ at 80 nm film thickness. Higher series resistance ($22 \Omega\text{-cm}^2$) at film thickness of 80 nm is responsible for very low FF and leads to overall reduction in efficiency. Nakamura *et al.* observed a sharp reduction in FF for the CdS film thickness below 85 nm [131]. Decreasing $Zn_{0.1}Cd_{0.9}S$ film thickness results in the decreased grain

size (as seen from AFM images). This decrease in grain size also leads to the deterioration of the crystallinity of CdTe films and increased roughness of the CdTe films. This combined effect raises the defects in the films and thus increases the series resistance. For very low film thickness (~ 60 nm) the entire $Zn_{0.1}Cd_{0.9}S$ layer could be consumed by CdTe in forming the interfacial layer, delaminating the cell efficiencies.

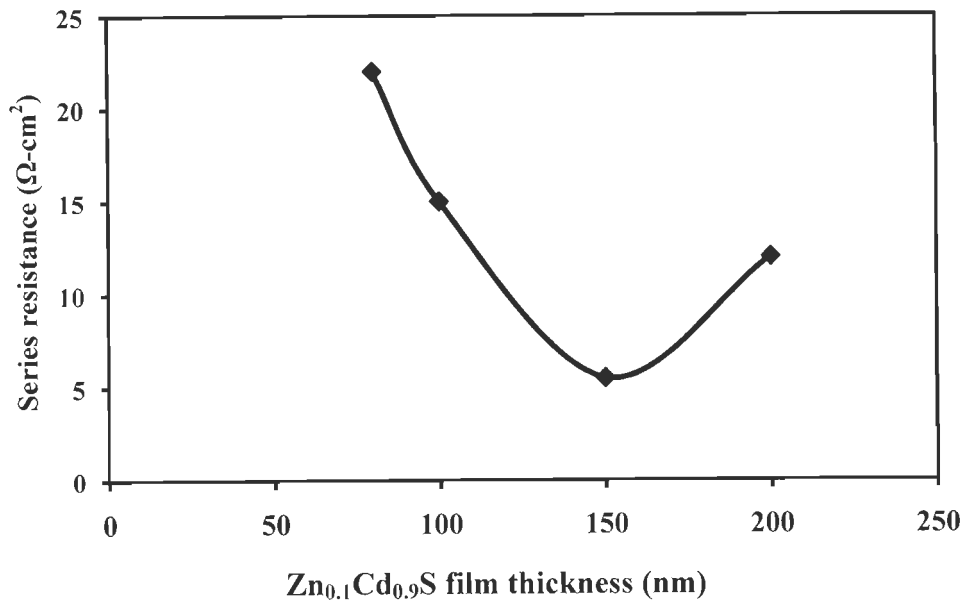


Figure 7.14: Series resistance of the CdTe/ $Zn_{0.1}Cd_{0.9}S$ /ITO/Glass device structure with $Zn_{0.1}Cd_{0.9}S$ film thickness

7.5.7 Effect of $Zn_{0.1}Cd_{0.9}S$ Film Deposition Temperature on Cell Parameters

This section investigates the effect of deposition temperature of $Zn_{0.1}Cd_{0.9}S$ film on the solar cell parameters. Four cells with deposition temperatures at 350, 400, 450 and 500 °C were fabricated. Compositional, structural and optical properties of $Zn_{0.1}Cd_{0.9}S$ layer with deposition temperature have already been discussed in section 5.4. Parameters utilized for deposition of $Zn_{0.1}Cd_{0.9}S$ film are shown in Table 7.7. Device fabrication parameters are shown in Table 7.3.

Table 7.7: Processing parameters of $Zn_{0.1}Cd_{0.9}S$ film with variation in deposition temperature

| Cell | Deposition temperature (°C) | Film thickness (nm) | Laser flux density (J/cm^2) | Mole fraction (x) | Base pressure (torr) | Working pressure (mtorr) |
|----------|-----------------------------|---------------------|---------------------------------|-------------------|----------------------|--------------------------|
| Cell #21 | 350 | 150 | 3.33 | 0.9 | 5×10^{-6} | 200 |
| Cell #10 | 400 | 150 | 3.33 | 0.9 | 5×10^{-6} | 200 |
| Cell #22 | 450 | 150 | 3.33 | 0.9 | 5×10^{-6} | 200 |
| Cell #23 | 500 | 150 | 3.33 | 0.9 | 5×10^{-6} | 200 |

When $Zn_{0.1}Cd_{0.9}S$ layer is made by pulsed laser deposition technique, deposition temperatures as low as 200 °C can be used, since the stoichiometry of $Zn_{0.1}Cd_{0.9}S$ layer is assured by the process itself. Nevertheless, the deposition of materials at moderate temperature guarantees high crystalline quality, due to the high adatoms superficial diffusion coefficient [32]. Figure 7.15(a) & (b) shows the AFM images of $Zn_{0.1}Cd_{0.9}S$ film at deposition temperatures of 400 and 500 °C. Deposition at 400 °C results in the uniformed grained structure. Deposition at 500 °C results in the non-uniformed grains with pinholes. Rms surface roughness of 4.0, 4.2, 5.8, and 18 nm were obtained at 350, 400, 450 and 500 °C respectively. It was seen that the roughness was lower for deposition temperature ≤ 450 °C. It increases sharply to 18 nm at 500 °C respectively. This increase in surface roughness is due to the non uniform grains.

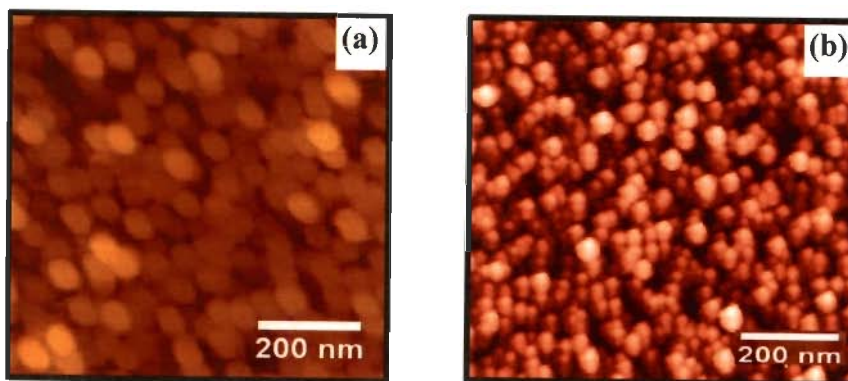
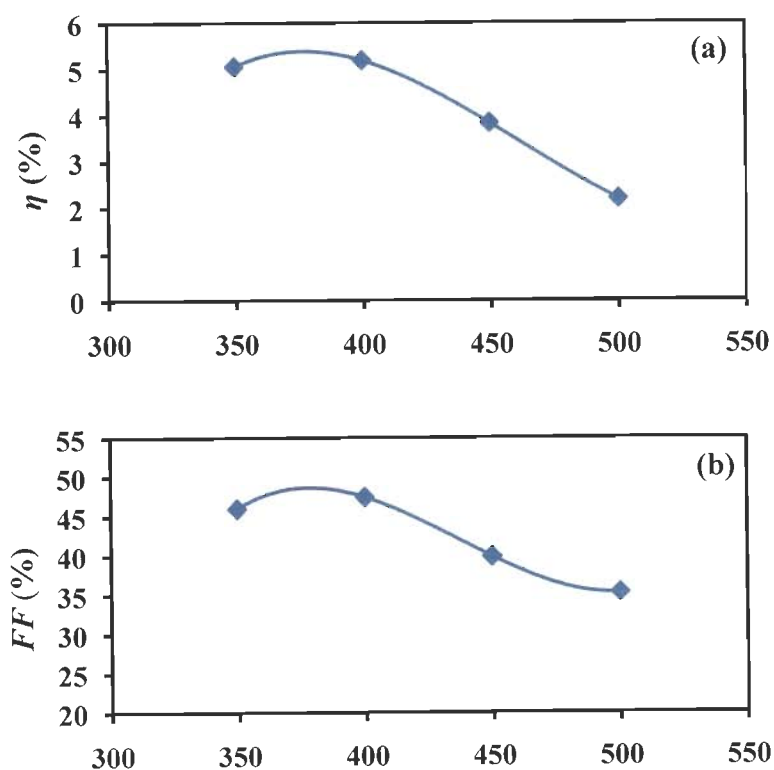


Figure 7.15: AFM image of the $Zn_{0.1}Cd_{0.9}S$ layer with deposition temperature (a) 400 and (b) 500 °C

Figure 7.16(a), (b), (c) and (d) shows the effect of variation in deposition temperatures of $Zn_{0.1}Cd_{0.9}S$ films on photoconversion efficiency (η), fill factor (FF), short circuit current density (J_{sc}) and open circuit voltage (V_{oc}). The surface morphology of

deposited films was similar at both 350 to 400 °C. The compact and uniform $Zn_{0.1}Cd_{0.9}S$ films results in better efficiencies. Photo conversion efficiency increases by 2.56% from 350 to 400 °C (η was 5.07% at 350 °C; 5.20% at 400 °C). With increase in deposition temperature from 400 to 450 °C, there is a slight increase in V_{oc} and can be attributed to improved interface properties. However the overall efficiency decreases and is due to reduction in both J_{sc} and FF . The photo conversion efficiency decreases drastically at 500 °C and reaches to 2.2%. This drastic decrease in photo conversion efficiency can be attributed to very poor quality of $Zn_{0.1}Cd_{0.9}S$ films.

It is established earlier in chapter 5, that $Zn_{0.1}Cd_{0.9}S$ films at 500 °C were crystalline and thus should not contribute to deterioration of cell efficiency. It is therefore suggested that the $Zn_{0.1}Cd_{0.9}S$ film thickness does play an important role in governing the cell photo conversion efficiency. The films which were investigated earlier were deposited at film thickness of ~ 500 nm. The considered film thickness for PV applications is ~ 150 nm. At higher deposition temperature there can be the partial consumption of $Zn_{0.1}Cd_{0.9}S$ film by CdTe layer. With increase in temperature, in addition to the $Zn_{0.1}Cd_{0.9}S$ film consumption, various impurities also inter-diffuse from glass substrate, this eventually degrades the cell performance.



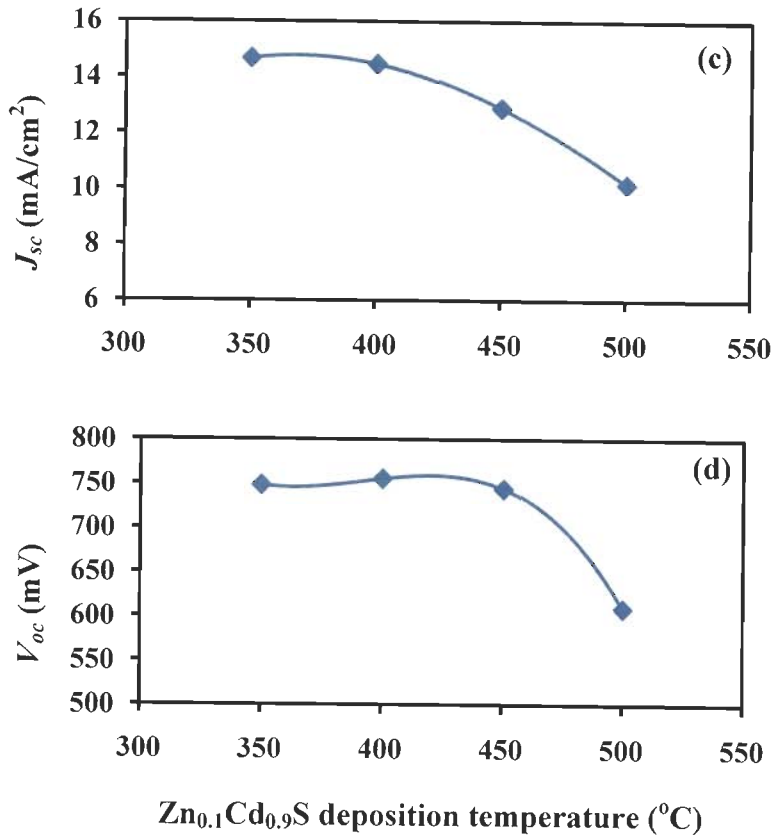


Figure 7.16: Cell parameters of the CdTe/ $Zn_{0.1}Cd_{0.9}S$ /ITO/Glass device with variation in $Zn_{0.1}Cd_{0.9}S$ film deposition temperature: (a) photo conversion efficiency, η (%) (b) fill factor, FF (%) (c) short circuit density, J_{sc} (mA/cm^2) (d) open circuit voltage, V_{oc} (mV)

7.5.8 Series Resistance (R_s) of Cells with $Zn_{0.1}Cd_{0.9}S$ Film Deposition Temperature

The series resistances of $Zn_{0.1}Cd_{0.9}S$ /CdTe (under illumination) solar cells with $Zn_{0.1}Cd_{0.9}S$ film deposition temperature are shown in Table 7.8.

Table 7.8: Series resistance of the cells with variation in $Zn_{0.1}Cd_{0.9}S$ film deposition temperatures

| Sample | Deposition Temperature | Series Resistance ($\Omega\text{-cm}^2$) |
|----------|------------------------|--|
| Cell #21 | 350 °C | 6.0 |
| Cell #10 | 400 °C | 5.5 |
| Cell #22 | 450 °C | 16.0 |
| Cell #23 | 500 °C | 32.0 |

Figure 7.17 shows the series resistance, R_s of the cells with variation in $Zn_{0.1}Cd_{0.9}S$ film deposition temperatures. It is observed that there is no significant change in R_s with increase in deposition temperature from 350 to 400 °C. Series resistance of 6.0 and 5.5 $\Omega\text{-cm}^2$ are obtained at deposition temperatures of 350 and 400 °C. It is due to the similar crystalline quality, surface roughness and particle size of the films. It increases to 16.0 $\Omega\text{-cm}^2$ at 450 °C, and can be attributed to the increased grain size of the $Zn_{0.1}Cd_{0.9}S$ films. Highest series resistance $\sim 32 \Omega\text{-cm}^2$ is obtained at 500 °C. Increased surface roughness is responsible for the degradation in cell efficiency. High deposition temperature leads to higher intermixing of $Zn_{0.1}Cd_{0.9}S$ and CdTe layer and could be responsible for the overall cell efficiency degradation. It is also important to note that high temperature processing conditions also facilitate the diffusion of impurities from glass and are responsible for reduced efficiencies. All these factors altogether increases the series resistance of the cells.

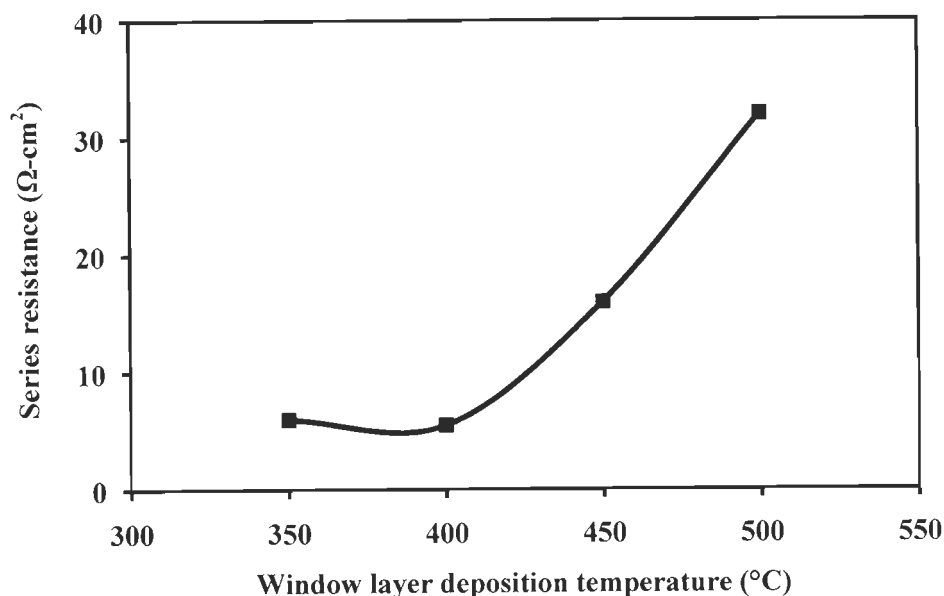


Figure 7.17: Series resistance of the CdTe/ $Zn_{0.1}Cd_{0.9}S$ /ITO/Glass device structure with $Zn_{0.1}Cd_{0.9}S$ film deposition temperature

7.6 IDENTIFICATION OF EFFICIENCY LIMITING FACTORS

The objective of this work is to study the effect of $CdCl_2$ treatment and $Zn_{0.1}Cd_{0.9}S$ layer properties on $Zn_{0.1}Cd_{0.9}S$ /CdTe solar cells. From the present results it can be suggested that there exist some factors which limit the efficiencies to meet their present level. The comparatively lower efficiencies obtained in this work could be of the following reasons:

- i) The first and foremost limiting factor can be identified as the poor conductivity of $Zn_{0.1}Cd_{0.9}S$ nanocrystalline thin films when compared to CdS. Though it was not possible to measure the conductivity behaviour of $Zn_{0.1}Cd_{0.9}S$ with mole fraction in this work, it is well established in previous reports, also discussed earlier in section 1.4, the resistive nature of the $Zn_{1-x}Cd_xS$ nanocrystalline thin films increases with increase in mole fraction. The higher series resistances obtained in this work is in corroboration of the above argument.
- ii) Back contact to CdTe can also deteriorate the cell performance. With high electron affinity ($\chi = 4.4$ eV) and high energy band gap (1.45 eV), a high work function metal is required to make good Ohmic contact to CdTe. Most metals, however, do not have sufficiently high work functions and therefore form Schottky-barrier contacts to CdTe absorber layers. Same is also discussed earlier in appendix A1.6. When the Fermi level at the metal/CdTe interface is pinned by surface states, a metal with a reasonably high work-function might not make an Ohmic contact. Recent studies have shown that the zinc telluride (ZnTe) and antimony telluride (Sb_2Te_3) as back contact to CdTe layer results in the enhanced efficiencies [53]. The use of graphite paste as back contact in this work might not lead to the pure Ohmic junction characteristic. In such situations the cell efficiencies degrades quickly;
- iii) ITO was used in this work as the front transparent conducting electrode (TCO). The higher efficiency from CdTe cells also requires change in the TCO properties. The highest efficiency CdTe cell fabricated by NREL utilizes the Cd_2SnO_4/Zn_2SnO_4 as TCO. The non availability of such TCO's could also limit the efficiencies;
- iv) It is also important to note that the solar concentrators are not used in this work which also limits in achieving the higher efficiencies;
- v) No special contact designing procedure was opted in this work to reduce the series resistance of the cell, which also degrade the cell performance.

Nevertheless, the present results show the successful incorporation of $Zn_{0.1}Cd_{0.9}S$ film as window layer of thin film solar cell structure.

7.7 SUMMARY

This chapter presents the fabrication and characterization of CdTe/ $Zn_{0.1}Cd_{0.9}S$ /ITO/Glass solar cell. Before the use of as-prepared $Zn_{0.1}Cd_{0.9}S$ thin films for device fabrication, a test has been taken to check the coverage quality of $Zn_{0.1}Cd_{0.9}S$ film by recording the I - V characteristic of Au/ $Zn_{0.1}Cd_{0.9}S$ /ITO stack. The Schottky characteristic shows that the $Zn_{0.1}Cd_{0.9}S$ film is free of pinholes. This test was found capable of detecting the suitable area for back contact deposition. Pre-heat treatment of $Zn_{0.1}Cd_{0.9}S$ /ITO stack did not alter the interface properties. This ensures that $Zn_{0.1}Cd_{0.9}S$ /ITO interface remains Ohmic for the processing temperatures considered in this study.

Cell activation step i.e. $CdCl_2$ treatment was found to be the dominant step in affecting the cell parameters. Two types of cell activation steps, wet and dry $CdCl_2$ treatment were investigated. Dry $CdCl_2$ treatment was found to be more effective than wet $CdCl_2$ treatment. It is attributed to the higher recrystallization and grain growth observed with dry $CdCl_2$ treatment. Photo conversion efficiency, η of 3.2% is obtained at heat treatment temperature of 450 °C for wet $CdCl_2$ treated cells. It increases appreciably to 5.2% at 425 °C for dry $CdCl_2$ treated cells. With a reduction of $Zn_{0.1}Cd_{0.9}S$ film thickness from 200 to 150 nm, η increases from 4.85 to 5.2% mainly by an increase in short circuit current density, J_{sc} . In contrast, at 100 nm thickness η decreases due to drop in open circuit voltage, V_{oc} and fill factor, FF even after a slight increase in J_{sc} . Increased pin-holes, increased surface roughness of the $Zn_{0.1}Cd_{0.9}S$ films were found to be responsible for the reduction in V_{oc} and FF . Series resistances were also found to vary with variation in cell parameters. Deposition temperature also affects the $Zn_{0.1}Cd_{0.9}S$ layer significantly affects the cell parameters. Deposition at 400 °C results in photo conversion efficiency of 5.2%. Higher deposition temperature (500 °C) results efficiencies close to ~ 2.2%. Moderate deposition temperature results in high crystalline quality, and avoids the diffusion of impurities, from the soda-lime glass substrate. Various efficiency limiting factors have also been identified.

CHAPTER 8

CONCLUSIONS & FUTURE SCOPE

8.1 CONCLUSIONS

The major objective of the present work is to prepare the $Zn_{1-x}Cd_xS$ semiconductor nanostructures for their potential applications in light emission and photovoltaic (PV). In particular the nanoparticles and nanocrystalline thin films of $Zn_{1-x}Cd_xS$ semiconductor are prepared via co-precipitation and pulsed laser deposition technique. The light emission from $Zn_{1-x}Cd_xS$ nanostructures is obtained by the Mn^{2+} incorporation. For PV applications, the $Zn_{1-x}Cd_xS$ nanocrystalline thin films have been utilized as the window layer of CdTe/ $Zn_{1-x}Cd_xS$ /ITO/Glass device structure. The following is a brief summary and conclusions drawn from work carried out in this thesis. The suggestions for the future work are proposed at the end.

In the framework of this thesis, low temperature synthesis of $Zn_{1-x}Cd_xS$ nanoparticles is facilitated via co-precipitation technique. The effects of mole fraction (x) on the structural, optical and emission properties of $Zn_{1-x}Cd_xS$ nanoparticles have been investigated. The following conclusions are made from the above study:

- A gradual shift of XRD peak to lower angles and linear dependence of lattice constant on mole fraction showed the successful formation of $Zn_{1-x}Cd_xS$ ternary nanoparticles. Vegard's law was applied to check the compositional homogeneity in the as-prepared nanoparticles. It was found that the percentage error in lattice constants of as-prepared nanoparticles and theoretical values lies within $\pm 5\%$. The EDS results also confirmed the stoichiometric composition of nanoparticles.
- TEM shows the particle size in the range of 2-5 nm with maxima at 3.5 nm and relative standard deviation of 12-15% while UV-Vis showed particle size in the range of 4-5 nm.
- $Zn_{1-x}Cd_xS$ nanoparticles were found to exhibit quantum confinement and composition effect. Energy band gap (E_g) shifts to higher energies due to quantum confinement effect with respect to their bulk counterparts. E_g varies from 3.91 to 3.02 eV with variation in mole fraction from 0.1 to 0.9. The bowing parameter of $Zn_{1-x}Cd_xS$ nanoparticles is estimated as 0.438 by curve fitting (quadratic) to the obtained energy band gap values.

- The visible light emissions from $\text{Zn}_{1-x}\text{Cd}_x\text{S}$ nanoparticles are obtained in blue and green spectral regions and were defect assisted. The near band edge emissions were obtained in UV spectral regions and shifts from 357 to 390 nm for mole fraction varying from 0.1 to 0.9.

On the basis of above findings it is concluded that the as-prepared $\text{Zn}_{1-x}\text{Cd}_x\text{S}$ nanoparticles are stoichiometric and uniformly distributed. This study provides a confidence of further use of these nanoparticles in the next phase experiments of this work. It is also noteworthy that the only a co-precipitation process in aqueous solution using simple inorganic precursors (metal nitrates and sodium sulfide) is employed. No organic solvents or toxic gases (e.g. H_2S) are involved. Therefore the $\text{Zn}_{1-x}\text{Cd}_x\text{S}$ nanoparticles in the current work are obtained via a “*green pathway*”, which should be considered as an important factor for practical applications.

Next phase of this study presented the deposition of device quality $\text{Zn}_{1-x}\text{Cd}_x\text{S}$ nanocrystalline thin films by pulsed laser deposition technique. In particular the deposition parameters such as laser flux density, working pressure, and deposition temperature have been optimized. Following are the conclusions made from this study:

- It is found that the surface morphology, gauged via rms surface roughness strongly depends upon the laser flux density. Minimum surface roughness ~ 8.0 nm was obtained at laser flux density of 3.33 J/cm^2 . Texture coefficient also shows a highest preferential *c*-axis orientation along (002) plane of wurtzite structure at 3.33 J/cm^2 .
- Working pressure was found to affect particle size of nanocrystalline thin films. Particle size increases ~ 4.5 times of its original value (15 nm), when chamber pressure increases from 0.015 to 200 mtorr.
- A structural phase transformation from zincblende to wurtzite was found to take place in as-deposited films. It is established that the structure transformation temperature decreases with increase in mole. The phase transformation takes place at deposition temperatures greater than 400, 300, and 200 °C at mole fractions 0.1, 0.3, and 0.5 respectively. Increase in mole fraction > 0.5 , results in the wurtzite structure irrespective of considered deposition temperature. Compositional homogeneity of the as-deposited films was also checked by applying Vegard’s law. The close agreement between the obtained and the computed lattice constant values (within $\pm 5 \%$) confirmed the stoichiometric deposition.

This study provides the control on the surface roughness, crystal structure, and particle size which resulted in the device quality films.

The work on light emitting applications includes the incorporation of Mn^{2+} dopant into the $\text{Zn}_{1-x}\text{Cd}_x\text{S}$ host nanostructures. It is experimentally established that the problem encountered to dope Mn^{2+} is caused by the lattice mismatch between dopant ion and semiconducting host. Experiments have been carried out to enhance the light emission from these nanostructures. The following are the results that have been obtained in this work:

- The orange emission (transition from Mn^{2+} incurred states ${}^4T_1 \rightarrow {}^6A_1$) from Mn^{2+} doped $\text{Zn}_{1-x}\text{Cd}_x\text{S}$ nanoparticles shows successful incorporation of dopant into host nanoparticles. Maximum orange emission intensity $\sim 10^5$ (counts) was obtained at mole fraction, $x = 0.45$, with 0.10% lattice mismatch with MnS . It is further validated by the increased manganese incorporation at $x = 0.45$ for comparable doping.
- Mn^{2+} concentration variation at optimized host conditions ($x = 0.45$) results in the enhanced orange emission intensity. The highest intensity was obtained at 5 mol% and it is found that it increases by a factor of ~ 4 with respect to 1 mol% Mn^{2+} concentration.
- A further enhancement in orange emission intensity was obtained via $\text{Zn}_{0.55}\text{Cd}_{0.45}\text{S}/\text{ZnS}$ core-shell nanoparticles. The shell-to-core (s/c) ratio of 0.5 results in emission intensity enhancement by a factor of ~ 15 with respect to the core nanoparticles. The light emission enhancement in core-shell nanoparticles is attributed to the effective surface states passivation. Higher s/c ratio results in the decreased intensities and is attributed to the ZnS defect emissions.
- Mn^{2+} doped $\text{Zn}_{0.55}\text{Cd}_{0.45}\text{S}$ nanocrystalline films consist of well crystallized zincblende phase at deposition temperature as low as 200°C . Since, the deposition temperature of 200°C at $x = 0.45$ results in zincblende structure, light emissions from thin films have been compared from the nanoparticles. The emission intensities of nanocrystalline films are found to be of poorer quality than their counterpart (nanoparticles). The highest orange emission intensity $\sim 10^4$ (counts) is obtained from Mn^{2+} doped $\text{Zn}_{0.55}\text{Cd}_{0.45}\text{S}$ nanocrystalline thin films.

- The fabrication of $\text{Zn}_{0.55}\text{Cd}_{0.45}\text{S}:\text{Mn}/\text{ZnS}$ nanocomposite results in the emission intensity enhancement by a factor of ~ 1.4 only with ZnS top layer corresponding to 5000 shots.

Thus a solid state method is established to get uniform surface passivated thin films. Mn^{2+} doped $\text{Zn}_{0.55}\text{Cd}_{0.45}\text{S}$ nanostructures prepared in this work should prove to be very effective in light emitting applications.

The work on PV applications includes the incorporation of $\text{Zn}_{0.1}\text{Cd}_{0.9}\text{S}$ nanocrystalline thin films as window layer of the CdTe based thin film solar cell structure. From the experimental results and discussion presented in this thesis the following conclusions are made:

- Coverage quality of $\text{Zn}_{0.1}\text{Cd}_{0.9}\text{S}$ nanocrystalline thin films on ITO has been tested via detecting the change in the junction properties.
- Occurrence of Ohmic behavior in I - V characteristic detects the pin holes in the films. It was found that for the mask where contacts are at edge-lines of the substrate $\sim 30\%$ contacts showed Ohmic characteristic. While the mask where the contacts are in the central region of the mask only $\sim 5\%$ result in Ohmic characteristic. This finding allows depositing the back contact of the cell on the pinholes free area.
- Pre-heat treatment of the $\text{Zn}_{0.1}\text{Cd}_{0.9}\text{S}/\text{ITO}$ stack performed in both oxidizing and reducing ambient, for various durations did not altered the junction properties. All samples showed Ohmic behavior, suggesting no significant heat treatment-induced change at $\text{Zn}_{0.1}\text{Cd}_{0.9}\text{S}/\text{ITO}$ interface.
- Dry CdCl_2 treatment was found to be more effective than wet CdCl_2 treatment. Photo conversion efficiency, η is 3.2% at heat treatment temperature of 450 °C for wet CdCl_2 treated samples while η increases appreciably to 5.2% at 425 °C. It was found that the (a) recrystallization was slower in the wet dipping, (b) a very little CdTe grain growth was observed with wet CdCl_2 treatment (grain size increased only by a factor of ~ 4), while it was substantial for dry CdCl_2 treatment (grain size increased by a factor of ~ 17) with respect to the as-deposited CdTe film, (c) the series resistance was consistently higher for wet treated cells. Series resistance of 5.5 $\Omega\text{-cm}^2$ at 425 °C and 25 $\Omega\text{-cm}^2$ at 450 °C were obtained for dry and wet treated cells respectively.

- Reduction in $\text{Zn}_{0.1}\text{Cd}_{0.9}\text{S}$ film thickness from 200 to 150 nm, leads to increase in photo conversion efficiency (η). It increases from 4.8 to 5.2% mainly by an increase in short circuit current density (J_{sc}). In contrast, at 100 nm film thickness, η turned to be decreased due to decrease in both open circuit voltage (V_{oc}) and fill factor (FF) even after a slight increase in J_{sc} . Increased pin-holes, increased surface roughness and decreased grain size of the $\text{Zn}_{0.1}\text{Cd}_{0.9}\text{S}$ films were found to be responsible for the reduction of V_{oc} and FF . Series resistance, R_s of $5.5 \Omega\text{-cm}^2$ was obtained at 150 nm film thickness. R_s is found to be maximum $\sim 22 \Omega\text{-cm}^2$ at 80 nm film thickness.
- Most efficient cell with variation in deposition temperature of the $\text{Zn}_{0.1}\text{Cd}_{0.9}\text{S}$ films was obtained at 400°C with, photo conversion efficiency, η of 5.2%. Moderate deposition temperature results in high crystalline quality, and avoids the diffusion of impurities from glass substrate. Higher deposition temperature (500°C) results in efficiencies close to $\sim 2.2\%$. Partial consumption of $\text{Zn}_{0.1}\text{Cd}_{0.9}\text{S}$ film by CdTe and inter-diffusion of impurities from glass substrate were found to degrade the cell performance.
- It is suggested that the higher series resistance of the constituting layers of thin film structure, higher lattice mismatch between window and absorber layer, back contact stability, lack of solar concentrators, front contact material and design issues limits the photo conversion efficiency obtained in this work to reach the efficiencies close to that have already been obtained with CdS/CdTe solar cell.

This study has been carried out in order to improve the understanding of nanocrystalline thin film $\text{Zn}_{0.1}\text{Cd}_{0.9}\text{S}/\text{CdTe}$ solar cells and to develop improved processing schemes. The main advantages of using a lower temperature in the production of the $\text{Zn}_{0.1}\text{Cd}_{0.9}\text{S}/\text{CdTe}$ solar cell device structure are economy during processing and are main attraction for the low-cost solar cells. From these results, it is concluded that $\text{Zn}_{0.1}\text{Cd}_{0.9}\text{S}$ film deposition parameters and cell fabrication steps crucially affects the device performance. The above findings shows that the $\text{Zn}_{1-x}\text{Cd}_x\text{S}$ nanostructures have been successfully fabricated and utilized in two different optoelectronic applications i.e. light emission and PV technology.

8.2 FUTURE SCOPE

Synthesis experience on $Zn_{1-x}Cd_xS$ nanostructures in this work should allow for the production of nanostructures covering the spectrum from the near-ultra-violet to the infrared in terms of emission spectra. Additionally, entraining various dopants into host (such as green emission in case of Cu doped $Zn_{1-x}Cd_xS$ nanoparticles) and creating either *in-situ* sensors or luminescent system poses many interesting challenges and exciting opportunities. In the biological labeling and tagging field, nanostructures have recently been touted in *Science* and other journals as a means to employ nanostructures in a very significant way. Future progress in doped nanostructures will require investigating and improving the phenomena that emerge in to the reduced FWHM of the emission peak. Low temperature PL and time resolved spectroscopy may be helpful in explaining the decay kinetics of such systems. Other synthesis techniques such as solid state reaction, solvo-thermal method, sputtering technique, evaporation technique etc. should be explored and results can be compared with the present techniques. The effect of co-dopants may also be explored to obtain the white light emission from such nanostructures.

Discussion on the PV performance for $Zn_{0.1}Cd_{0.9}S/CdTe$ cells shows, that there is much scope for the improvement, which may in turn lead to cheap and stable modules. Such improvements require profound understanding of both the CdTe properties and electrical conductivity of $Zn_{1-x}Cd_xS$ layer with mole fraction. In all studied samples CdTe film thickness was kept constant. It should also be varied and should be optimized for further investigations. The thermal and junction stability of back contact are the major issues with CdTe based PV technology. The understanding of junction properties between CdTe and back contact will certainly be helpful in achieving the higher efficiencies. These issues should be analyzed and present the future scope of this work, making $Zn_{0.1}Cd_{0.9}S/CdTe$ a rich area of research. Pursuing these goals and applications will be an exciting and challenging task.

REFERENCES

1. Acevedo, A. M., "Physical basis for the design of CdS/CdTe thin film solar cells", *Solar Energy Materials and Solar Cells*, vol. 90, pp. 678-685, (2006).
2. Ad-Hoc Panel on Solar Cell Efficiency, *Solar cells, Outlook for improved Efficiency*, Space Science Board, 2101 Constitution Ave., Washington, D.C. 20418, USA (1972).
3. Adams, W. G., and Day, R. E., "The action of light on Selenium", *Proceedings of the Royal Society of London*, vol. 25, pp. 113-117, (1876).
4. Aguiar, R., Logvinovich, D., Weidenkaff, A., Karl, H., Schneider, C. W., Reller, A., and Ebbinghaus, S. G., "Physical properties of (La,Sr)Ti(O,N)₃ thin films grown by pulsed laser deposition", *Materials Research Bulletin*, vol. 43, pp. 1376-1383, (2008).
5. Alamri, S. N., and Brinkman, A. W., "The effect of the transparent conductive oxide on the performance of thin film CdS/CdTe solar cells", *Journal of Physics D: Applied Physics*, vol. 33, pp. L1-L4, (2000).
6. Aldana, J., Wang, Y. A., Peng, X. G., "Photochemical instability of CdSe nanocrystals coated by hydrophilic thiols", *Journal of American Chemical Society*, vol. 123, pp. 8844-8850, (2001).
7. Alivisatos, A. P., "Perspectives on the physical chemistry of semiconductor nanocrystals", *Journal of Physical Chemistry*, vol. 100, pp. 13226-13239, (1996).
8. Alturkestani, M., "CdTe solar cells: Key layers and electrical effects", Ph.D. Thesis, Durham University, UK (2008).
9. Andersen, R. L., "Experiments on Ge-GaAs heterojunctions", *Solid-State Electronics*, vol. 5, pp. 341-344, (1962).

10. Aramoto, T., Kumazawa, S., Higuchi, H., Arita, T., Shibutani, S., Nishio, T., Nakajima, J., Hanafusa, M., Hibino, T., Omura, K., Ohyama, H., and Murozono, "16% efficient thin-film CdS/CdTe solar cells," *Journal of Applied. Physics*, vol. 36, pp. 6304-6305, (1997).
11. Arora, S., and Manoharan, S. S., "Tuning of Mn(II)-doped CdS–ZnS solid solutions for broadband emission", *Materials Chemistry and Physics*, vol. 110, pp. 34–37, (2008).
12. Arora, S., Rajouria, S. K., Kumar, P., Bhatnagar, P. K., Arora, M., and Tandon, R. P., "Role of donor/acceptor domain formation and interface states in initial degradation of P3HT:PCBM-based solar cells", *Physica Scripta*, vol. 83, pp. 035804, (2011).
13. Ashcroft, N. W., and Mermin, N. D., "Solid State Physics", 1st edition, Brace College Publishers, Harcourt, Florida, (1976).
14. Ayyub, P., Vasa, P., Taneja, P., Banerjee, R. and Singh, B. P., "Photoluminescence enhancement in nanocomposite thin films of CdS-ZnO", *Journal of Applied Physics*, vol. 97, pp. 104310, (2005).
15. Barrioz, V., Irvine, S. J. C., Jones, E. W., Rowlands, R. L., and Lamb, D.A., "In situ deposition of cadmium chloride films using MOCVD for CdTe solar cells", *Thin Solid Films*, vol. 515, pp. 5808-5813, (2007).
16. Baskoutas, S., and Terzis, A. F., "Size-dependent band gap of colloidal quantum dots" *Journal of Applied Physics*, vol. 99, pp. 013708, (2006).
17. Bhargava, R. N., Gallagher, D., Hong, X., Nurmikko, A., "Optical properties of manganese-doped nanocrystals of ZnS", *Physical Review Letters*, vol. 72, pp. 416-419, (1994).

18. Bhatti, K. P., Chaudhary, S., Pandya, D. K., and Kashyap, S. C., "Extrinsic nature of the room temperature ferromagnetism in $(\text{ZnO})_{1-x}(\text{MnO}_2)_x$ for $0.01 \leq x \leq 0.97$ ", *Solid State Communications*, vol. 140, pp. 23-27, (2006).
19. Blanchard, C. R., "Atomic force microscopy", *The Chemical Educator*, Springer-Verlag, vol. 1, New York, (1996).
20. Böer, K. W., "Electrons and other particles in bulk semiconductors", *Survey of Semiconductor Physics*, Van Nostrand, vol. 1, New York, (1990).
21. Britt, J. and Ferekides, C., "Thin film CdS/CdTe solar cell with 15.8% efficiency," *Applied Physics Letters*, vol. 62, pp. 2851-2852, (1993).
22. Brovelli, F., Rivas, B. L., and Bernède, J. C., "Synthesis of polymeric thin films by electrochemical polymerization of 1-furfuryl pyrrole: Characterization and charge injection mechanism", *Journal of the Chilean Chemical Society*, vol. 52, pp. 1065-1068, (2007).
23. Brus, L. E., "Electron-electron and electron-hole interactions in small semiconductor crystallites: The size dependence of the lowest excited electronic state", *Journal of Chemical Physics*, vol. 80, pp. 4403-4409, (1984).
24. Camasse, J., Laurenti, J. P., Bouhemadou, A., Legros, R., Lusson, A., and Toulouse, B., "Composition dependence of the $\Gamma_8-\Gamma_6$ transition in mercury cadmium telluride: an examination", *Physical Review B*, vol. 38, pp. 3948-3959, (1988).
25. Cao, L., Zhang, J., Ren, S., and Huang, S., "Luminescence enhancement of core-shell ZnS:Mn/ZnS nanoparticles", *Applied Physics Letters*, vol. 80, pp. 4300, (2002).
26. Casali, R. A., and Christensen, N. E., "Elastic constants and deformation potentials of ZnS and ZnSe under pressure", *Solid State Communications*, vol. 108, pp.793-798, (1998).

27. Cervantes, P., Williams, Q., Cote, M., Zakharov, O., and Cohen, M. L., "Band structure of CdS and CdSe at high pressure", *Physical Review B*, vol. 54, pp. 17585-17590, (1996).
28. Chandra, R., Chawla, A. K., and Ayyub, P., "Optical and structural properties of sputter-deposited nanocrystalline Cu₂O films: Effect of sputtering gas", *Journal of Nanoscience and Nanotechnology*, vol. 6, pp.1119-1123, (2006).
29. Chatwal, G. R. and Anand S. K. "Instrumental methods of chemical analysis" 5th edition, Himalaya Publishing House, Mumbai, (2002).
30. Chaudhary, S., Bhatti, K. P., Pandya, D. K., Kashyap, S. C., and Nigam, A. K., "Effect of indium incorporation in Zn_{1-x}Co_xO thin films", *Journal of Magnetism and Magnetic Materials*, vol. 321, pp. 966-970, (2009).
31. Chawla, A. K., Singhal, S., Gupta, H. O., and Chandra, R., "Effect of sputtering gas on structural and optical properties of nanocrystalline tungsten oxide films", *Thin Solid Films*, vol. 517, pp. 1042–1046, (2008).
32. Chawla, V., "Synthesis and characterization of Titanium based hard coatings" Ph.D. Thesis, Indian Institute of Technology Roorkee, India, (2008).
33. Chen, Z. Q., Lian, C., Zhou, D., Xiang, Y., Wang, M., Ke, M., Liang, L. B., and Yu, X. F., "Greatly enhanced and controlled manganese photoluminescence in water-soluble ZnCdS:Mn/ZnS core/shell quantum dots", *Chemical Physics Letters*, vol. 488, pp. 73-76, (2010).
34. Cheong, H. M., Burnett, J. H., Paul, W., Hopkins, P. F., Campman, K., and Gossard, A. C., "Hydrostatic-pressure coefficient of the direct band-gap energy of Al_xGa_{1-x}As for $x = 0-0.35$ ", *Physical Review B*, vol. 53, pp. 10916–10920, (1996).
35. Chopra, K. L., Paulson, P. D., and Dutta, V., "Thin-film solar cells: An overview" *Progress in Photovoltaics: Research and Applications*, vol. 12, pp. 69–92, (2004).

36. Chou, H. C., Rohtagi, A., Jokerst, N. M., Kamra, S., Stock, S. R., and Lowrie, S. L., "Approach toward high efficiency CdTe/CdS heterojunction solar cells", *Material Chemistry and Physics*, vol. 43, pp. 178-182, (1996).
37. Chynoweth, T. A., and Bube, R. H., "Electrical transport in ZnCdS films deposited by spray pyrolysis", *Journal of Applied Physics*, vol. 51, pp. 1844 – 1846, (1980).
38. Coe, S., Woo, W. K., Bawendi, M., and Bulovic, V., "Electroluminescence from single monolayers of nanocrystals in molecular organic devices", *Nature*, vol. 420, pp. 800- 803, (2002).
39. Cohen, J., Cohen, P., Aiken, L., and West, S., "Applied multiple regression/correlation analysis for the behavioral sciences", 3rd edition, Hillsdale New Jersey, Lawrence Erlbaum, (2003).
40. Colvin, V., Schlamp, M. C., and Alivisatos, A. P., "Light-emitting diodes made from cadmium selenide nanocrystals and a semiconducting polymer", *Nature*, vol. 370, pp. 354-357, (1994).
41. Compagn, A. D., Sites, J. R., Birkmire, R. W., Ferekides, C. S., and Fahrenbruch, A. L., "Critical issues and research needs for CdTe based solar cells," *Electrochemical Society Symposium Proceedings*, vol. 9911, Photovoltaics for the 21st Century, Seattle, WA., (1999).
42. Counio, G., Gacoin, T., and Boilot, J. P., "Synthesis and photoluminescence of Cd_{1-x}Mn_xS (x ≤ 5) nanocrystals", *Journal of Physical Chemistry B*, vol. 102, pp. 5257-5260, (1998).
43. Cullity, B. D., and Stock, S. R., "Elements of X-ray diffraction", 3rd edition, Prentice Hall, New Jersey, (2001).

44. Cullity, B. D., and Graham, C. D., "Introduction to magnetic materials", 2nd edition, Addison-Wesley, Reading, (1972).
45. Dabbousi, B. O., Bawendi, M. G., Onitsuka, O., and Rubner, M. F., "Electroluminescence from CdSe quantum-dot/polymer composites", *Applied Physics Letters*, vol. 66, pp. 1316, (1995).
46. Dabbousi, B. O., Rodriguez, V. J., Mikulec, F. V., Heine, J. R., Mattoussi, D. D., Olschewski, M., and Settler, K., "Luminescence studies of localized gap states in colloidal ZnS nanocrystals", *Journal of Applied Physics*, vol. 84, pp. 2841, (1998).
47. Dalpian, G. M., and Chelikowsky, J. R., "Self-purification in semiconductor nanocrystals", *Physical Review Letters*, vol. 96, pp. 226802, (2006).
48. David, L., and Prior, K. A., "Determination of the lattice constant of CrS from Mn_{1-x}Cr_xS MBE epitaxial layers", *Physica Status Solidi B*, vol. 243, pp. 778–781 (2006).
49. Deore, S., and Navrotsky, A., "Oxide melt solution calorimetry of sulfides: Enthalpy of formation of sphalerite, galena, greenockite, and hawleyite", *American Mineralogist*, vol. 91, pp. 400-403, (2006).
50. Dho, J., "Electrode size dependent I-V characteristics and photovoltaic effect in the oxide p-n junctions Pr_{0.7}Ca_{0.3}MnO₃/Nb:SrTiO₃ and La_{0.7}Ca_{0.3}MnO₃/Nb:SrTiO₃", *Solid State Communications*, vol. 150, pp. 2243-2247, (2010).
51. Dmitrenko, K. A., Shevel, S. G., Taranenko, L. V., and Marintchenko, A. V., "The temperature dependence (4.2 to 293 K) of the resonance energies of excitonic transitions in II–VI compounds", *Physica Status Solidi B*, vol. 134, pp. 605, (1986).
52. Durose, K., Boyle, D., Abken, A., Ottley, C. J., Nollet, P., Degrave, S., Burgelman, M., Wendt, R., Beier, J., and Bonnet, D., "Key aspects of CdTe/CdS

- solar cells “, *Physica Status Solidi B-Basic Research*, vol. 229, pp. 1055-1064, (2002).
53. Durose, K., Edwards, P. R., and Halliday, D. P., “Materials aspects of CdTe/CdS solar cells,” *Journal of Crystal Growth*, vol. 197, pp. 733-742, (1999).
 54. Eason, R., “Pulsed laser deposition of thin films”, College edition, Wiley, New Jersey, (2007).
 55. Erwin, S. C., Zu, L., Haftel, M. I., Efros, A. L., Kennedy, T. A., and Norris, D. J., “Doping semiconductor nanocrystals”, *Nature*, vol. 436, pp. 91-94, (2005).
 56. Ethayaraja, M., Ravikumar, C., Muthukumar, D., Dutta, K., and Bandyopadhyay, R., “CdS–ZnS core–shell nanoparticle formation: Experiment, mechanism, and simulation”, *Journal of Physical Chemistry C*, vol. 111, pp. 3246-3252 (2007).
 57. Ferekides, C., Britt, J., Ma, Y., and Killian, L., “ High efficiency CdTe solar cells by close spaced sublimation”, *Photovoltaic Specialists Conference, Conference Record of the Twenty Third IEEE*, pp. 389 – 393, (1993).
 58. Ferekides, C. S., Balasubramanian, U., Mamazza, R., Viswanathan, V., Zhao, H., and Morel, D. L., “CdTe thin film solar cells: Device and technology issues”, *Solar Energy*, vol. 77, pp. 823-830, (2004).
 59. Flegler, S. L., Heckman, J. W., Karen, Jr., and Klomparens, L., “Scanning and transmission electron microscopy: An introduction”, Oxford University Press, New York (1993).
 60. Fouassier, C., “Luminescence in encyclopedia of inorganic chemistry”, 7th edition, John Wiley & Sons, (1994).
 61. Francisco, B., Bernabé, L. R., and Jean, C. B., “Synthesis of polymeric thin films by electrochemical polymerization of 1-furfuryl pyrrole: Characterization and

- charge injection mechanism”, *Journal of the Chilean Chemical Society*, vol. 52, pp.1-7, (2007).
62. Fritsche, J., Kraft, D., Thißen, A., Mayer, T., Klein, A., and Jaegermann, W., “Band energy diagram of CdTe thin film solar cells”, *Thin Solid Films*, vol. 403-404, pp. 252-257, (2002).
 63. Fritsche, J., Klein, A., and Jaegermann, W., “Thin film solar cells: Materials science at interfaces”, *Advanced Engineering Materials*, vol. 7, pp. 914–920, (2005).
 64. Gallardo, I., Hoffmann, K., and Keto, J. W., “CdSe & ZnS core/shell nanoparticles generated by laser ablation of microparticles”, *Applied Physics A*, vol. 94, pp. 65–72, (2009).
 65. Ge, J. P., Wang, J., Zhang, H. X., Wang, X., Peng, Q., and Li, D. Y., “Halide-transport chemical vapor deposition of luminescent ZnS:Mn²⁺ one-dimensional nanostructures”, *Advanced Functional Materials*, vol. 15, pp. 303-308, (2005).
 66. Gfroerer, T.H., “*Encyclopedia of analytical chemistry*”, John Wiley & Sons, Chichester, UK, (2000).
 67. Gleiter, H., “Nanostructured materials basic concepts and microstructure”, *Acta Materialia*, vol. 48, 1-29, (2000).
 68. Gobbo, S. D., “Cadmium sulphide quantum, dots: Growth and optical properties” Ph. D. Thesis, University of Rome, Italy, (2009).
 69. Graf, C., Vossen, D. L. J., Imhof, A., and Blaaderen, A. V., “A general method to coat colloidal particles with silica”. *Langmuir*, vol. 19, pp. 6693–6700, (2003).
 70. Grundy, P. J. and Jones, G. A., “*Electron microscopy in the study of materials*”, Edward Arnold Limited, London (1976).

71. Gullapalli, S. K., Vemuri, R. S., Manciu, F. S., Enriquez, J. L., and Ramana, C. V., "Tungsten oxide (WO_3) thin films for application in advanced energy systems", *Journal of Vacuum Science & Technology A: Vacuum, Surfaces, and Films*, vol. 28, pp. 824-828, (2010).
72. Gunasekaran, M., and Ichimura, M., "Photovoltaic cells based on pulsed electrochemically deposited SnS and photochemically deposited CdS and $\text{Cd}_{1-x}\text{Zn}_x\text{S}$," *Solar Energy Materials and Solar Cells*, vol. 91, pp. 774-778, (2007).
73. Gunasekaran, M., and Ichimura, M., "Deposition of $\text{Cd}_{1-x}\text{Zn}_x\text{S}$ ($0 \leq x \leq 1$) alloys by photochemical deposition", *Japanese Journal of Applied Physics*, vol. 44, pp. 7345- 7350, (2005).
74. Gupta, A., Chrisey, D. B., and Hubler, G. K., "Pulsed laser deposition of thin films", Wiley, New York, (1994).
75. Gupta, A., Matulionis, I., Drayton, J., and Compaan, A. D., "Effect of CdTe thickness reduction in high efficiency CdS/CdTe solar cells", *Materials Research Society Symposium Proceedings*, vol. 668, Materials Research Society, (2001).
76. Harmann, H., Mach, R., and Sell, B., "Current topics in material science", ed. by E. Kaldis (North-Holland, Amsterdam), Vol.9, (1982).
77. He, Z., Su, Y., Chen, Y., Cai, D., Jiang, J., and Chen, L., "Self-catalytic growth and photoluminescence properties of ZnS nanostructures" *Material Research Bulletin*, vol. 40, pp. 1308-1313, (2005).
78. Hines, M. A., and Sionnest, P. G., "Synthesis and characterization of strongly luminescing ZnS-capped CdSe nanocrystals", *Journal of Physical Chemistry*, vol. 100, pp. 468-471, (1996).
79. Huang J. H., Lau K. W. and Yu, G. P., "Effect of nitrogen flow rate on structure and properties of nanocrystalline TiN thin films produced by unbalanced

- magnetron sputtering”, *Surface and Coatings Technology*, vol. 191, pp. 17-24 (2005).
80. Hussain, M., “Vapor CdCl₂ Processing of CdTe solar cells”, M.S. Thesis, University of South Florida, USA, (2004).
 81. Isah, K. U., Hariharan, N. and Oberafo, A., “Optimization of process parameters of chemical bath deposition of Cd_{1-x}Zn_xS thin film”, *Leonardo Journal of Sciences*, vol. 12, pp. 111-120, (2008).
 82. Islam, M. M., Ishizuka, S., Yamada, A., Sakurai, K., Niki, S., Sakurai, T., and Akimoto, K., “CIGS solar cell with MBE-grown ZnS buffer layer”, *Solar Energy Materials & Solar Cells*, vol. 93, pp. 970–972, (2009).
 83. Jiang, D., Cao, L., Liu W., Su, G., Qu, H., Sun Y., and Dong, B., “Synthesis and luminescence properties of core/shell ZnS:Mn/ZnO nanoparticles”, *Nanoscale Research Letters*, vol. 4, pp. 78–83, (2009).
 84. John, P., and Wikswo, Jr., “SQUID magnetometers for biomagnetism and nondestructive testing: Important questions and initial answers”, *IEEE Transactions on Applied Superconductivity*, vol. 5, pp. 74, (1995).
 85. Jung, D. R., Son, D., Kim, J., Kim, C., and Parka, B., “Highly luminescent surface-passivated ZnS:Mn nanoparticles by a simple one-step synthesis”, *Applied Physics Letters*, vol. 93, pp. 163118, (2008).
 86. Kalele, S., Gosavi, S. W., Urban, J. and Kulkarni, S. K., “Nanoshell particles: synthesis, properties and applications”, *Current Science*, vol. 91, pp. 1038, (2006).
 87. Kampmann, A., and Lincot, D., “Photoelectromechanical study of thin film semiconductor heterostructures: Junction formation process in CdS/CdTe solar cells,” *Journal of Electroanalytical Chemistry*, vol. 418, pp. 73-81, (1996).

88. Karasawa, T., Ohkawa, K., and Mitsuyu, T., "Molecular-beam epitaxial growth and characterization of ZnS/Zn_xCd_{1-x}S strained-layer superlattices", *Journal of Applied Physics*, vol. 69, pp. 3226-3230, (1991).
89. Katari, J. E. B., Colvin, V. L., and Alivisatos, A. P., "X-ray photoelectron spectroscopy of CdSe nanocrystals with applications to studies of the nanocrystal surface", *Journal of Physical Chemistry*, vol. 98, pp. 4109-4117, (1994).
90. Kayanuma, Y., "Quantum size effects of interfacing electrons and holes in semiconductor microcrystals with spherical shape", *Physical Review B*, vol. 38, pp. 9797-9805, (1988).
91. Kim, J. U., Kim, Y. K., and Yang, H. "Reverse micelle-derived Cu-doped Zn_{1-x}Cd_xS quantum dots and their core/shell structure", *Journal of Colloid and Interface Science*, vol. 341, pp. 59-63, (2010).
92. Kos, Š., Achermann, M., Klimov, V. I., and Smith, D. L., "Different regimes of Förster-type energy transfer between an epitaxial quantum well and a proximal monolayer of semiconductor nanocrystals", *Physical Review B*, vol. 71, pp. 205309, (2005).
93. Koyama, R. Y., and Spicer, W. E., "Photoemission studies of Indium", *Physical Review B*, vol. 15, pp. 4318-4329, (1971).
94. Krishnakumar, V., Han, J., Klein, A., and Jaegermann, W., "CdTe thin film solar cells with reduced CdS film thickness", *Thin Solid Films*, DOI: 10.1016/j.tsf.12.118, (2010).
95. Kulkarni, S. K., Winkler, U., Deshmukh, N., Borse, P. H., Fink, R., and Umbach, E., "Investigations on chemically capped CdS, ZnS and ZnCdS nanoparticles", *Applied Surface Science*, vol. 169-170, pp. 438-446, (2001).

96. Kumar, P., Jain, S.C., Kumar, V., Chand, S., and Tandon, R.P., "A model for the current-voltage characteristics of organic bulk heterojunction solar cells", *Journal of Physics D: Applied Physics*, vol. 42, pp. 055102, (2009).
97. Lee, J., "Effects of heat treatment of vacuum evaporated CdCl₂ layer on the properties of CdS/CdTe solar cells", *Current Applied Physics*, vol. 11, pp. S103-S108, (2011).
98. Lee, J. H., Lee, H. Y., Park, Y. K., Shin, S. H., and Park, K. J., "Effects of the annealing temperature and CdCl₂ treatment on the photovoltaic properties of the CdS/CdTe solar cell", *Japanese Journal of Applied Physics*, vol. 37, pp. 3357-3362, (1998).
99. Lee, M., and Dho, J., "Controlling the electrical and optical properties of amorphous IGZO film prepared by pulsed laser deposition", *Journal of Korean Society of Physics*, vol. 58, pp. 492-497, (2011).
100. Levy, L., Feltin, N., Ingert, D., and Pileni, M. P., "Three dimensionally diluted magnetic semiconductor clusters Cd_{1-y}Mn_yS with a range of sizes and compositions: Dependence of spectroscopic properties on the synthesis mode", *Journal of Physical Chemistry B*, vol. 101, pp. 9153-9160, (1997).
101. Li, L., Choo, S. G. E., Liu, Z., Ding, J. and Xue, J. M., "Double-layer silica core-shell nanospheres with superparamagnetic and fluorescent functionalities", *Chemical Physical Letters*, vol. 461, pp. 114-117, (2008).
102. Li, S. Z., Gana, C. L., Cai, H., Yuan, C. L., Guo, J., Lee, P. S., and Ma, J., "Enhanced photoluminescence of ZnO/Er₂O₃ core-shell structure nanorods synthesized by pulsed laser deposition", *Applied Physics Letters*, vol. 90, pp. 263106, (2007).
103. Lide, E. (Ed.), "Handbook of chemistry and physics", Edition 2, CRC, Boca Raton, (1973).

104. Lifshitz, E., Dag, I., Litvin, I., Hodes, G., Gorer, S., Reisfeld, R., Zelner, M., and Minti, H., "Optical properties of CdSe nanoparticle films prepared by chemical deposition and sol-gel methods", *Chemical Physics Letters*, vol. 288, pp. 188-196, (1998).
105. Lincot, D., and Vedel, J., "Surface modifications and recombination processes at the n-CdTe/electrolyte interface", *Journal of Crystal Growth*, vol. 72, pp. 426-431, (1985).
106. Liu, J. Z., Yan, P. X., Yue, G. H., Chang, J. B., Qu, D. M., and Zhuo, R. F., "Red light photoluminescence emission from Mn and Cd co-doped ZnS one-dimensional nanostructures", *Journal of Physics D: Applied Physics*, vol. 39, pp. 2352-2356, (2006).
107. Logothetidis, S., Cardona, M., Lautenschlager, P., and Garriga, M., "Temperature dependence of the dielectric function and the interband critical points of CdSe", *Physical Review B*, vol. 34, pp. 2458-2469, (1986).
108. Lomascolo, M., Creti, A., Leo, G., Vasanelli, L., and Manna, L., "Exciton relaxation processes in colloidal core/shell ZnSe/ZnS nanocrystals", *Applied Physics Letters*, vol. 82, pp. 418 (2003).
109. Lu, H. Y., Chu, S. Y., and Tan, S. S., "The low-temperature synthesis and optical properties of near-white light emission nanophosphors based on manganese-doped zinc sulfide", *Japanese Journal of Applied Physics*, vol. 44, pp. 5282-5288, (2005).
110. Lu, M. Y., Song, J., Lu, M. P., Lee, C. Y., Chen, L. J., and Wong, Z. L., "ZnO/ZnS heterojunction and ZnS nanowire arrays for electricity generation", *ACS Nano*, vol. 3, pp. 357-362, (2009).
111. Lu, S. W., Lee, B. I., Wang, Z. L., Tong, W., Wagner, B. A., Park, W., and Summers, C. J., "Synthesis and photoluminescence enhancement of Mn²⁺-doped ZnS nanocrystals", *Journal of Luminescence*, vol. 92, pp. 73-78, (2000).

112. Lui, T. Y., Zapien, J. A., Tang, H., Ma, D. D. D., Liu, Y. K., Lee, C. S., Lee, S. T., Shi, S. L., and Xu, S. J., "Photoluminescence and photoconductivity properties of copper-doped $\text{Cd}_{1-x}\text{Zn}_x\text{S}$ nanoribbons", *Nanotechnology*, vol. 17, pp. 5935, (2006).
113. Maissel, L. I., and Glang, R., "Handbook of Thin Film Technology", New York: McGraw-Hill, (1970).
114. Maity, R. and Chattopadhyay, K. K., "Synthesis and optical characterization of ZnS and ZnS:Mn nanocrystalline thin films by chemical route", *Nanotechnology*, vol. 15, pp. 812-816, (2004).
115. Major, J. D., and Durose, K., "Study of buried junction and uniformity effects in CdTe/CdS solar cells using a combined OBIC and EQE apparatus", *Thin Solid Films*, vol. 517, pp. 2419-2422, (2009).
116. Manificier, J. C., Gasiot, J., and Fillard, J. P., "A simple method for the determination of n , k and the thickness of a weakly absorbing thin film", *Journal of Physics E: Scientific Instruments*, vol. 9, pp. 1002-1004, (1976).
117. Manna, L., Scher, E. C., Li, L. S., and Alivisatos, A. P., "Epitaxial growth and photochemical annealing of graded CdS/ZnS shells on colloidal CdSe nanorods", *Journal of American Chemical Society*, vol. 124, pp. 7136-7145, (2002).
118. Margolis, R., Mitchell, R. and Zweibel, K., "Technical report", National Renewable Energy Laboratory, vol. 6, pp. 1301, (2006).
119. Mason, M. G., Hung, L. S., Tang, C. W., Lee, S. T., Wong, K. W., and Wang, M., "Characterization of treated indium-tin-oxide surfaces used in electroluminescent devices", *Journal of Applied Physics*, vol. 86, pp. 1688-1692, (1999).
120. Mathieu, H., Richard, T., Allègre, J., Lefebvre, P., Arnaud, G., Granier, W., Boudes, L., Marc, J. L., Pradel, A., and Ribes, M., "Quantum confinement effects

- of CdS nanocrystals in a sodium borosilicate glass prepared by the sol-gel process”, *Journal of Applied Physics*, vol. 77, pp. 287, (1995).
121. McCandless, B. E., Moulton, L. V. and Birkmire, R. W., “Recrystallization and sulfur diffusion in CdCl₂-treated CdTe/CdS thin films”, *Progress in Photovoltaics: Research and Applications*, vol. 5, pp. 249-260, (1997).
 122. Mendoza-Pe´rez, R., Aguilar-Herna´ndez, J., Sastre-Herna´ndez, J., Ximello-Quiebras, N., Contreras-Puente, G., Santana-Rodri´guez, G., Vigil-Gala´n, O., Moreno-Garci´a, E., and Morales-Acevedo, A., “Photoluminescence characteristics of CdS layers deposited in a chemical bath and their correlation to CdS-CdTe solar cell performance”, *Solar Energy*, vol. 80, pp. 682–686, (2006).
 123. Mendoza-Pe´rez, R., Hern´andez, J. S., Puente, G. C., and Gal´an, O. V., “CdTe solar cell degradation studies with the use of CdS as the window material”, *Solar Energy Materials and Solar Cells*, vol. 93, pp. 79-84,(2009).
 124. Mishra, P., Yadav, R. S., and Pandey, A. C., “Growth mechanism and photoluminescence property of flower-like ZnO nanostructures synthesized by starch-assisted sonochemical method”, *Ultrasonics Sonochemistry*, vol. 17, pp. 560-565, (2010).
 125. Mørup, S., Jiang, J. Z., Bødker, F. and Horsewell, A., “Crystal growth and the steady-state grain size during high-energy ball-milling”, *Europhysics Letters*, vol. 56, pp. 441–446, (2001).
 126. Moutinho, H. R., Dhere, R. G., Ballif, C., Al-Jassim, M. M., and Kazmerski, L. L., “Alternative procedure for the fabrication of close-spaced sublimated CdTe solar cells”, *Journal of Vacuum Science and Technology A*, vol. 18., pp. 1599-1603, (2000).
 127. Murray, C. B., Kagan, C. R., and Bawendi, M. G., “Synthesis and characterization of monodisperse nanocrystals and close-packed nanocrystal assemblies”, *Annual Review of Material Science*, vol. 30, pp. 545–610, (2000).

128. Murray, C. B., Norris, D. J. and Bawendi, M. G., "Synthesis and characterization of nearly monodisperse CdE (E = sulfur, selenium, tellurium) semiconductor nanocrystallites", *Journal of American Chemical Society*, vol. 115, pp. 8706-8715, (1993).
129. Nag, A., Chakraborty, S., and Sarma, D. D., "To Dope Mn²⁺ in a semiconducting nanocrystal", *Journal of American Chemical Society*, vol. 130, pp. 10605–10611, (2008).
130. Nag, A., Sapra, S., Nagamani, C., Sharma, A., Pradhan, N., Bhat, S. V., and Sarma, D. D., "A study of Mn²⁺ doping in CdS nanocrystals", *Chemistry of Materials*, vol. 19, pp. 3252-3259, (2007).
131. Nakamura, K., Gotoh, M., Fujihara, T., Toyama, T., and Okamoto, H., "Influence of CdS window layer on 2-mm thick CdS/CdTe thin film solar cells", *Solar Energy Materials and Solar Cells*, vol. 75, pp. 185–192, (2003).
132. Nalwa, H. S., and Rohwer, L. S., "Handbook of luminescence, display materials and devices", vol. 3, American Scientific Publishers, (2003).
133. Nanda, J., Ph.D. Thesis, Indian Institute of Science, Bangalore (2000).
134. Neumann, H., "Trends in the thermal expansion coefficients of the A^IB^{III}C₂^{VI} and A^{II}B^{IV}C₂^V chalcopyrite compounds", *Kristall und Technik*, vol. 15, pp. 849-857, (1980).
135. Nicolau, Y. F., Dupuy, M., and Bruner, M., "ZnS, CdS, and Zn_{1-x}Cd_xS thin films deposited by the successive ionic layer adsorption and reaction process", *Journal of Electrochemical Society*, vol. 137, pp. 2915-2924, (1990).
136. Nien, Y. T., Chen P. W., Chen, I. G., "Synthesis and characterization of Zn_{1-x}Cd_xS:Cu, Cl red electroluminescent phosphor powders", *Journal of Alloys and Compounds*, vol. 462, pp. 398-403, (2008).

137. Niles, D. W., Waters, D., and Rose, D., "Chemical reactivity of CdCl_2 wet-deposited on CdTe films studied by X-ray photoelectron spectroscopy", *Applied Surface Science*, vol. 136, pp. 221-229, (1998).
138. Norris, D. J., Efros, A. L., and Erwin, S. C., "Doped Nanocrystals", *Science*, vol. 319, pp. 1776, (2008).
139. Ocana, M., Hsu, W. P. and Matijevic, E., "Preparation and properties of uniform coated colloidal particles. 6. Titania on zinc oxide". *Langmuir*, vol. 7, pp. 2911–2916 (1991).
140. Oladeji, I. O., Chow, L., Ferekides, C. S., Viswanathan, V., and Zhao, Z., "Metal/CdTe/CdS/ $\text{Cd}_{1-x}\text{Zn}_x\text{S}$ /TCO/glass: A new CdTe thin film solar cell structure", *Solar Energy Materials & Solar Cells*, vol. 61, pp. 203 – 211, (2000).
141. Park, K., Yu, H. J., Chung, W. K., Kim, B. J., and Kim, S. H., "Effect of heat-treatment on CdS and CdS/ZnS nanoparticles", *Journal of Material Science*, vol. 44, pp. 4315–4320, (2009).
142. Patel, B. K., Nanda, K. K., and Sahu, S. N., "Interface characterization of nanocrystalline CdS/Au junction by current–voltage and capacitance–voltage studies", *Journal of Applied Physics*, vol. 85, pp. 3666-3670, (1999).
143. Patel, S. P., Chawla, A. K., Chandra, R., Prakash, J., Kulriya, P. K., Pivin, J. C., Kanjilal, D., and Kumar, L., "Structural phase transformation in ZnS nanocrystalline thin films by swift heavy ion irradiation", *Solid State Communications*, vol. 150, pp. 1158-1161, (2010).
144. Patel, S. P., Pivin, J. C., Kumar, V. V. S., Tripathi, A., Kanjilal, D., Kumar, L., "Grain growth and structural transformation in ZnS nanocrystalline thin films", *Vacuum*, vol. 85, pp. 307-311, (2010).

145. Paulson, P. D., and Dutta, V., "Study of in situ CdCl₂ treatment on CSS deposited CdTe films and CdS/CdTe solar cells", *Thin Solid Films*, vol. 370, pp. 299-306, (2000).
146. Peng, W. Q. , Qu, S. C. , Cong, G. W. , Zhang, X. Q. and Wang, Z. G. "Optical and magnetic properties of ZnS nanoparticles doped with Mn²⁺", *Journal of Crystal Growth*, vol. 282, pp.179-185, (2005).
147. Peng, X., "Green chemical approaches toward high-quality semiconductor nanocrystals", *Chemistry- A European Journal*, vol. 8, pp. 334-339, (2002).
148. Peng, X., Schlamp, M. C., Kadavanich, A. V., and Alivisatos, A. P., "Epitaxial growth of highly luminescent CdSe/CdS core/shell nanocrystals with photostability and electronic accessibility", *Journal of American Chemical Society*, vol. 119, pp. 7019–7029, (1997).
149. Peng, Z. A. and Peng, X., "Formation of high-quality CdTe, CdSe, and CdS nanocrystals using CdO as precursor", *Journal of American Chemical Society*, vol. 123, pp. 183-184, (2001).
150. Pickett, N. L., and O'Brien, P. "Syntheses of Semiconductor Nanoparticles Using Single-Molecular Precursors", *The Chemical Record*, vol. 1, pp. 467–479, (2001).
151. Purkayastha, Yan, Q., Raghuveer, M. S., Gandhi, D. D., Li, H., Liu, W., Ramanujan, R., Tasciuc, T. B., Ramanath, G., "Surfactant-directed synthesis of branched bismuth telluride-sulfide core-shell nanorods", *Advanced Materials*, vol. 20, pp. 2679–2683, (2008).
152. Qu, L., Peng, Z. A. and Peng, X., "Alternative routes toward high quality CdSe nanocrystals", *Nano Letters*, vol. 1, pp. 333, (2001).

153. Qu, L. and Peng, X., "Control of photoluminescence properties of CdSe nanocrystals in growth", *Journal of American Chemical Society*, vol. 124, pp. 2049-2055, (2002).
154. Ramana, C. V., Vemuri, R., Fernandez, S. I., and Campbell, A. L., "Size-effects on the optical properties of zirconium oxide thin films", *Applied Physics Letters*, vol. 95, pp. 231905, (2009).
155. Reiss, P., Bleuse, J. and Pron, A., "Highly luminescent CdSe/ZnSe core/shell nanocrystals of low size dispersion", *Nano Letters*, vol. 2, pp. 781-784, (2002).
156. Ren Z., Yang H., Shen L., Han S. D., "Hydrothermal preparation and properties of nanocrystalline ZnS:Mn", *Journal of Material Science : Mater Electron*, vol. 19, pp. 124, (2008).
157. Reynolds, D. C., Leies, G., Antes, L. L. and Marburger, R. E., "Photovoltaic effect in Cadmium Sulfide", *Physical Review*, vol. 96, pp. 533-534, (1954).
158. Robert, Mammaza, Jr., "Ternary spinal Cd_2SnO_4 , $CdIn_2O_4$, and Zn_2SnO_4 and binary SnO_2 and In_2O_3 transparent conducting oxides as front contact materials for CdS/CdTe photovoltaic devices," Ph.D. Thesis , University of South Florida, (2003).
159. Roh, J. S., and Im, H. B., "Effects of $CdCl_2$ in CdTe on the properties of sintered CdS/CdTe solar cells", *Journal of Material Science*, vol. 23, pp. 2267-2272, (1988).
160. Romeo, A., Bätzner, D. L., Zogg, H., and Tiwari, A. N., "Recrystallization in CdTe/CdS", *Thin Solid Films*, vol. 361-362, pp. 420-425, (2000).
161. Romeo, N., Bosio, A., Tedeschi, R., and Canevari, V., "Growth of polycrystalline CdS and CdTe thin layers for high efficiency thin film solar cells", *Materials Chemistry and Physics*, vol. 66, pp. 201-206, (2000).

162. Rose, D. H., Hasoon, F. S., Dhere, R. G., Albin, D. S., Ribelin, R. M., Li, X. S., Mahathongdy, Y., Gessert, T. A., and Sheldon, P., "Fabrication procedures and process sensitivities for CdS/CdTe solar cells", *Progress in Photovoltaics: Research and Applications*, vol. 7, pp. 331-340, (1999).
163. Rudolph, P., Schäfer, N., and Fukuda, T., "Crystal growth of ZnSe from the melt" *Materials Science and Engineering: R- Reports*, vol. 15, pp. 85-133, (1995).
164. Rüggeberg, F., and Klein, A., "The $\text{In}_2\text{O}_3/\text{CdTe}$ interface: A possible contact for thin film solar cells", *Applied Physics A*, vol. 82, pp. 281-285, (2006).
165. Sapra, S., "Experimental and theoretical investigations of the electronic and optical properties of semiconductor nanocrystals", Ph.D. Thesis, Indian Institute of Science, Bangalore, India, (2004).
166. Sapra, S., Prakash, A., Ghangrekar, A., Periasamy, N., and Sarma, D. D., "Emission properties of manganese-doped ZnS nanocrystals", *Journal of Physical Chemistry B*, vol. 109, pp. 1663-1668, (2005).
167. Sapra, S., and Sarma, D. D., "Evolution of the electronic structure with size in II-VI semiconductor nanocrystals", *Physical Review B*, vol. 69, pp. 125304, (2004).
168. Schenck, P. K., Vaudin, M. D., Bonnell, W., Hasti, J. W., and Paul, A. J., "Particulate reduction in the pulsed laser deposition of barium titanate thin films", *Applied Surface Science*, vol. 127, pp. 655-661, (1998).
169. Schiavello, M., "Photoelectrochemistry, photocatalysis, and photoreactors: fundamentals and developments", Springer, (1985).
170. Schon, S., Chaichimansour, M., Park, W., Yang, T., Wagner, B. K., and Summers, C. J., "Homogeneous and h-doped ZnS:Mn grown by MBE", *Journal of Crystal Growth*, vol. 1751176, pp. 598-602, (1997).

171. Scofield, J. H., Asher, S., Albin, D., Tuttle, J., Contreras, M., Niles, D., Reedy, R., Tennant, A., and Noufi, R., "Sodium diffusion, selenization, and microstructural effects associated with various molybdenum back contact layers for CIS-based solar cells", Proc. of the 24th IEEE Photovoltaic Specialists Conference, IEEE, New York, pp. 164-167, (1995).
172. Sebastian, P. J. and Ocampo, M., "A photodetector based on ZnCdS nanoparticles in a CdS matrix formed by screen printing and sintering of CdS and ZnCl₂", Solar Energy Materials and Solar Cells, vol. 44, pp. 1-10, (1996).
173. Shan, W., Walukiewicz, W., Ager, J. W., Yu, K. M., Wu, J., and Haller, E. E. "Pressure dependence of the fundamental band-gap energy of CdSe", Applied Physics Letters, vol. 84, pp. 67-69, (2004).
174. Shan W., Song, J. J., Luo, H., and Furdyna, J. K., "Determination of the fundamental and split-off band gaps in zinc-blende CdSe by photomodulation spectroscopy", Physical Review B, vol. 50, pp. 8012, (1994).
175. Sharma, R.C., and Chang, Y.A., "Thermodynamic analysis and phase equilibria calculations for the Zn-Te, Zn-Se and Zn-S systems", Journal of Crystal Growth, vol. 88, pp. 193-204, (1988).
176. Shetty, R., Balasubramanian, R., and Wilcox, W. R., "Surface tension and contact angle of molten semiconductor compounds : I. cadmium telluride" Journal of Crystal Growth, vol. 100, pp. 51, (1990).
177. Shinoya, S. and Yin, W. M., Phosphor Handbook, CRC Press, Washington, DC, 1999.
178. Singh, J., "Optoelectronics an introduction to materials and devices", Macgraw Hill, New Delhi, (1996).
179. Sites, J. R., Enzenroth, R. A., Sampath, W. S., and Barth, K. L., Materials Research Society Symposium Proceedings, vol. 1012, pp. 1012-Y03-23, (2007).

180. Sites, J. R., Granata, J. E., and Hiltner, J. F., "Losses due to polycrystallinity in thin-film solar cells", *Solar Energy Materials and Solar Cells*, vol. 55, pp. 43-50, (1998).
181. Smart, L., and Moore, E., "Solid State Chemistry", Edition 2, Chapman Hall, New York, (1995).
182. Sombuthawee, C., Bonsall, S. B., and Hummel, F. A., "Phase equilibria in the systems ZnS---MnS, ZnS---CuInS₂, and MnS---CuInS₂", *Journal of Solid State Chemistry*, vol. 25, pp. 391-399, (1978).
183. Son, D., Jung, D. R., Kim, J., Moon, T., Kim, C., and Park, B., "Synthesis and photoluminescence of Mn-doped zinc sulfide nanoparticles", *Applied Physics Letters*, vol. 90, pp. 101910, (2007).
184. Sooklal, K., Cullum, B. S., Angel, S. M., and Murphy, C. J., "Photophysical properties of ZnS nanoclusters with spatially localized Mn²⁺", *Journal of Physical Chemistry*, vol. 100, pp. 4551-4555, (1996).
185. Streetman, B., and Banarjee, S., "Solid state electronic devices", 5th edition, Person Education, New Delhi, India, (2000).
186. Subbaiah, Y. P. V., Prathap, P., and Reddy, K. T. R., "Structural, electrical and optical properties of ZnS films deposited by close-spaced evaporation", *Applied Surface Science*, vol. 253, pp. 2409-2415, (2006).
187. Sze, S. M., "Physics of Semiconductor Devices," Edition 2, New York: John Wiley & Sons, (1981).

188. Talapin, D. V., Rogach, A. L., Kornowski, A., Haase, M. and Weller, H., "Highly luminescent monodisperse CdSe and CdSe/ZnS nanocrystals synthesized in a hexadecylamine– trioctylphosphine oxide– trioctylphosphine mixture", *Nano Letters*, vol. 1, pp. 207-211, (2001).
189. Taneja, P., Vasa, P., and Ayyub, P., "Chemical passivation of sputter-deposited nanocrystalline CdS thin films", *Materials Letters*, vol. 54, pp. 343-347, (2002)
190. Tauc J., "Amorphous and Liquid Semiconductor", Plenum Press, New York (1974).
191. Thornton, J. A., in "Semiconductor materials and process technology, Handbook", (G. E. McGurie, Ed.) *Physical Vapor Deposition*, Noyes Publications, New Jersey (1988).
192. Tong, X. L., Jiang, D. S., Yan, Q. Y., Hu, W. B., Liu, Z. M., and Luo, M. Z., "Deposition of CdS thin films onto Si(111) substrate by PLD with femtosecond pulse", *Vacuum*, vol. 82, pp. 1411–1414, (2008).
193. Ueda, M., Kanzaki, H., Kobayashi, K., Toyozawa, Y., and Hanamura, E., "Excitonic processes in solids", *Springer Series in Solid State Sciences*, vol. 60, (1986).
194. Ullal, H. S., and Roedern, B. V., "Thin film CIGS and CdTe photovoltaic technologies: commercialization, critical issues, and applications" 22nd European Photovoltaic Solar Energy Conference (PVSEC) and Exhibition, Milan, Italy September 3–7, 2007.
195. Vasa, P., Singh, B. P. and Ayyub P., "Nonlinear photoresponse in II-VI-based nanocomposite thin films: A semi-quantitative four-level model", *Journal of Optical Society of America B*, vol. 23, pp. 692, (2006).

196. Vasa, P., Singh, B. P. and Ayyub, P., "Coherence properties of the photoluminescence from CdS-ZnO nanocomposite thin films", *Journal of Physics: Condensed Matter*, vol. 17, pp. 189, (2005).
197. Wang, L., Jiang, Y., Wang, C., Wang, W., Cao, B., Niu, M., and Qian, Y., "Composition-controllable synthesis and optical properties of non-integral stoichiometry compound $Zn_xCd_{1-x}S$ nanorods", *Journal of Alloys and Compounds*, vol. 454, pp. 255–260, (2008).
198. Weblink 1: <http://www.ecec.utep.edu/research/CdTe/fabrication/index.html>
199. Weblink 2: http://cdiac.ornl.gov/trends/emis/tre_glob.html
200. Weblink 3: http://en.wikipedia.org/wiki/Electron_microprobe
201. Weblink 4: http://encyclobeamia.solarbotics.net/articles/solar_cell.html dated January 04.
202. Weblink 5: <http://www.iclei.org/efacts/photovol.htm>
203. Weblink 6: <http://www.science24.com/paper/11606>
204. Weblink 7: <http://en.wikipedia.org/wiki/Sphalerite>
205. Weblink 8: http://www1.eere.energy.gov/solar/solar_cell_structures.htm
206. Wells, A. F., "Structural inorganic chemistry", Edition 5, Oxford: Clarendon Press, (1984).
207. William, D. B., and Carter, C. B., "Transmission electron microscopy", Plenum Publishing Cooperation, 233, Spring Street, New York, (2009).
208. Williams, R., "Becquerel photovoltaic effect in binary compounds". *The Journal of Chemical Physics*, vol. 32, pp. 1505–1514, (1960).

209. Wolf, C. M., Holonyak, N., and Stillman, G. E., "Properties of semiconductors", Physical (Prentice Hall, New York), (1989).
210. Wong, M.S., Chou, H.P., and Yang, T.S., "Reactively sputtered N-doped titanium oxide films as visible-light photocatalyst", Thin Solid Films, vol. 494, pp. 244–249, (2006).
211. Wu, X., Asher, S., Levi, D. H., King, D. E., Yan, Y., Gessert, T. A., and Sheldon, P., "Interdiffusion of CdS and Zn₂SnO₄ layers and its application in CdS/CdTe polycrystalline thin-film solar cells", Journal of Applied Physics, vol. 89, pp. 4564-4569, (2001).
212. Yadav, R. S., Mishra, P., Mishra, R., Kumar, M., Pandey, A. C., "Growth mechanism and optical property of CdS nanoparticles synthesized using amino-acid histidine as chelating agent under sonochemical process", Ultrasonics Sonochemistry, vol. 17, pp. 116-122, (2010).
213. Yamamoto, N., Horinaka, H., Okada, K. and Miyauchi, T., "Excitonic structure of CuGaS_{2x}Se_{2(1-x)} and CuAlS_{2x}Se_{2(1-x)}", Japanese Journal of Applied Physics, vol. 16, pp. 1817-1822, (1977).
214. Yang, M. C., Yang, T. S., and Wong, M. S., "Nitrogen-doped titanium oxide films as visible light photocatalyst by vapor deposition", Thin Solid Films, vol. 469-470, pp. 1-5, (2004).
215. Yang, P., Lv, M., Xu, D., Yuan, D., and Zhou, G., "Synthesis and photoluminescence characteristics of doped ZnS nanoparticles", Applied Physics A, vol. 73, pp. 455-458, (2001).
216. Yao, T., Ogura, M., Matsuoka, S., and Morishita, T., "High-quality ZnSe thin films grown by molecular beam epitaxy", Applied Physics Letters, vol. 43, pp. 499, (1993).

217. Yin, S.Y., Fahrenbruch, A. L., and Bube, R. H., "Photovoltaic properties of ZnCdS/CdTe heterojunctions prepared by spray pyrolysis" *Journal of Applied Physics*, vol. 49, pp. 1294- 1296, (1978).
218. Yu, K., Zaman, B., Romanova, S., Wang, D., and Ripmeester, J. A., "Sequential Synthesis of type II colloidal CdTe/CdSe core-shell nanocrystals", *Small*, vol. 1, pp. 332-338, (2005).
219. Zhang, S., Yu, J., Li, X., and Tian, W., "Photoluminescence properties of mercaptocarboxylic acid stabilized CdSe nanoparticles covered with polyelectrolyte", *Nanotechnology*, vol. 15, pp. 1108-1112, (2004).
220. Zhong, X. and Feng, Y., "New strategy for band-gap tuning in semiconductor nanocrystals" *Research on Chemical Intermediates*, vol. 34, pp. 287-298, (2008).
221. Zhong, X., Han, M., Dong, Z., White, T. J., and Knoll, W., "Composition-tunable $Zn_xCd_{1-x}Se$ nanocrystals with high luminescence and stability", *Journal of American Chemical Society*, vol. 125, pp. 8589-8594, (2003).
222. Zhong, X., Feng, Y., Knoll, W., and Han, M., "Alloyed $Zn_xCd_{1-x}S$ nanocrystals with highly narrow luminescence spectral width", *Journal of American Chemical Society*, vol. 125, pp. 13559-13563, (2003).
223. Zhong, X., Xie, R., Zhang, Y., Basche, T. and Knoll, W., "High-quality violet- to red-emitting $ZnSe/CdSe$ core/shell nanocrystals", *Chemistry of Materials*, vol. 17, pp. 4038-4042, (2005).
224. Zweibel, K., "Harnessing solar power – The photovoltaics challenge," Plenum Press, New York & London, (1990).

A1.1 Energy Band Gap and Wavelength Relation [185]

$$E_g (eV) = \frac{1237}{\lambda (nm)} \quad (A1.1)$$

A1.2 Vegard's Law for Energy Band Gap [178]

$$E_{g_{Zn_{1-x}Cd_xS}} = (1 - x)E_{g_{ZnS}} + xE_{g_{CdS}} \quad (A1.2)$$

- Energy band gap of bulk $Zn_{1-x}Cd_xS$ in zincblende structure

Table A1.1: Energy band gap of bulk $Zn_{1-x}Cd_xS$ semiconductor with mole fraction in zincblende structure and corresponding wavelengths

| Mole Fraction, x | E_{gZnS} (eV) | E_{gCdS} (eV) | E_g (eV) | λ (nm) |
|-----------------------|--------------------|--------------------|---------------|-------------------|
| 0.00 | 3.68 | 2.35 | 3.680 | 336 |
| 0.10 | 3.68 | 2.35 | 3.547 | 348 |
| 0.20 | 3.68 | 2.35 | 3.414 | 362 |
| 0.25 | 3.68 | 2.35 | 3.347 | 369 |
| 0.30 | 3.68 | 2.35 | 3.281 | 377 |
| 0.40 | 3.68 | 2.35 | 3.148 | 392 |
| 0.45 | 3.68 | 2.35 | 3.081 | 401 |
| 0.50 | 3.68 | 2.35 | 3.015 | 410 |
| 0.75 | 3.68 | 2.35 | 2.682 | 461 |
| 0.90 | 3.68 | 2.35 | 2.483 | 498 |
| 1.00 | 3.68 | 2.35 | 2.350 | 526 |

- Energy band gap of bulk $Zn_{1-x}Cd_xS$ in wurtzite structure

Table A1.2: Energy band gap of bulk $Zn_{1-x}Cd_xS$ semiconductor with mole fraction in wurtzite structure and corresponding wavelengths

| Mole Fraction, x | E_{gZnS} (eV) | E_{gCdS} (eV) | E_g (eV) | λ (nm) |
|-----------------------|--------------------|--------------------|---------------|-------------------|
| 0.00 | 3.9 | 2.42 | 3.900 | 317 |
| 0.10 | 3.9 | 2.42 | 3.752 | 330 |
| 0.20 | 3.9 | 2.42 | 3.604 | 343 |
| 0.25 | 3.9 | 2.42 | 3.530 | 350 |
| 0.30 | 3.9 | 2.42 | 3.456 | 358 |
| 0.40 | 3.9 | 2.42 | 3.308 | 374 |
| 0.45 | 3.9 | 2.42 | 3.234 | 382 |
| 0.50 | 3.9 | 2.42 | 3.160 | 391 |
| 0.75 | 3.9 | 2.42 | 2.790 | 443 |
| 0.90 | 3.9 | 2.42 | 2.568 | 482 |
| 1.00 | 3.9 | 2.42 | 2.420 | 511 |

A1.3 Vegard's Law for Lattice Constant [178]

$$a_{Zn_{1-x}Cd_xS} = (1-x)a_{ZnS} + xa_{CdS} \quad (A1.3)$$

- Lattice Constant, a in zinblende structure

Table A1.3: $Zn_{1-x}Cd_xS$ lattice constant, a , with mole fraction in zinblende structure

| Mole Fraction x | a_{ZnS} (nm) | a_{CdS} (nm) | $a_{Zn_{1-x}Cd_xS}$ (nm) |
|----------------------|-------------------|-------------------|-----------------------------|
| 0.00 | 0.541 | 0.582 | 0.541 |
| 0.10 | 0.541 | 0.582 | 0.545 |
| 0.20 | 0.541 | 0.582 | 0.549 |
| 0.25 | 0.541 | 0.582 | 0.551 |
| 0.30 | 0.541 | 0.582 | 0.553 |
| 0.40 | 0.541 | 0.582 | 0.557 |
| 0.45 | 0.541 | 0.582 | 0.559 |
| 0.50 | 0.541 | 0.582 | 0.562 |
| 0.75 | 0.541 | 0.582 | 0.572 |
| 0.90 | 0.541 | 0.582 | 0.578 |
| 1.00 | 0.541 | 0.582 | 0.582 |

- Lattice Constant, a in wurtzite structure

Table A1.4: $Zn_{1-x}Cd_xS$ Lattice Constant, a , with mole fraction in wurtzite structure

| Mole Fraction x | a_{ZnS} (nm) | a_{CdS} (nm) | $a_{Zn_{1-x}Cd_xS}$ (nm) |
|----------------------|-------------------|-------------------|-----------------------------|
| 0.00 | 0.3811 | 0.4135 | 0.3811 |
| 0.10 | 0.3811 | 0.4135 | 0.3843 |
| 0.20 | 0.3811 | 0.4135 | 0.3876 |
| 0.25 | 0.3811 | 0.4125 | 0.3892 |
| 0.30 | 0.3811 | 0.4135 | 0.3908 |
| 0.40 | 0.3811 | 0.4135 | 0.3941 |
| 0.45 | 0.3811 | 0.4135 | 0.3956 |
| 0.50 | 0.3811 | 0.4135 | 0.3973 |
| 0.75 | 0.3811 | 0.4135 | 0.4054 |
| 0.90 | 0.3811 | 0.4135 | 0.4103 |
| 1.00 | 0.3811 | 0.4135 | 0.4135 |

- **Lattice Constant, c in wurtzite structure**

$$c_{Zn_{1-x}Cd_xS} = (1-x)c_{ZnS} + xc_{CdS} \quad (A1.4)$$

Table A1.5: $Zn_{1-x}Cd_xS$ lattice constant, c , with mole fraction in wurtzite structure

| Mole Fraction x | c_{ZnS} (nm) | c_{CdS} (nm) | $c_{Zn_{1-x}Cd_xS}$ (nm) |
|----------------------|-------------------|-------------------|-----------------------------|
| 0.00 | 0.6234 | 0.6749 | 0.623 |
| 0.10 | 0.6234 | 0.6749 | 0.629 |
| 0.20 | 0.6234 | 0.6749 | 0.634 |
| 0.25 | 0.6234 | 0.6749 | 0.636 |
| 0.30 | 0.6234 | 0.6749 | 0.639 |
| 0.40 | 0.6234 | 0.6749 | 0.644 |
| 0.45 | 0.6234 | 0.6749 | 0.646 |
| 0.50 | 0.6234 | 0.6749 | 0.649 |
| 0.75 | 0.6234 | 0.6749 | 0.662 |
| 0.90 | 0.6234 | 0.6749 | 0.669 |
| 1.00 | 0.6234 | 0.6749 | 0.675 |

A1.4 Solar AM1.5 Spectrum

Since the sun is the light source for solar cells, knowledge of the exact distribution of the energy content in sunlight is important in solar cell work. The radiation reaching earth is scattered and absorbed in the atmosphere and the intensity is dependent upon the angle of incidence. The power level of the solar spectrum in outer space, where there is no absorption of the radiation, is about 1300 W/m^2 [224]. This is termed as air-mass-zero (AM0) spectrum. AM1.5 spectrum is the most widely used terrestrial standard for evaluating solar cells and corresponds to an elevation angle of 42° , and power density of $\sim 1000 \text{ W/m}^2$. The AM1.5 spectrum is shown in figure A1.1.

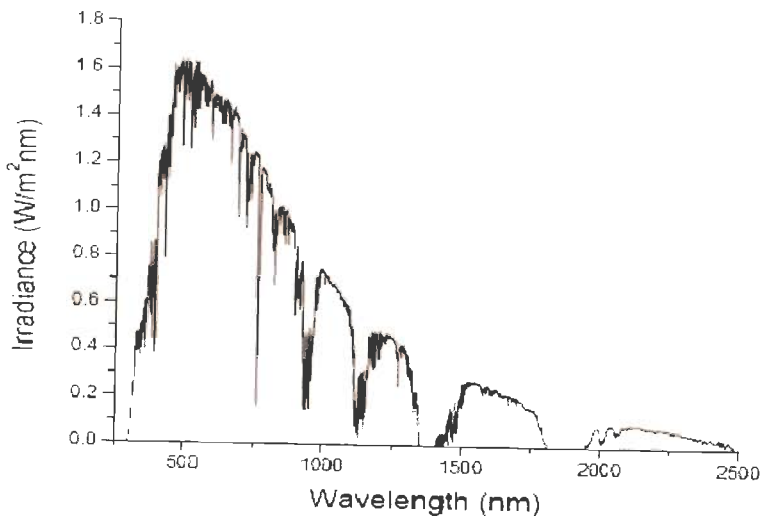


Figure A1.1: Solar Cell AM1.5 Spectrum [224]

A1.5 Photovoltaic Effect

The photovoltaic effect is the generation of an electromotive force as a result of the absorption of radiation. It can occur in gases, liquids, and solids, but it is in solids, especially in semiconductors, that acceptable efficiencies for conversion of solar energy into electric power have been observed [2]. The photovoltaic effect consists of the following essential processes.

- **Absorption of radiation and generation of charge carriers**

Absorption coefficient is a function of the wavelength or photon. It determines how far below the surface of the cell light of a given wavelength is absorbed. Figure A1.2 shows a plot of $\ln \alpha$ vs $h\nu$ for several semiconductors used in fabricating solar cells.

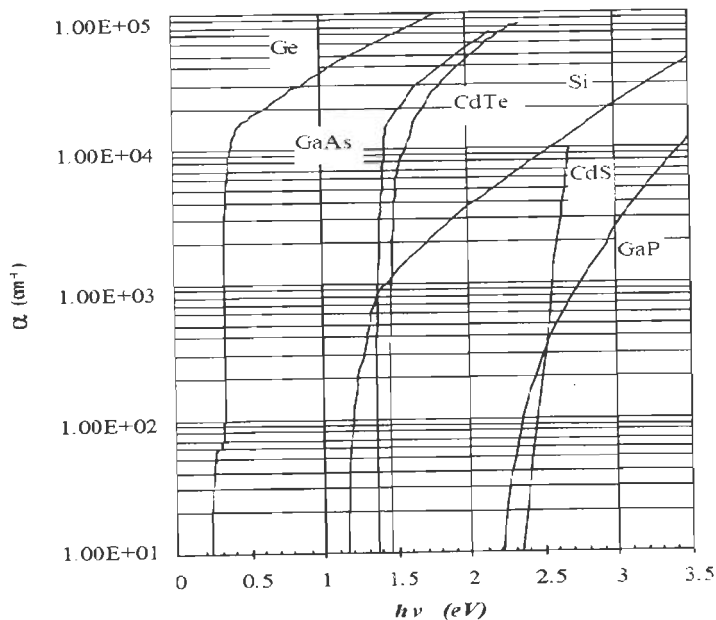


Figure A1.2: Absorption coefficient of few direct and indirect band gap semiconductors [2]

Curves shown in figure A1.2 are characterized by a threshold for absorption which corresponds to photon energy equal to the energy band gap (E_g) of the semiconductor. For a photon with an energy $h\nu < E_g$ the values of α in general are very small while α rises for $h\nu > E_g$ to values of 10^4 to 10^5 cm^{-1} [2]. Absorption of photons occurs when $h\nu \geq E_g$ and electron-hole pairs are generated. There are basically two kinds of absorption curves, those for direct band gap semiconductors such as gallium arsenide (GaAs), CdS, CdTe etc. which rise very sharply near the

band gap energy, and those for indirect band gap semiconductors like Si which increase gradually. Since most of the incident solar energy will be absorbed in a few micrometers in direct gap semiconductors, they are suitable for the fabrication of thin film solar cells. CdTe has high absorption coefficient and a layer as thin as $2\ \mu\text{m}$ can absorb most of the incident radiation.

- **Separation of generated carrier pairs at the junction, a region of electrostatic field**

Absorption of each photon results in the creation of a free electron and a free hole. In order to get a photo-generated current these free carrier pairs have to be separated before they recombine. The built-in field is a very powerful separator of oppositely charged free carriers once they are within its influence. The electric field opposes electrons flowing from the *n*-type region to the *p*-type region but it favors electrons moving from the *p*-type region to the *n*-type region.

A1.6 Thin Film Solar Cell Structure

Thin film solar cell is a device made of different layers (figure A1.3). These layers can be deposited with different techniques on a substrate and have particular functions in the device. The functions of the different layers are as follows:

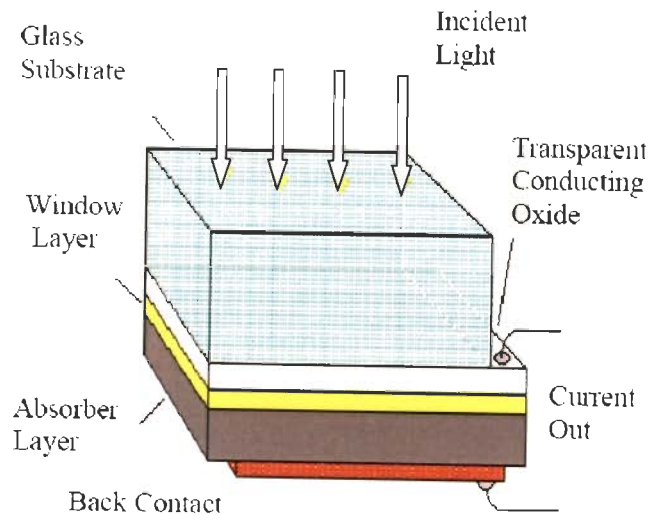


Figure A1.3: Schematic of thin film solar cell in superstrate configuration

[35]

Substrate

The choice of an appropriate substrate is very important. It should withstand the cell fabrication process temperatures and must not contaminate the layers that are subsequently grown. CdTe solar cells in superstrate configuration require a transparent substrate because the incident light has to pass through the substrate before reaching to the CdS/CdTe layers; any absorption in the substrate would be detrimental to the current generation of the cell. The general choice is glass because it is transparent, and cheap. At the same time glass should withstands relatively high temperatures to avoid the diffusion of impurities, such as sodium from glass to overlying layers.

Transparent Conducting Oxide (Front Contact)

The front contact must be highly conducting and transparent to allow the light transmission and to provide the electrical connection. It is needed to reduce the series resistance of the device. For high efficiency cells, it is required that the sheet resistance of the front contact is no more than $10 \Omega/\text{square}$. The widely used material is indium doped tin oxide (ITO), with a thickness of $\sim 500 \text{ nm}$.

Window Layer

The polycrystalline CdS layer is *n*-type doped (as CdS invariably is), and therefore provides one half of the *p-n* junction. Being a wide band gap material ($E_g \sim 2.4 \text{ eV}$ at 300 K) it is transparent down to wavelengths of around 515 nm, and so is referred to as the window layer.

Absorber Layer

The CdTe layer is polycrystalline layer and should be electrically *p*-type to form the *p-n* junction. Its energy gap (1.45 eV) is ideally suited to the solar spectrum, and it has a high absorption coefficient for energies above this value. It acts as an efficient absorber and is used as the *p*-side of the junction, and therefore named as “absorber layer”. Since CdTe has lower carrier concentration than the CdS, the depletion region is mostly within the CdTe layer and in this region most of the carrier generation and collection occur. Typically thickness of this layer, depending on the growth method, is between 2 and 10 μm , with grain sizes from 0.5 μm to 8 μm .

Back Contact

The back contact provides a low resistance electrical connection to the absorber layer. Formation of low resistance back contacts to p -CdTe is needed for the fabrication of high efficiency solar cells. CdTe has a high electron affinity ($\chi = 4.5$ eV) and no metal exists with a high work function (Φ_m); consequently a Schottky barrier height given by the expression $\Phi_b = (\chi + E_g) - \Phi_m$, where χ is the electron affinity and E_g is the band gap of the semiconductor exists [53]. Given that a back contact barrier is inevitable, some consider that a barrier height of less than 200 meV will be acceptable for device operation [53]. The back contact generally includes two layers: the primary layer is a heavily doped layer that makes a low-loss electrical contact to the CdTe; and the secondary contact is metal that carries the current laterally [41]. The primary layer employs Cu, because the Cu diffuses into the CdTe and produces a heavily doped p -layer. This helps to reduce barrier height between CdTe and back contact. The copper can be introduced by mixing HgTe:Cu into the graphite.

A2.1 PARTICLE SIZE MEASUREMENT

A2.1.1 Average size

Average size of nanoparticles is given by equation (A2.1)

$$\bar{x} = \frac{1}{n} \sum_{i=1}^n x_i = \frac{1}{n} (x_1 + \dots + x_n) \tag{A2.1}$$

where ,

\bar{x} = Average size / length

n = Nmber of samples measured

A2.1.2 Standard deviation

The standard deviation is a measure of how precise the average is, that is, how well the individual numbers agree with each other. It is a measure of a type of error called random error - the kind of error people can't control very well. It is calculated as follows equation (A2.2) [39]:

$$\sigma = \sqrt{\frac{1}{N-1} \sum_{i=1}^N (x_i - \bar{x})^2} \tag{A2.2}$$

where,

x = Average size/length

N = Number of samples measured

A2.1.3 Relative standard deviation

The relative standard deviation (RSD) is often times more convenient. It is expressed in percent and is obtained by multiplying the standard deviation by 100 and dividing this product by the average.

$$RSD = 100 * \frac{\sigma}{\bar{x}} \tag{A2.3}$$

A2.2 Polynomial Fit & Regression Coefficient

The general multiple regression model [39] can be written as

$$y = \beta_0 + \beta_1 x_1 + \beta_2 x_2 + \dots + \beta_i x_i + u \tag{A2.4}$$

where β_0 is the intercept, β_1 is the parameter associated with x_1 , and so on. The performance of the regression model is judged in terms of a statistical parameter R^2 . By definition, R^2 is a number between zero and one. R^2 can also be shown to equal the squared correlation coefficient between the actual y_i and the fitted \hat{y}_i . A high value of R^2 , suggests that the regression model explains the relationship in a better way.

A3.1 Calculation of Particle Size via UV-Vis Absorption Spectroscopy of Core-Shell Nanoparticles

The following calculation has been carried out by using equation (1.1), chapter1. The values of the parameters involved in equation (1.1) have been taken from Table 2.1, chapter 2.

| s/c ratio | Mole-fraction x | UV-Vis E_g | E_g (ZnS) | E_g (CdS) | E_{g0} (bulk) |
|-----------|-------------------|--------------|-------------|-------------|-----------------|
| 0 | 0.45 | 3.58 | 3.68 | 2.36 | 2.903 |
| 0.05 | 0.45 | 3.52 | 3.68 | 2.36 | 2.903 |
| 0.1 | 0.45 | 3.45 | 3.68 | 2.36 | 2.903 |
| 0.2 | 0.45 | 3.3 | 3.68 | 2.36 | 2.903 |
| 0.5 | 0.45 | 3.288 | 3.68 | 2.36 | 2.903 |
| 1 | 0.45 | 3.272 | 3.68 | 2.36 | 2.903 |

| $E_g - E_{g0}$ | $m_e^*(\text{ZnS})$ | $m_e^*(\text{CdS})$ | $m_e^*(\text{Zn}_{1-x}\text{Cd}_x\text{S})$ | $m_h^*(\text{ZnS})$ | $m_h^*(\text{CdS})$ |
|----------------|---------------------|---------------------|---|---------------------|---------------------|
| 0.677 | 0.25 | 0.19 | 0.223 | 0.51 | 0.8 |
| 0.617 | 0.25 | 0.19 | 0.223 | 0.51 | 0.8 |
| 0.547 | 0.25 | 0.19 | 0.223 | 0.51 | 0.8 |
| 0.397 | 0.25 | 0.19 | 0.223 | 0.51 | 0.8 |
| 0.385 | 0.25 | 0.19 | 0.223 | 0.51 | 0.8 |
| 0.369 | 0.25 | 0.19 | 0.223 | 0.51 | 0.8 |

| $m_h^*(\text{Zn}_{1-x}\text{Cd}_x\text{S})$ | ϵ (ZnS) | ϵ (CdS) | $\epsilon\epsilon_0$ | μ^*m_0 | h |
|---|------------------|------------------|----------------------|------------|----------|
| 0.6405 | 5.2 | 5.7 | 4.40E-11 | 1.505E-31 | 6.64E-34 |
| 0.6405 | 5.2 | 5.7 | 4.40E-11 | 1.505E-31 | 6.64E-34 |
| 0.6405 | 5.2 | 5.7 | 4.40E-11 | 1.505E-31 | 6.64E-34 |
| 0.6405 | 5.2 | 5.7 | 4.40E-11 | 1.505E-31 | 6.64E-34 |
| 0.6405 | 5.2 | 5.7 | 4.40E-11 | 1.505E-31 | 6.64E-34 |
| 0.6405 | 5.2 | 5.7 | 4.40E-11 | 1.505E-31 | 6.64E-34 |

| $h^*h/8\mu$ | $1.8q/4\pi$ | $b*b-4ac$ | $\text{sqrt}(b^2-4ac)$ | $\text{sqrt}(b^2-4ac)/2a$ | Particle Size(2*R) |
|-------------|-------------|-----------|------------------------|---------------------------|--------------------|
| 2.288E-18 | 5.205E-10 | 5.926E-18 | 2.434E-09 | 1.798E-09 | 3.596E-09 |
| 2.288E-18 | 5.205E-10 | 5.377E-18 | 2.319E-09 | 1.879E-09 | 3.758E-09 |
| 2.288E-18 | 5.205E-10 | 4.736E-18 | 2.176E-09 | 1.989E-09 | 3.978E-09 |
| 2.288E-18 | 5.205E-10 | 3.363E-18 | 1.834E-09 | 2.310E-09 | 4.619E-09 |
| 2.288E-18 | 5.205E-10 | 3.253E-18 | 1.804E-09 | 2.342E-09 | 4.685E-09 |
| 2.288E-18 | 5.205E-10 | 3.107E-18 | 1.763E-09 | 2.388E-09 | 4.777E-09 |

A3.2 Absorption Spectra of $Zn_{1-x}Cd_xS$ nanoparticles with Variation mole fraction

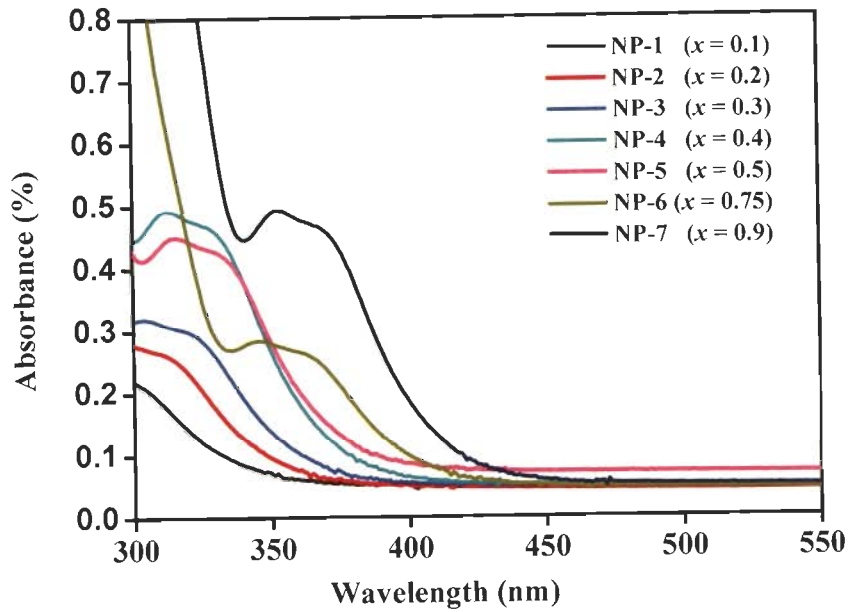


Figure A3.1: Absorption spectra of $Zn_{1-x}Cd_xS$ nanoparticles with variation in mole fraction

A3.3 Absorption Spectra of $Zn_{0.55}Cd_{0.45}S:Mn$ Nanoparticles with Variation in Manganese Concentration

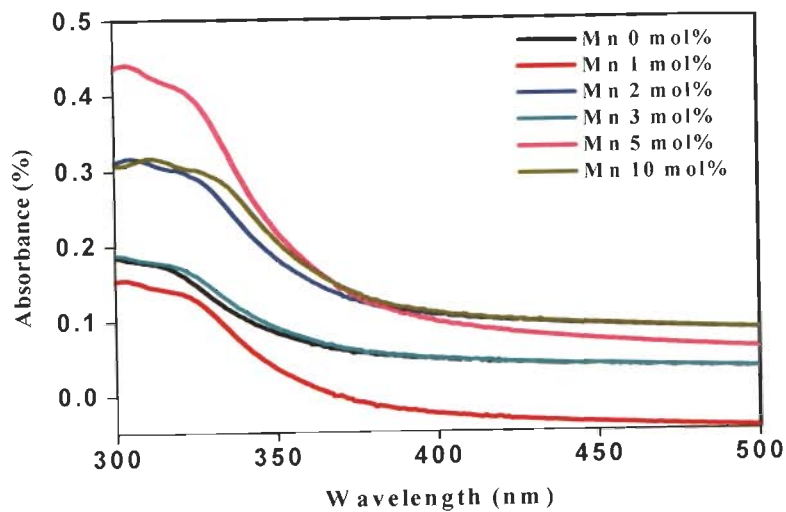


Figure A3.1: Absorption spectra of $Zn_{0.55}Cd_{0.45}S:Mn$ nanoparticles with variation in manganese concentration

A4.1 CdTe Properties

Table A4.1: CdTe properties at room temperature [8, 35, 52, 53, 80]

| Properties | CdTe |
|--|---------------------|
| Crystal structure | Zincblende |
| Energy band gap (eV) | 1.45 |
| Absorption coefficient (cm ⁻¹) | 5 x 10 ⁵ |
| Melting point (K) | 1370 |
| Density (gm.cm ⁻³) | 5.86 |
| Electron effective mass, m_e | 0.11 |
| Hole effective mass, m_h | 0.35 |
| Dielectric constant ($\epsilon_0 / \epsilon_\infty$) | 2.27 |
| Electron affinity χ (eV) | 4.4 |
| Work function Φ (eV) | 5.9 |
| Lattice constant (nm) | 0.648 |

A4.2 Solar Cell Device Physics

A solar cell is a large area diode with shallow junction depth to collect solar radiation effectively. The forward dark current relationship of a solar cell can be expressed as [80]

$$J = J_o \left[\left(\exp \left(\frac{qV}{Ak_bT} \right) \right) - 1 \right] \tag{A4.1}$$

where,

J is the external current flow, in amp/cm²

J_o is the reverse saturation current, in amp/cm²

q is the electronic charge ($q = 1.602 \times 10^{-19}$ Coulombs),

V is the applied voltage, in volt

k_b is the Boltzmann constant (1.38×10^{-23} J/K),

T is the absolute temperature and

A is the “ideality factor” of a diode, which depends on the dominating transport mechanism and usually varies from 1 to 2. A equals 1 when the diffusion current

dominates and A equals 2 when the recombination current dominates. When both currents are comparable, A has a value between 1 and 2.

A non-ideal solar cell can be described with an equivalent-circuit model as shown in figure A4.1. The simplest equivalent circuit used consists of a non-ideal diode, representing the $p-n$ junction, coupled with a current source to account for the collection of light-generated carriers. J_L is the magnitude of the photo generated current, and R_s , R_{sh} represent the series and shunt resistance respectively. The dimension for J_L is amp/cm² and for R_s , R_{sh} are $\Omega\text{-cm}^2$. R_s is due to the bulk resistance of the semiconductor and the resistance of the contacts and interconnections. The losses due to leakage currents and lattice defects are represented by R_{sh} .

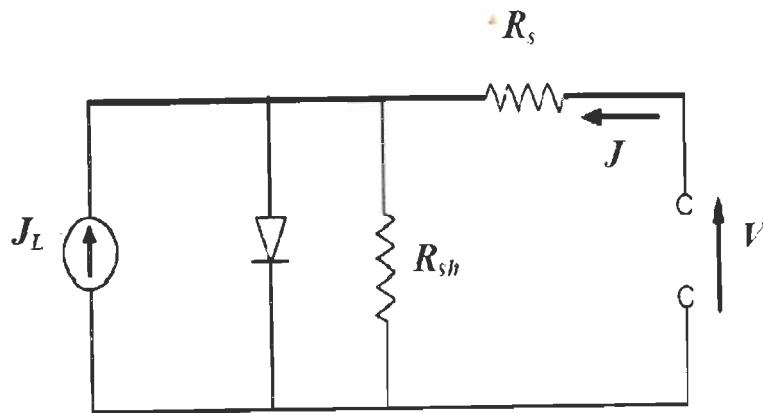


Figure A4.1: equivalent circuit for solar cell under illumination [80]

In ideal case, ($R_s = 0$, and $R_{sh} = 0$) the current through a device as depicted in above figure can be given by

$$J = J_o \left[\left(\exp \left(\frac{qV}{Ak_bT} \right) \right) - 1 \right] - J_L \quad (\text{A4.2})$$

In practical device series and shunt resistance affects the device performance and can no longer be neglected. Figure A4.2 shows a current – voltage (J - V) curve of a typical solar cell measured both in the dark (curve a) and under illumination (curve b).

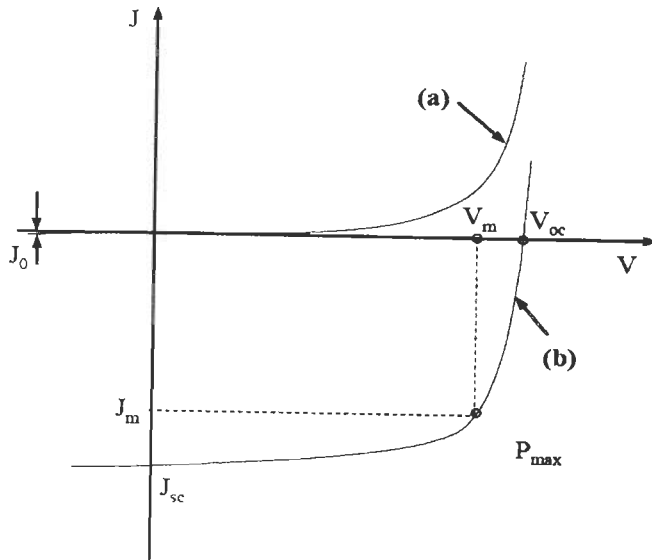


Figure A4.2: The current-voltage curve of a *p-n* junction solar cell (a) in the dark and (b) under illumination [185]

The J - V curve describes three important parameters that give complete description of the solar cell: (a) short circuit current density (J_{sc}) (b) open circuit voltage V_{oc} (c) fill factor, FF . Photo conversion efficiency can be determined from the knowledge of these three parameters.

Short-circuit current density

If no voltage is applied in the equivalent circuit then the current density measured is called the short-circuit current density, J_{sc} . This value is affected primarily by series resistance losses in the device.

$$J_{sc} \sim J_L \quad (\text{A4.3})$$

Open-circuit voltage

The open-circuit voltage is the applied voltage relative to an open circuit where no current flows through the device. When the external terminals are opened, there is no current flow in the external circuit. V_{oc} is obtained when $J = 0$.

$$V_{oc} = \frac{AkT}{q} \ln \left(\frac{J_L}{J_o} + 1 \right) \quad (\text{A4.4})$$

Fill factor

The maximum output power, P_{max} is determined from the power rectangle, which is a rectangle with maximum area that can be fitted between the x and y-axis of the illuminated J - V curve.

$$P_{max} = J_m * V_m \quad (A4.5)$$

The fill factor is then defined as the inverse of the ratio of the ideal power to the maximum power in operating conditions. It can be defined also as the area of the maximum power rectangle to the product of the short-circuit current and the open-circuit voltage.

$$FF = \frac{J_m * V_m}{J_{sc} * V_{oc}} \quad (A4.5)$$

Photo conversion efficiency

The photo conversion efficiency, η of a solar cell is calculated in terms of power converted from electromagnetic radiation to electric power (Amperes x Volts = Watts).

$$\eta = \frac{P_{out}}{P_{in}} = FF * \left(\frac{V_{oc} * J_{sc}}{P_{in}} \right) \quad (A4.6)$$

The normalized standard of P_{in} is 100 mW/cm^2 .

A4.3 Estimation of Series Resistance

The series resistance is the resistance the carriers find on their way and it is given by the resistivity of the materials of the device. There are many effects that give rise to this resistance:

- Low conductivity of the window layer or of the absorber,
- non-ohmic contacts,
- recombination of carriers into the gap or into the bulk materials.

The voltage drop is not only given by the junction but also by the series resistance. In open-circuit condition the current is zero and the voltage drop of the series resistance is also zero, so the open-circuit voltage is not affected. In short-circuit condition, current flows also through the series resistance and the current at short circuit is changed.

In practical device series and shunt resistance affects the device performance and can no longer be neglected. Incorporating R_s and R_{sh} in equation (A4.1):

$$J = J_o \left[\left\{ \left(\exp \left(\frac{q(V - JR_s)}{Ak_bT} \right) \right) - 1 \right\} + \left\{ \left(\frac{V - JR_s}{R_{sh}} \right) \right\} - J_L \right] \quad (\text{A4.7})$$

R_s can be calculated from the inverse of the slope of the J - V curve at $V \sim V_{oc}$ as shown in Figure A4.3.

If R_{sh} is high, then equation (A4.7) can be written as:

$$V = \frac{AkT}{q} \ln \left(\frac{J + J_{sc} - J_o}{J_o} \right) + JR_s \quad (\text{A4.8})$$

Differentiating above equation,

$$\frac{dV}{dJ} = \frac{AkT}{q} \ln \left(\frac{1}{J + J_{sc} - J_o} \right) + R_s \quad (\text{A4.9})$$

$$R_s = \left(\frac{dV}{dJ} \right)_{V=V_{oc}} - \frac{AkT}{q} \ln \left(\frac{1}{J_{sc} - J_o} \right) \quad (\text{A4.10})$$

since second term is negligible, therefore

$$R_s = \left(\frac{dV}{dJ} \right)_{V=V_{oc}} \quad (\text{A4.11})$$

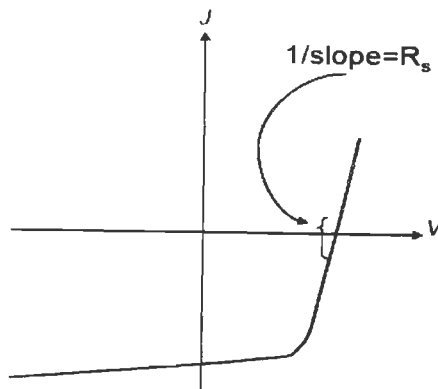


Figure A4.3: Typical J - V curves for solar cells under illumination. Figure shows the division of the curve from which R_s is measured [8]

A5.1 Metal-Semiconductor (M-S) contacts

The metal-semiconductor contact is formed by a metal contact to a semiconductor. Many of the useful properties of p-n junction can be achieved by these contacts. This approach is attractive because of its simplicity of fabrication. Depending on work function relation of metal and semiconductor Schottky contacts are dividing into two categories [185]:

- Rectifying contact
- Ohmic contact

A5.2 Formalism

The physical parameters of interest are the

- electron affinity χ of a semiconductor and is defined as the energy difference between the vacuum level and CB of the semiconductor
- the work function of a metal Φ_m is the energy between the vacuum level and the fermi level of the metal
- the work function of a semiconductor Φ_s is the energy between the vacuum level and the fermi level of the metal

When these materials are isolated, their vacuum levels are shown in figure A5.1.

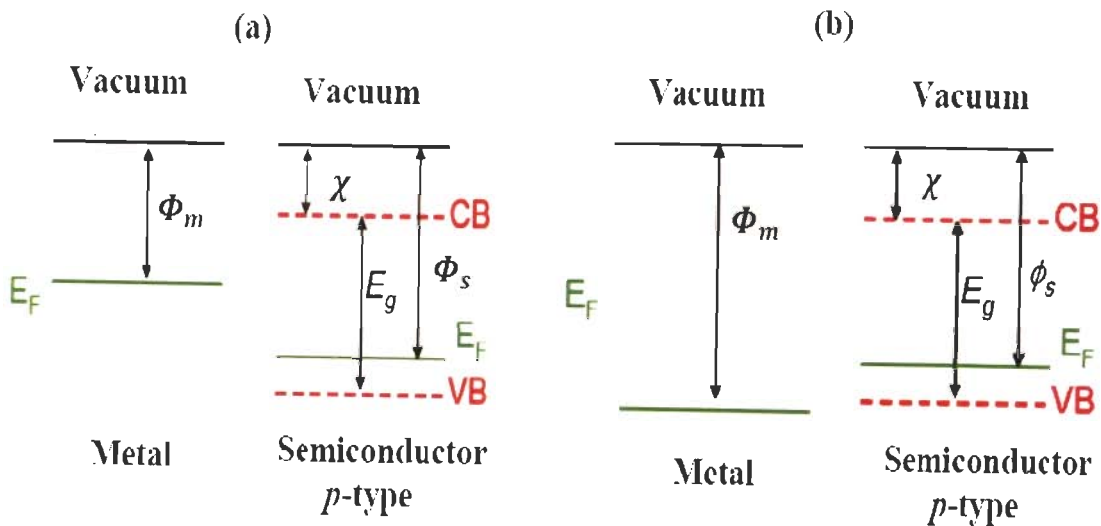


Figure A5.1: The energy band diagrams of a p-type semiconductor and metal before contact (a) $\Phi_m < \Phi_s$ and (b) $\Phi_m > \Phi_s$ [185]

Depending upon the difference between Φ_m and Φ_s , with $\chi > 0$, and the type of semiconductors, the following four situations are possible.

Table A5.1: Four possible metal-semiconductor junction configurations and the resulting contact types

| Conditions | Semiconductor | Junction |
|-------------------|----------------|----------|
| $\Phi_m > \Phi_s$ | <i>n</i> -type | Schottky |
| $\Phi_m < \Phi_s$ | <i>p</i> -type | Schottky |
| $\Phi_m > \Phi_s$ | <i>p</i> -type | Ohmic |
| $\Phi_m < \Phi_s$ | <i>n</i> -type | Ohmic |

As an illustrative for *p*-type semiconductor the band bending has been shown for the two cases where the semiconductor is of *p*-type and (a) $\Phi_m < \Phi_s$ (b) $\Phi_m > \Phi_s$ and resulting Schottky and Ohmic junctions are shown.

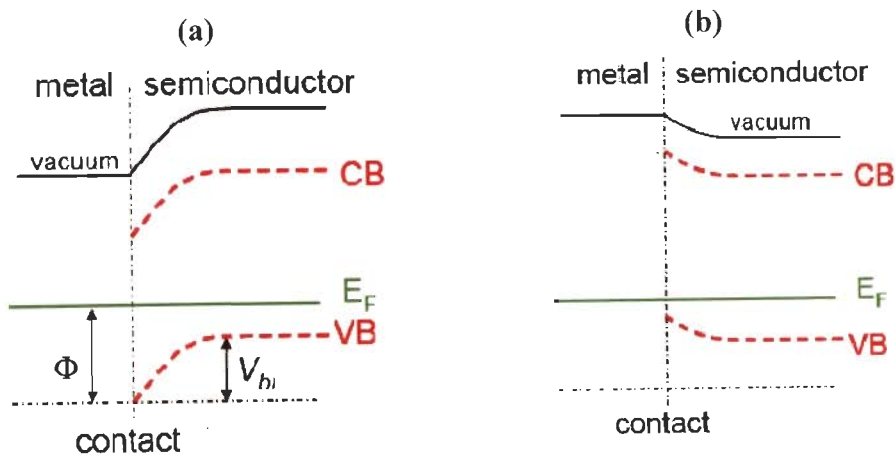


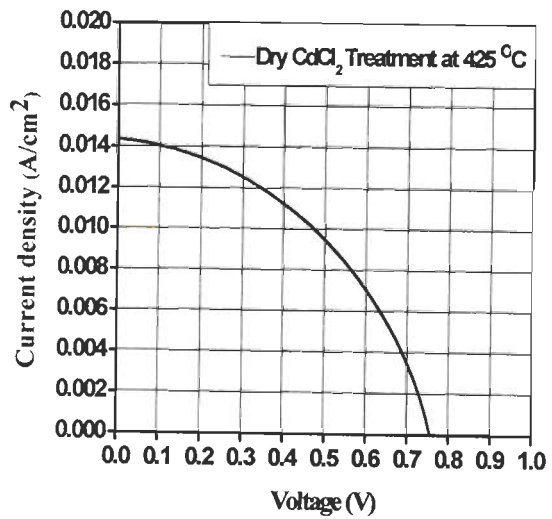
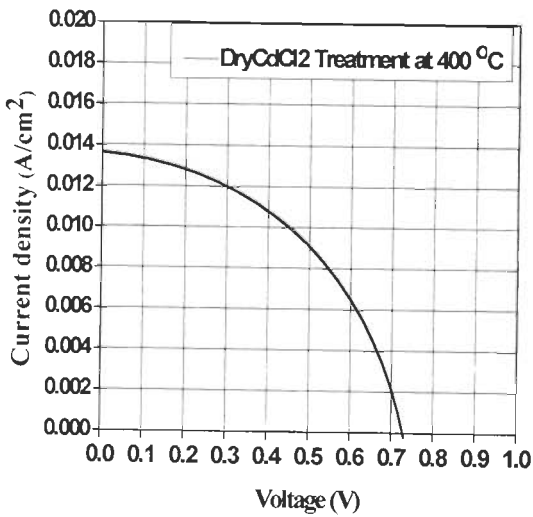
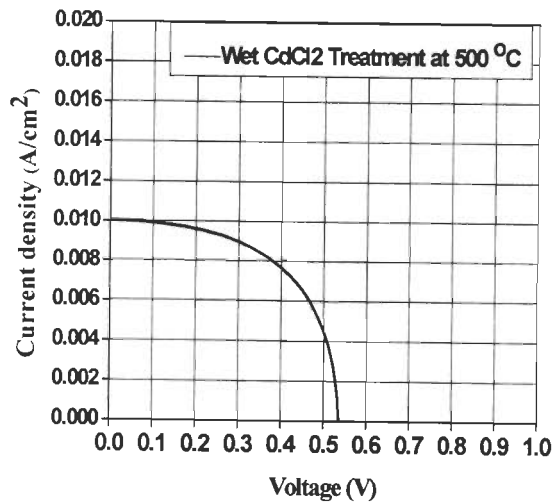
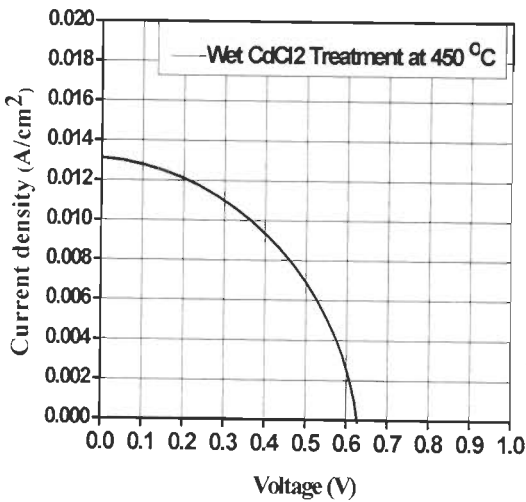
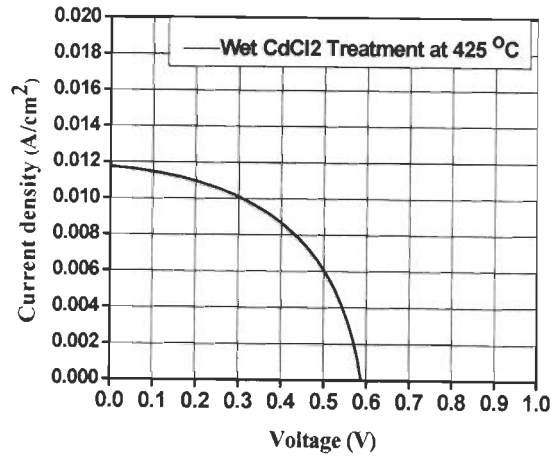
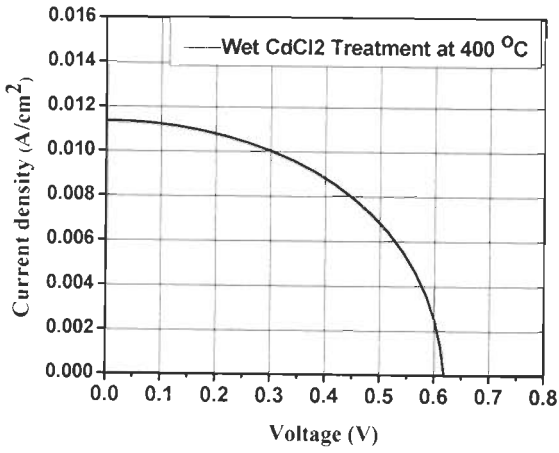
Figure A5.2: The energy band diagrams of a *p*-type semiconductor and metal after contact (a) $\Phi_m < \Phi_s$ resulting in Schottky contact and (b) $\Phi_m > \Phi_s$ resulting in Ohmic contact [185]

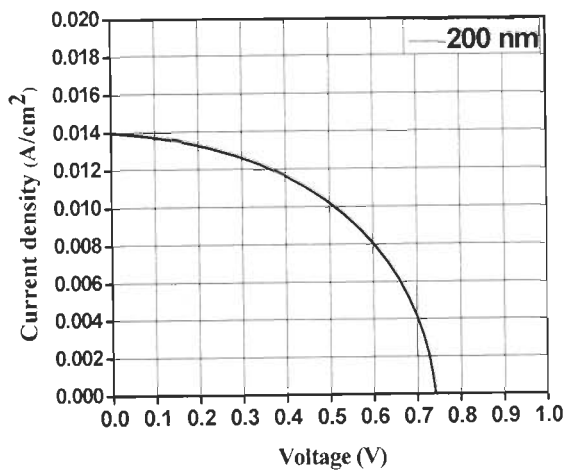
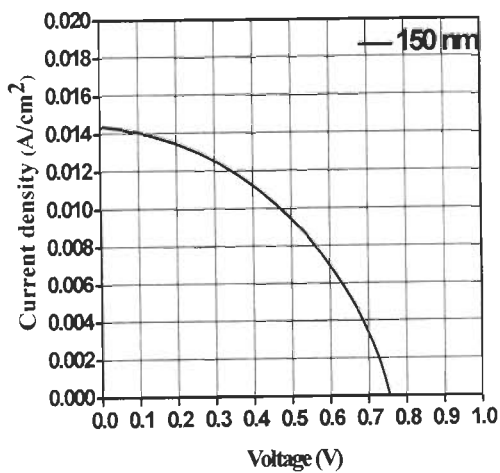
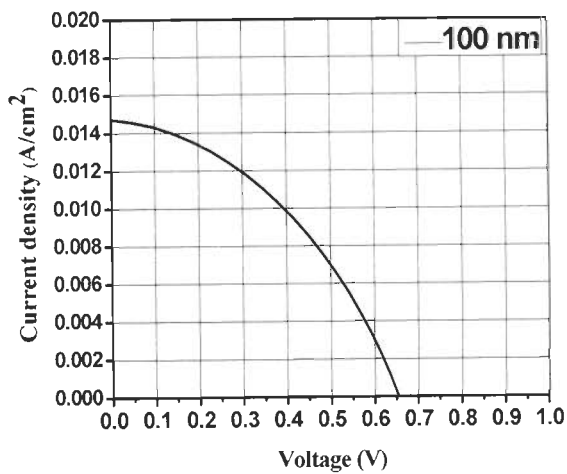
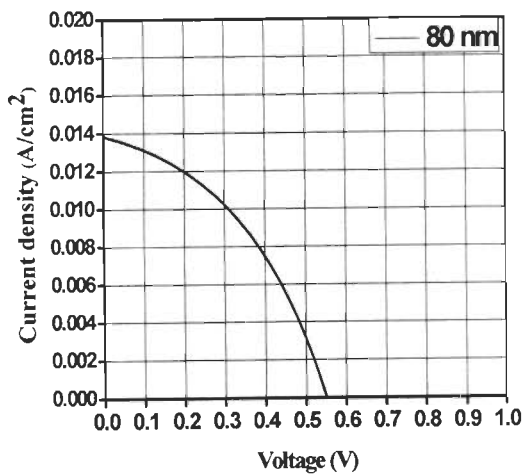
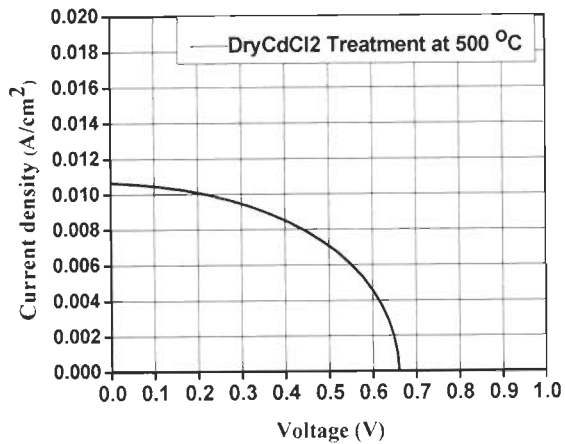
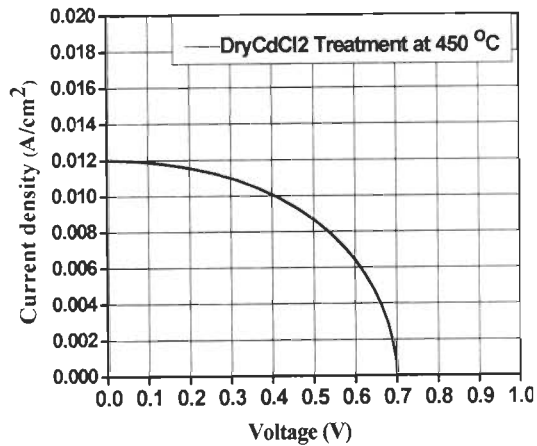
Along with work function differences, one also needs to satisfy the conditions

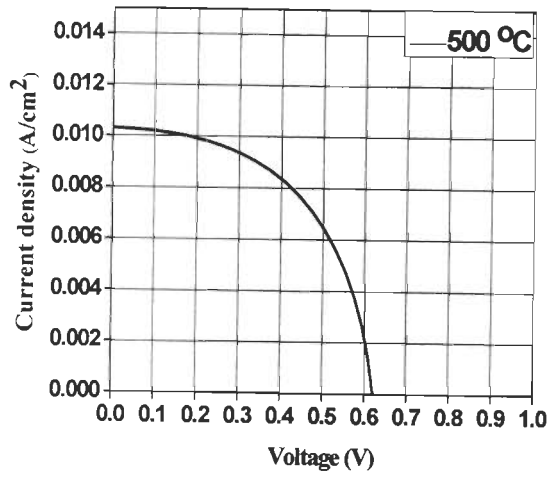
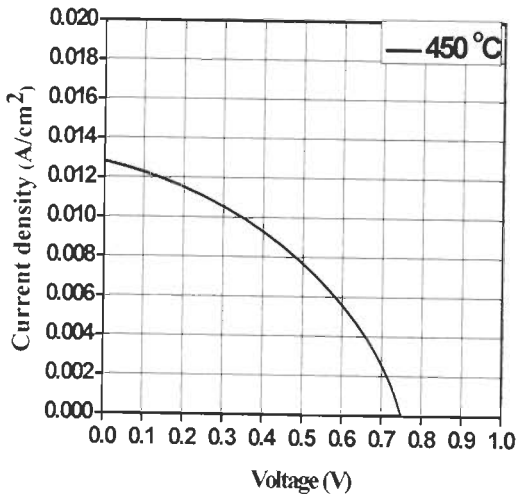
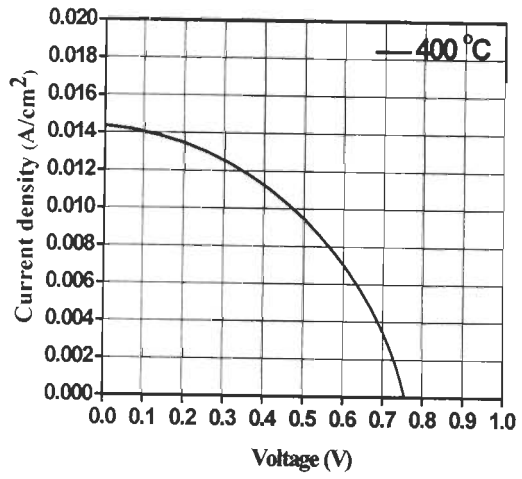
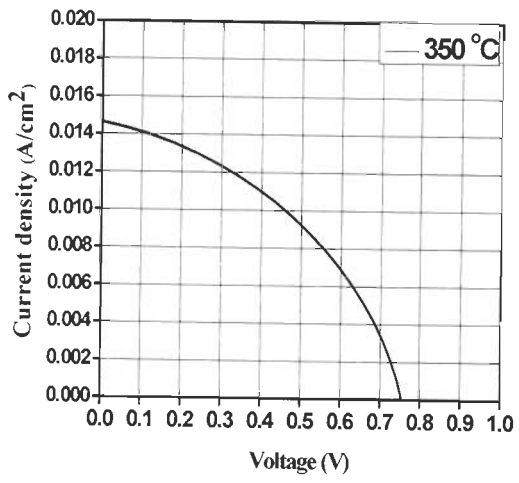
- when $\chi + E_g \leq \Phi_m$ with E_g being the band gap of the *p*-type semiconductor, a
- low-resistance ohmic *p*-type semiconductor/metal contact is formed
- When $\chi + E_g > \Phi_m$, a Schottky-junction contact is formed

The similar energy band diagrams can be shown for the *n*-type semiconductors, resulting into the Schottky and Ohmic junctions satisfying the conditions shown in Table A5.1.

A6.1 Current density-Voltage Curves









LIST OF PUBLICATIONS

1. Sonal Singhal, Amit Kumar Chawla, Sandeep Nagar, Hari Om Gupta and Ramesh Chandra “Photoluminescence measurements in the phase transition region of $Zn_{1-x}Cd_xS$ films”, *Journal of Nanoparticle Research* 12 (2010) 1415-1421.
2. Sonal Singhal, Amit Kumar Chawla, Hari Om Gupta and Ramesh Chandra, “Effect of Laser Flux Density on ZnCdS Thin Films”, *Thin Solid Films* 518 (2009) 1402-1406.
3. Amit Kumar Chawla, Sonal Singhal, Hari Om Gupta and Ramesh Chandra “Optical properties of $Zn_{1-x}Cd_xS$ nanoparticles in the quantum confinement regime”, *Current Nanoscience* 6 (2010) 94-98.
4. Sonal Singhal, Amit Kumar Chawla, Hari Om Gupta and Ramesh Chandra “Synthesis and characterization of $Zn_{1-x}Cd_xS:Mn$ nanoparticles”, *Journal of Nanoparticle Research* (Under Review).
5. Sonal Singhal, Amit Kumar Chawla, Hari Om Gupta and Ramesh Chandra “Enhanced light emission from $Zn_{0.55}Cd_{0.45}S:Mn/ZnS$ nanostructures”, *Journal of Applied Physics* (Under Review).
6. Sonal Singhal, Amit Kumar Chawla, Hari Om Gupta and Ramesh Chandra “Effect of laser fluence on ZnCdS thin films”, *International Conference on Metallurgical Coatings and Thin Films, (ICMCTF) held at San Diego, California, USA (April 27-May 01, 2009)*.
7. Sonal Singhal, Amit Kumar Chawla, Hari Om Gupta and Ramesh Chandra “Study of the structural and optical properties of $Zn_{0.55}Cd_{0.45}S:Mn/ZnS$ nanostructures”, *International Conference on Metallurgical Coatings and Thin Films, (ICMCTF) held at San Diego, California, USA (May 2-May 06, 2011)*.
8. Sonal Singhal, Amit Kumar Chawla, Hari Om Gupta and Ramesh Chandra “Study of the optical constant of ZnCdS nanocrystalline thin films for solar energy application”, *Solar Energy Materials and Solar Cells* (Under Review).

